A Cryogenic Paul Trap for the Hyperfine Structure Spectroscopy of the Nuclear Clock Isomer $^{229m}Th^{3+}$

Kevin Scharl

München 2025

Eine kryogene Paul-Falle für die Spektroskopie der Hyperfeinstruktur des Kernuhr-Isomers $^{229m}Th^{3+}$

Kevin Scharl

Dissertation
an der Fakultät für Physik
der Ludwig–Maximilians–Universität
München

vorgelegt von
Kevin Scharl
aus Landsberg am Lech

München, den 22.10.2025

Gutachter: Prof. Dr. Peter G. Thirolf
Zweiter Gutachter: Prof. Dr. Thorsten Schumm
Tag der mündlichen Prüfung: 03.12.2025

Viel Geld und noch mehr Forschungsgelder,
für Magnet- und Elektrofelder,
für Spannung, Licht und Spiegel,
gutes Vakuum hinterm Inox-Riegel.

Studenten sind da der wahre Segen,
kommen unwissend, doch sehr gelegen,
sind arbeitswillig für das hehre Ziel,
und kosten nichts oder nicht zu viel.

Arbeit und nichts als Arbeit im Labor,
über Tag und Nacht und es kommt so vor,
schafft man auch noch so besessen,
die Zeit, sie ist zu knapp bemessen.

Doch schau, in der Kammer rührt sich was.
Licht überm Untergrund, was ist denn das?
Dreh den Spiegel, den Heliumdruck nieder,
was auch immer, aber da ist es wieder!

Jetzt nur noch mehr Geld für mehr Maschinen,
die hoffentlich dem Zwecke dienen.
Mehr Spiegel, Spannung und auch Licht,
und vergesst die andere Kamera nicht.

Dann Signal, nach tollen Kurven sieht es aus!
Und alles folgt wieder dem Herrn Gauß,
oder exponentiell auf dem Weg zum Glück.
Lob den Wundern der Experimentalphysik.

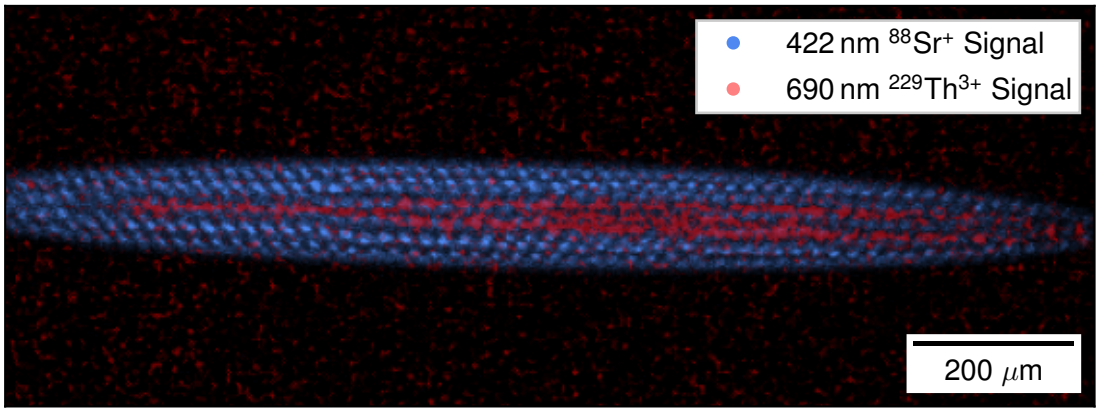

Two-color image of an $^{88}Sr^{+}$-$^{229}Th^{3+}$ Coulomb crystal recorded in June 2025. The fluorescence signal at 422 nm *wavelength from the strontium ions is depicted in blue, and the overlaid fluorescence signal at* 690 nm *wavelength from the thorium ions in red.*

Kurzdarstellung

Nach heutigem Wissensstand besitzt der isomere erste angeregte Zustand von ^{229}Th mit etwa 8.4 eV die niedrigste Anregungsenergie unter den rund 3400 bekannten Nukliden. Damit liegt dieser nukleare Zustand in der Reichweite modernster VUV-Lasersysteme und stellt einen vielversprechenden Kandidaten für die Realisierung einer Kernuhr dar. Die Entwicklung einer solchen Kernuhr ist für mehrere Forschungsbereiche von großem Interesse und hat das Potenzial, nicht nur die Grenzen der hochpräzisen Zeitmessung zu verschieben, sondern auch einen Beitrag zur Dunkle-Materie-Forschung und anderen fundamentalphysikalischen Fragestellungen als neuartiger Quantensensor zu leisten.

In der jüngsten Vergangenheit wurden mehrere Meilensteine auf dem Weg zur Kernuhr durch VUV-spektroskopische Messungen an ^{229}Th, eingebettet in einem Festkörper, erreicht. Komplementär dazu, ist der Aufbau einer kryogenen Paul-Falle an der LMU München darauf ausgelegt, $^{229(\mathrm{m})}Th^{3+}$-Ionen zu speichern, die durch gleichzeitig gefangene $^{88}Sr^{+}$-Ionen sympathetisch Doppler-gekühlt werden. Mit Fallenspeicherzeiten, die die Halbwertszeit des isomeren Zustands übertreffen, erlaubt dieser Ansatz spektroskopische Messungen der elektronischen Hyperfeinstruktur in $^{229(\mathrm{m})}Th^{3+}$. Eine solche Spektroskopie stellt eine effiziente Methode dar, zwischen den beiden Kernzuständen zu unterscheiden und bietet ein mögliches Ausleseschema für den isomeren Zustand – ein entscheidender Schritt für die Realisierung einer Kernuhr. Darüber hinaus kann der Aufbau verwendet werden, um die Vakuum-Halbwertszeit des isomeren Zustands mit höherer Präzision zu bestimmen als bisher bekannt. Langfristig soll das System auch als Plattform für die VUV-Spektroskopie des Isomers dienen und ebnet damit den Weg zu einem fallenbasierten Prototyp einer Thorium-Kernuhr.

Diese Arbeit gibt einen detaillierten Überblick über den experimentellen Aufbau an der LMU München und beschreibt mehrere Charakterisierungsmessungen, die während der Inbetriebnahme durchgeführt wurden. Außerdem beschreibt sie die erfolgreiche und zuverlässige Erzeugung von $^{88}Sr^{+}$ Ionen sowie deren Einfang und Laserkühlung in der kryogenen Paul-Falle als Ausgangspunkt für sympathetisches Kühlen von $^{229(\mathrm{m})}Th^{3+}$ Ionen. Zudem, wird die angestrebte Langzeitspeicherung von $^{229}Th^{3+}$ in einer $^{88}Sr^{+}$ Coulomb-Kristall Umgebung mit einer Temperatur von wenigen mK mit einer Lebensdauer von $\tau \approx 8000\,\mathrm{s}$ demonstriert.

Abstract

To this day, the isomeric first excited state of ^{229}Th has the lowest excitation energy of about 8.4 eV among the about 3400 known nuclides. Like this, the nuclear state is within the reach of state-of-the-art VUV laser systems and represents a candidate for the realization of a nuclear clock. The development of such a device is of high interest for several research fields and holds promise not only to push the limits of high-precision time keeping but also to contribute to dark matter and other fundamental physics research as a novel type of quantum sensor.

Only recently, several milestones towards the nuclear clock were achieved in VUV spectroscopic measurements of ^{229}Th embedded in a solid-state environment. Complementary to that, the cryogenic Paul-trap setup at LMU Munich is designed to confine $^{229(\mathrm{m})}\mathrm{Th}^{3+}$ ions that are sympathetically Doppler cooled with co-trapped $^{88}\mathrm{Sr}^{+}$ ions. With storage times exceeding the half-life of the isomeric state, this approach allows for spectroscopy measurements of the electronic hyperfine structure in $^{229(\mathrm{m})}\mathrm{Th}^{3+}$. Such a spectroscopy provides an efficient method to distinguish between the two nuclear states and represents a possible scheme for the isomeric-state readout necessary for the realization of a nuclear clock. Furthermore, the apparatus can be used to determine the vacuum ionic half-life of the isomeric state with a higher precision than the so far reported value. In the long run, the setup will also serve as a platform for VUV spectroscopy of the isomer, paving the way towards a trap-based thorium nuclear clock prototype.

This work gives a detailed overview of the experimental setup at LMU Munich and describes several characterization measurements performed during the commissioning phase. In addition, it successfully demonstrates the reliable generation of $^{88}\mathrm{Sr}^{+}$ ions as well as their confinement and Doppler cooling in the cryogenic Paul trap as the starting point for sympathetic cooling of $^{229(\mathrm{m})}\mathrm{Th}^{3+}$ ions. Furthermore, the intended long-time storage of $^{229}\mathrm{Th}^{3+}$ within a few mK $^{88}\mathrm{Sr}^{+}$ Coulomb crystal environment is shown with a lifetime of $\tau \approx 8000\,\mathrm{s}$.

Abstract

Contents

List of Figures **xiii**

List of Tables **xv**

1 Introduction and Motivation **1**
1.1 The Unique Role of ^{229m}Th . . . 1
1.2 ^{229m}Th Decay Properties . . . 2
1.3 Working Principle of an Optical $^{229}Th^{3+}$ Nuclear Frequency Standard . . 4
1.4 Possible Applications of a $^{229}Th^{3+}$ Nuclear Clock . . . 8
1.5 Current State of Research and Motivation for this Thesis . . . 9
1.6 Theoretical Treatment of the Isomeric Radiative Lifetime . . . 14

2 Theoretical Background **19**
2.1 Charged Particle Confinement in Linear Paul Traps . . . 19
2.1.1 Radial Confinement in an Ideal Paul Trap . . . 19
2.1.2 Three-Dimensional Confinement . . . 22
2.1.3 Confinement in a Real Paul Trap . . . 27
2.1.4 Cryogenic Paul Traps . . . 28
2.2 Laser Cooling of Trapped Ions . . . 28
2.2.1 Light Interaction with an Atomic Two-Level System . . . 28
2.2.2 Principles of Doppler Cooling . . . 30
2.3 Formation of Coulomb Crystals . . . 32
2.4 Sympathetic Laser Cooling of $^{229}Th^{3+}$ . . . 34
2.5 Hyperfine-Structure Spectroscopy of $^{229(m)}$Th . . . 36
2.5.1 Nuclear Moments and Hyperfine Splitting . . . 36
2.5.2 Angular Momenta . . . 41
2.5.3 Transition Intensities . . . 42
2.5.4 Isomeric Hyperfine Structure of $^{229m}Th^{3+}$ . . . 43
2.6 Electro-Optic Modulation . . . 50

3 Experimental Setup **53**
3.1 Design Aspects . . . 53
3.2 General Overview . . . 54
3.3 Extraction of $^{229(m)}Th^{3+}$ Ions . . . 55
3.4 $^{88}Sr^{+}$ Laser Ablation . . . 57
3.5 Ion Mass Filtering . . . 60
3.6 The Cryogenic Paul Trap . . . 62
3.7 Ion Detection . . . 66
3.8 Laser Setup for Doppler Cooling of $^{88}Sr^{+}$ . . . 67
3.9 Setup for HFS Spectroscopy of $^{229(m)}Th^{3+}$ . . . 72
3.10 Four-Wave Laser Incoupling into the Paul Trap . . . 77
3.11 Fluorescence Imaging . . . 78
3.12 Setup for Sr^{+} Laser Ablation Characterization Measurements . . . 82
3.13 Setup for the $^{229}Th^{3+}$ Spectroscopy in the Extraction RFQ . . . 83
3.14 Setup Control System . . . 84

4 Preparatory Measurements **87**
4.1 Characterization of the Sr^{+} Laser Ablation Source . . . 87
4.2 Trapping and Laser Cooling of Sr^{+} Ions . . . 94
4.2.1 Sr^{+} Ion Trapping . . . 94
4.2.2 Doppler Cooling of $^{88}Sr^{+}$ . . . 98
4.2.3 Linewidth of Laser Cooled Sr^{+} . . . 101
4.2.4 $^{88}Sr^{+}$Fluorescence Lifetime and Estimate of Vacuum Pressure . . . 106
4.3 Extraction of $^{229}Th^{3+}$ Ions . . . 111

5 Trapping and Sympathetic Cooling of $^{88}Sr^{+}$ and $^{229}Th^{3+}$ Ions **115**

6 $^{229}Th^{3+}$ Spectroscopy Experiments **121**
6.1 $^{229(m)}Th^{3+}$ Spectroscopy in the Extraction RFQ . . . 121
6.2 $^{229(m)}Th^{3+}$ Spectroscopy in the Cryogenic Paul Trap . . . 129
6.3 Fluorescence Lifetime of Trapped $^{229(m)}Th^{3+}$ Ions . . . 133

7 Conclusion and Outlook **135**

Appendices **139**

A HFS Calculations **141**

B SIMION Simulation Model **145**
B.1 Model Geometry . . . 145
B.2 SIMION Workbench Script . . . 156

References **161**

Publications and Presentations **179**

Acknowledgements **181**

List of Figures

1.1 The Unique Role of ^{229m}Th Among the Nuclear Isomers 2
1.2 Main Decay Processes of ^{229m}Th 3
1.3 Principle of an Optical Frequency Standard 6
1.4 Measurements of the Isomeric Excitation Energy 10
1.5 Measurements and Estimates of the Isomeric Half-Life 13

2.1 Radial Confinement in a Linear Paul Trap 21
2.2 Stable Solutions for the Mathieu Equation in Radial Direction 22
2.3 Axial Confinement in a Linear Segmented Paul Trap 23
2.4 Parabolic Fit to the Axial Trap Potential 24
2.5 Single Ion Stable Solutions of the Mathieu Equation for the Linear Paul Trap 25
2.6 Secular and Micromotion 26
2.7 Principle of Doppler Cooling 31
2.8 Shapes of Coulomb Crystals 34
2.9 Doppler Cooling Scheme of $^{88}Sr^{+}$ 36
2.10 The Four Lowest Lying Hyperfine States in $^{229}Th^{3+}$ 38
2.11 Calculated Electronic Hyperfine Transitions $5F_{5/2} \rightarrow 6D_{5/2}$ and $5F_{7/2} \rightarrow 6D_{5/2}$ in $^{229}Th^{3+}$ 40
2.12 Calculated Electronic Hyperfine Transitions $5F_{5/2} \rightarrow 6D_{5/2}$ and $5F_{7/2} \rightarrow 6D_{5/2}$ in $^{229}Th^{3+}$ with Relative Intensity Distribution 44
2.13 Calculated Electronic Hyperfine Transitions $5F_{5/2} \rightarrow 6D_{5/2}$ and $5F_{7/2} \rightarrow 6D_{5/2}$ in $^{229m}Th^{3+}$ with Relative Intensity Distribution 46
2.14 Temperature Effects on the Hyperfine Structure in $^{229(m)}Th^{3+}$ 49
2.15 Relative Power of Modulated Light 52
2.16 EOM Sideband Generation at Different Modulation Depths 52

3.1 Overview of the Cryogenic Paul-Trap Setup at LMU Munich 55
3.2 Overview of the *Buffer-Gas Stopping Cell* and the *Extraction RFQ* 58
3.3 Overview of the *Ion Guide* for $^{88}Sr^{+}$ Laser Ablation 60

3.4 Overview of the *QMS 2* for Ion Mass Filtering . . . 61
3.5 Overview of the Cryogenic Paul Trap . . . 62
3.6 Rise Time of the Trapping Voltages . . . 64
3.7 422 nm Laser Setup . . . 68
3.8 Saturated Absorption Spectroscopy of $^{85+87}$Rb . . . 69
3.9 AOM Double-Pass Setup . . . 70
3.10 Transmission and Diffraction Efficiencies of the Double-Pass AOM Setup . 71
3.11 Schemes to Address the Hyperfine Structure of $^{229(m)}Th^{3+}$ . . . 73
3.12 Outline of the RF Electronics for EOM Modulation . . . 76
3.13 Schematic of the Four-Wave Incoupling Setup . . . 77
3.14 Schematic of the Lens System for Ion Imaging . . . 81
3.15 Cryogenic Paul-Trap Setup for Strontium Ablation Characterization . . . 82
3.16 Cutaway Drawing of the Setup for $^{229}Th^{3+}$ Spectroscopy in the *Extraction RFQ* . . . 84
3.17 Hardware and Software Scheme . . . 86

4.1 Mass Scan of Ablated Ions from the $SrTiO_3$ Target . . . 88
4.2 Ablation of Sr^+ Ions at Different Pulse Energies . . . 89
4.3 Ablation Plume Temperature and Velocity with the Ablation Laser-Pulse Energy . . . 91
4.4 Ablated Sr^+ Ions with Axial Blocking Voltage . . . 92
4.5 Ablated $^{88}Sr^+$ Ions with Axial Blocking Voltage . . . 93
4.6 Axial Potentials for Sr^+ Ion Trapping and Release . . . 95
4.7 Measurement Cycle of the Loading Time Scan . . . 96
4.8 Loading Time Scan of Sr^+ . . . 97
4.9 $^{88}Sr^+$ Coulomb Crystal in Comparison with Simulations . . . 100
4.10 Resonance Scans of Trapped $^{88}Sr^+$ Ions . . . 102
4.11 $^{88}Sr^+$ Resonance Scans at 1092 nm . . . 105
4.12 Evolution of the Dark-State Dip Positions with the Laser Detuning . . . 106
4.13 Fluorescence Lifetime Measurement at Room Temperature . . . 107
4.14 Fluorescence Lifetime Measurement at Cryogenic Temperatures . . . 108
4.15 Remaining $^{88}Sr^+$ after Fluorescence Decay at Cryogenic Temperatures . . 109
4.16 Axial Potential for $^{229}Th^{3+}$ Ion Extraction . . . 111
4.17 Mass Scan of the Extracted Ions from the *Buffer-Gas Stopping Cell* . . . 112

5.1 Overall Axial Potential for $^{88}Sr^+$ Ion Loading . . . 116
5.2 Overall Axial Potential for Th^{3+} Ion Loading . . . 117
5.3 $^{88}Sr^+$-$^{229}Th^{3+}$ Coulomb Crystals in Comparison with Simulations . . . 118
5.4 $^{88}Sr^+$ Coulomb Crystal filled with $^{229}Th^{3+}$ . . . 119

6.1 Background Monitoring Strategy for $^{229}Th^{3+}$ Spectroscopy in the *Extraction RFQ* . . . 123
6.2 $^{229}Th^{3+}$ Hyperfine Structure Spectroscopy in the *Extraction RFQ* at 690 nm 124

6.3 Scaled $^{229}Th^{3+}$ Hyperfine Structure Spectroscopy at 690 nm Measured in the *Extraction RFQ* 126
6.4 $^{229}Th^{3+}$ Hyperfine Structure Spectroscopy in the *Extraction RFQ* at 984 nm 127
6.5 Scaled $^{229}Th^{3+}$ Hyperfine Structure Spectrum at 984 nm Measured in the *Extraction RFQ* 128
6.6 Two-Color Fluorescence Signal of $^{88}Sr^{+}$-$^{229}Th^{3+}$-Coulomb Crystals 131
6.7 Storage Time Measurement of Trapped $^{229}Th^{3+}$ 134

List of Tables

1.1 Isomeric Half-Lives of ^{229}Th in Crystal Structures 12
1.2 Isomeric Electromagnetic Decay Probabilities 15
1.3 Electromagnetic Single-Particle Decay Probabilities of ^{229}Th in Weisskopf Units 16
1.4 Different Reduced Transition Probabilities $B(M1)$ for ^{229}Th 17

2.1 Characteristics of the $^{88}Sr^{+}$ Laser Cooling Scheme 36
2.2 $^{229}Th^{3+}$ Hyperfine Structure Results by Campbell et al. [199] and Zitzer et al. [213] 39
2.3 Hyperfine Splitting in $^{229m}Th^{3+}$ at 690 nm 47
2.4 Hyperfine Splitting in $^{229m}Th^{3+}$ at 984 nm 48

3.1 EOM Modulation Scheme to drive the 690 nm HFS in $^{229(m)}Th^{3+}$ 74
3.2 EOM Modulation Scheme to drive the 984 nm HFS in $^{229(m)}Th^{3+}$ 75
3.3 Part Number Designation for Fig. 3.12 76
3.4 Fluorescence Photon Collection and Detection Efficiencies 80
3.5 Different Versions of the Ion Imaging System 81

4.1 Results of the $^{88}Sr^{+}$ Resonance Scans 104
4.2 DC Voltage Settings for $^{229}Th^{3+}$ Extraction 112

A.1 Hyperfine Splitting in $^{229}Th^{3+}$ 142
A.2 Hyperfine Structure Transitions in $^{229}Th^{3+}$ at 690 nm 143
A.3 Hyperfine Structure Transitions in $^{229}Th^{3+}$ at 984 nm 144

1 Introduction and Motivation

1.1 The Unique Role of ^{229m}Th

The wonder of nature lies in its unpredictability. By far not every natural phenomenon can be explained by the laws of physics, but they are indeed very helpful to make certain statements on the how and why in natural circumstances. One of these exotic, unpredicted phenomena and a true gift by nature for science that might open new research fields and may lead to more complete physical models, is the isomeric nuclear first excited state in ^{229}Th (mass number $A = 229$, proton number $Z = 90$, neutron number $A - Z = 139$).

First discovered by Otto Hahn in 1921 [1], isomers are defined as nuclei excited in a metastable state. Metastable refers herein to a lifetime of a nanosecond or more [2]. According to the Nubase2020 evaluation [3], there can be found 1938 nuclear isomers with a half-life of $t_{1/2} \geq 100\,\mathrm{ns}$ among the considered 3340 nuclear isotopes. Defining isomerism by a half-life longer than 100 ns is an arbitrary choice and does not show the complete picture, since there have also been reported fission isomeric states with picosecond half-lives [2, 4].

Usually, the excitation of nuclear states requires energies in the keV or MeV region, which can often be provided only by large accelerators. So far, ^{229m}Th with an energy lowered by three orders of magnitude is the only low-energy ($< 10\,\mathrm{eV}$) extruder among the huge amount of isomeric states.

Investigations on the nucleus of ^{229}Th date back to the late 40s of the last century [5, 6]. Roughly 30 years later, Kroger and Reich got the first indirect hints on the existence of a low-lying isomeric state in ^{229}Th from γ-spectroscopic studies [7]. Still, it took another 40 years until the first signal of an isomeric decay was observed by Lars von der Wense and his colleagues at LMU Munich [8].

Even before the existence of the thorium isomeric state was experimentally proven, it was already proposed to take advantage of the low-lying excitation energy. Peik and Tamm suggested using the thorium nucleus as an absolute reference for a frequency standard in a configuration comparable to optical atomic clocks [9]. Although the value of the transition energy was revised several times over the years and shifted more and more from the optical to the VUV range, it stayed in a frequency range reachable by state-of-the-art laser systems, as demonstrated impressively by recent laser-spectroscopic breakthrough experiments [10–12]. To underline the unique selling feature of ^{229m}Th in

comparison to other nuclear isomers and currently used references for optical atomic clocks, the excitation energy and the most recent result for the ionic half-life [13] are included in the overview plot of nuclear isomer properties shown in Fig. 1.1.

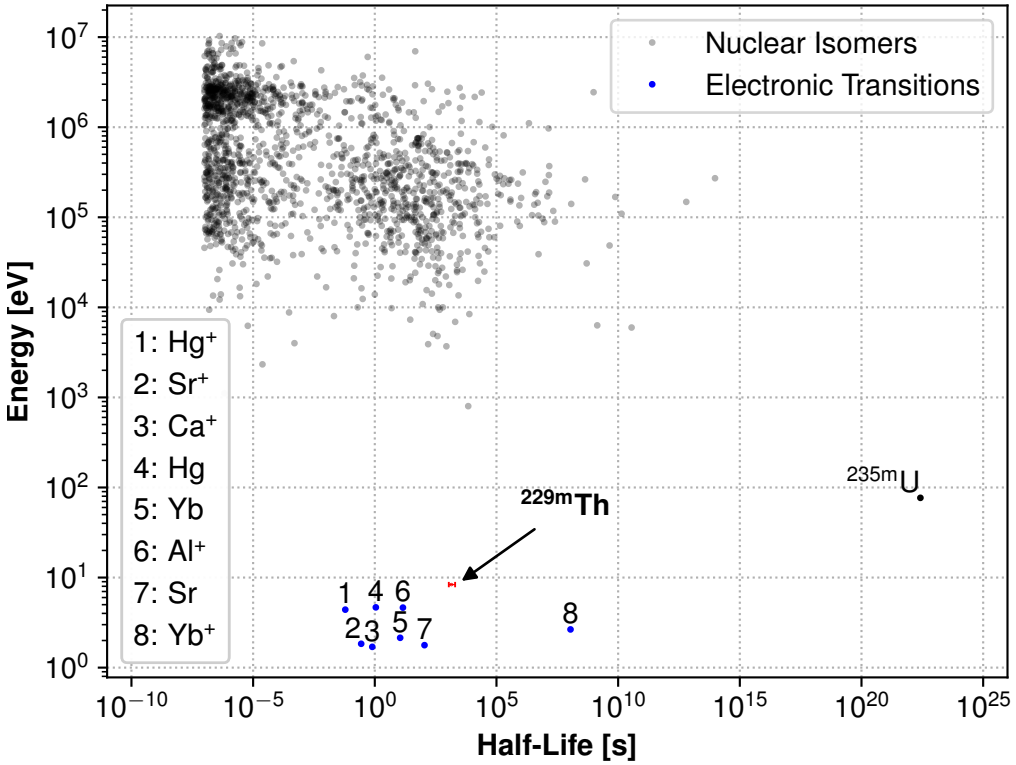

Figure 1.1 *1650 of the total 1938 isomeric states with half-lives $t_{1/2} \geq 100\,\mathrm{ns}$ listed in the NUBASE2020 evaluation of nuclear physics properties [3] are plotted versus their decay half-lives. The data of the two low energy nuclear isomers ^{229m}Th and ^{235m}U are modified and updated in comparison to the NUBASE2020 evaluation. Uranium is depicted with its radiative half-life as derived in [14, pp. 31, 32] in contrast to its internal-conversion dominated half-life of* 26 min. *The thorium isomer is plotted with the most recent energy value [12] and the so far only direct measurement of the ionic half-life [13]. To underline the prospect of ^{229m}Th as a nuclear clock candidate, a selection of electronic transitions used in current optical frequency standards is shown in blue (values taken from [15]). Own representation, adapted from [8].*

1.2 ^{229m}Th Decay Properties

The natural population of the low-energy excited isomeric state in ^{229}Th happens either via the α-decay of ^{233}U with a 2 % probability [16, 17] or via the β^--decay of ^{229}Ac with a probability of over 14 % [17, 18]. In 2024, several research groups worldwide also successfully populated the first excited state via VUV laser sources [10–12]. In contrast

to that, the focus of this work lies rather on the characterization of the isomeric decay properties.

In the case of the nuclear decay of ^{229m}Th, there can be distinguished between four main decay processes: direct photon emission (γ), internal conversion (IC), bound internal conversion (BIC) and electronic bridge (EB). All schemes are visualized in Fig. 1.2 and are briefly discussed below. For more theoretical details, see Sec. 1.6 or a more elaborate review in [14, 19].

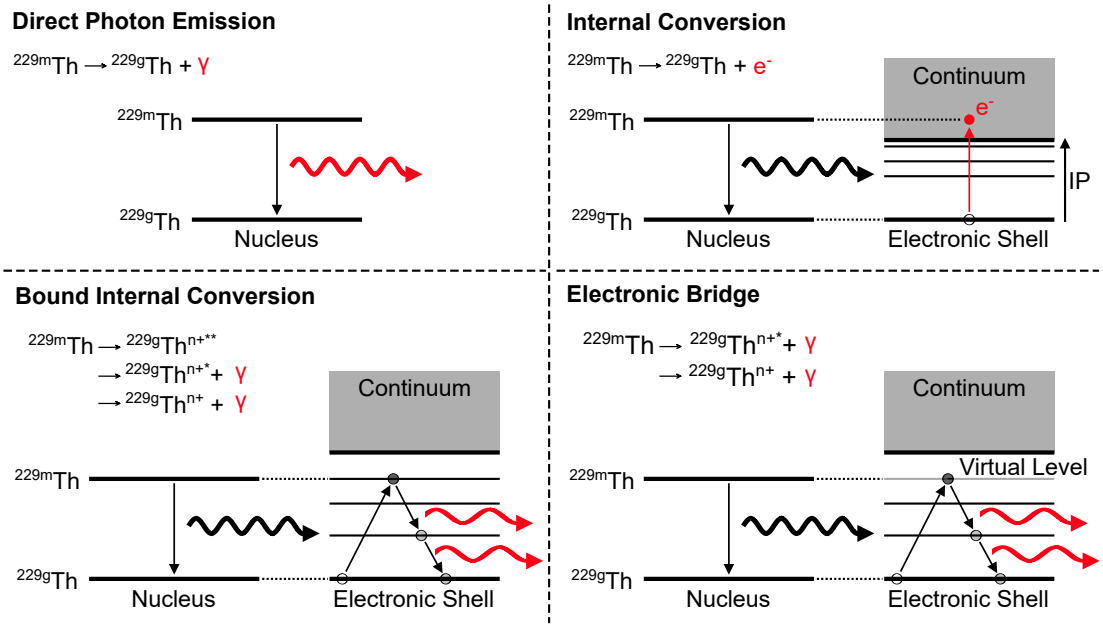

Figure 1.2 *The four main decay processes of ^{229m}Th to the ground state ^{229g}Th. Possible is a direct energy transition via photonic emission at* 8.355 732 820 024(8) eV *[12]. Internal conversion (with the ionization potential $IP \sim 6.3$ eV [20], lower than the isomeric energy), bound internal conversion, and electronic bridge decay represent indirect energy transitions via the electronic shell and the emission of either electrons or photons. The emitted particles of the individual channels are highlighted in red. Own representation, adapted from [21, p. 5].*

Direct gamma decay (see upper left image in Fig. 1.2) implies the emission of a photon with an energy corresponding to the energy difference between the nuclear ground state and the isomeric state. The most precise and only recently measured energy value is $E_\gamma =$ 8.355 732 820 024(8) eV (148.382 182 882 723(1) nm) [12]. Regarding the photonic decay, the isomeric state is rather long-lived with a half-life of $t_{1/2} = 1400^{+600}_{-300}$ s ($\tau = 2020^{+866}_{-433}$ s) measured in ^{229}Th^{3+} [13]. However, direct gamma decay is only energetically possible in ionic ^{229m}Th. As soon as it is neutralized, for example, by implantation in a solid-state material or via the interaction with a surface providing the electronic environment, the internal conversion decay will become the dominant de-excitation mode. Here, the released energy from the nucleus during the decay is transferred to the electronic shell,

resulting in electron emission into the continuum with a kinetic energy depending on its initial state, which usually lies close to the nucleus [22, pp. 98–99]. Because of the low-lying isomeric state in ^{229}Th, this process is energetically only allowed in the neutral state when the first ionization potential is reduced to 6.3067(2) eV [20]. Once opened, the internal conversion decay proceeds several orders of magnitude faster than the photonic decay with a half-life of $t_{1/2;IC} = 7(1)$ µs, which was measured in ^{229}Th neutralized on a Si surface [23]. As the half-life of the nuclear transition in thorium also strongly depends on the chemical surroundings of the nucleus [24], this value is expected to change for different surface materials [23].

If the isomeric state excitation energy is lower than the ionization potential of the atom, the IC channel will be strongly suppressed, but the released energy can still be transferred to the electronic shell within the scheme of bound internal conversion. An electronic transition with an energy exactly matching the released nuclear energy is then driven, and decay may occur via several photon emissions. As this energy matching criterion is not fulfilled in the case of ^{229}Th, the BIC has a vanishing probability and can be neglected in comparison to the first two decay channels [25]. The situation is different for the higher-order electronic bridge process, where the released isomeric energy excites a virtual state in the electronic shell, which then decays via photon emission(s) [25, 26]. Beginning in the 1990s until now, the electronic bridge has also been widely discussed to be used for the excitation of the thorium isomer [27–36], but so far no experimental evidence of its realization has been reported.

1.3 Working Principle of an Optical $^{229}Th^{3+}$ Nuclear Frequency Standard

The right choice of a frequency standard to measure time has always been a tough decision. For millennia, the Earth's rotation with an approximate periodicity of 24 h was the best choice at hand because it was universally available, reliable, and overall very stable [37, p. 20]. With the expansion of worldwide trade and ever-higher requirements for accurate and precise navigation, the position of the sun or the moon was no longer stable enough. Indeed, the duration of the day changes over the year and also differs with the location on the planet. So, alternative frequency references were needed.

Already in 1879, William Thomson (Lord Kelvin) mentioned the major advantage of atoms and their excited states as standard particles given by nature [38, pp. 61–62][15]. Atoms do not change their physical properties, are universally and abundantly available, and are absolutely alike within the same species. These characteristics make them the perfect candidates for an absolute reference and the basis of an absolute clock or frequency standard.

Even though the first idea of the atomic clock was born, it took until 1949 when the first prototype started its operation at the National Bureau of Standards (USA) under the supervision of Harold Lyons [39, 40]. However, the used absorption line in ammonia molecules did not prove to be reliable enough for a frequency standard and could not beat the accuracy of the quartz crystal oscillators used in those days. More

promising was the development of the first atomic clock based on a microwave hyperfine transition in the ground state of ^{133}Cs, built in 1955 at the National Physical Laboratory (UK) by Louis Essen and Jack Parry [41]. In the end, time measurements based on the Cs-clock turned out to be more accurate than measurements based on astronomical observations. Therefore, in 1967, the SI second was redefined as 9192631770 cycles of the hyperfine transition in the ground state of ^{133}Cs at the 13th General Conference on Weights and Measures (CGPM) and has been in use ever since. Developing clocks with higher accuracy and precision has not stopped in the 1950s, though, and with the evolution of narrowband laser sources, metrology research focused more and more on frequency standards in the optical range.

A noteworthy quantity in this regard is the so-called quality factor Q defined by the resonance frequency or clock frequency ν_c of the atomic transition used as frequency reference and its linewidth $\delta\nu$ [40]:

$$Q = \frac{\nu_c}{\delta\nu} \tag{1.1}$$

This formula illustrates how the quality of an atomic clock with respect to accuracy and stability can be improved by either using higher transition frequencies or transitions with lower linewidth. Targeting narrowband transitions in the optical range with hundreds of THz frequencies, therefore, seems evident.

In general, the building blocks for an optical atomic clock are always the same and apply also to a future thorium-based nuclear clock. All building blocks are visualized in Fig. 1.3 with the quantum-mechanical two-level system existing either in the electronic shell or the nucleus of a chosen atom as the core element. In order to use the energy of the transition in the atom as an absolute reference, it has to be continuously driven on resonance by a stabilized oscillator. Speaking of optical clocks, this oscillator is nothing else than a narrowband laser. Stabilization of the oscillator is provided by a feedback loop, indicating if the oscillator is resonantly tuned or not. The readout of a successful excitation, or in other words, the population of either state $|1\rangle$ or $|2\rangle$ of the reference atom, usually happens via the presence or the absence of fluorescence [15]. Although the fluorescence can be induced by the oscillator light itself, in many cases an additional transition between a third state to the lower reference state $|1\rangle$ or the upper reference state $|2\rangle$ is chosen to probe the oscillator tuning [15].

With a stabilized oscillator at hand, the task remains to convert the high optical frequency to the microwave or RF range to facilitate the electronic processing and the comparison to other microwave atomic clocks. Since the emergence of the femtosecond frequency comb at the end of the last century [42, 43], which was also awarded with a Nobel prize in 2005 [44, 45], a direct link between optical and microwave frequencies can be achieved without losing the stability of the optical clock [15].

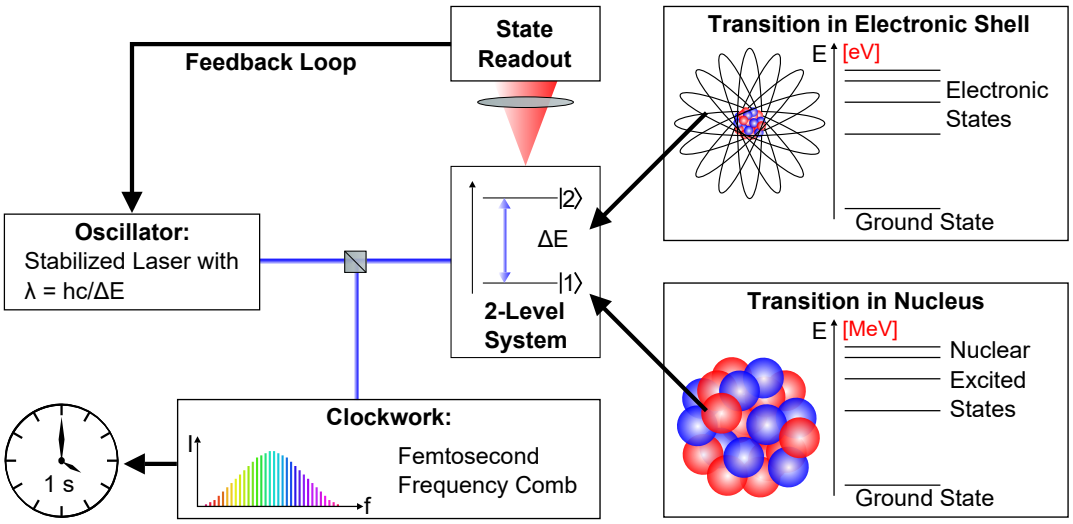

Figure 1.3 *Shown is the principle of an optical frequency standard, either based on an energy transition in the electronic shell or between nuclear states. Own representation, adapted from [25, 46–49].*

Like every other clock, atomic clocks are also limited in their stability and accuracy by external perturbations and readout errors, which systematically shift the clock frequency ν_c and can be categorized as follows [15, 50]:

Static magnetic and electric fields representing external perturbations can modify the transition of an atomic reference system via Zeeman or Stark shifts. Also, blackbody radiation resulting from non-zero temperatures at the position of the reference atom can cause Stark shifts, as well as collisions with other atoms or ions.

A second category of systematic shifts during the readout of the reference frequency is due to relativistic effects. Since the atom or ion of interest lives in a different reference frame with respect to the oscillator, an observer or another atomic clock, Doppler shifts and gravitational redshifts have to be accounted for.

Other errors during the sampling of the atomic reference can be attributed to the design of the clock apparatus and mainly have technical reasons.

Every single systematic error shifting the atomic reference frequency has to be known precisely for each individual atomic clock in order to determine its overall frequency uncertainty and to compare it with other clocks. One way to quantify the systematic frequency errors $\Delta\nu_x$ with respect to the measured reference frequency ν_0 is the fractional frequency uncertainty $\Delta\nu_x/\nu_0$ [15].

All other statistical errors appearing during variations in the frequency measurements and also from fluctuations in the systematic errors can only be characterized by increasing

the number of measurements over a long time and are expressed in the form of the so-called Allan variance [15, 51][52, p. 14]:

$$\sigma_y^2(M,\tau) = \frac{1}{2(M-1)} \sum_{i=1}^{M} [y_{i+1}(\tau) - y_i(\tau)]^2 \tag{1.2}$$

with $y_i = \left\langle \frac{\Delta\nu}{\nu_0} \right\rangle_i$ the i-th fractional frequency deviation averaged over the total sampling time τ with a sampling number M. In many cases, only the square-root value is given as the so-called Allan deviation σ_y. For more reading on the theoretical treatment and experimental determination of long-term frequency deviations, see [53, p. 50][52, p. 14].

A theoretical limit for the Allan deviation is given by the quantum projection noise arising from the statistical measurement uncertainty of entangled quantum states

$$\sigma_y(\tau) > \frac{1}{2\pi\nu_0\sqrt{NT_m\tau}} = \frac{\lambda_0}{2\pi c_0\sqrt{NT_m\tau}} \tag{1.3}$$

with the speed of light c_0 for the frequency-wavelength conversion of ν_0, the measurement or interrogation time $T_m = \tau/M$ of a single measurement, and the number of interrogated atoms N [15, 50, 54]. This expression underlines once again the aim for high transition frequencies or short wavelengths in combination with a large number of atoms and long averaging times to achieve the best stability.

Today's most precise and stable atomic clocks are NIST's most recent version of the $^{27}Al^+$ quantum-logic clock [55] and JILA's ^{87}Sr optical lattice clock [56], both with systematic frequency uncertainties in the 10^{-19} range and clock stabilities of $\sigma(\tau) = 3.5 \times 10^{-16}/\sqrt{\tau/s}$ (measured) and $\sigma(\tau) = 5 \times 10^{-17}/\sqrt{\tau/s}$ (expected), respectively.

According to the estimated systematic error budget compilation by Campbell et al. [57], an optical clock based on the first nuclear transition in $^{229}Th^{3+}$ would be even more accurate than that with a total frequency uncertainty of around 1.5×10^{-19}. Further following Campbell's approximation for the long-term frequency instability of a single ion clock with the most recent energy value of the nuclear transition [12] ends up at $\sigma(\tau) \approx 5 \times 10^{-16}/\sqrt{\tau}$ (see also [25]).

The extraordinary low inaccuracy for a nuclear clock mainly results from the lower susceptibility to external perturbations from electric and magnetic fields, leading to systematic shifts of the clock frequency like Stark or Zeeman shifts in usual atomic clocks [9]. This can be explained by the nuclear moments (magnetic dipole moments and electric quadrupole moments) being up to 9 orders of magnitude smaller than the electronic moments [25], as well as by the smaller size of the nucleus in comparison to the electronic shell. In contrast to modern atomic clocks involving electronic transitions, the expected long-term stability of a nuclear clock is limited, though. Estimates for different types of clock concepts comprising trapped ion setups with one or more particles or a solid-state approach with thorium embedded in a crystal lattice are discussed in [25]. Eventually, the choice of concept for a nuclear clock will be a trade-off between the maximum stability and the required averaging time to reach the desired accuracy level of the clock.

1.4 Possible Applications of a $^{229}Th^{3+}$ Nuclear Clock

In the first place, a nuclear clock is expected to be a very accurate and precise frequency standard, which would still outperform hitherto existing atomic clocks. From a practical point of view, a future nuclear clock could then contribute to a more accurate definition of the SI second, which is expected to be enacted around 2030. Also closely linked to a more accurate time measurement is the further development of global satellite-based navigation systems like the Global Positioning System (GPS) to narrow down positional uncertainties from the current m [58, p. 44] to the cm or sub-cm range, which could be a breakthrough in, e.g., autonomous driving [59, 60].

Another important application within the scope of geodesy is the use of highly accurate and precise clocks in combination with global navigation satellite systems as gravitational field sensors to determine the Earth's geoid [61]. Changes in the gravitational field corresponding to sub-cm height differences due to, e.g., tectonic movements, ground uplifts, or filling magma chambers could be detected within a network of synchronized clocks with accuracies better than 10^{-18} [62]. Like this, a thorium nuclear clock could be part of a world-spanning early warning system for earthquakes or volcanic eruptions. For more details, see [59, 63] and references therein.

However, in view of constant progress in accuracy and stability of the "traditional" atomic clocks in the next years, the focus of a future thorium nuclear clock for physical research will shift more and more to quantum sensing for fundamental physics than on precise time-keeping, as also pointed out in [25]. Furthermore, with the nuclear transition being sensitive not only to weak and electromagnetic interactions but also to the strong interaction, the nuclear clock is expected to open the door to identifying effects of new physics beyond the standard model of particle physics [60].

One prominent topic in this context is the measurement of temporally varying fundamental constants [64, 65] like the fine-structure constant α or the coupling constant of the strong interaction, which was already remarked by Peik and Tamm in their first proposal for the nuclear clock back in 2003 [9].

According to theoretical studies, the nuclear transition from the first excited state in ^{229}Th would be more sensitive by several orders of magnitude to variations in α and the strong interaction parameter m_q/Λ_{QCD} [66, 67]. In the case of the fine-structure constant, the sensitivity of the transition frequency to $\dot{\alpha}$ is expressed by the so-called enhancement factor K. Following Berengut et al. [68], it can be determined by comparing the electric quadrupole moments deduced from electric hyperfine measurements and the squred nuclear mean charge radii in the nuclear ground state and the isomeric state. Based on the experimental findings in [12], Beeks et al. [69] provided an approximation for the K-factor and predicted a three orders of magnitude enhancement of the nuclear transition over electronic shell transitions. Their calculations further indicate that the octupole deformation of the nucleus during the transition may affect the sensitivity to an α variation. The sensitivity of the nuclear transition to variations in fundamental constants has also been discussed with different theoretical models in Refs. [66, 70–74]. However, in order to deliver a final answer for the enhancement factor, more theoretical

and experimental investigations into the nuclear properties of the ^{229}Th isomer have to be done.

Strongly linked to the variation of fundamental constants is the search for dark matter [75]. Ultralight dark matter candidates, like e.g., axion-like scalar fields or topological features like monopoles or domain walls traveling through the universe, can change the frequencies of electronic and nuclear transitions by varying, for example, the fine-structure constant [76–80]. Within a worldwide network of synchronized atomic and potentially more sensitive nuclear clocks performing comparative frequency measurements, such variations could be probed [25, 60].

For more detailed information on the application fields of the thorium nuclear clock, the reader is referred to the reviews in [25, 46, 59, 60, 63, 81].

1.5 Current State of Research and Motivation for this Thesis

It was 2016, when the isomeric state in ^{229}Th was finally directly experimentally confirmed [8], but investigations on $^{229(\mathrm{m})}$Th date back to the 1970s [7] and are still ongoing. Several review articles give a good overview of the research progress until 2021 [14, 25, 81, 82], which is why this chapter's focus is on the most recent publications.

For the realization of a nuclear frequency standard based on the isomer's photonic transition, there are two main properties of interest: the transition energy and the isomeric state's half-life or lifetime. The progress made over the years to determine or to further explore these two properties is also visualized in Fig. 1.4 and Fig. 1.5.

After over 40 years of rough estimates or measurements with high uncertainties, Seiferle et al. performed a groundbreaking experiment at LMU Munich to determine the isomeric energy and reduce the uncertainty by one order of magnitude [83]. The result, based on the kinetic energy of electrons released in the internal conversion decay channel, was confirmed a little later with the same precision in magnetic microcalorimetry measurements [84]. Another milestone experiment followed in 2022 at the ISOLDE facility (CERN), where the isomeric radiative decay was observed for the first time after the implantation of β-decaying ^{229}Ac in large-bandgap crystals [85]. The VUV spectroscopy of the emitted photons could provide an improved value for the isomeric energy and reduce the uncertainty by another order of magnitude. Moreover, the advantage of solid-state crystals with a large number of implanted thorium atoms (up to $10^{18}\,1/\mathrm{cm}^3$ [12, 86, 87]) has been demonstrated, and the reduced range where to search for the isomeric decay paved the way for the major progress made in 2024.

By focusing VUV light generated by a pulsed four-wave mixing laser on a CaF_2 crystal doped with $^{229}Th^{4+}$, Tiedau et al. could, for the first time, directly excite the nuclear transition at PTB, Braunschweig [10]. Now working with laser spectroscopic precision, the uncertainty of the energy value could be further reduced by three orders of magnitude. Shortly after, a similar experiment performed with a thorium-doped $LiSrAlF_6$ crystal at UCLA confirmed the PTB results [11].

Even those results were outperformed in the same year by a high-precision absolute frequency measurement (already mentioned above) of the transition energy in thorium-doped CaF_2 with a VUV frequency-comb and the simultaneous comparison with a ^{87}Sr atomic clock at JILA, Boulder [12]. This experiment can also be understood as a solid-state nuclear clock prototype, and there are investigations ongoing to further characterize the nuclear transition in the crystal structures by studying, e.g., dopant concentrations or temperature dependencies [88–90]. At the same time, several research groups worldwide are working on and have already achieved the development of a narrowband continuous-wave VUV laser source to be implemented as the final oscillator in a nuclear clock [91–93].

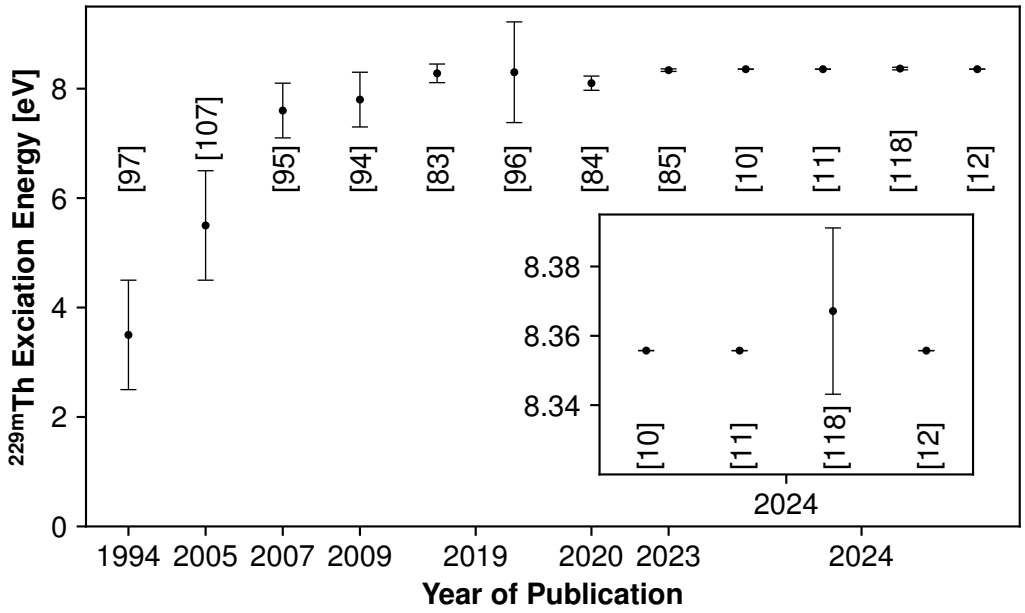

Figure 1.4 *Evolution of excitation energy measurements of ^{229m}Th over the last thirty years. The second value of Beck et al. [94] is only an improved re-analysis of their previous result [95].*

Scarcely less complex than the search for the isomeric transition energy is the precise determination of the isomeric decay time (half-life $t_{1/2}$ or lifetime $\tau = t_{1/2}ln2$) of the M1 transition between the low-lying $I = 3/2^+$ state and the $I = 5/2^+$ ground state, which defines the minimum linewidth of a thorium nuclear clock transition.

A more theoretical summary of the electromagnetic decay properties of a nucleus is given in Sec. 1.6, whereas here the focus is more on the history of research on the isomeric half-life:

Already in 1994, Helmer and Reich gave an estimate for the half-life of the isomeric decay in ^{229}Th based on their experimental result for the isomeric energy of 3.5(10) eV and the reduced transition probability $B(M1)$ (see also Sec. 1.6 for more information) of the similar M1 transition in ^{233}U to end up at 45^{+75}_{-25} h [97]. A little later in 1998,

Dykhne and Tkalya arrived at a much lower approximation for the half-life boundaries at a maximum of 2.5 h and a minimum of 10^{-2} s, based on a new calculation of the reduced transition probability [98] and an updated isomeric energy value of 3.5(5) eV provided by Irwin et al. [99]. They also took into account the existence of an isomeric decay via the electronic bridge decay channel, which would reduce the half-life. Shortly after, another theoretical approach to determine the isomeric half-life in thorium dioxide $^{229}ThO_2$ by Tkalya et al. [100, 101] especially took into account the influence of a dielectric medium on the isomeric half-life in comparison to an isolated nucleus in vacuum. Considering transition energies between 2.5 eV and 4.5 eV and a refractive index of $n = 2$ in $^{229}ThO_2$, the half-life would lie between 10 min and 1 h compared to the vacuum half-life of 80 min and 8 h [101]. The scaling of half-lives measured in solids with $\propto n^3$ (n being the index of refraction at the wavelength of the isomeric transition) to get an approximation for the vacuum value will be very important for the more recent results.

Browne et al. performed a γ-ray spectroscopy experiment with a ^{229}Th extracted from a ^{233}U source to search for the isomeric decay at 3.5 eV. From the negative outcome of their experiment, they concluded an isomeric half-life of either $t_{1/2} < 6$ h or $t_{1/2} > 20$ d [102]. In 2006, Ruchowska et al. used the quasiparticle-plus-phonon model including Coriolis coupling [103–105] to provide a theoretical update for the reduced transition probability of the isomeric state $B(M1) = 0.025\mu_N^2$. This was then used to estimate the half-life as a function of the transition energy according to $t_{1/2} = 10.95\,\mathrm{h}/E_\gamma B(M1)$ [106]. With the back then most cited and accepted isomeric excitation energy value of 3.5(10) eV they assumed a half-life of 10^{+18}_{-5} h, and with an energy value of 5.5(10) eV taken from [107] they concluded a half-life of $2.6^{+2.2}_{-1.0}$ h.

One year later, Beck et al. reported a revised value of 7.6(5) eV for the isomeric transition energy, based on high-resolution microcalorimeter γ-ray spectroscopy using a double-difference analysis of transitions between rotationally excited states at 29 keV and 42 keV [95]. Applying the same scaling approach as Helmer and Reich [97], they could estimate the isomeric half-life to be ~ 5 h.

Only in 2015, another theoretical estimate for the radiative half-life of the isomeric state as a function of the isomer's transition energy E_{is} was provided [108]:

$$0.46 \times 10^6\,\mathrm{s\,eV^3}/E_{is}^3 \leq t_{1/2} \leq 1.5 \times 10^6\,\mathrm{s\,eV^3}/E_{is}^3 \tag{1.4}$$

$$0.66 \times 10^6\,\mathrm{s\,eV^3}/E_{is}^3 \leq \tau \leq 2.2 \times 10^6\,\mathrm{s\,eV^3}/E_{is}^3 \tag{1.5}$$

In general, the connection between the half-life $t_{1/2}$ and the lifetime τ is given by $\tau = t_{1/2}/ln(2)$. Inserting the most recent energy value for the isomeric transition from Zhang et al. [12] into this parametrization results in a possible range for the isomeric half-life of $800\,\mathrm{s} \lesssim t_{1/2} \lesssim 2600\,\mathrm{s}$.

After the first direct observation of the thorium isomer via its internal conversion decay, von der Wense et al. also gave a lower limit of 60 s for the ionic nuclear lifetime, which could not be further investigated due to limited ion storage times in their room-temperature experimental setup [8].

In another theoretical work by Minkov and Pàlffy in 2017, the reduced magnetic dipole and electric quadrupole transition probabilities were re-evaluated [109]. Their

value of $B(M1) = 0.0076$ W. u. in combination with the Eq. (1.4) and Eq. (1.5) and the most recent transition energy value given in [12] provides an estimate for the isomeric half-life lying around 5000 s, which is clearly overestimated regarding the recent experimental results. Also, an update of their theoretical model in 2019 [110] based on new experimental findings on the magnetic dipole moment in [111] did not change this estimate.

In 2021, Shigekawa et al. experimentally derived the reduced transition probability for $B(\Lambda L) = B(M1)$ for magnetic dipole transitions ($\Lambda = M$, $L = 1$, see also in next section) of states belonging to the $5/2^+[633]$ and the $3/2^+[631]$ orbitals from coincidence measurements between γ rays and α particles emitted from a ^{233}U source. By applying the Alaga rule (see [112–114]), they could estimate the reduced transition probability of the first excited isomeric state to be $B(M1) = 0.014(3){\mu_N}^2$ and the respective isomeric half-life for the ground state transition energy of 8.28 eV (taken from [83]) to be 5000(1100) s [115].

With the ISOLDE measurement in 2022 began the series of milestone measurements of the radiative decay in crystals (or thin films, respectively). In all cases, radiative half-lives were measured and scaled with the refractive index n of the chemical environment to extrapolate the vacuum half-life with $t_{1/2;vac.} = t_{1/2;n} \times n^3$, as already shown in [100, 101, 108] and summarized in Tab. 1.1:

Table 1.1 *Results of isomeric half-life measurements of ^{229}Th embedded in different crystal environments. The actually measured half-life $t_{1/2;n}$ is scaled with the refractive index n at the wavelength of the isomeric transition to get an estimate for the vacuum half-life $t_{1/2;vac.}$.*

Measurement	Crystal	n	$t_{1/2;n}$	$t_{1/2;vac.}$
Kraemer et al. [85]	^{229}Th:MgF_2	1.488	670(102) s	2210(340) s
Tiedau et al. [10]	^{229}Th:CaF_2	1.586 [116, 117]	630(15) s	1740(50) s
Hiraki et al. [118]	^{229}Th:CaF_2	1.588	447(25) s	1790(102) s
Elwell et al. [11]	^{229}Th:$LiSrAlF_6$	1.485 [119]	406(17) s	1289(55) s
Zhang et al. [12]	^{229}Th:CaF_2	1.586 [116, 117]	444(3) s	1773(11) s
Zhang et al. [88]	$^{229}ThF_4$ on Al_2O_3	1.95(30)	104(11) s	771(86) s
	$^{229}ThF_4$ on MgF_2	1.95(30)	106(8) s	786(65) s

Depending on the chosen crystal structure, the estimate of the refractive index for the VUV wavelength, and the experimental method, huge differences are visible. The results from the thorium thin film experiments [88] deviate from the other estimates of the isomeric half-life. As the model for the approximation of the half-life with the refractive index is only valid for thorium implanted in the crystal bulk, the applicability of

the model for all of the results is questionable. Apart from the thin film experiments with near-surface thorium only, the implantation depth of ^{229}Th in the MgF_2 crystal is also reported to be shallow [85]. Elwell et al. performed density functional theory calculations and explained their short-timescale fluorescence half-life with crystal-induced quenching processes [11]. Nevertheless, the three independent experiments with the same crystal type performed by Tiedau et al. [10], Hiraki et al. [118], and Zhang et al. [12] provided results that agree within their respective uncertainties.

So far, only one direct measurement of the ionic vacuum half-life by Yamaguchi et al. exists with $t_{1/2} = 1400^{+600}_{-300}$ s [13]. It was obtained in combination with a measurement of the electronic hyperfine structure of $^{229(m)}Th^{3+}$ in a room-temperature buffer-gas environment, which possibly caused the rather large uncertainty.

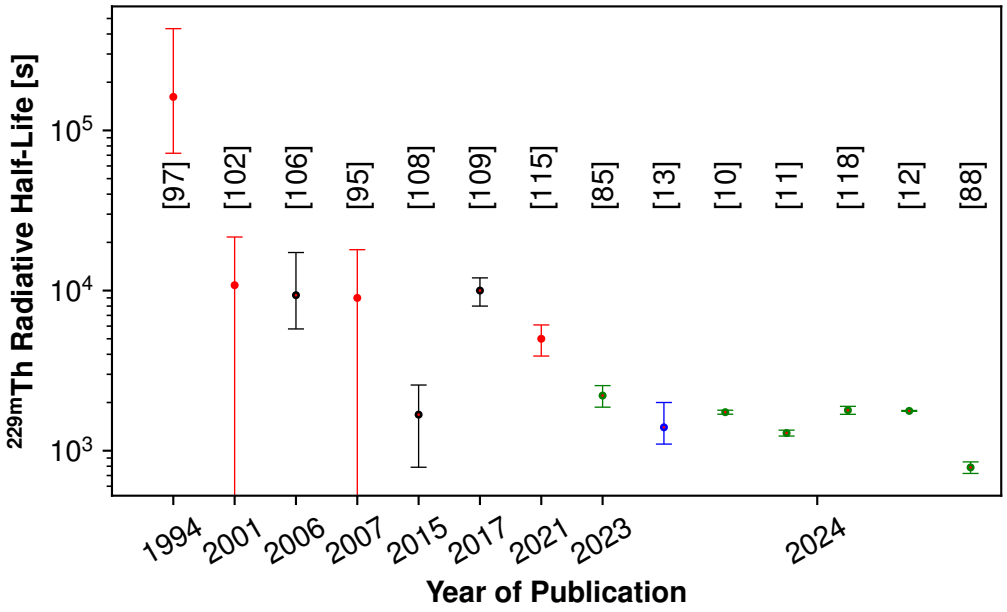

Figure 1.5 *Evolution of approximations, theoretical estimates, and measurements of the decay half-life of ^{229m}Th. Estimates based on experimental results are shown in red, and theoretical work is shown in black. The value presented for Ruchowska et al. [106] is calculated with the energy value given in [107]. In the case of Tkalya et al. [108], the theoretical boundaries for the half-life value are calculated for the most recent energy value by [12]. The only decay time data recorded with trapped ions is visualized in blue, and the green data points are based on isomeric decays measured in a crystal environment and are scaled by n^3 to the vacuum value.*

The need for a more precise measurement of the ionic vacuum lifetime of the isomeric state to assess the natural linewidth of the nuclear transition, as well as the quality factor of a future nuclear clock, is the main motivation for this work and the experimental setup described and characterized in the following chapters.

1.6 Theoretical Treatment of the Isomeric Radiative Lifetime

Since the focus of this work lies on the long-lived isomeric lifetime of isolated ions, the theoretical descriptions below are restricted to the γ decay of the thorium isomer. See the references [25, 120, 121] and further mentioned literature therein to get more information on the underlying theoretical physics of the internal conversion, bound internal conversion, or electronic bridge processes.

Due to their smaller size and their location shielded by the electronic shell, nuclei usually do not easily interact with other particles. So, they predominantly transfer energy not via collision processes (nuclear stopping) but mainly via electromagnetic interactions (electronic stopping) [22, pp. 90–91]. Furthermore, it is not sufficient to restrict the treatment of the nuclear decay to simple electromagnetic dipole transitions as in the atomic shell. In fact, also higher-order multipole radiation has to be taken into account [22, pp. 90–91].

The Hamiltonian describing the interaction of the nucleus with electromagnetic radiation can be written as

$$H_{int} = \int \rho(\mathbf{r},t)\Phi(\mathbf{r},t)d\mathbf{r} - \int \frac{1}{c}\mathbf{j}(\mathbf{r},t)\mathbf{A}(\mathbf{r},t)d\mathbf{r} \tag{1.6}$$

with the electric charge density $\rho(\mathbf{r},t)$, the electric scalar potential $\Phi(\mathbf{r},t)$, electric current density $\mathbf{j}(\mathbf{r},t)$, and the magnetic vector potential $\mathbf{A}(\mathbf{r},t)$ [122, p. 97][21, p. 29][123, p. 379]. Assuming a constant magnetic field extending over the nuclear volume, the link to the involved electric and magnetic fields $\mathbf{E}$ and $\mathbf{B}$ is given by [122, pp. 97, 98]

$$\mathbf{E} = -\nabla\Phi(\mathbf{r},t) \tag{1.7}$$

$$\mathbf{B} = \nabla \times \mathbf{A}(\mathbf{r},t) \tag{1.8}$$

Further following [122, p. 203][21, p. 29], the probability for an electromagnetic transition from an initial state $|\psi_i\rangle = |I_i, m_i\rangle$ to a final state $|\psi_f\rangle = |I_f, m_f\rangle$ defined by the nuclear angular momentum I and its z-component m with a state density of $g(E_f)$ can be expressed by Fermi's Golden Rule and is also a direct link to the rate Γ and the half-life $t_{1/2}$ of the transition

$$\Gamma = \frac{2\pi}{h}|\langle I_f, m_f|\,\mathrm{H_{int}}\,|I_i, m_i\rangle|^2 g(E_f) \tag{1.9}$$

$$t_{1/2} = ln(2)\tau = ln(2)/\Gamma \tag{1.10}$$

As the static electric and magnetic potentials involved in photon emission (and absorption) can also be expressed in a multipole expansion [123, pp. 91–95], the transition probability reduces to

$$\Gamma_{fi} = \frac{8\pi(L+1)}{\hbar L[(2L+1)!!]^2}(k)^{2L+1}|\langle I_f, m_f|\,\mathcal{M}(\Lambda, kL\sigma)\,|I_i, m_i\rangle|^2 \tag{1.11}$$

where $\mathcal{M}(\Lambda, kL\sigma)$ denotes the multipole transition operator dependent on the type of transition Λ, which can be either electric or magnetic (E or M), the wave vector $k = E_\gamma/(\hbar c)$, the multipolarity $L \in 1, 2, 3, 4, ...$ (dipole, quadrupole, octupole, hexadecapole,...), and the polarization σ of the electromagnetic wave resulting from the orientations of the involved angular momenta [122, p. 204][21, p. 29].

After some further approximations and evaluations using either the Wigner–Eckart theorem and the 3j symbol or the Clebsch–Gordan coefficients (see also Sec. 2.5), this expression can be further reduced to

$$\Gamma(\Lambda L; I_i \to I_f) == \frac{8\pi(L+1)}{\hbar L[(2L+1)!!]^2} \left(\frac{E_\gamma}{\hbar c}\right)^{2L+1} B(\Lambda L; I_i \to I_f) \tag{1.12}$$

with the previously mentioned reduced transition probability $B(\Lambda L; I_i \to I_f)$ [122, pp. 204–205][123, pp. 380–383].

To further assess these reduced transition probabilities, the multipolarity L and the parity $\Pi_{i,f}$ of the involved states have to obey the following selection rules [122, p. 205]:

$$|I_i - I_f| \leq L \leq I_i + I_f \qquad \text{and} \qquad \Pi_i \Pi_{\Lambda L} \Pi_f = 1 \tag{1.13}$$

$$\Pi_{EL} = (-1)^L \qquad \text{for electric transitions} \tag{1.14}$$

$$\Pi_{ML} = (-1)^{(L+1)} \qquad \text{for magnetic transitions} \tag{1.15}$$

For the first three values of L and Π, the probabilities for electric or magnetic transitions (type indicated by Λ) are given in Tab. 1.2:

Table 1.2 *Transition probabilities for the isomeric decay of ^{229}Th with the related reduced transition probabilities. Table adapted from [122, p. 206][123, p. 382].*

Λ	L	Parity change	$\Gamma(\Lambda L)$ [1/s]
E	1	yes	$\Gamma(E1) = 1.59 \times 10^{15} E_\gamma^3 B(E1)$
E	2	no	$\Gamma(E2) = 1.22 \times 10^{9} E_\gamma^5 B(E2)$
E	3	yes	$\Gamma(E3) = 5.67 \times 10^{2} E_\gamma^7 B(E3)$
E	4	no	$\Gamma(E4) = 1.69 \times 10^{-4} E_\gamma^9 B(E4)$
M	1	no	$\Gamma(M1) = 1.76 \times 10^{13} E_\gamma^3 B(M1)$
M	2	yes	$\Gamma(M2) = 1.35 \times 10^{7} E_\gamma^5 B(M2)$
M	3	no	$\Gamma(M3) = 6.28 \times 10^{0} E_\gamma^7 B(M3)$
M	4	yes	$\Gamma(M4) = 1.87 \times 10^{-6} E_\gamma^9 B(M4)$

with the transition energy E_γ in MeV, $B(EL)$ in $\mathrm{e^2fm^{2\lambda}}$ and $B(ML)$ in $\mathrm{e\hbar/(2mc)^2(fm)^{2\lambda\text{-}2}}$ [122, p. 206][123, p. 382].

For a better comparison of the calculated or observed electromagnetic transition rates, the reduced transition probability is often given in Weisskopf units. This unit implies a simplification of the EL or ML matrix elements based on a single-particle transition within the nuclear shell model and is given as a function of the multipolarity L and the nuclear mass number A [123, p. 389]:

$$B_{W.u.}(EL) = \frac{1.2^{2L}}{4\pi}\left(\frac{3}{L+3}\right)^2 A^{2L/3} e^2(\mathrm{fm})^{2L} \tag{1.16}$$

$$B_{W.u.}(ML) = \frac{10}{\pi}1.2^{2L-2}\left(\frac{3}{L+3}\right)^2 A^{(2L-2)/3}\left(\frac{e\hbar}{2Mc}\right)^2 (\mathrm{fm})^{2L-2} \tag{1.17}$$

Considering the isomeric decay of ^{229}Th, the involved states in the electromagnetic transitions are $|I_i, \Pi_i\rangle = |3/2, +\rangle$ and $|I_f, \Pi_f\rangle = |5/2, +\rangle$. On the basis of the selection rules and parity conservation, this implies four different multipolarities $L \in \{1, 2, 3, 4\}$ and four possible decays via E2, E4, M1 or M3. In Weisskopf units, the single particle transition probabilities are then given in Tab. 1.3:

Table 1.3 *Single-particle transition probabilities for the isomeric decay of ^{229}Th with the reduced transition probabilities in Weisskopf units. $\mu_n = \frac{e\hbar}{2Mc}$ denotes the nuclear magneton.*

Λ	L	$B_{W.u.}$	$\Gamma(\Lambda L)$ [1/s]
E	2	83.23 $\mathrm{e^2fm^4}$	$\Gamma(E2) = 1.02 \times 10^{11} E_\gamma^5$
E	4	123361.93 $\mathrm{e^2fm^8}$	$\Gamma(E4) = 2.08 \times 10^{-5} E_\gamma^7$
M	1	1.79 μ_N^2	$\Gamma(M1) = 31.51 \times 10^{12} E_\gamma^3$
M	3	3115.22 $\mu_n^2\mathrm{fm}^4$	$\Gamma(M3) = 19.56 \times 10^{3} E_\gamma^7$

Due to the low isomeric excitation energy in ^{229}Th, the probability for an electric quadrupole transition E2 is usually assumed to be negligibly small in comparison to the magnetic dipole transition M1 [109]. In the review of Sec. 1.5, several works were already mentioned that used different values of the reduced transition probability to estimate the isomeric half-life. Below, these values are once again listed in Tab. 1.4 and used to calculate the isomeric half-life according to the formula for $\Gamma(M1)$ (see Tab. 1.3) with the most recent isomeric energy value for the isomer taken from [12].

Table 1.4 *Different reduced transition probabilities for a magnetic dipole decay of the ^{229m}Th in SI and Weisskopf units as well as the resulting estimate for the decay half-life.*

Reference	$B_{SI}(M1)$	W.u.	$t_{1/2}$ [s]
[97]	0.0061 μ_N^2	0.0034	11089
[98]	0.086 μ_N^2	0.048	785
[106]	0.025 μ_N^2	0.014	2693
[109]	0.0136 μ_N^2	0.0076	4961
[115]	0.014(3) μ_N^2	0.008(2)	4712(1178)

The calculated estimates show huge differences and none of them lies within the error margin of the experimentally deduced half-life by Yamaguchi et al. [13]. So, these results emphasize once more the need for a precise in-vacuum half-life measurement.

2 Theoretical Background

2.1 Charged Particle Confinement in Linear Paul Traps

The basic idea of an ion trap is the confinement of charged particles at a defined point in space by electric fields only. For the realization of that, a repelling electric force dependent on the distance r_0 to the trapping point is needed to act on the ions. This can be achieved by letting the charged particles move in a three-dimensional parabolic potential around the desired point in space [124, 125]:

$$\Phi\left(x,y,z,t\right) = \frac{\Phi_0(t)}{r_0^2}\left(\alpha x^2 + \beta y^2 + \gamma z^2\right) \tag{2.1}$$

According to Earnshaw's theorem, such a parabolic potential cannot be created by purely static electric fields [126]. In the case of the Penning trap configuration, this problem is solved by applying an additional static magnetic field, and in the case of the Paul trap approach, the potential Φ_0 is a time-dependent quantity [127]. Moreover, an electric potential in charge-free space needs to satisfy the Laplace equation $\Delta\Phi\left(x,y,z\right) = 0$ with $\alpha + \beta + \gamma = 0$ [128, p. 5]. This can be achieved in two ways, giving rise to a two-dimensional and three-dimensional solution of the problem, respectively, and eventually also different design options for an ion trap [125].

$$\alpha = 1 = -\beta, \gamma = 0 \qquad \rightarrow \qquad \Phi\left(x,y,t\right) = \frac{\Phi_0(t)}{r_0^2}\left(x^2 - y^2\right) \tag{2.2}$$

$$\alpha = \beta = 1, \gamma = -2 \qquad \rightarrow \qquad \Phi\left(x,y,z,t\right) = \frac{\Phi_0(t)}{r_0^2}\left(x^2 + y^2 - 2z^2\right) \tag{2.3}$$

From a historic point of view, Wolfgang Paul and his coworkers started with the two-dimensional approach to design their mass spectrometers in the early 1950s [124, 129]. Since the linear Paul trap uses the same principle as the quadrupole mass separator (QMS) to radially confine charged particles along one central axis, the further description of the first solution is presented in the following section.

2.1.1 Radial Confinement in an Ideal Paul Trap

The mathematical derivations below for charged particle movement and confinement in an ideal two-dimensional quadrupole field follow Wolfgang Paul's original publications

[124, 125, 129, 130]. In practice, such a field in the x-y-plane is generated with a symmetrical arrangement of four parallel electrodes around a common central axis z. The distance r_0 is defined as the minimum distance between each electrode surface and the confinement axis z. To each of the four electrode rods, voltages varying in time with radio frequencies $\Omega_{RF} = 2\pi f_{RF}$ are applied. Two opposing electrodes are electrically connected, and the RF voltages of each pair are oscillating 180° out-of-phase with respect to each other. Mathematically, the applied voltages can be described as a sum of a trigonometric functions with amplitude V_{RF} and a constant offset U_{DC}^{rad} of the form:

$$\Phi_0(t) = U_{DC}^{rad} + V_{RF}\cos(\Omega_{RF}t) \tag{2.4}$$

For an ideal parabolic potential with its minimum along the z-axis to be formed, the four electrodes must also have a hyperbolic shaped cross-section. However, in order to simplify the manufacturing of a radiofrequency quadrupole (*RFQ*), the electrode shape is often cylindrical (see in Sec. 2.1.3). Such a design is also used in the experiments carried out for this thesis. Both configurations are presented in Fig. 2.1.

According to the two-dimensional solution in Eq. (2.2) and the resulting electric field $\vec{E} = -\nabla\Phi$, the Newtonian equations of motion for a single particle with charge Q and mass m in a quadrupole field are written as follows:

$$m\ddot{\vec{r}} - \vec{E}Q = 0 \tag{2.5}$$

$$\rightarrow m\ddot{x} + \frac{2Q}{r_0^2}\left[U_{DC}^{rad} + V_{RF}\cos(\Omega_{RF}t)\right]x = 0 \tag{2.6}$$

$$\rightarrow m\ddot{y} - \frac{2Q}{r_0^2}\left[U_{DC}^{rad} + V_{RF}\cos(\Omega_{RF}t)\right]y = 0 \tag{2.7}$$

$$\tag{2.8}$$

The following substitutions can then be used to transform the second-order differential equations:

$$a_x = -a_y = a = \frac{4QU_{DC}^{rad}}{m\Omega_{RF}^2 r_0^2} \qquad q_x = -q_y = q = \frac{2QV_{RF}}{m\Omega_{RF}^2 r_0^2} \qquad \zeta = \frac{\Omega_{RF}t}{2} \tag{2.9}$$

$$\Rightarrow \frac{\mathrm{d}^2x}{\mathrm{d}\zeta^2} + [a_x + 2q_x\cos(2\zeta)]\,x = 0 \tag{2.10}$$

$$\Rightarrow \frac{\mathrm{d}^2y}{\mathrm{d}\zeta^2} - [a_y + 2q_y\cos(2\zeta)]\,y = 0 \tag{2.11}$$

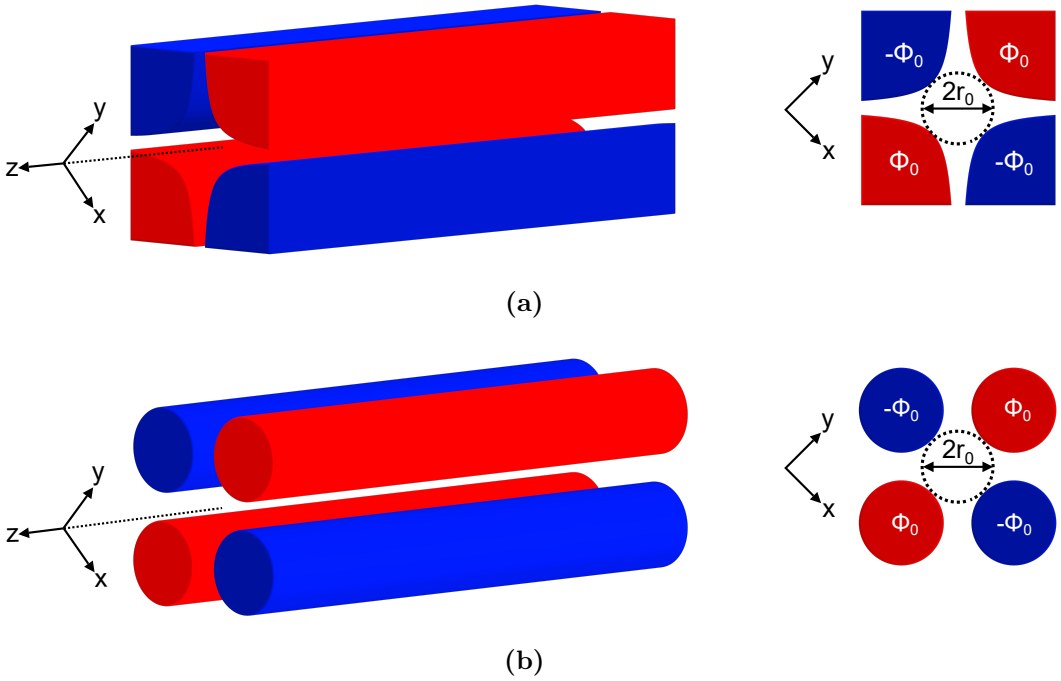

Figure 2.1 *Two different RFQ configurations for radial confinement of charged particles along an axis z. (**a**) shows the case for hyperbolically shaped electrodes and (**b**) shows the simplified case with cylindrical electrodes. Own representation, inspired by [130][131, p. 14].*

Eq. (2.10) and Eq. (2.11) correspond to special cases of the Mathieu equation $\mathrm{d}^2\rho/\mathrm{d}\zeta^2 + [a_\rho - 2q_\rho cos(2\zeta)]\,\rho$ [132, p. 152][133, p. 10], whose solution is known and can be written in its general form:

$$\rho(\zeta) = A_\rho e^{\mu\zeta} \sum_{n=-\infty}^{\infty} C_{2n} e^{\mathrm{i}2n\zeta} + B_\rho e^{-\mu\zeta} \sum_{n=-\infty}^{\infty} C_{2n} e^{-\mathrm{i}2n\zeta} \tag{2.12}$$

Here, A_ρ and B_ρ are constants depending on the starting conditions ρ_0, $\dot{\rho}_0$, and ζ_0, whereas the so-called characteristic exponent $\mu = \alpha_\rho + \mathrm{i}\beta_\rho$, with the real parameters α_ρ, β_ρ, as well as the constant C_{2n}, depend only on the stability parameters a_ρ and q_ρ [133, p. 59][130][128, pp. 19–21]. To keep the further derivations more compact, the reader is referred to references [128, pp. 17–22][133] for a more detailed mathematical treatment of the Mathieu equation. The main consequence of Eq. (2.12) for the motion of an ion with defined mass and charge in a quadrupolar field is the existence of stable and unstable solutions defined by the characteristic exponent μ. When the solutions of the Mathieu equation are visualized in an a-q-plot, as in Fig. 2.2, regions of stable and unstable ion-trajectories can be clearly distinguished from each other. In the two-dimensional picture, stable ion motion is only possible in the overlap region of stable domains for a_x, q_x and

a_y, q_y. Then, the ion performs an oscillatory movement along the z-axis. The spectrum of these oscillations is further discussed in the case of three-dimensional confinement.

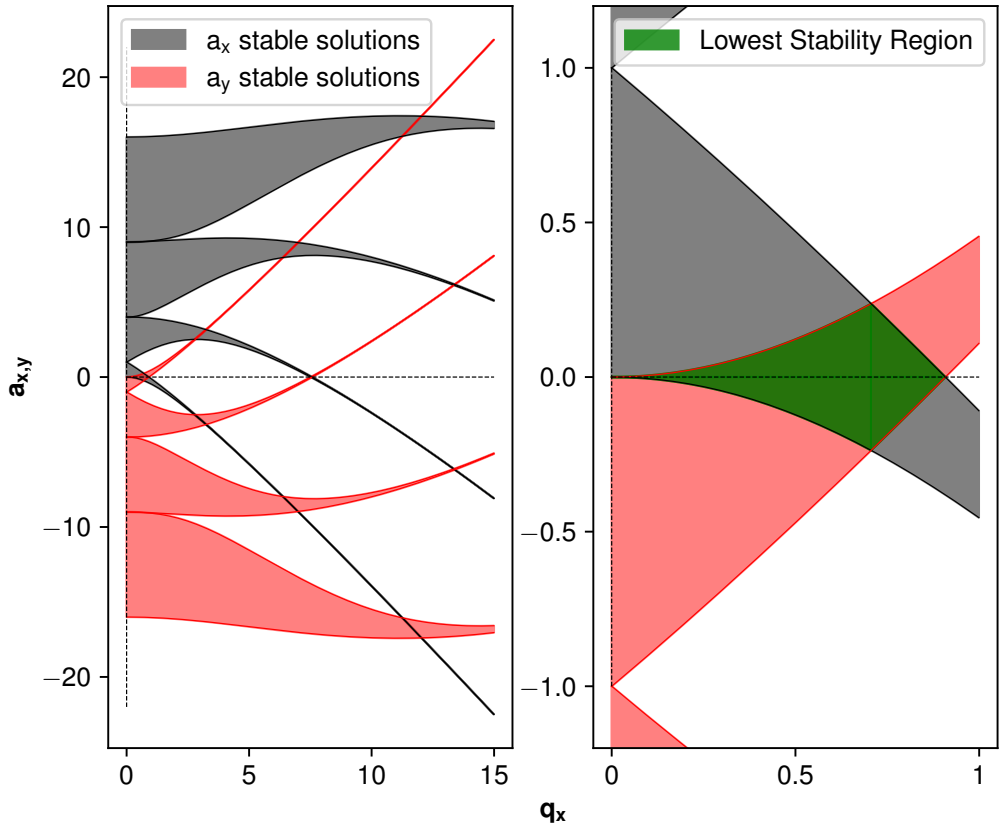

Figure 2.2 *Single-ion stable solutions for the Mathieu equation in the radial directions x and y up to the fourth order are depicted in the left plot. Overlapping regions of the a_x and a_y stable solutions represent the parameter domains for stable radial ion confinement. The usually employed domain of lowest order is shown in the right plot. Own representation, inspired by [128, pp. 19, 20].*

2.1.2 Three-Dimensional Confinement

In the two-dimensional *QMS* configuration, the trapped ion is so far limited to oscillate around the central axis of the quadrupole, but is free to move along the z-axis. For an additional confinement of the charged particle in the z-direction, the *RFQ* has to be further segmented into two longer endcap electrodes and a shorter central electrode, as visible in Fig. 2.3.

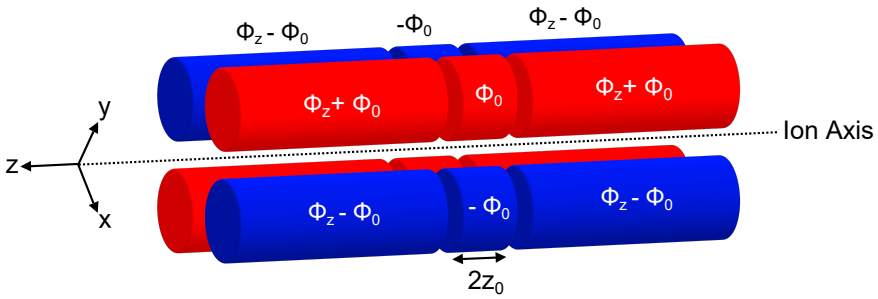

Figure 2.3 *Design scheme of a linear cylindrical Paul trap with a central trap electrode and two longer endcap electrodes for the axial confinement. The length of the central segment is given with* $2 \times z_0$*. Own representation, adapted from [134].*

By applying additional static potentials $\Phi_z = U_{EC}$ with the DC voltage U_{EC} to the two outer endcap segments, the resulting potential in the trap center can be approximated with a static harmonic potential along the z axis [135]:

$$\Phi_z(z) = \eta U_{EC} \frac{z^2}{z_0^2} \tag{2.13}$$

Here, η denotes a geometric correction factor depending on the trap design and U_{EC} is defined with respect to the potential of the central segment. Following the ansatz in [131, p. 17], a parabolic fit of the form

$$\Phi_z(z) = \eta U_{EC} \frac{z^2}{z_0^2} + \kappa U_{EC} \tag{2.14}$$

applied to a simulation of the axial potential can be used to retrieve the specific geometric factor for this work. z_c and κ are additional fit parameters for the definition of the trap center and the trap potential as a function of the trap geometry. With a center segment of length $2z_0 = 8\,\text{mm}$, endcaps of length $l = 30\,\text{mm}$, and a typical endcap voltage of $U_{EC} = 30\,\text{V}$, the fit shown in Fig. 2.4 yields $\eta = 0.224$ and $\kappa = 0.180$. The total three-dimensional quadrupole potential for the linear Paul trap, consisting of the static and the time-dependent radial potential, then writes as follows (see [131, p. 18][135, 137]):

$$\Phi(x, y, z, t) = \frac{\Phi_0}{2r_0^2}\left(x^2 - y^2\right) + \frac{\eta U_{EC}}{z_0} z^2 - \frac{\eta U_{EC}}{2z_0}\left(x^2 + y^2\right) \tag{2.15}$$

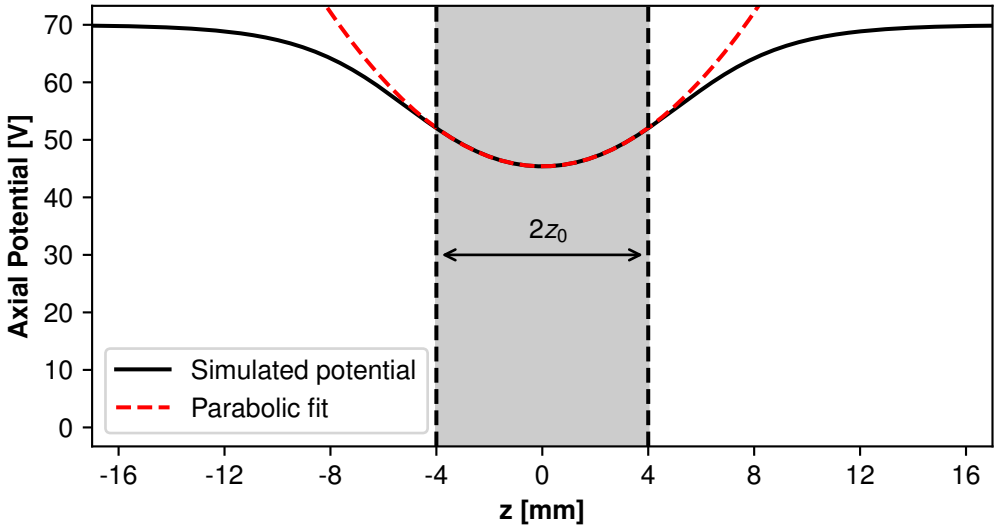

Figure 2.4 *The simulated potential along the z axis of the Paul-trap geometry used in this work (SIMION simulation software, Version 8.1.1.32 [136]). Shown is the case for typical DC trapping voltages of* 70 V, 40 V, 70 V *at the three central trap segments. A parabolic fit curve applied to the potential in the trapping region* (±1 mm) *can be used to retrieve the geometric factor* η*. Own representation, adapted from [131, p. 17].*

Using slightly adjusted substitutions for the a and q parameters leads again to Mathieu's equations of motion [137][131, pp. 18, 19]

$$a_x \to a_x + a_z = \frac{4Q}{m\Omega_{RF}^2}\left(\frac{U_{DC}^{rad}}{r_0^2} - \frac{\eta U_{EC}}{z_0^2}\right) \tag{2.16}$$

$$a_y \to a_y + a_z = -\frac{4Q}{m\Omega_{RF}^2}\left(\frac{U_{DC}^{rad}}{r_0^2} + \frac{\eta U_{EC}}{z_0^2}\right) \tag{2.17}$$

$$a_z = -\frac{4Q\eta U_{EC}}{m\Omega_{RF}^2 z_0^2} \tag{2.18}$$

$$q_x = -q_y = q = \frac{2QV_{RF}}{m\Omega_{RF}^2 r_0^2} \tag{2.19}$$

$$\zeta = \frac{\Omega_{RF} t}{2} \tag{2.20}$$

$$\Rightarrow \frac{\mathrm{d}^2\rho}{\mathrm{d}\zeta^2} + [a_\rho + 2q_\rho \cos(2\zeta)]\, x = 0 \qquad \rho \in x, y \tag{2.21}$$

$$\overset{a_\rho = 0}{\Longrightarrow} \frac{\mathrm{d}^2\rho}{\mathrm{d}\zeta^2} + [a_z + 2q_\rho \cos(2\zeta)]\, x = 0 \tag{2.22}$$

If no DC voltage U_{DC}^{rad} is applied to the trap electrodes, which is also the case for the setup used in this work, the stability region for three-dimensional confinement of a charged particle reduces to a domain of negative a_z values and can be seen in Fig. 2.5.

To get further insights into the motional frequency spectrum of the confined charged particle oscillating in a non-homogeneous electric field, the so-called *adiabatic approximation* comes into play. As already shown by Dehmelt in 1968 [138], the changes in the electric field can be assumed to be small in comparison to the particle oscillation for stable solutions of the Mathieu equation near the origin where $a_\rho < q_\rho^2 \ll 1$. Then, the characteristic exponent is $\mu = i\beta_\rho$ with $\alpha_\rho = 0$, and $0 < \beta_\rho < 1$ β_ρ can be further approximated with $\beta_\rho = \sqrt{a_\rho + q_\rho^2/2}$. Consequently, Eq. (2.12) can be reduced to [137, 139][128, pp. 20–25][131, p. 20]

$$\rho(t) = A_\rho cos\left(\omega_\rho t\right)\left(1 - \frac{q_\rho}{2} cos\left(\Omega_{RF} t\right)\right) \tag{2.23}$$

with A_ρ depending on the initial conditions.

From this expression, the spectrum of the ionic motion can be identified as an oscillation at the slower *secular frequency* $\omega_\rho = \beta_\rho \Omega_{RF}/2$. The *secular frequency*, in turn, is further modulated by the fast *micromotion* corresponding to the higher orders of the trap drive frequency at Ω_{RF} and $2\Omega_{RF}$ [137, 139][128, p. 25].

As visible in Fig. 2.6, the secular motion describes the ion trajectories in good approximation for $q < 0.4$. For larger q values, the deviations from the real solutions increase more and more, and the adiabatic approximation is no longer valid to describe the ion's behavior [140, p. 39].

Keeping the *adiabatic approximation* and neglecting the *micromotion* results in an effective pseudopotential that confines the charged particle in the center of the trap [134, 135, 137][131, p. 18]:

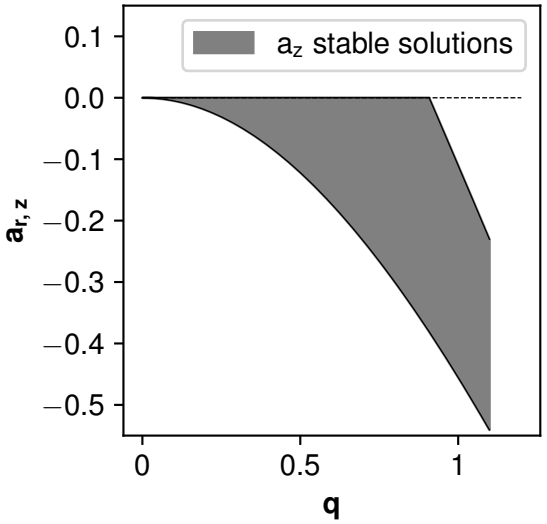

Figure 2.5 *Region of stable solutions of the Mathieu equation in radial and z-direction of a linear Paul trap with $U_{DC}^{rad} = a_\rho = 0$ and a negative a_z. Own representation, adapted from [134].*

$$\Phi_{Pseudo}(x, y, z) = \frac{m}{2Q}\left(\omega_x^2 x^2 + \omega_y^2 y^2 + \omega_z^2 z^2\right) \tag{2.24}$$

with the secular frequencies in all three dimensions given by

$$\omega_x = \frac{\Omega_{RF}}{2}\sqrt{\frac{q_x^2}{2} + a_x} = \sqrt{\frac{Q^2V_{RF}^2}{2M^2\Omega_{RF}^2 r_0^4} + \frac{QV_{DC}^{rad}}{Mr_0^2} - \frac{1}{2}\omega_z^2} \tag{2.25}$$

$$\omega_y = \frac{\Omega_{RF}}{2}\sqrt{\frac{q_y^2}{2} + a_y}\sqrt{\frac{Q^2V_{RF}^2}{2M^2\Omega_{RF}^2 r_0^4} - \frac{QV_{DC}^{rad}}{Mr_0^2} - \frac{1}{2}\omega_z^2} \tag{2.26}$$

$$\omega_z = \frac{\Omega_{RF}}{2}\sqrt{-a_z} = \sqrt{\frac{2Q\eta U_{EC}}{mz_0^2}} \tag{2.27}$$

If no additional DC voltage V_{DC}^{rad} is applied to the trap electrodes, which is also the case in this work, $\omega_x = \omega_y = \omega_r$, and the pseudopotential further simplifies to [134, 135][131, p. 22]

$$\Phi_{Pseudo}(r, z) = \frac{m}{2Q}\left(\omega_r^2 x^2 + \omega_z^2 z^2\right) \tag{2.28}$$

with $\omega_r = (QV_{RF})/(\sqrt{2}m\Omega_{RF}r_0^2)$. Here, special attention is drawn to the direct dependency of the potential on the trapped ion's mass-to-charge ratio m/Q, which has to be taken care of in case of different ion species in the trap volume.

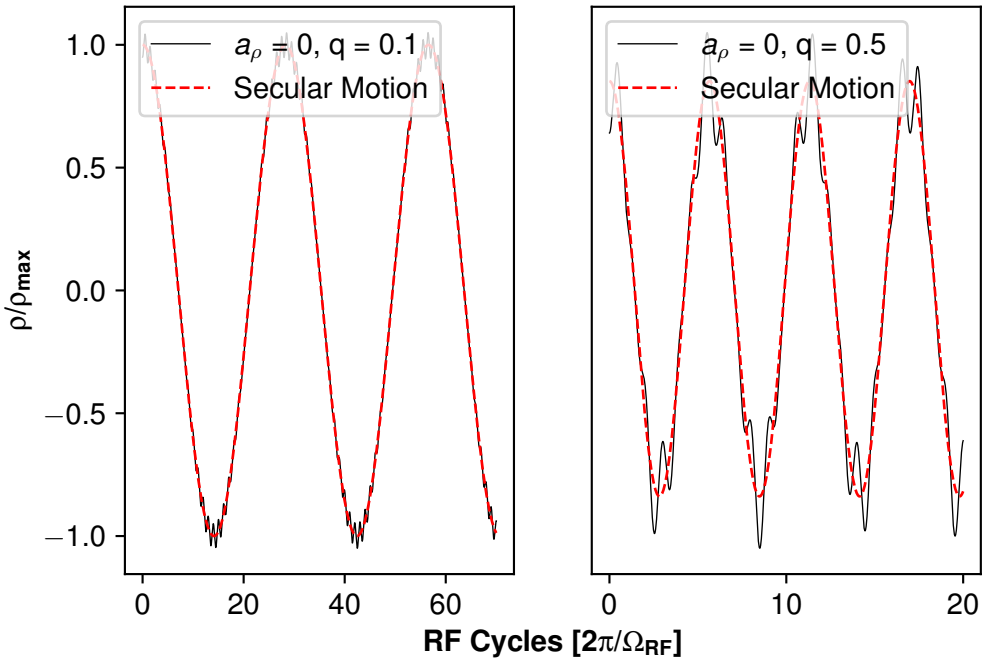

Figure 2.6 *Ionic motion in radial direction according to the approximation in Eq. (2.23) for different values of q. The secular motion is shown as the red dashed line and shows more or less deviation from the exact solution as a function of the q value. The calculations were done with* $\Omega_{RF} = 2\,\mathrm{MHz}$. *Own representation, adapted from [131, p. 20].*

2.1.3 Confinement in a Real Paul Trap

It has to be disclaimed that the derivations above only describe a single-particle motion in a perfect quadrupolar field. As soon as the real trapping potential deviates from the ideal one, and higher-order field components have to be considered, the parameters for stable trapping are shifted. In the case of the linear Paul trap used in this work, one reason for the occurrence of spatial harmonics distorting the ideal quadrupole field is the use of cylindrical electrodes instead of rods with hyperbolical cross section [141–143]. The influences of higher-order multipoles can be minimized by using cylindrical electrodes with radius r in a trap configuration such that $r/r_0 \approx 1.146$ [141, 142].

In general, special care has to be taken in the manufacturing of the trap electrodes and the alignment of the rods with respect to each other in order to keep the quadrupole field as perfect as possible.

Another reason for extra field components is the confinement of more than one charged particle in the trap. The individual particles are then not only affected by the trap potential but also by the repelling Coulomb forces of co-trapped ions. Space charge effects limit the number of charged particles in the trap volume and also change their motional frequencies [140, 144][128, pp. 28–33].

Additional quasi-static stray fields can also arise from so-called patch potentials on the trap electrodes, usually generated by an atom or ion source close to the trap (see e. g.[145–149]). These stray fields can be dealt with by compensation electrodes close to the trap volume.

In theory, the ion motion discussed in the formulas above happens in an ideal vacuum, which is not realistic. No matter how good the vacuum conditions in an experimental setup may be, there will always be residual neutral gas particles in the trap interacting with the confined ions. As described in detail in [128, pp. 36–39], these collisions can either increase or decrease the kinetic energy distribution of the trapped charged particles depending on the relative masses of the collision partners. If the confined ions interact with lighter gas particles, the elastic collisions lead on average to a lower ion temperature and an increased storage time in the trap. This process is especially beneficial in buffer-gas cooled ion trapping experiments [150, 151]. On the other hand, if the background gas particles are heavier than the trapped ions, multiple collision events, momentum transfers, and orbit changes can eventually lead to an ion loss and thus a reduced overall storage time.

Interactions with background particles become even more disadvantageous in the case of inelastic collisions and chemical reactions of the collision partners. The formed molecules may still be trapped, but potentially no longer useful for further examination in an experiment. Therefore, in most precision ion trapping experiments, it is crucial to keep the trap volume in an ultra-high vacuum environment.

2.1.4 Cryogenic Paul Traps

One way to drastically improve the vacuum conditions inside an ion trap is cryogenic cooling to temperatures of a few Kelvin leading to residual gas pressures of $< 10^{-12}$ mbar and thus an increase of the ion storage times [152–156].

Molecules like N_2, CO_2, and H_2O, which are usually responsible for high ion collision rates at room temperature and often the cause for ion loss and or fluorescence decay, are completely frozen at cryogenic temperatures [157]. More information on the technical details and challenges to install such a cryogenic system is given in Ch. 3.

2.2 Laser Cooling of Trapped Ions

Single ions can be confined in Paul traps in order to examine their properties. Still, their degrees of freedom need to be further reduced, e.g., for high-resolution spectroscopy and imaging. Without any additional cooling measures, the trapped charged particle temperature can be several tens of eV or several 10^5 K [139]. Minimizing the ion's Doppler-width and temperature is done by means of an optically driven deceleration via radiation pressure. The commonly called laser cooling was almost simultaneously proposed, for the first time, in 1975 by Hänsch and Schawlow [158], as well as by Wineland and Dehmelt [159]. First implementations of laser cooling followed in 1978 [160, 161] and it is nowadays routinely used in laboratories. Laser cooling works not only for ions but also for atoms and represents the baseline for, e.g., the generation of Bose-Einstein condensates, quantum computing, and many other experimental applications.

2.2.1 Light Interaction with an Atomic Two-Level System

Before a deeper insight into the principles of laser cooling is given, it is useful to introduce some basic properties and present the theoretical model of a two-level atom interacting with electromagnetic radiation:

According to Heisenberg's energy-time uncertainty relation, the emission of a first excited and then spontaneously radiating atom is not given by a sharp line, but is broadened to a certain width around the center frequency ν_0. This broadening δE is linked to the mean lifetime or decay time τ of the respective atomic energy level via $\delta E \sim \hbar/\tau$ [162][163, pp. 103–104]. The resonance curve in frequency space of an atomic transition is given by a Lorentzian with its FWHM defined as the natural linewidth $\delta\nu_n$ [164, pp. 42–43][165, pp. 1088–1090]. The natural linewidth in frequency space is linked to the Einstein coefficient for spontaneous emission A_{eg} from an excited state e to a lower or ground state g. In addition, it connects the transition probability $\delta\omega_n$ (also denoted as γ or λ), the lifetime, and the energetic width of an atomic level as follows [164, pp. 43–44]:

$$\delta E \sim \frac{\hbar}{\tau} = \hbar\delta\omega_n \tag{2.29}$$

$$\delta\nu_n = \frac{A_{eg}}{2\pi} = \frac{\delta\omega_n}{2\pi} = \frac{\delta E}{h} = \frac{1}{2\pi\tau} \tag{2.30}$$

Considering an atomic two-level system and following the derivations in [166, pp. 3–27], the respective density of states can be described by a 2 x 2 matrix

$$\rho = \begin{pmatrix} \rho_{ee} & \rho_{eg} \\ \rho_{ge} & \rho_{gg} \end{pmatrix} \tag{2.31}$$

By solving the Schrödinger equation involving a Hamiltonian describing the atomic system, the light field, and their interaction, the temporal evolution of the individual states can be found. These so-called *optical Bloch equations* (OBE) describe the population probabilities of the ground and the excited state as well as the transition probabilities for resonant absorption and spontaneous emission [166, p. 23].

$$\frac{d\rho_{gg}}{dt} = \delta\omega_n\rho_{ee} + \frac{i}{2}\left(\Omega^*\tilde{\rho}_{eg} - \Omega\tilde{\rho}_{ge}\right) \tag{2.32}$$

$$\frac{d\rho_{ee}}{dt} = -\delta\omega_n\rho_{ee} + \frac{i}{2}\left(\Omega\tilde{\rho}_{ge} - \Omega^*\tilde{\rho}_{eg}\right) \tag{2.33}$$

$$\frac{d\tilde{\rho}_{ge}}{dt} = -\left(\frac{\delta\omega_n}{2} + i\delta\right)\tilde{\rho}_{ge} + \frac{i}{2}\Omega^*\left(\rho_{ee} - \rho_{gg}\right) \tag{2.34}$$

$$\frac{d\tilde{\rho}_{eg}}{dt} = -\left(\frac{\delta\omega_n}{2} - i\delta\right)\tilde{\rho}_{eg} + \frac{i}{2}\Omega^*\left(\rho_{gg} - \rho_{ee}\right) \tag{2.35}$$

$$\frac{d\rho_{ee}}{dt} = -\frac{d\rho_{gg}}{dt} \qquad \text{and} \qquad \rho_{gg} + \rho_{ee} = 1 \tag{2.36}$$

Expressions with tilde are defined as $\tilde{\rho}_{xy} = \rho_{xy}e^{-i\delta t}$ and the spontaneous emission evolves as $d\rho_{eg}/dt = -\delta\omega_n/2\rho_{eg}$ with a fixed decay rate $\delta\omega_n$ and the respective lifetime of the excited state $\tau = 1/\delta\omega_n$. Ω denotes the Rabi frequency with its complex conjugate Ω^* and δ the detuning of the light field from the atomic resonance frequency.

In the steady-state case of the OBE, the saturation intensity of the laser at the wavelength λ in resonance with the energy transition is given as a function of the transition lifetime τ by [166, p. 25]:

$$I_{sat} = \frac{\pi hc}{3\lambda^3\tau} \tag{2.37}$$

The saturation intensity indicates the required laser intensity to reach an excited state population probability of 25 %. With this, the saturation parameter s as a function of the specific saturation intensity and the applied intensity I_{laser} of the laser can be written as:

$$s = \frac{s_0}{1 + (2\delta/\delta\omega_n)^2} \qquad s_0 = \frac{I_{laser}}{I_{sat}} \tag{2.38}$$

As a main parameter of interest for laser cooling, the population ρ_{ee} of the excited state in the two-level system can be expressed as:

$$\rho_{ee} = \frac{I/I_{sat}}{2\left[1 + I_{laser}/I_{sat} + (2\delta/\delta\omega_n)^2\right]} = \frac{s_0}{2\left[1 + s_0 + (2\delta/\delta\omega_n)^2\right]} \tag{2.39}$$

This equation implies that also for high saturation parameters the probability to populate the upper state can only reach 50 %. Moreover, with increasing laser power and increasing saturation, the natural linewidth $\delta\omega_n$ is broadened to a width $\delta\omega$ [166, p. 26],[167]

$$\delta\omega = \delta\omega_n\sqrt{1+s_0} \tag{2.40}$$

Power broadening is one of the most important effects to account for when the linewidth of an atomic or ionic transition is examined.

2.2.2 Principles of Doppler Cooling

Another effect that leads to an additional broadening of a transition's spectral linewidth at room temperature conditions is the Doppler effect [164, pp. 45–47][165, pp. 617, 1089]. Since temperature is directly linked to the particle's velocity around its rest point, an external observer sees the center or resonance frequency ν_0 of an energy level either shifted to higher or lower frequencies, depending on the particle's motion towards or away from him. In turn, the particle also sees ν_0 as up- or down-shifted radiation frequency for movements relative to the radiation's source. Based on the assumption of Maxwell's velocity distribution for the particles, the FWHM of the Doppler-broadened spectral line is given by [164, p. 47]

$$\delta\nu_D = \frac{\nu_0}{c}\sqrt{\frac{8k_BT\ln(2)}{m}} \tag{2.41}$$

with the speed of light c, the Boltzmann constant k_B, the particle's temperature T, and its mass m.

Although the Doppler effect often complicates high-resolution spectroscopy experiments, it plays a crucial role in the optical cooling of atoms and ions.

For the explanation of the general mechanism, there are considered free moving particles with an atomic transition at frequency ν_0 in a laser light field slightly detuned to an off-resonant frequency $\nu_L = c/\lambda_L$ (or wavelength λ_L) smaller than ν_0. Each photon of the laser field has an energy $E_L = h\nu_L$ and a momentum $p_l = \hbar k_L = h/\lambda_L$ that can be transferred to an atom or ion in a scattering event [168]. When particles travel in the opposite direction of the laser beam with a certain velocity, they see a laser frequency that is blue-shifted to the resonance frequency and a scattering event is likely to occur [158]. The photon's energy is then absorbed, and due to momentum conservation, the whole particle recoils in the light's propagation direction [128, p. 222]. The spontaneous re-emission of the absorbed photon occurs in a random direction and also leads to a recoil momentum. Because of the symmetry of the emission process, the additional recoil momentum averages to zero after N scattering events, such that the net momentum transfer to the particle is $\Delta p = N\hbar k_L$, as depicted also in Fig. 2.7. This momentum transfer simultaneously results in a lower particle velocity and temperature [168][128, p. 222].

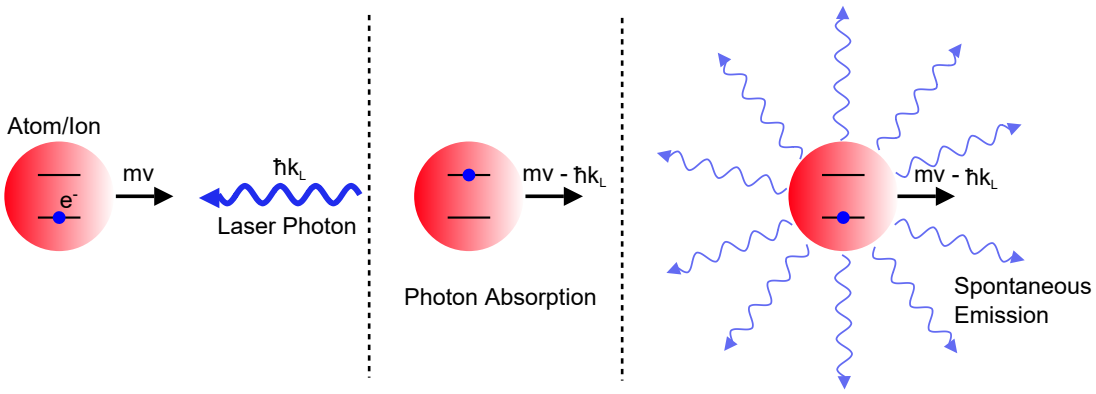

Figure 2.7 *The Doppler cooling principle is shown in three steps for free particles counterpropagating the laser radiation. A first step illustrates the moment before the light-matter interaction. The second step describes the absorption of the photon and the momentum change of the particle. In the third step, the undirected spontaneous emission during the decay of the particle is depicted that eventually, after after N scattering events, results in an average ion momentum change of* $\Delta p = N\hbar k_L$ *in the direction of the laser propagation. Own representation, adapted from [131, p. 26].*

In the case of free atoms with a successively driven cooling mechanism, a certain theoretical lower temperature limit can be reached. Due to the constant gain of energy during each photon emission and recoil, the unbound atom cannot reach the zero Kelvin point [168, 169]. In other words, the cooling process arrives at its limit when the laser-induced energy loss compensates the recoil heating of a particle after a spontaneous photon emission, and the particle's velocity is predominantly governed by the recoil processes [128, p. 223]. By assuming a Maxwell-Boltzmann atomic distribution, the temperature T_D, also known as the Doppler cooling limit at the minimum kinetic energy, is given by the following equation [168, 169] and lies typically in the sub-mK range [170]

$$T_D = \frac{\hbar\omega_n}{2k_B} = \frac{\hbar}{2k_B\tau} \tag{2.42}$$

By means of Doppler cooling, this temperature limit is usually not reached in real Paul traps because of several heating effects induced by the micromotion, cooling laser instabilities, imperfections in the quadrupole potential, and Coulomb interactions in the case of multiple charged particles [131, p. 33]. In order to reach the Doppler limit and even realize particle temperatures below, more advanced techniques like *Sisyphus Cooling* or *Resolved Sideband Cooling* have to be applied, which are beyond the scope of this work. The interested reader is referred to [127, 128, 139, 140] for more information on these cooling methods.

Even though an atom can be slowed down in one dimension by laser cooling, it cannot be preserved at the Doppler limit because of spontaneous photon emissions and the subsequent recoil heating. Since an absorption of laser photons for particles moving along the direction of laser propagation is rather unlikely, the previously cooled particles

will eventually move and reheat in all directions not facing the laser beam [169]. Consequently, in order to sustainably cool unbound atoms in one dimension, it is necessary to irradiate them with counterpropagating laser beams at exactly the same frequency and intensity. The consideration of Doppler cooling in three dimensions then implies six antiparallel laser beams [168, 169, 171][128, p. 223].

For trapped charged particles, it is also possible to laser cool in all three dimensions with a single laser beam only as long as the beam has a projection on each of the dimensions [128, p. 223]. In general, and especially for the cooling of higher amounts of ions (> 100), it is recommended to align the cooling laser beam with the ion axis to increase the interaction cross section with the ions, which also spread out along the trap axis for low potentials. Besides, the Coulomb interactions between the confined particles distribute the cooling force in the radial direction [172].

2.3 Formation of Coulomb Crystals

Considering multiple charged particles confined in a Paul trap and Doppler cooled by a laser beam, they can at some point no longer be described as individual particles, but have to be regarded as a non-neutral plasma. In other words, they have to be treated as a plasma as soon as the Debye length λ_D is smaller than the size of the ion cloud with particle density n_0 [173] [128, p. 261].

$$\lambda_D = \sqrt{\frac{\epsilon_0 k_B T}{n_0 Q^2}} \tag{2.43}$$

Usually, ion traps contain only particles with one charge state, which is why such a plasma is also called *one-component plasma*, where the confining quadrupole potential acts as the uniform background of opposite charge [174, 175].

As the charged particles are constantly laser cooled, they successively lose energy and are more and more accumulated at the minimum of the quadrupole potential or the trap center. This process peaks at the moment when the repelling Coulomb forces of the ions prohibit further convergence. In the equilibrium state, Coulomb crystals can then be formed with inter-ion distances d_{int} defined by the trapping parameters and the repelling Coulomb forces [176]. For a one-dimensional string of ions in equilibrium state along the z-axis of a linear Paul trap d_{int} is given as a function of the ion mass m and the axial trapping frequency ω_z (see in Sec. 2.1.2) [176–178][179, p. 41]

$$d_{int} = \left(\frac{e^2}{2\pi\epsilon_0 m \omega_z^2} \right)^{1/3} \tag{2.44}$$

Inserting typical trapping parameters for this work with an RF frequency of $\Omega_{RF} \approx 2\pi \times 2\,\mathrm{MHz}$ and a potential depth of 1 V, the inter-ion distance for a linear chain of strontium ions results in $d_{int} \approx 60\,\mu\mathrm{m}$, which corresponds to the typical order of magnitude.

First observations of phase transitions of laser-cooled ions in Paul traps were made in 1987 by Diedrich et al. and Wineland et al [180, 181]. Since then, the formation

of Coulomb crystals has been intensively studied, as summarized in the reviews by Thompson and Drewsen [176, 182].

To further quantify the process of crystallization, the so-called plasma coupling parameter is introduced:

$$\Gamma_P = \frac{Q^2}{4\pi\epsilon_0 a_{WS} k_b T} \tag{2.45}$$

with the Wigner-Seitz radius $a_{WS} = (3n_0/4\pi)^{1/3}$ as a function of the particle density n_0 [174, 183]. In the so-called *weak-coupling regime* for $\Gamma_P < 1$, the plasma reveals a gaseous behavior, and in the *strong-coupling case* for $\Gamma > 2$, a liquid one [128, p. 263][176]. The phase transition into a crystalline structure occurs at parameters $\Gamma_P \gtrsim 175$ [182, 184–187]. With an assumed Wigner-Seitz radius of $a_{WS} \approx 10\,\mu$m, this corresponds to an upper limit for the ion temperature for crystallization of $T \lesssim 10\,$mK, which is in reach by the means of Doppler cooling [182].

The shape of a Coulomb crystal is of a spherical nature and depends on the depth of the axial trapping potential, as visible also in Fig. 2.8.

The more shallow the potential, the more prolate the crystal becomes. In turn, it gets more oblate for steeper axial potentials. Inside this spherical structure, the ions are arranged in concentric shells depending on the ion number N. Molecular-dynamics simulations of large spherical ion crystals delivered an approximation for the number of ion shells M that can also be used to estimate the number of ions on the basis of crystal images [188].

$$M = \left(\frac{3}{10}N\right)^{\frac{1}{3}} - \frac{1}{2} \tag{2.46}$$

For arbitrary crystal shapes, upcoming simulation techniques based on neural networks can deliver more accurate results to determine the number of ions from projection images [189, 190].

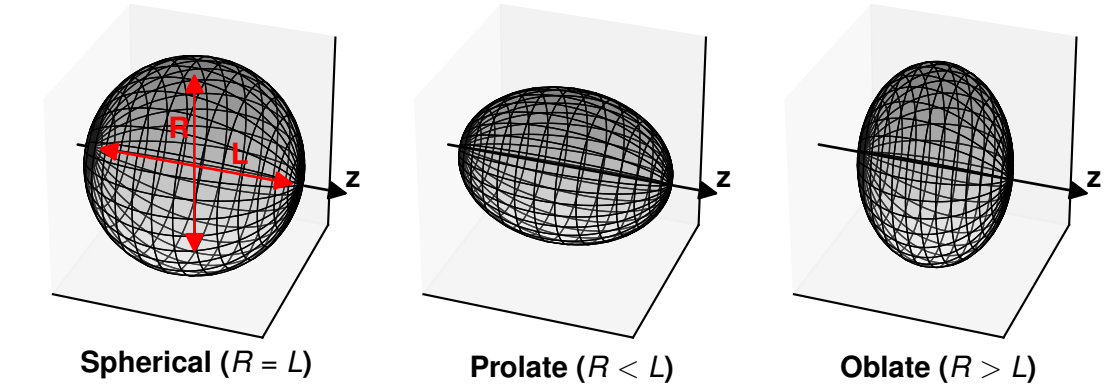

(a)

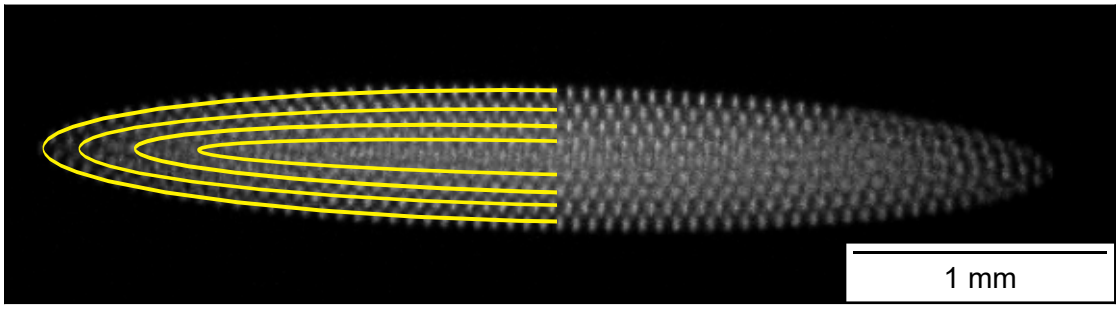

(b)

Figure 2.8 *Different Coulomb crystal shapes depending on the trapping potential are shown in (**a**). Own representation, adapted from [191, p. 13].*
*(**b**) Prolate, Doppler cooled $^{88}Sr^{+}$ Coulomb crystal at an axial potential depth of* 2 V *with 4 ion shells around a central linear chain of ions visible in the focal plane(highlighted in yellow). Due to the prolate crystal shape, Eq. (2.46) is not applicable to estimate the ion number.*

2.4 Sympathetic Laser Cooling of $^{229}Th^{3+}$

Trapped particles do not necessarily need to be cooled directly with a laser-driven cooling cycle, especially when the involved wavelengths cannot easily be provided. Another reason to avoid direct cooling of a particle can also be its energy level structure that is either too complicated (like in molecules), not known exactly, or completely absent (like in protons) [192]. Sometimes, the cooling laser also changes the energy level-structure of the particle to be probed and limits the experimental precision [192]. In such cases, it becomes more appropriate to cool the particle of spectroscopic interest in combination with another particle species, as already proposed in 1978 [161]: One component of the particle mix in the trap can be Doppler cooled and is then able to cool the other component sympathetically via particle collisions and Coulomb repulsions. The

technique of sympathetic laser cooling is routinely applied in all kinds of particle trap experiments. Due to their easily accessible cooling cycle, the most often used cooling ions are Be^+ [192, 193], Mg^+ [194, 195], Ca^+ [196, 197], but also the use of Cd^+ has been reported [198].

In the case of linear Paul traps and already pointed out in Sec. 2.1.2, the trapping pseudopotential changes for ions of different mass-to-charge ratios. Therefore, prior to an experiment involving sympathetic cooling, the cooling ion should be chosen according to the second ion species of interest.

When two different ion species form a Coulomb crystal, the mass dependence of the trap potential also results in stronger confinement for lighter particles that accumulate along the ion axis surrounded by the heavier particle species [176].

$^{229}Th^{3+}$ has hyperfine structure, which makes laser cooling not trivial. Indeed, a closed Λ system with a main cooling and a repumping cycle can be found [171, 199], but several exactly tuned light fields and an exact knowledge of the hyperfine transitions to prevent immediate dark state pumping are required. In addition, all involved transitions reveal natural linewidths below 150 kHz [200] and are less suitable for fast cooling cycles.

Consequently, it seems reasonable to go for a sympathetic laser cooling approach with another ion species that can be cooled down more conveniently. In the case of $^{229}Th^{3+}$ ions, this has already been shown in 2012 by Campbell et al. [199] in combination with $^{232}Th^{3+}$, which were both created simultaneously from a thorium nitrate ablation target and confined in a Paul trap. The same combination of laser wavelengths could be used to Doppler cool ^{232}Th free of hyperfine structure on the one hand and to measure the hyperfine structure in ^{229}Th on the other hand.

In another thorium experiment carried out at the University of Mainz, sympathetic cooling and crystal formation of $^{232}Th^+$ with significantly lighter $^{40}Ca^+$ ions confined in a linear Paul trap has been shown [196, 197].

When the first planning stage for the cryogenic Paul trap setup at the LMU began in 2015, a running source of thorium ions already existed. The main advantage of this ^{233}U recoil source in a buffer-gas stopping cell over the laser ablation from a thorium nitrate target used by Campbell et al. [199], is the possibility to extract not only ^{229}Th ions in the nuclear ground but also the isomeric state [8]. However, there are no suitable ion side products in the extraction process that could be used for sympathetic laser cooling. Therefore, $^{88}Sr^+$ free of hyperfine structure with its easy-to-access Doppler cooling cycle at 422 nm and 1092 nm (see also Fig. 2.9) was chosen as trapping partner for the thorium ions.

As listed in Tab. 2.1, the low-lying transitions in $^{88}Sr^+$ are very short-lived with natural linewidths of up to 20 MHz and are therefore ideal for efficient laser cooling and fluorescence detection.

The choice of $^{88}Sr^+$ was also motivated by its mass-to-charge ratio $m/Q = 88.0$, which lies close to the one of $^{229}Th^{3+}$ with $m/Q = 76.3$. Like this, favorable cooling conditions via Coulomb interaction can be achieved, and the optimum trapping potentials do not differ too much for both ion species.

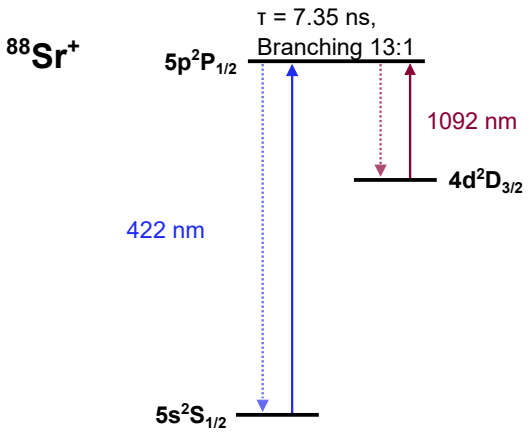

Figure 2.9 *Fine-structure levels in $^{88}Sr^{+}$ used for Doppler cooling with one main cooling cycle at* 422 nm *and a repumping cycle at* 1092 nm*. The upper state lifetime and the branching ratio are taken from [201].*

Table 2.1 *Wavelengths (in air), linewidths, and lifetimes of the fine structure transitions in $^{88}Sr^{+}$ chosen for Doppler cooling.*

Transition	Wavelength [nm]	Frequency [THz]	$\delta\nu$ [MHz]	τ [ns]	I_{sat} [W/m^2]
5p $^2P_{1/2}$ - 5s $^2S_{1/2}$	421.5524(1) [202, 203]	711.1630(2) [202, 203]	20.1(16) [201]	7.9(6) [201]	352(27)
5p $^2P_{1/2}$ - 4d $^2D_{3/2}$	1091.4874(3) [202, 203]	274.66415(8) [202, 203]	1.5(3) [201]	105(24) [201]	1.5(3)

2.5 Hyperfine-Structure Spectroscopy of $^{229(m)}$Th

2.5.1 Nuclear Moments and Hyperfine Splitting

Being fermions, protons as well as neutrons have a spin angular momentum of $s_{p,n} = 1/2$. Being also the building blocks of an atomic nucleus, they contribute together with their orbital angular momenta l_p, l_n to the total nuclear spin I [22, p. 55]. Nuclei with an even mass number A have an integer spin. If the numbers of protons (Z) and neutrons (N) forming the nucleus are also even, the nuclear spin reduces to $I = 0$ because of the pair-wise filling of proton or neutron orbitals according to Pauli's principle and the pairing force of the nuclear binding. For uneven mass numbers and with either Z or N being an uneven number, the total nuclear spin is a half-integer. As an example, ^{232}Th has $Z = 90$ and $N = 142$, resulting in a nuclear spin of $I = 0$, whereas ^{229}Th has $I = 5/2$ because of the unpaired neutron.

With the non-vanishing nuclear spin in ^{229}Th, the electronic energy levels undergo not only a splitting due to the spin-orbit coupling (fine structure) but also a further splitting resulting from the interaction between the electronic shell and the nucleus. This

so-called hyperfine splitting can be described by the total atomic angular momentum $F = J + I$ with a $|J - I| \leq F \leq |J + I|$. $J = L + S$ denotes the total electronic angular momentum consisting of the total electronic spin S and the electronic orbital angular momentum L. Considering an electronic state with $J = 5/2$ in ^{229}Th, the interaction of the nucleus and the electronic shell therefore causes a hyperfine splitting to six different states with $F \in 1, 2, 3, 4, 5, 6$. This can also be calculated via the so-called multiplicity, which is $2I + 1$ for $I \geq J$ and $2J + 1$ for $J \leq I$ [22, p. 66][204, p. 160].

In first-order perturbation theory, the hyperfine splitting can be calculated with the following formula [111, 171, 205]

$$E_{HFS}(J, F, S) = \frac{AK}{2} + \frac{B[(3/4)K(K+1) - I(I+1)J(J+1)]}{2I(I-1)J(2J-1)} \tag{2.47}$$

where K is the so-called cosine or Casimir factor that writes as:

$$K = F(F+1) - I(I+1) - J(J+1) \tag{2.48}$$

A and B are the so-called hyperfine constants and describe the interaction of magnetic (A) and electric (B) fields generated by the electronic shell at the position of the nucleus with the nuclear moments [204, p. 159] and are given by [206, 207]:

$$A = \frac{\mu}{IJ}\langle \mathcal{T}_1^e \rangle_J \qquad B = 2Q\langle \mathcal{T}_2^e \rangle_J \tag{2.49}$$

μ is the nuclear magnetic dipole moment, Q the nuclear electric quadrupole moment, and $\mathcal{T}_k^e$ is the spherical, irreducible tensor operator of rank k acting on the electronic coordinates.

This model neglects all effects of higher-order nuclear multipolarities with constants (C, D, E, etc.) on the hyperfine splitting because they are considered small [171, p.70][207, 208].

For more detailed information on the calculation of A, B, and other hyperfine constants, the reader is referred to the suitable literature [204, 205, 207, 209].

For several systems, a solution for the hyperfine constants is hard to find or can only be approximated because of a lack of knowledge on the nuclear moments or the huge amount of particles in the system. Especially the electric quadrupole moments required for the B constant are unknown for many nuclei [67, 210]. However, since the information on the nucleus is imprinted in the electronic hyperfine splitting, precision spectroscopy measurements in combination with a suitable fit function can be used to retrieve the missing parameters of the hyperfine constants.

In the case of $^{229}Th^{3+}$, there existed only few experimental and theoretical studies on the nuclear moments [68, 211] for a long time, until Campbell et al. delivered further high precision spectroscopy data [199], which paved the way for refined theoretical models and calculations [67, 212]. Only recently, the measurements of Campbell were partially confirmed by Zitzer et al. at PTB, Braunschweig [213].

Campbell et al. performed hyperfine structure spectroscopy of the four lowest lying hyperfine states $5F_{5/2}$, $5F_{7/2}$, $6D_{3/2}$ and $6D_{5/2}$ in $^{229}Th^{3+}$ that are also shown in Fig. 2.10.

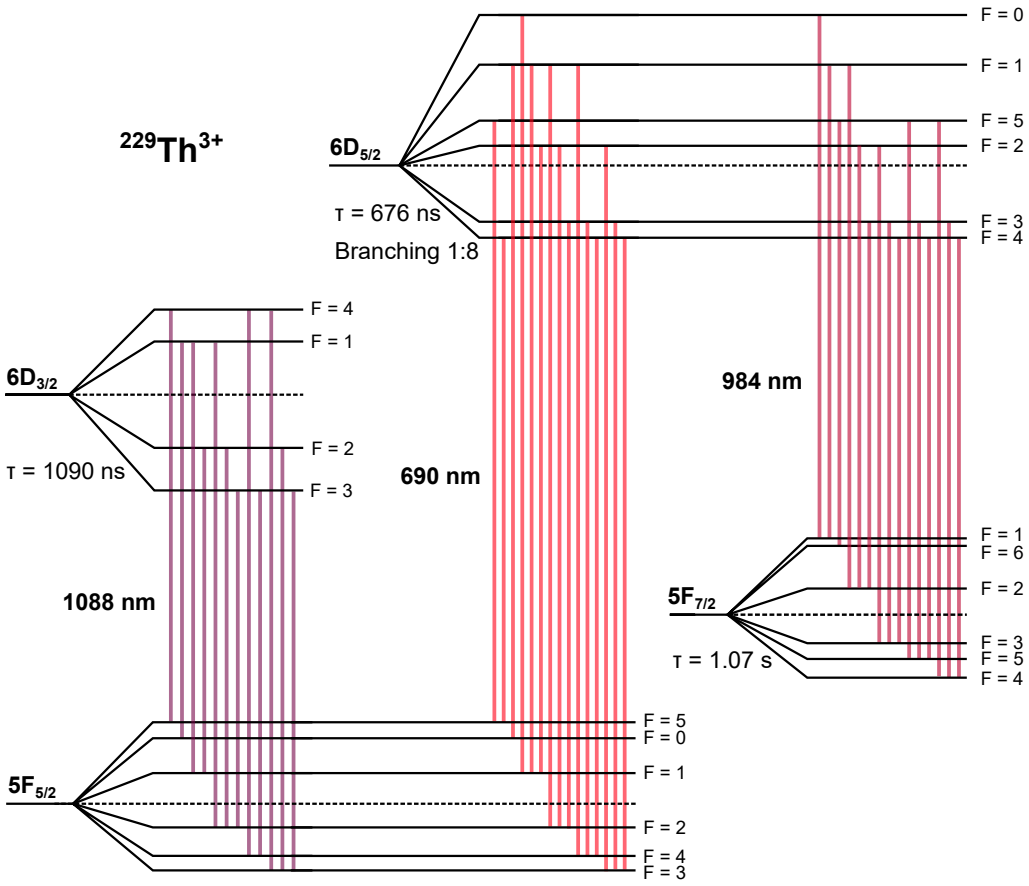

Figure 2.10 *The four lowest lying hyperfine transitions in $^{229}Th^{3+}$ with their respective upper state lifetimes given by [200].*

The wavelengths of the transitions between these states are at 690 nm, 984 nm, and 1088 nm, and all correspond to the electric dipole transitions that satisfy the following selection rules and undergo a parity change [204, p. 170].

$$\Delta F = \{0, \pm 1\}; \qquad F + F' \geqq 1 \tag{2.50}$$

The upper-state lifetime values, which also define the natural linewidths of the transitions, are calculated in [200]: For $6D_{5/2}$ the lifetime is 676 ns, which corresponds to $\delta\nu_n = 1/(2\pi\tau) = 235$ kHz. The width of the transition to the $5F_{5/2}$ state at 690 nm results from the branching ratio of 1:8 and is $\delta\nu_n \approx 26$ kHz [214]. In the same way, the nat-

ural linewidth of the transition to $5F_{7/2}$ at 984 nm is calculated to be $\delta\nu_n \approx 209$ kHz. The 1088 nm transition with a lifetime of 1090 ns has a natural linewidth of $\delta\nu_n \approx 146$ kHz.

In a second step, Campbell et al. used Eq. (2.47) for the respective excited state and ground state to fit a global least-squares method to the measured hyperfine transitions.

$$\delta E_{e,g}(J_{e,g}, F_{e,g}, S_{e,g}) = \frac{A_e K_e}{2} + \frac{B_e[(3/4)K_e(K_e+1) - I_e(I_e+1)J_e(J_e+1)]}{2I_e(I_e-1)J_e(2J_e-1)} - \frac{A_g K_g}{2} - \frac{B_g[(3/4)K_g(K_g+1) - I_g(I_g+1)J_g(J_g+1)]}{2I_g(I_g-1)J_g(2J_g-1)} + \Delta^{iso} \quad (2.51)$$

Since their data were recorded with respect to the resonance of $^{232}Th^{3+}$, the isotope shift Δ^{iso} was included in the fit function. A summary of the experimental results found in [199, 213] is given in Tab. 2.2.

Table 2.2 *Results by Campbell et al. [199] and Zitzer et al. [213] for the hyperfine constants in $^{229}Th^{3+}$ and the isotope shifts with respect to the $^{232}Th^{3+}$ transitions. The data are in MHz, and the given uncertainties correspond to one sigma.*

State	A [MHz]	B [MHz]	Transition	Isotope shift [MHz]
$5F_{5/2}$	82.2(6) [199]	2269(6) [199]	$5F_{5/2} \leftrightarrow 6D_{3/2}$	−9856(10) [199]
	82.0(2) [213]	2270.30(18) [213]		
$5F_{7/2}$	31.4(7) [199]	2550(12) [199]	$5F_{5/2} \leftrightarrow 6D_{5/2}$	−10509(7) [199]
$6D_{3/2}$	155.3(12) [199]	2565(9) [199]	$5F_{7/2} \leftrightarrow 6D_{5/2}$	−9890(9) [199]
$6D_{5/2}$	−12.6(7) [199]	2694(7) [199]		
	−12.9(3) [213]	2695.70(19) [213]		

For this work, only the transitions at 690 nm and 984 nm were of interest. Implementing the reported experimental results for A and B from Eq. (2.51) can be used to retrieve the position of the hyperfine transitions between the respective hyperfine states in $^{229}Th^{3+}$ with respect to the center frequencies of the hyperfine structure found in [171] and are shown in Fig. 2.11. To inspect the calculated hyperfine splittings retrieved from the different experimental results, see Tab. A.1. The values found by Zitzer et al. slightly deviate from the previously found results of Campbell et al. and also reveal smaller uncertainties, but still lie within the uncertainty range of the old measurements.

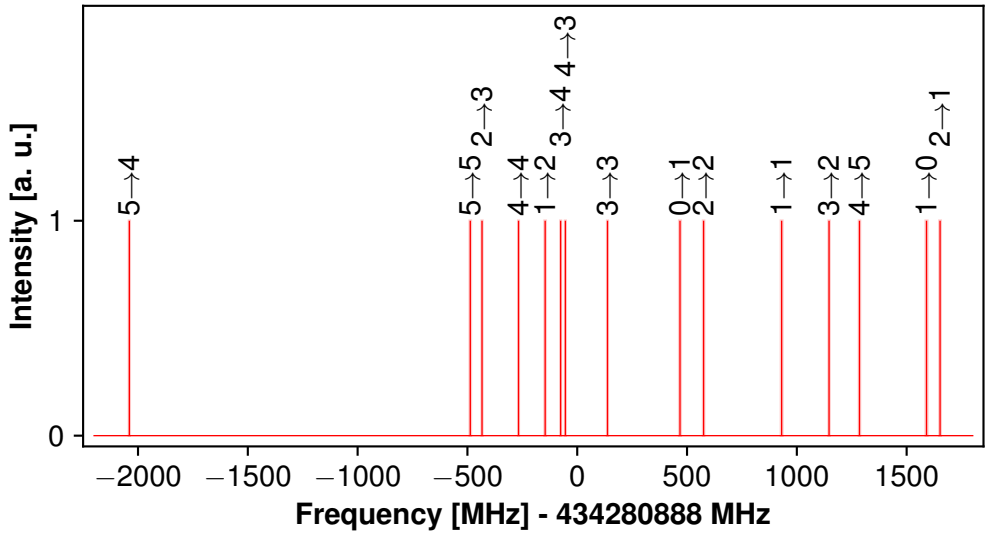

(a) 690 nm hyperfine-structure transitions in $^{229}Th^{3+}$

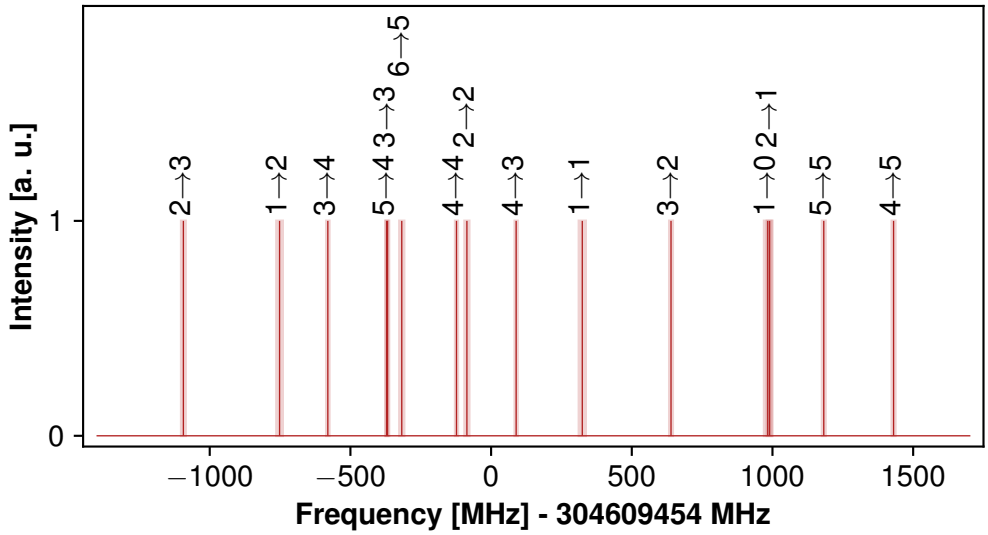

(b) 984 nm hyperfine-structure transitions in $^{229}Th^{3+}$

Figure 2.11 *Calculated electronic hyperfine splittings of the nuclear ground state of $^{229}Th^{3+}$ for the $5F_{5/2} \rightarrow 6D_{5/2}$ transition (690 nm) based on the results in [213] in (**a**) and for the $5F_{7/2} \rightarrow 6D_{5/2}$ transition (984 nm) based on the results in [171, 199] in (**b**). The center frequencies of the hyperfine structures were found in [171]. Intensities are normalized to 1, and the labels indicate the individual change of the quantum number $F \rightarrow F'$. Uncertainties are indicated as transparent rectangles with a width of twice the standard deviation.*

2.5.2 Angular Momenta

The line strengths S or intensities of individual hyperfine transitions from an initial state $|\gamma JIF\rangle$ to a final state $|\gamma' J'IF'\rangle$, with γ, γ' as the additional quantum numbers necessary to describe the state, are dependent on the eigenvalues of the electric dipole operator $\hat{P}$ [209, p. 465]:

$$S = \left| \langle \gamma JIF | \hat{P} | \gamma' J'IF' \rangle \right|^2 \tag{2.52}$$

For the evaluation of this matrix element, it is necessary to find a common base of eigenstates of the coupled operator $\hat{\mathbf{P}}$, which requires introducing some additional algebra for angular momenta.

Considering two angular momenta $\hat{\mathbf{J}}_1$ and $\hat{\mathbf{J}}_2$ that couple to a total angular momentum $\hat{\mathbf{J}} = \hat{\mathbf{J}}_1 + \hat{\mathbf{J}}_2$, the so-called *Clebsch-Gordan coefficients* $C^{JM}_{j_1 m_1 j_2 m_2}$ can be used to express the eigenstates of the individual momenta $|j_1, m_1\rangle$ and $|j_1, m_1\rangle$ in a coupled base of eigenstates $|J, M\rangle$ via [209, p. 441]:

$$|j_1 j_2 JM\rangle = \sum_{M1,M2} |j_1 m_1 j_2 m_2\rangle \langle j_1 m_1 | j_1 j_2 JM\rangle = \sum_{M1,M2} C^{JM}_{j_1 m_1 j_2 m_2} |j_1 m_1 j_2 m_2\rangle \tag{2.53}$$

The j-quantum numbers denote the spin quantum numbers, and the m-quantum numbers indicate the projection of the angular momenta on the z-axis. For non-vanishing Clebsch-Gordan coefficients, the following conditions have to be satisfied [209, pp. 441–442]:

$$J = |j_2 - j_1|, |j_2 - j_1| + 1, ...|j_2 + j_1| \tag{2.54}$$

$$m_i = -j_1, -j_i + 1, ...j_i \qquad \text{for} \qquad i \in 1, 2 \tag{2.55}$$

$$M = m_1 + m_2 \tag{2.56}$$

Because of their higher symmetry, it is often more advantageous to work instead with so-called *Racah V coefficients* (after Racah [215]) or *Wigner 3j symbols* to write the Clebsch-Gordan coefficients in the following form [204, p. 61]:

$$\langle j_1 m_1 | j_1 j_2 JM\rangle = (-1)^{-j_1 + j_2 - M} \sqrt{2J+1} \begin{pmatrix} j_1 & j_2 & J \\ m_1 & m_2 & -M \end{pmatrix} \tag{2.57}$$

$$\langle j_1 m_1 | j_1 j_2 JM\rangle = (-1)^{J+M} V(j_1 j_2 J; m_1 m_2 - M) \tag{2.58}$$

$$V(j_1 j_2 J; m_1 m_2 M) = (-1)^{j_1 - j_2 + J} \sqrt{2J+1} \begin{pmatrix} j_1 & j_2 & J \\ m_1 & m_2 & M \end{pmatrix} \tag{2.59}$$

Following the derivations in [204, 209], three angular momenta couple to a single total momentum $\hat{\mathbf{J}} = \hat{\mathbf{J}}_1 + \hat{\mathbf{J}}_2 + \hat{\mathbf{J}}_3$. Depending on the way of summation, there are two possible intermediate momenta that have to be accounted for:

$$\hat{\mathbf{J}}_1 + \hat{\mathbf{J}}_2 = \hat{\mathbf{J}_{12}} \rightarrow \hat{\mathbf{J}_{12}} + \hat{\mathbf{J}}_3 = \hat{\mathbf{J}} \tag{2.60}$$

$$\hat{\mathbf{J}}_2 + \hat{\mathbf{J}}_3 = \hat{\mathbf{J}_{23}} \rightarrow \hat{\mathbf{J}_{23}} + \hat{\mathbf{J}}_1 = \hat{\mathbf{J}} \tag{2.61}$$

Then, the eigenstates $|(j_1 j_2) J_{12} j_3; JM\rangle$ and $|j_1 (j_2 j_3) J_{23}; JM)\rangle$ of the different coupling schemes for $\hat{\mathbf{J}}^2$ and $\hat{\mathbf{J}}_\mathbf{z}$ with the eigenvalues J and M can be written as a linear combination:

$$|(j_1 j_2) J_{12} j_3; JM\rangle = \sum_{J_{23}} |j_1 (j_2 j_3) J_{23}; JM)\rangle \, \langle j_1 (j_2 j_3) J_{23}; JM | (j_1 j_2) J_{12} j_3; JM\rangle \quad (2.62)$$

The right part of the sum can be denoted as a combination of several Clebsch-Gordan coefficients or in terms of the so-called *Racah W function* or *Wigner 6j symbols* [209, pp. 446, 447]:

$$\langle j_1 (j_2 j_3) J_{23}; JM | (j_1 j_2) J_{12} j_3; JM\rangle = \sqrt{2J_{12}+1}\sqrt{2J_{23}+1} W(j_1 j_2 J j_3; J_{12} J_{23}) \quad (2.63)$$

$$W(j_1 j_2 J j_3; J_{12} J_{23}) = (-1)^{-j_1-j_2-j_3-J} \begin{pmatrix} j_1 & j_2 & J_{12} \\ j_3 & J & J_{23} \end{pmatrix} \quad (2.64)$$

In turn, the Wigner 6j symbol can be expressed as

$$\begin{pmatrix} j_1 & j_2 & J_{12} \\ j_3 & J & J_{23} \end{pmatrix} = \sqrt{\Delta(j_1 j_2 J_{12}) \Delta(j_1 J J_{23}) \Delta(j_3 j_2 J_{23}) \Delta(j_3 J J_{12})} \sum_t \frac{(-1)^t (t+1)!}{f(t)} \quad (2.65)$$

with

$$\begin{aligned} f(t) =& (t - j_1 - j_2 - J_{12})!(t - j_1 - J - J_{23})!(t - j_3 - j_2 - J_{23})! \\ & \times (t - j_3 - J - J_{12})!(j_1 + j_2 + j_3 + J - t)! \\ & \times (j_2 + J_{12} + J + J_{23} - t)!(J_{12} + j_1 * J_{12} + j_3 - t)! \end{aligned} \quad (2.66)$$

and the so-called triangular function

$$\Delta(abc) = \frac{(a+b-c)!(a-b+c)!(-a+b+c)!}{(a+b+bc+1)!} \quad (2.67)$$

The summation is carried out for all t values, resulting in non-negative factorial expressions.

2.5.3 Transition Intensities

By using the Wigner-Eckart theorem, the *Wigner-6j symbol*, and an expression found in [216, p. 111], the transition strength of Eq. (2.68) can then be written like in [217, p. 17]

$$S = \left| \langle \gamma J I F | \hat{P} | \gamma' J' I F' \rangle \right|^2 = (2F+1)(2F'+1) \begin{pmatrix} J' & F' & I \\ F & J & 1 \end{pmatrix}^2 \left| \langle \gamma J | \hat{P} | \gamma' J' \rangle \right|^2 \quad (2.68)$$

Normalized, relative intensities of the HFS transitions between states of different J are estimated by Sonnenschein et al. [218] and also by Thielking [217, p. 17] to be

$$S_{rel} = \frac{(2F+1)(2F'+1)}{2I+1} \begin{pmatrix} J' & F' & I \\ F & J & 1 \end{pmatrix}^2 \tag{2.69}$$

Evaluating Eq. (2.69) with the *Racah coefficients* for the individual transitions can be used to calculate a refined hyperfine structure spectrum for $^{229}Th^{3+}$ at 690 nm and 984 nm, respectively, which is also shown in Fig. 2.12. The results for the relative transition strengths are summarized in Tab. A.2 and Tab. A.3, shown in the Appendix.

2.5.4 Isomeric Hyperfine Structure of $^{229m}Th^{3+}$

The calculation of the electronic hyperfine splitting of the isomeric state $^{229m}Th^{3+}$ works analogously to that of the nuclear ground state. Only the different nuclear spin of the isomer $I_{is} = 3/2$, and the different hyperfine constants have to be taken into account.

Up to now, there exist only two reports on measurements of the electronic hyperfine structure in ^{229m}Th [13, 111]. Still, the hyperfine constants for the splitting of the $5F_{5/2} \rightarrow 6D_{5/2}$ and $5F_{7/2} \rightarrow 6D_{5/2}$ in $^{229m}Th^{3+}$, which are of special interest for this thesis, are not known precisely. However, calculations based on experimental findings can be used to approximate the hyperfine structure as a basis for the laser spectroscopy carried out in this work.

In the experiment performed by Thielking et al. [111], the HFS spectra of $^{229}Th^{2+}$ and $^{229m}Th^{2+}$ were measured and used to extract the hyperfine constants from fits to the data. In addition, the isotope shifts Δ^{iso} between the $^{229}Th^{2+}$ and $^{232}Th^{2+}$ spectra were determined and put in relation with the observed spectral shifts Δ^m between the centers of the hyperfine structure of the nuclear ground state and isomeric state: $\Delta^m/\Delta^{iso} = 0.035(4)$. Physically, the spectral shifts due to a different nuclear configuration in an isotope or a different nuclear energetic state can also be put in relation with the shape of the nucleus and its mean-square charge radius (see also [68, 219]).

The found values of the relative hyperfine constants $A^m/A^g = -1.73(25)$, $B^m/B^g = 0.555(19)$ can be used to give an approximation for the isomeric hyperfine splitting in $^{229}Th^{3+}$ on the basis of the experimental results of Zitzer et al. [213] for 690 nm and Campbell et al. [171, 199] for 984 nm, respectively. The splittings for the respective wavelength calculated with the respective combination of data sets are shown in Fig. 2.13 in light green (690 nm) and orange (984 nm).

In contrast to Thielking et al., the more recent work by Yamaguchi and colleagues comprises hyperfine structure measurements directly in buffer-gas cooled $^{229(m)}Th^{3+}$. Isomeric hyperfine constants for the $6D_{3/2}$ state as well as the isomer shift for the transitions $5F_{5/2} \rightarrow 6D_{3/2}$ (1088 nm) were determined. Taking the nuclear ground state constant for $6D_{3/2}$ from [171, 199] gives another set of ratios $A^m/A^g = -1.719(19)$, $B^m/B^g = 0.569(5)$, which can then be used, in the same way as the data given by

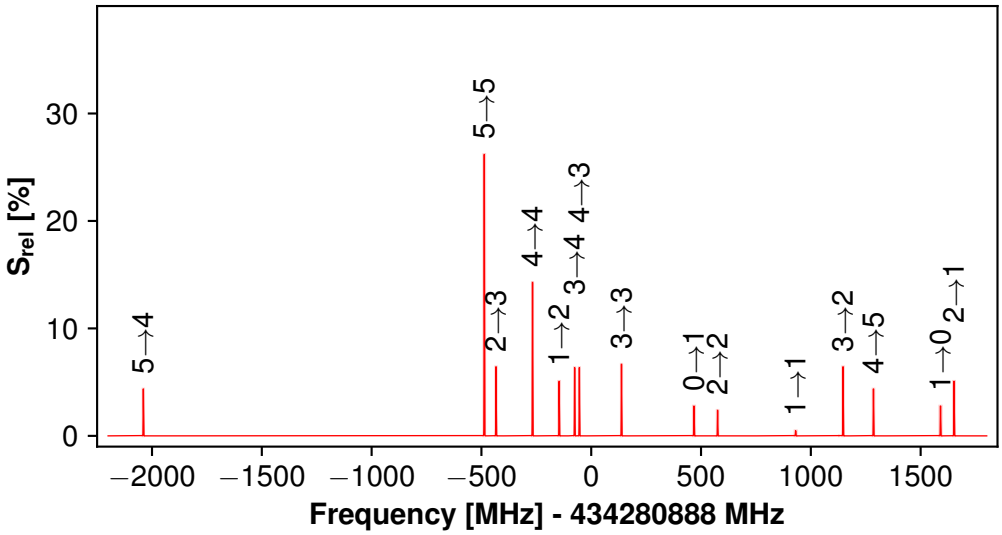

(a) **690 nm hyperfine-structure transitions in $^{229}Th^{3+}$**

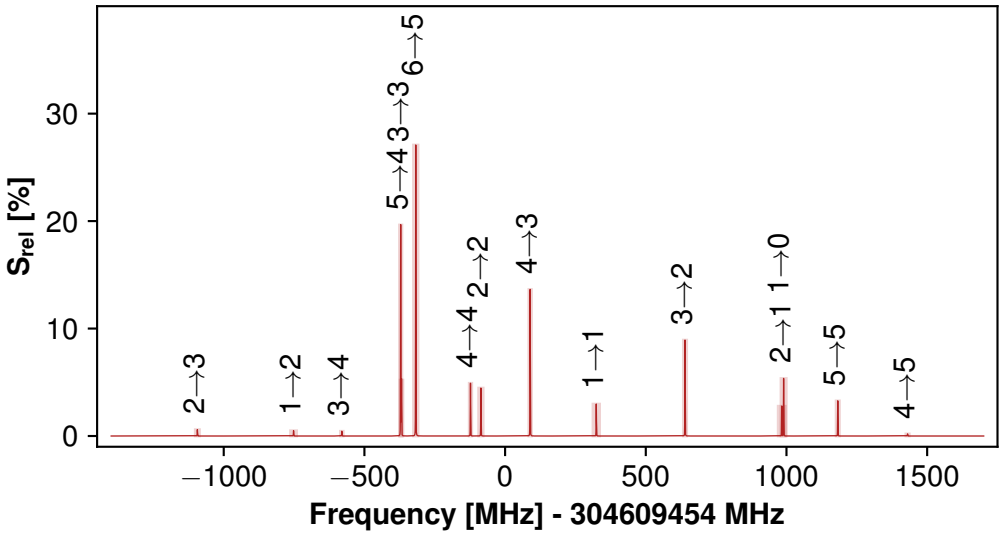

(b) **984 nm hyperfine-structure transitions in $^{229}Th^{3+}$**

Figure 2.12 *Calculated electronic hyperfine splittings of the nuclear ground state of $^{229}Th^{3+}$ for the $5F_{5/2} \rightarrow 6D_{5/2}$ transition (690 nm) in (**a**) and for the $5F_{7/2} \rightarrow 6D_{5/2}$ transition (984 nm) in (**b**), analogous to Fig. 2.11, but now given with a relative intensity distribution.*

Thielking et al., to derive the isomeric hyperfine structure for the two other lowest transitions in $^{229(m)}Th^{3+}$. The splitting calculated with this combination of experimental data is visualized in Fig. 2.13 in dark blue and dark green, respectively. By looking at the plots and also at the absolute values listed in Tab. 2.3 and Tab. 2.4, the differences in the splitting as well as the significantly lower uncertainties are visible. This can be mainly explained by the larger measurement error in the experiment performed by Thielking et al. and the isomer shifts measured by Thielking et al. and Yamaguchi et al. that differ by around 26 MHz (984 nm) and almost 50 MHz (690 nm).

Also in 2024, Zhang et al. measured the nuclear electric quadrupole structure in ^{229}Th between the ground and the isomeric state and could provide an updated value for the B hyperfine constant with $Q_m/Q_g = B_m/B_g = 0.57003(1)$. For both wavelengths, the hyperfine splittings calculated with this new B constant do not change significantly, which is why the differences are only accounted for in the tables Tab. 2.3 and Tab. 2.4.

Assigning absolute frequencies to the isomeric transitions at the two wavelengths of interest in relation to the nuclear ground state introduces the biggest uncertainty to this approximation of the hyperfine structure. Thielking et al. measured the isomer shift for $^{229}Th^{2+}$, and Yamaguchi et al. measured the shift for a different transition in $^{229}Th^{3+}$. Nevertheless, the hyperfine structures of the different nuclear states are shown with respect to a common center frequency for different ion temperatures (T =300 K and T =0.01 K) and Doppler broadenings in Fig. 2.14. Similar to the descriptions in [81], these plots emphasize the spectral differences in the electronic hyperfine spectrum as a function of the nuclear state and angular momentum. Apart from that, it underlines the requirement for a low-temperature or an almost Doppler-free spectroscopy method to resolve the isomeric transitions relative to the ground state transitions. From an experimental point of view, the electronic hyperfine spectrum of the two nuclear states also represents a non-negligible challenge, if an individual nuclear state has to be examined without addressing the other one.

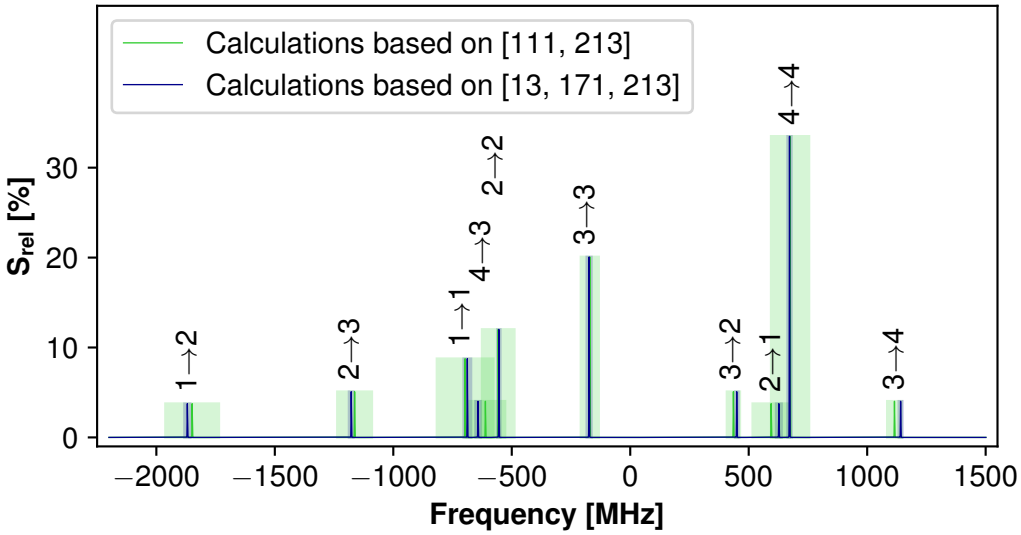

(a) 690 nm hyperfine-structure transitions in $^{229m}Th^{3+}$

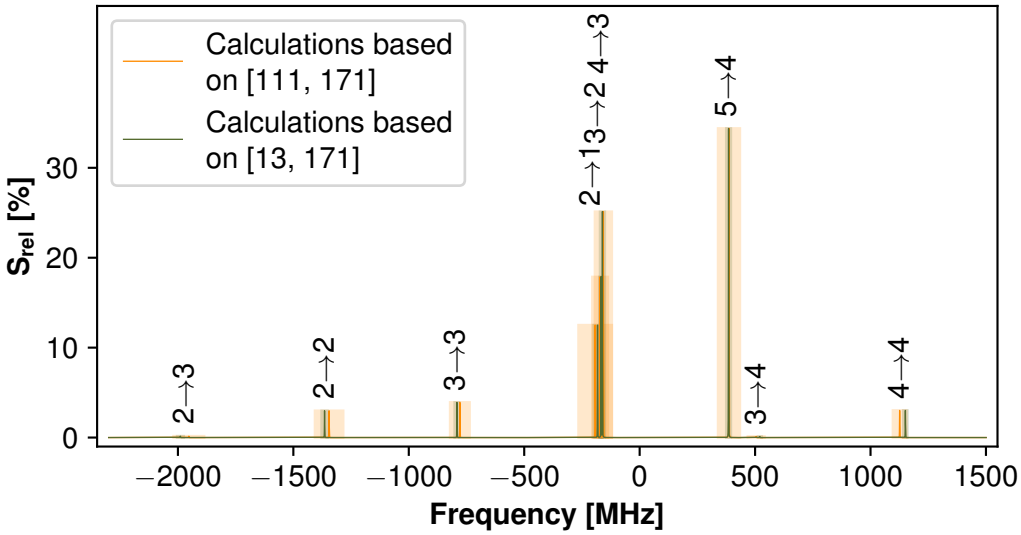

(b) 984 nm hyperfine-structure transitions in $^{229m}Th^{3+}$

Figure 2.13 *Calculated electronic hyperfine splitting for the isomeric state of* $^{229}Th^{3+}$ *of the* $5F_{5/2} \rightarrow 6D_{5/2}$ *transition (*690 nm*) in (**a**) and the* $5F_{7/2} \rightarrow 6D_{5/2}$ *transition (*984 nm*) in (**b**). The calculations for (**a**) are based on the combined results of either [111, 213] (light green) or [13, 171, 213] (dark blue). The calculations for (**b**) are based on the combined calculations of [111, 171] (orange) and [13, 171] (dark green). The linewidths of the transitions are given for an ion temperature of* 10 mK *and the labels indicate the different quantum numbers* $F \rightarrow F'$*. Uncertainties are indicated as shaded rectangles with a width of twice the standard deviation.*

Table 2.3 *Results for the HFS transitions in $^{229m}Th^{3+}$ at 690 nm based on own calculations with the results of either [111, 213], [13, 171, 213] or [12, 13, 171, 213]. F is the quantum number of the lower state, F' the quantum number of the upper state, ν is the transition frequency with respect to the center of the hyperfine spectrum and the uncertainty given as Gaussian error, $\Delta_2\nu$ is the minimum and maximum frequency uncertainty, and S_{rel} is the relative transition intensity rounded to the first decimal.*

F	F'	Calculation [111, 213]		Calculation [13, 199, 213]		Calculation [12, 13, 199, 213]		S_{rel} [%]
		ν [MHz]	$\Delta_2\nu$	ν [MHz]	$\Delta_2\nu$	ν [MHz]	$\Delta_2\nu$	
$5F_{5/2} \rightarrow 6D_{5/2}$								
1	1	−696(119)	$^{197}_{55}$	−688(15)	$^{40}_{1}$	−687(13)	$^{16}_{5}$	8.8
1	2	−1849(112)	$^{158}_{73}$	−1869(12)	$^{27}_{3}$	−1872(9)	$^{14}_{4}$	3.8
2	1	595(78)	$^{128}_{40}$	627(11)	$^{26}_{2}$	630(11)	$^{12}_{3}$	3.8
2	2	−557(68)	$^{90}_{58}$	−554(6)	$^{13}_{3}$	−555(6)	$^{9}_{3}$	12.0
2	3	−1163(73)	$^{102}_{34}$	−1178(9)	$^{19}_{1}$	−1179(9)	$^{8}_{3}$	5.1
3	2	435(27)	$^{47}_{14}$	450(7)	$^{14}_{1}$	451(2)	$^{4}_{1}$	5.1
3	3	−171(37)	$^{59}_{9}$	−174(10)	$^{20}_{1}$	−174(7)	$^{2}_{0}$	20.1
3	4	1115(30)	$^{57}_{16}$	1141(7)	$^{17}_{2}$	1144(4)	$^{4}_{1}$	4.0
4	3	−611(83)	$^{119}_{38}$	−643(10)	$^{22}_{1}$	−645(10)	$^{9}_{4}$	4.0
4	4	675(80)	$^{116}_{63}$	672(8)	$^{19}_{3}$	672(7)	$^{11}_{3}$	33.5

Table 2.4 *Results for the HFS transitions in $^{229m}Th^{3+}$ at 984 nm based on own calculations with the results of either [111, 171], [13, 171] or [12, 13, 171]. F is the quantum number of the lower state, F' the quantum number of the upper state, ν is the transition frequency with respect to the center of the hyperfine spectrum and the uncertainty given as Gaussian error, $\Delta_2\nu$ is the minimum and maximum frequency uncertainty, and S_{rel} is the relative transition intensity rounded to the first decimal.*

F	F'	Calculation [111, 199]		Calculation [13, 199]		Calculation [12, 13, 199]		S_{rel} [%]
		ν [MHz]	$\Delta_2\nu$	ν [MHz]	$\Delta_2\nu$	ν [MHz]	$\Delta_2\nu$	
$5F_{7/2} \rightarrow 6D_{5/2}$								
2	1	−193(72)	$^{152}_{1}$	−183(17)	$^{48}_{0}$	−182(15)	$^{27}_{2}$	12.5
2	2	−1345(61)	$^{110}_{21}$	−1365(13)	$^{32}_{1}$	−1367(11)	$^{21}_{2}$	3.0
2	3	−1953(66)	$^{122}_{3}$	−1989(14)	$^{38}_{3}$	−1993(13)	$^{19}_{1}$	0.1
3	2	−171(33)	$^{64}_{16}$	−167(7)	$^{18}_{1}$	−167(7)	$^{13}_{2}$	17.9
3	3	−779(42)	$^{75}_{8}$	−792(10)	$^{24}_{1}$	−793(10)	$^{11}_{1}$	3.9
3	4	505(36)	$^{74}_{13}$	521(8)	$^{22}_{1}$	522(8)	$^{15}_{2}$	0.1
4	3	−157(36)	$^{59}_{8}$	−161(10)	$^{24}_{0}$	−162(8)	$^{6}_{1}$	25.1
4	4	1126(29)	$^{58}_{13}$	1151(9)	$^{23}_{3}$	1154(7)	$^{10}_{0}$	3.0
5	4	387(47)	$^{92}_{20}$	385(10)	$^{27}_{0}$	385(10)	$^{18}_{1}$	34.4

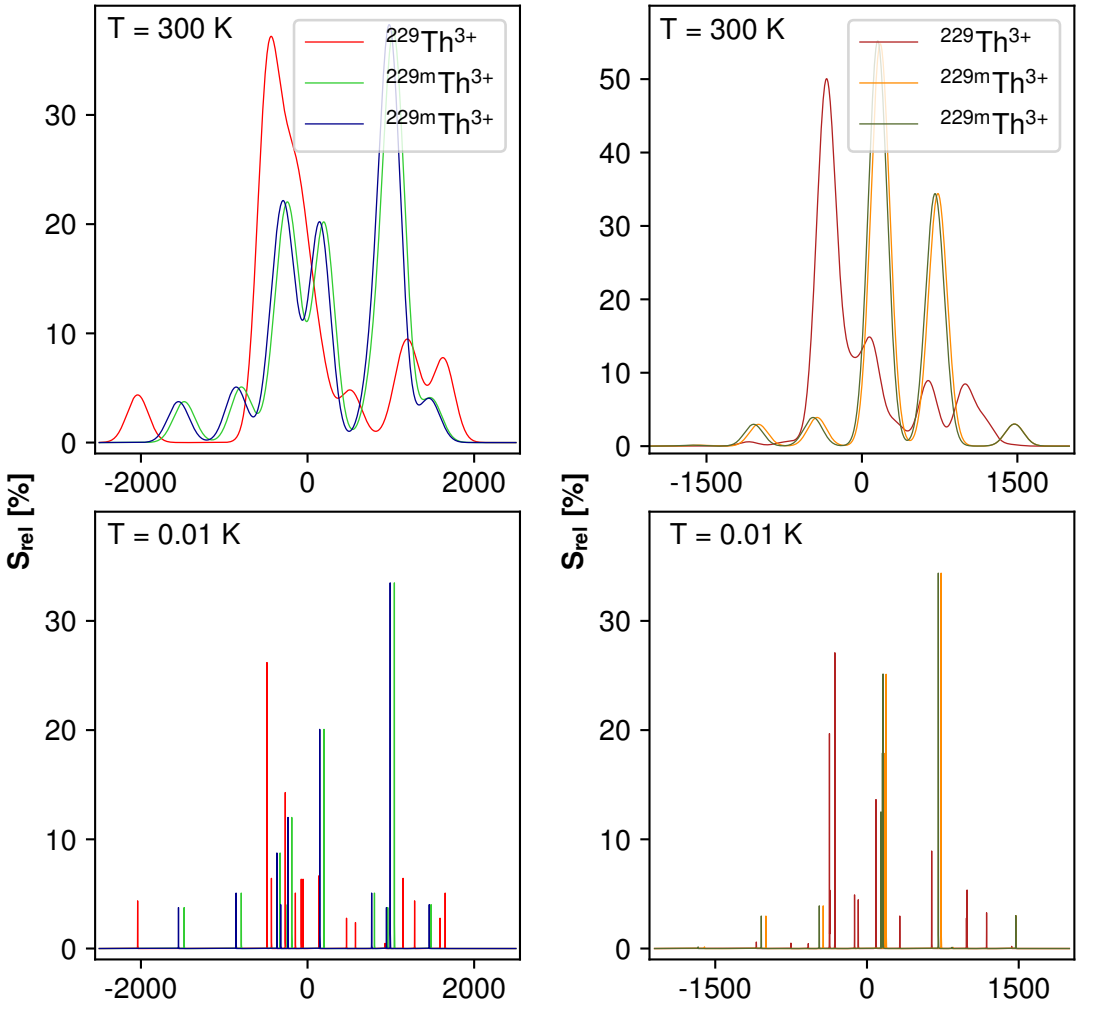

(a) 690 nm hyperfine-structure transitions in $^{229(m)}$Th^{3+}

(b) 984 nm hyperfine-structure transitions in $^{229(m)}$Th^{3+}

Figure 2.14 *Shown are the effects of Doppler broadening on the electronic hyperfine structures in $^{229(m)}Th^{3+}$ for the two different transitions $5F_{5/2} \rightarrow 6D_{5/2}$ (690 nm) in (**a**) and $5F_{7/2} \rightarrow 6D_{5/2}$ states (984 nm) in (**b**). For the 690 nm transitions, the calculations of the nuclear ground state are based on the results of [171, 213], and in the case of the isomeric state, there is again distinguished between results calculated according to [111, 171, 213] (light green) and [13, 171, 213] (dark blue). For the 984 nm transitions, the calculations of the nuclear ground state are based on the results of [171] and in the case of the isomeric state, they are either based on [111, 171] (orange) or [13, 171] (dark green). For better visibility, the shaded uncertainty bars are neglected in this plot.*

2.6 Electro-Optic Modulation

After discussing the hyperfine structure of $^{229(m)}Th^{3+}$, it is necessary to introduce the experimental method of electro-optic modulation to tackle the challenges of hyperfine spectroscopy and the coherent addressing of multiple spectral components with a single laser. An *electro-optic modulator* (EOM) is a device, which takes advantage of the Pockels effect or electro-optic effect for the modulation of the phase, polarization, or intensity of laser light (see also in [220, 221]). It is used to tailor a light field exactly to fit the drive of atomic or ionic energy transitions and is therefore indispensable in many AMO experiments.

In principle, an EOM consists of a birefringent crystal to which an oscillatory electric field of RF frequency is applied. Some examples for birefringent crystals are $LiNbO_3$, $NH_4H_2PO_4$ (ADP), KH_2PO_4 (KDP), BBO, etc. [221, p. 699]. A birefringent crystal has one optical axis and two different refractive indices in parallel ($n_\parallel$) or orthogonal ($n_\perp$) directions to this optical axis. By applying an electric RF field E_{RF} along the optical axis, $n_\parallel$ can be modulated according to the Taylor expansion of the refractive index [221, p. 698]:

$$n_\parallel(E_{RF}) = n_\parallel + a_1 E_{RF} + \frac{1}{2} a_2 E_{RF}^2 + ... \tag{2.70}$$

$$= n_\parallel - \frac{1}{2}\mathfrak{r} n_\parallel^3 E_{RF} - \frac{1}{2}\mathfrak{s} n_\parallel^3 E_{RF}^2 + ... \tag{2.71}$$

The Taylor coefficients a_n are dependent on the polarization of the susceptibility and later rewritten with the coefficients $\mathfrak{r} = -2a_1/n_\parallel^3$ and $\mathfrak{s} = -a_2/n_\parallel^3$. For materials revealing the Pockels effect, mainly the first-order contributes to the modulation of the refractive index, which is then imprinted on the laser light guided through the crystal. For a pure phase modulation, the light passing the EOM has to be polarized parallel to the crystal's optical axis, which is usually adjusted with a polarizer or a waveplate in front of the EOM. Otherwise, there would also occur an amplitude modulation of the light.

Light of wavelength λ passing through a Pockels cell of length L with an electric field applied over the distance d experiences a phase shift according to [221, p. 700]:

$$\varphi = \varphi_0 - \pi \frac{V}{V_\pi} = \frac{2\pi n_\parallel L}{\lambda} - \pi \frac{\mathfrak{r} n_\parallel^3 E L}{\lambda} \tag{2.72}$$

V_π denotes the so-called half-wave voltage at which the phase change is π. It is dependent on the crystal material in use (via $n_\parallel$ and $\mathfrak{r}$) and the ratio between the interaction length L and the distance d.

If the voltage applied to the crystal is not static but oscillates with an RF frequency, the phase of the transmitted light is also modulated with this RF frequency. After the EOM, the light is then not monochrome anymore but spectrally broadened by sidebands around its central (and initial) frequency $\omega_0 = 2\pi\nu_0$. These sidebands are spaced by the RF frequency $\Omega_{RF} = 2\pi f_{RF}$ of the electric field E_{RF}.

Closely following the derivations in [222], the generation of RF sidebands and their behavior can be described mathematically:

Consider a monochromatic light field, which is guided to the EOM. For simplicity, only the electric field part of the light wave is used:

$$E(t) = E_0 \exp(\mathrm{i}\omega_0 t + \mathrm{i}\varphi(t)) \tag{2.73}$$

When the RF voltage with a peak-to-peak amplitude V_{pp} and phase φ_{RF} is applied to the EOM crystal, the phase of the light wave is modulated:

$$E(t) = E_0 \exp\left(\mathrm{i}\omega_0 t + \mathrm{i}\varphi_0 + \mathrm{i}\pi \frac{V_{pp}}{2V_\pi} sin(\Omega_{RF} t + \varphi_{RF})\right) \tag{2.74}$$

$$= E_0 \exp(\mathrm{i}\omega_0 t + \mathrm{i}\varphi_0) E_{NL} \tag{2.75}$$

The phase of the RF voltage can usually be neglected and plays only a role in the case of multiple, consecutive phase modulations of the light. $\pi V_{pp}/V_\Pi$ is also known as the modulation depth β. E_{NL} symbolizes the nonlinear part responsible for the sideband generation and can be expressed by a series of Bessel functions of the first kind, such that:

$$E_{NL} = \sum_{k=-\infty}^{\infty} J_k(\beta) \exp(\mathrm{i}k\Omega_{RF} t + \varphi_{RF}) \tag{2.76}$$

By looking only at the real part of the total expression, the modulated light field after an EOM can be written in a convenient form as:

$$E(t) = E_0 \sum_{k=-\infty}^{\infty} J_k(\beta) cos(\omega_0 t + k\Omega_{RF} t + \varphi_0 + \varphi_{RF}) \tag{2.77}$$

So, the initial light wave is modulated by a sum of sinusoidal wave functions, each multiplied by a constant. In the frequency space, this corresponds to a sum of Dirac peaks with amplitudes $E_0 J_k(\beta)$. The behavior of the Bessel functions $J_k(\beta)$ as a function of the modulation depth and the consequences for the spectrum of the modulated light are shown in Fig. 2.15 and Fig. 2.16 for the first three sideband orders.

Considering now a spectrum of hyperfine transitions similar to the one presented in Sec. 2.5, where the different spectral components have no equidistant relation with respect to each other, a single RF modulation frequency will not be sufficient to address the whole spectrum. Therefore, multiple RF modulation frequencies, depending on the hyperfine lines of interest and their respective spectral distances to a chosen central laser frequency, have to be mixed together. The intensities of the individual sidebands can then be adjusted with the respective RF signal power, although it is usually sufficient to only enhance the first-order sidebands.

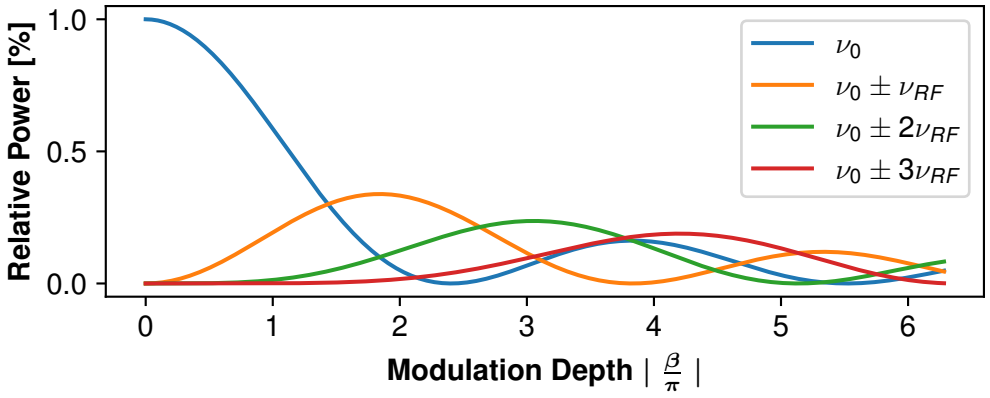

Figure 2.15 *The relative power of the fundamental light frequency and up to three RF sidebands is shown as a function of the applied modulation depth of the RF signal at the EOM device.*

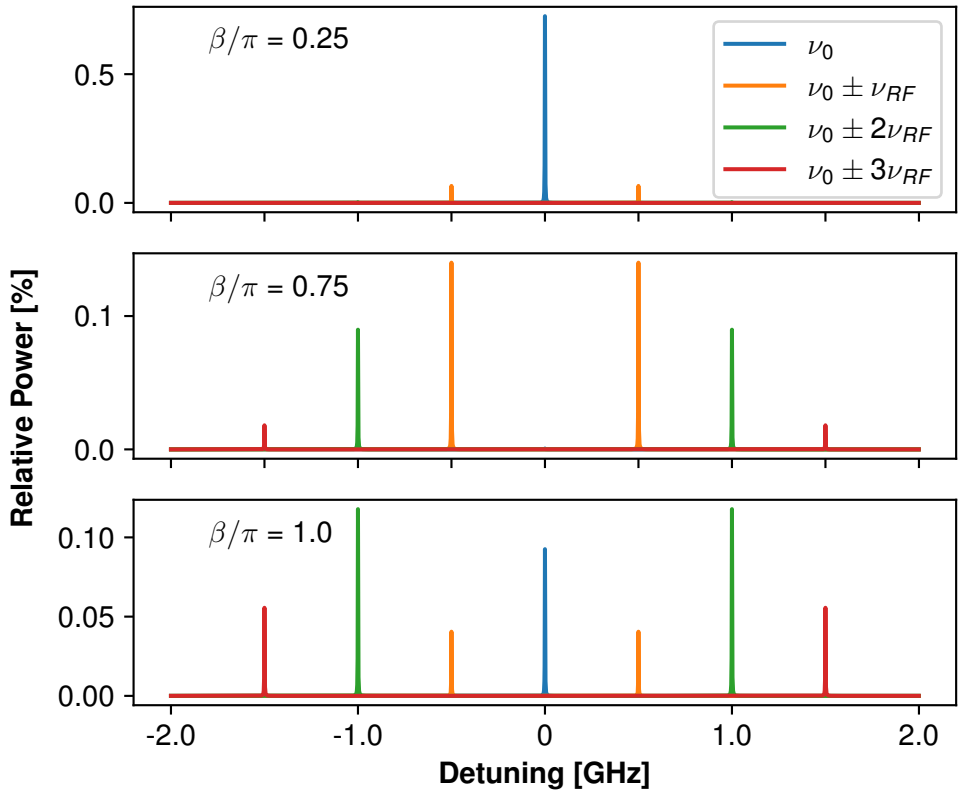

Figure 2.16 *Frequency spectrum of EOM broadenend light with a linewidth of* 2 MHz *and up to three sidebands generated at* 500 MHz*. The spectra for three different modulation depths are shown. All signal powers are given in relation to the unmodulated case.*

3 Experimental Setup

This chapter presents the complete experimental platform at the LMU Munich designed for laser spectroscopic measurements in laser-cooled $^{229(m)}Th^{3+}$ ions, such as hyperfine structure spectroscopy of both nuclear states and the ionic lifetime of the isomeric state. Additionally, the setup is intended to be used for an all-optical vacuum excitation of the isomeric state in thorium with VUV light and would thus also act as a prototype for a trap-based nuclear clock.

The following descriptions mainly summarize the information in the already existing literature on the apparatus [223–226], but also focus on the most recent status.

3.1 Design Aspects

As already emphasized in Sec. 2.5.4, $^{229}Th^{3+}$ ions have to be cooled down below 1 K to clearly distinguish between the electronic hyperfine structure of the isomeric and the nuclear ground state. Such low temperatures can be reached by sympathetic Doppler cooling of the thorium ions confined in a Paul trap together with $^{88}Sr^{+}$ as the main cooling species. Consequently, the cryogenic setup has to be capable of generating and confining the two chosen ion species.

The population probability of the isomeric state during the α decay of ^{233}U to ^{229}Th lies only around 2 % [16], which statistically implies only one isomer within 50 thorium ions. In order to increase the probability of trapping isomers, the design of the Paul trap should also allow the confinement of a huge amount of $^{229(m)}Th^{3+}$ ions together with an at least as large amount of $^{88}Sr^{+}$ ions. Therefore, the architecture of the linear Paul trap is a suitable option with a comparably large region of low micromotion along the z axis and reported storage capacities of more than 10^5 [227]. Moreover, the construction allows for easy laser access and fluorescence readout.

Regarding the measurement of the radiative decay time of isomeric ^{229m}Th ions, the confinement in a Paul trap already provides a suitable environment. Non-radiative decay channels, like internal conversion, are suppressed and the inter-ion distances of µm-range in a Coulomb crystal are more than three orders of magnitude larger than the interaction ranges in a solid-state crystal. Hence, the chemical environment created by laser-cooled strontium ions can be considered as negligible.

Still, the ion confinement times need to be longer than the expected ionic lifetime of about 2000 s. In general, trap confinement times are only limited by the amount of

residual particles (noble gases, hydrocarbons, etc.) in the trap region that can interact with the trapped ions. Consequently, the trap has to be operated in a cryogenic environment to provide the best possible vacuum conditions with estimated pressures below 10^{-13} mbar [154, 156, 228].

3.2 General Overview

Fig. 3.1 depicts the current status of the cryogenic Paul trap setup at LMU Munich. Previous design stages of the experimental apparatus described in [223–225] were discarded in the course of this work. It comprises the following main building blocks that were all designed to meet the previously summarized requirements:

- source of $^{229(m)}Th^{3+}$ ions
- source of $^{88}Sr^{+}$ ions
- macroscopic Paul trap
- cryopump for ultra-high vacuum conditions
- laser setup for Doppler cooling of $^{88}Sr^{+}$ ions
- laser setup for hyperfine spectroscopy $^{229(m)}Th^{3+}$ ions
- electronic detection of the generated ions
- fluorescence imaging of the trapped ions

The vacuum chamber containing the Paul trap, the segmented extraction radio-frequency quadrupole (*Extraction RFQ*), the RFQ ion guide (*Ion Guide*), and two quadrupole mass spectrometers (*QMS 1 & QMS 2*), the imaging system as well as parts of the laser setup are mounted on an optical table (*Clean Top 784 series, 784-43811-01,* 1 m × 2 m, TMC, Peabody, MA, USA) with an active pneumatic vibration isolation system (*Gimbal Piston,* TMC, Peabody, MA, USA). According to the manufacturer, this system should damp 95 % of vibrations exceeding 10 Hz in vertical and horizontal direction and thus also the mechanical noise introduced by the vacuum pumps directly attached to the vacuum chamber with typical frequencies around 1000 Hz.

As a space-saving solution, the cooling and HFS spectroscopy lasers, and first fiber-coupling assemblies are stored in five 19″-rack drawers. With a maximum load capacity of 25 kg and a ball-bearing slide-in rail for smooth opening and closing, these heavy steel-plate drawers (*87404 19″ Rack Drawer 4U,* Adam Hall GmbH, Neu-Anspach, Germany) provide sufficient vibrational stability for the laser operation. For additional decoupling of the breadboards carrying the laser setups inside the drawers from the drawer walls, they are mounted on rubber feet (*AV4/M,* Thorlabs GmbH, Bergkirchen, Germany), damping vibrations above 100 Hz.

To transport the light between individual drawers or the optical table with the Paul-trap vacuum chamber, several polarization maintaining optical fibers are used. Together

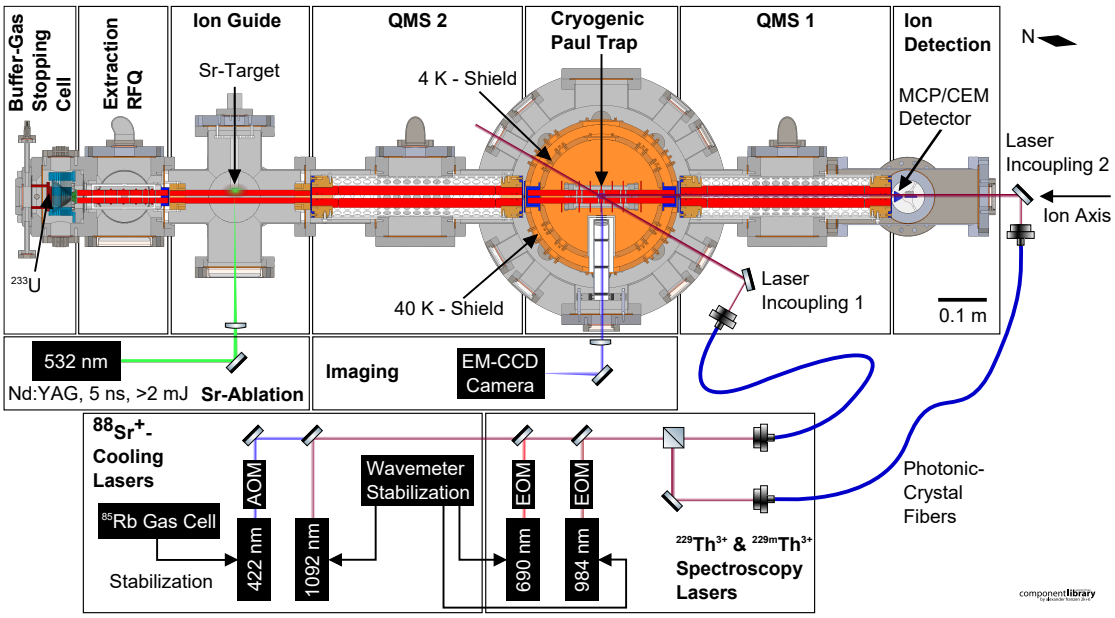

Figure 3.1 *Schematic overview of the cryogenic Paul-trap setup dedicated for the $^{229m}Th^{3+}$ radiative lifetime measurement. Visible is a horizontal cross-sectional cut of the trap vacuum chamber along the ion axis with a not-to-scale but logical arrangement of the different laser setup sections. For a better visualization, the imaging system and the laser incoupling setup 1 are horizontally mirrored along the ion axis with respect to their actual positions. Updated version of own image that is also shown in [226].*

with the power supply and control cables of the lasers, the fibers can be passed through the drawer casings via dedicated feedthroughs. By covering the holes with synthetic foam, dust protection of the drawer content and laser safety can be optimized.

3.3 Extraction of $^{229(m)}Th^{3+}$ Ions

How to design a *Buffer-Gas Stopping Cell* and to use it for the extraction of $^{229(m)}Th^{3+}$ is known from previous experiments performed at LMU Munich [8, 23, 83, 229]. In contrast to the previous version, the newly-built *Buffer-Gas Stopping Cell* and the adjoining radio-frequency quadrupole for ion collection, phase-space cooling, and ion bunching (*Extraction RFQ*) are more compact and adapted for a beam-line configuration based on CF100 vacuum tubes.

In Fig. 3.2, the technical drawing illustrates how the ^{233}U source of 10 kBq activity is mounted inside the *Buffer-Gas Stopping Cell* providing thorium ions via the α decay with a 2 % population branch to the isomeric first excited state. For the storage of a single up to several hundred thorium ions in the Paul trap, the reduced source activity of 10 kBq

in comparison to the 270 kBq activity available for the previous thorium experiments at LMU, was considered as sufficient.

The uranium source was provided by the radiochemistry department of the University of Mainz and is made of a circular silicon substrate of 0.5 mm thickness and a diameter of 25 mm covered with a titanium-uranium coating of 100 nm thickness. More information on the source production is given in [230]. For laser access to the ion axis, the source has a central hole of 5 mm in diameter, and it is also possible to apply a DC offset voltage to the source's metal surface.

As the $^{229(m)}$Th ions recoiling from the source after an α decay of ^{233}U possess a kinetic energy of up to 84 keV [8, 14], they need to be slowed down before they can be further transported. Therefore, the chamber of the stopping cell can be filled with He gas with a purity of $\geq 99.9999\,\%$ (He 6.0) to generate typical chamber pressures of 32 mbar. The fast recoil ions from the source are then thermalized during the collision processes with the gas particles. Especially thorium, and even more when occurring in an ionized charge state, is highly reactive and can easily get lost during the collisional cooling, which makes the further purification of the helium buffer-gas a crucial prerequisite for the desired thorium ion extraction. A detailed description of the dedicated gas purification section is given in [226]. Since the buffer-gas is not the only source of impurities in the source volume, the whole vacuum chamber section housing the *Buffer-Gas Stopping Cell* and the *Extraction RFQ* can be baked. Without the He gas pressure applied, typical pressures for the two chambers after the bake-out are in the low 10^{-9} mbar range.

During the operation with buffer-gas, the high-energetic recoil ions can be stopped within a few cm distance from the source surface [59]. Then, the divergently emitted recoils are guided by an RF-DC funnel away from the source and in the direction of the ion axis before they are eventually dragged by a supersonic gas jet through an on-axis de Laval nozzle into the adjoining *Extraction RFQ* . The funnel structure consists of 29 electrically isolated ring electrodes of different inner diameter arranged to create the tapered shape of a total length of 37 mm. RF voltages of typically 800 kHz and amplitudes of 90 Vpp with a phase difference of 180° are applied to the electrodes such that neighboring segments have an alternating polarity. Like this, the collision of the charged particles with the electrode surfaces is prevented. To form a voltage gradient of around 3 V/cm, dragging the ions to the central axis and the de Laval nozzle, additional DC voltages can be applied to the ring electrodes. More information on the funnel structure is given in [226].

The de Laval nozzle is designed for the creation of a supersonic helium gas-jet to transport the collimated ions to the *Extraction RFQ* . It is also electrically isolated from the surrounding elements and can be used as an electrode or aperture of 0.4 mm inner diameter (see also in [226]).

When the CF35 flexible bypass hose between the *Buffer-Gas Stopping Cell* and the *Extraction RFQ* is closed with a vacuum valve during the extraction of thorium ions, the de Laval nozzle represents the only passage between the *Buffer-Gas Stopping Cell* and the *Extraction RFQ* and is an important prerequisite for differential pumping. As the *Buffer-Gas Stopping Cell* has no vacuum pump attached to its chamber, it can only

be evacuated through the nozzle via the turbomolecular pump (*HiPace 300 H*, Pfeiffer Vacuum GmbH, Aßlar, Germany) below the chamber of the *Extraction RFQ* with a pumping speed of 255 l/s for He. This configuration is crucial to build up pressures of over 30 mbar in the *Buffer-Gas Stopping Cell* and simultaneously reducing the gas pressure again to 1×10^{-3} mbar in the following chamber. If no thorium has to be extracted or the system is baked, the bypass between the *Buffer-Gas Stopping Cell* and the *Extraction RFQ* is opened to provide optimum vacuum conditions in both chamber sections. Additional information on the total vacuum setup for the cryogenic Paul-trap setup is given in [226].

The *Extraction RFQ* is an assembly of four cylindrical electrodes with a total length of 174 mm, an electrode diameter of 11 mm, and a distance of $r_0 = 4.8$ mm between the ion axis and the electrode surface. To use the RFQ for the collection of ions and ion bunching, it is segmented into eight sections of different lengths for the application of different axial DC potentials. The DC voltages up to 100 V are simultaneously applied to all four electrodes of the segment with a precision power supply (*NHS 60 01p*, iseg Spezialelektronik GmbH, Rossendorf, Germany). Starting with the first segment after the de Laval nozzle, the electrodes have following lengths: 1×28 mm, 4×23 mm, 2×11.5 mm and 1×24 mm. To prevent the transmission of ions after the *Extraction RFQ* , an exit aperture with a thickness of 1 mm and a diameter of 2 mm is positioned 1 mm after the eighth segment. Voltages up to 800 V can be applied with another precision power supply (*MHV-4*, mesytec GmbH & Co. KG, Putzbrunn, Germany). The aperture is also the only passage in the gas-tight intersection of the *Extraction RFQ* and the subsequent vacuum chamber housing another RFQ called *Ion Guide*.

3.4 $^{88}Sr^{+}$ Laser Ablation

Several attempts to reliably provide strontium ions with stable and sufficient count rates out of a heated cathode source (*#101139-11 and #103060-11,* HeatWave Labs Inc., Watsonville, CA, USA) failed. Ion emitters of the same design work pretty well with other alkali metals or rubidium, caesium, and potassium. However, the cathode source meant for strontium apparently came to its mechanical limits before reaching the required high temperatures for strontium emission.

Therefore, a change of strategy was necessary, and the laser ablation of strontium atoms from a solid-state target with simultaneous ionization was targeted. Following the approach of previous works [231–233], a $SrTiO_3$ crystal (*Strontium Titanate Single Crystal Substrate <100>, 634689-1EA,* Sigma Aldrich, Merck KGaA, Darmstadt, Germany) is used as a target. It is a 10 mm × 10 mm plate of 0.5 mm thickness and can be easily clamped or glued with Kapton tape on a flat surface inside a vacuum chamber.

For the ablation and generation of ions on the surface of this target, a frequency doubled Nd:YAG laser (*Q-switched Nd:YAG laser, SN: #03022502,* Quantel USA Inc., Bozeman, MT, USA) running at 532 nm with pulse durations of around 5 ns and tunable repetition rates up to 50 Hz is used. The system can be operated with pulse energies of up to 125 mJ, while for the measurements carried out in this work 3–5 mJ were sufficient. To

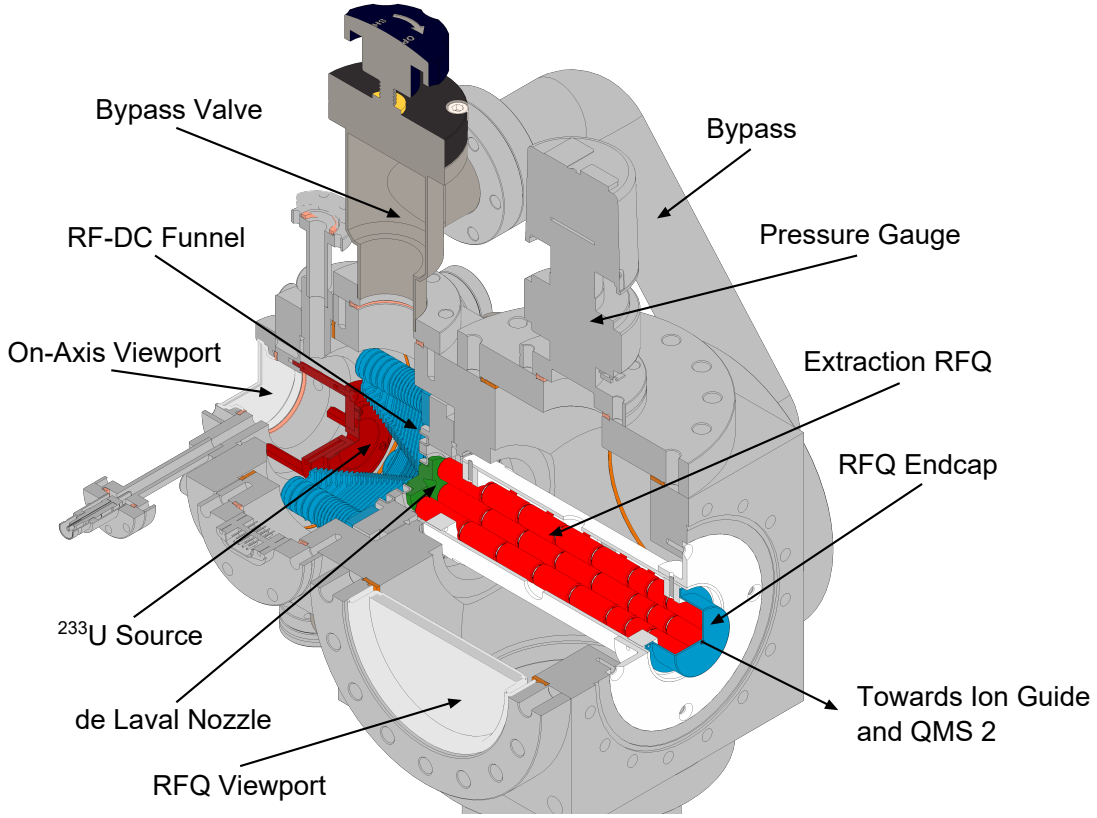

Figure 3.2 *Cutaway drawing of the Buffer-Gas Stopping Cell containing a ^{233}U source for the generation of $^{229(m)}Th^{3+}$ ions and the adjoining Extraction RFQ for ion collection and further buffer-gas cooling.*

monitor the energy of an ablation pulse, a pyroelectric energy sensor is used (*QE25LP-S-MB-QED-D0*, Gentec Electro-Optics Inc., Quebec, Canada and *ESC120C*, Thorlabs GmbH, Bergkirchen, Germany). The laser beam is usually focused on the target with a spot size of about 300 µm after passing a dedicated viewport in the vacuum chamber facing the target position.

Several research groups reported atom or ion ablation in the close vicinity of a cryogenic Paul trap [155, 232, 234, 235]. However, in contrast to the macroscopic linear Paul trap used in this work, mainly surface ion traps with low numbers of loaded ions were used. With the goal of efficient loading several thousands of strontium ions generated without additional photoionization lasers, it was decided to collimate and mass filter the generated ions before trapping. It has to be mentioned that the direct ablation of ions from a solid-state target can be controlled only to a certain extent. During the process, a large amount of charged and neutral particles is generated and can coat the electrode surfaces. Consequently, laser ablation outside the cryogenic trapping region minimizes the risk of generating patch potentials on the trap electrodes and thus also negative

influences on the motional heating rate or the position of the trapped ions [145, 146, 148, 149].

During the operation of the *Buffer-Gas Stopping Cell* as a separate test setup in parallel to the earlier version of the cryogenic Paul-trap apparatus (see Fig. 3.15), the necessity of an additional differential pumping stage became apparent. In the initial design of the setup (see [224]), the thorium-extraction setup was directly followed by a QMS similar to the experimental arrangement used in [8, 83]. However, to reach gas pressures in the low 10^{-9} mbar range in the Paul-trap chamber during the operation of the buffer-gas cell with 32 mbar He pressure, an additional almost gas-tight section between a QMS and the *Extraction RFQ* had to be inserted. At this point, it was also decided to load both ion species from the same side through *QMS 2* into the Paul trap in contrast to the initial design of the apparatus presented in [224]. The additional chamber section, including an additional RFQ, would then also provide the ideal position for the ablation target. As also described in [225], the target does not necessarily have to be mounted on axis to deliver sufficient ion transmission through the apparatus. So, the ion axis would be free for thorium ion transmission.

The development stage of the apparatus shown in [225] was used for characterization measurements of the strontium ablation process and is once again presented in Sec. 3.12.

The required additional RFQ section between *Extraction RFQ* and *QMS 2* , the so-called *Ion Guide* is mounted in a CF100 6-way cross. It has a total length of 269 mm and consists of four rod-shaped electrodes with the same dimensions as the *Extraction RFQ* (see also Fig. 3.3).

Electronics-wise, the *Ion Guide* is linked to the *Extraction RFQ* and basically acts as an additional segment. Therefore, RF voltages at 790 kHz with an amplitude of up to 360 Vpp are usual operation parameters. To use the *Ion Guide* also for mass filtering, additional DC voltages of ±800 V can be applied to the electrodes with a precision power supply (*MHV-4*, mesytec GmbH & Co. KG, Putzbrunn, Germany).

Mounted to the *QMS 2* assembly with a distance of 1 mm to the end of the *Ion Guide* rods is an aperture of 3.0 mm clearance and a thickness of 1 mm. This is the only passage to the subsequent vacuum chamber of *QMS 2* and ensures the differential pumping stage.

If no thorium ions are extracted from the *Buffer-Gas Stopping Cell*, the vacuum pump (*HiPace 300 H*, Pfeiffer Vacuum GmbH, Aßlar, Germany) mounted from below to the 6-way CF100 cross ensures pressures below the measurable range of the vacuum gauge (*IKR 251*, Pfeiffer Vacuum GmbH, Aßlar, Germany). During the operation with He buffer-gas at 32 mbar, a pressure of 2×10^{-6} mbar builds up.

For the laser ablation and the generation of strontium ions, the $SrTiO_3$ target is mounted on an aluminum rod at 90° with respect to the ion axis. Like this, it has a distance of roughly 16 mm to the ion axis and, following the axis, a distance of 697 mm to the Paul trap center. In this way, the influences of the ablation process on the ion trapping stability should be minimized.

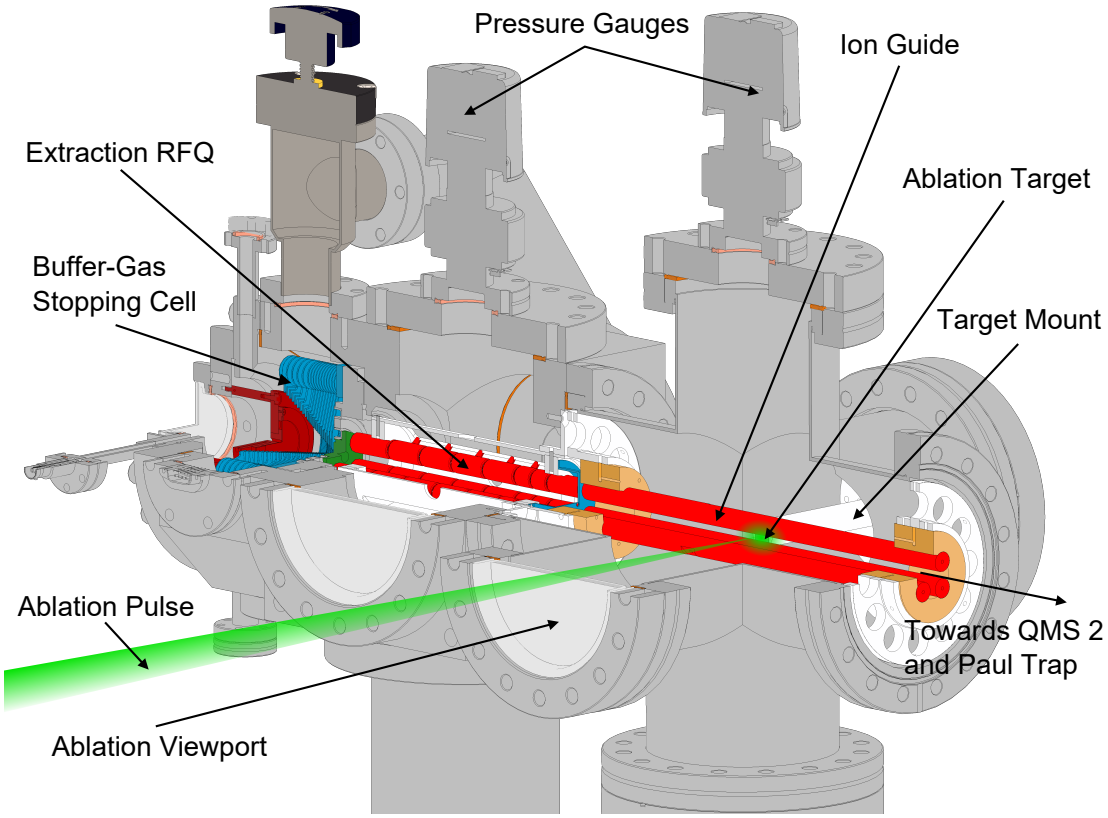

Figure 3.3 *Cutaway drawing of the Ion Guide assembly adjoining the Buffer-Gas Stopping Cell and the Extraction RFQ. The* 532 nm *Nd:YAG laser pulse for ablation and ionization on the surface of a $SrTiO_3$ crystal is shown in green.*

The ablation laser pulses are focused with a lens of 200 mm focal length (*LA1708-A*, Thorlabs GmbH, Bergkirchen, Germany) through the CF100 viewport facing the ablation target.

3.5 Ion Mass Filtering

Leaving the *Buffer-Gas Stopping Cell*, the $^{229(m)}Th^{3+}$ ions are accompanied by other daughter products of the α decay of ^{233}U. Also, the laser ablation process does not inherently deliver $^{88}Sr^{+}$ ions with sufficient isotopic purity. Consequently, the mass filtering of the extracted or generated ions is inevitable before they can be confined in the cryogenic Paul trap for laser cooling and spectroscopy experiments.

Fig. 3.4 depicts the assemply of *QMS 2* after the *Ion Guide*. It is mounted in a CF100 cube and surrounded by a gas-tight housing to create a differential pumping stage with *QMS 2 Entrance Aperture* at the intersection to the *Ion Guide* and the *QMS 2 Exit Aperture* in the direction of the cryogenic Paul trap as the only feedthroughs for

gas exchange. Without the application of a He buffer-gas, the turbo pump (*STP-iX457*, Edwards GmbH, Feldkirchen, Germany) mounted on top of the cubic chamber can pump the section down to pressures of 2×10^{-8} mbar. During the extraction of thorium ions, the pressure is elevated by an order of magnitude to 2×10^{-7} mbar.

The electrode design of *QMS 1* and *QMS 2* is the same and based on the work of Haettner et al. [236, 237]. The four electrode rods have a total length of 402 mm and are segmented into a central element of 300 mm length with two side elements of 50 mm length. They reveal an ion-axis-to-electrode distance of $r_0 = 7.98$ mm and have a rod diameter of 18 mm. All segments can be applied with RF voltages at frequencies around 950 kHz with amplitudes running between 8 Vpp to 1200 Vpp. For the mass filtering of the ions in the central segments, additional DC voltages of ± 300 V can be applied. Like this, the QMS modules can transport and filter particles with mass-to-charge ratios up to $m/Q = 120$ e/u. The side segments without the DC voltage act as so-called Brubaker lenses [238] and improve the ion transmission and thus the signal on the ion detector. Characterization and calibration measurements performed with the two QMS assemblies at the targeted mass resolution of $\frac{m/Q}{\Delta(m/Q)} \approx 150$ are described in detail in [223, 226].

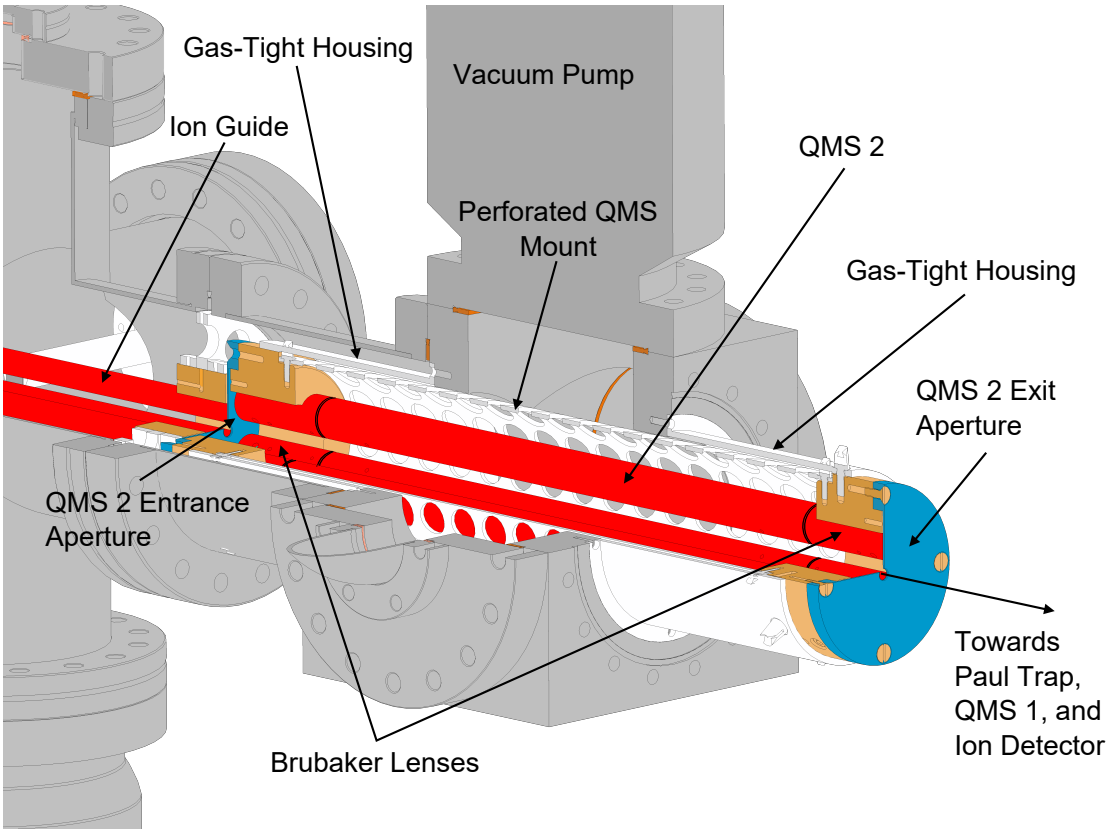

Figure 3.4 *Cutaway drawing of the QMS 2 assembly adjoining the Ion Guide.*

3.6 The Cryogenic Paul Trap

The key component of the whole apparatus is the cryogenic Paul-trap assembly, especially designed for a large number of ions ($> 10^3$) and long ion storage times. An overview of the apparatus housed in the central CF350 vacuum chamber on the optical table is shown in Fig. 3.5.

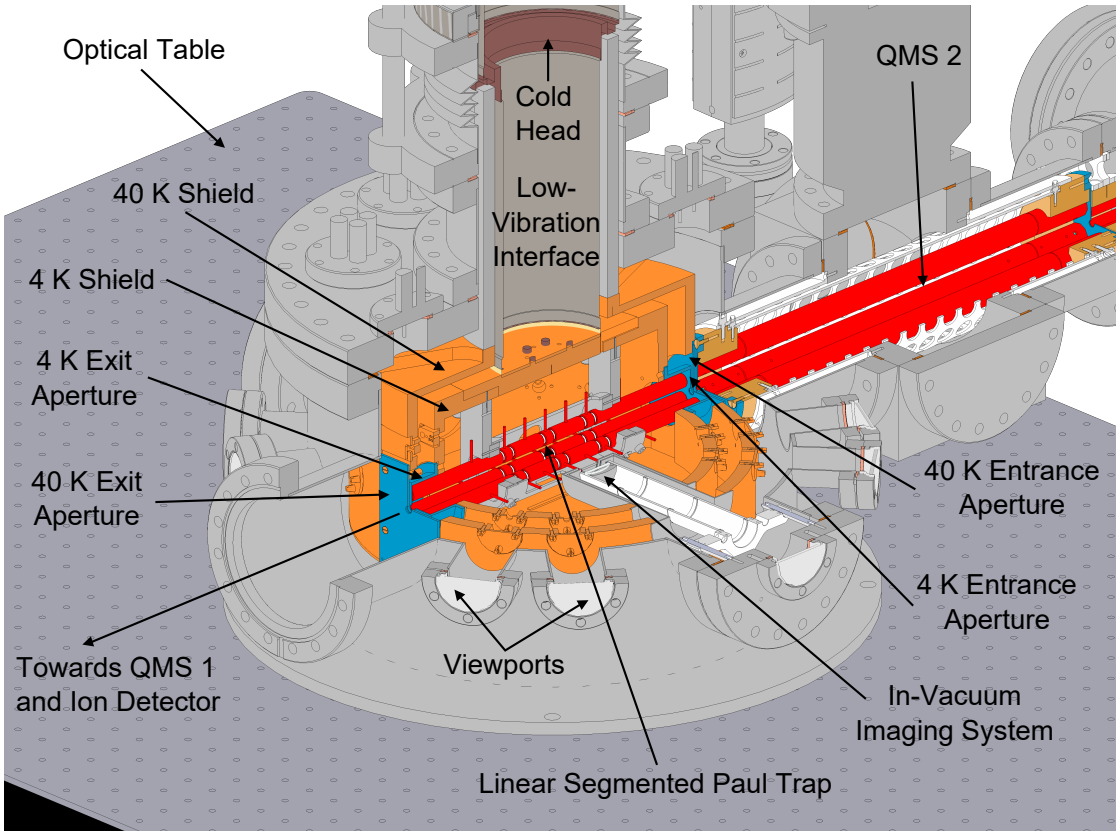

Figure 3.5 *Cutaway drawing of the cryogenic Paul-trap assembly adjoining the QMS 2.*

The linear Paul trap itself is again an RFQ with 7 segments and has a total length of 282 mm. Each of the four rods has a diameter of 11 mm and is arranged with an ion-axis-to-electrode distance of $r_0 = 4.8$ mm. Beginning from the center, the middle segment 4 has a length of 8 mm, the neighboring segments 3 and 5 have a length of 30 mm followed by another pair of 8 mm electrodes as segments 2 and 6. At the sides, segments 1 and 7 both have a length of 93 mm. For electrical isolation, neighboring electrodes are separated by 2 mm spacers made of Al_2O_3. For enhanced electrical conductance, the copper electrodes are coated with a gold layer of 0.5 μ thickness on top of a 10 μm silver layer acting as a diffusion barrier.

Two different schemes can be used for the application of the RF voltages to the trap electrodes. One possibility is to connect the two RF phases to a pair of diagonally opposing rods to reach resonance frequencies of around 1.5 MHz. If one pair of rods is grounded and only one RF phase is used, the overall capacitance in the RF resonance circuit is reduced and results in a higher resonance frequency of around 2 MHz and amplitudes up to 800 Vpp. To generate DC potentials along the ion axis and to confine charged particles in the trap volume, individual voltages up to 400 V can be applied via a precision power supply (*HV400*, Stahl-Electronics, Mettenheim, Germany) to every single trap segment.

The Stahl power supply can deliver the voltages for the trap electrodes only within 150 ms, which is too slow for the trapping of ions with several eV of kinetic energy. Due to this reason, the central trap segments are equipped with fast voltage switches (custom-made HV switches for continuous drive up to 3 kV provided by Dr. T. Dickel, GSI Helmholtzzentrum für Schwerionenforschung GmbH, Darmstadt, Germany and Justus-Liebig-Universität Gießen, II. Physikalisches Institut, Gießen, 35392, Germany). Their characteristic rise time is shown in Fig. 3.6. The upper image, Fig. 3.6(a), shows the case where the switcher is directly connected to an oscilloscope with a cable of 2 m length to reveal a time constant of roughly 400 ns. When it is connected to the Paul trap and the RF-DC mixing electronics, the time constant is increased to about 1.2 ms and the rise of the voltage clearly indicates a charging process (see Fig. 3.6(b)). The consequences of the high capacities in the RF circuit of the Paul trap are further discussed in Sec. 4.2.1.

The infrastructure to create the cryogenic environment in the trap volume is based on the designs of the MPI Heidelberg group for highly charged ion dynamics and their experiences with the CryPTEx cryogenic Paul-trap setup [131, 154, 155, 239]. As can also be seen in Fig. 3.5, the Paul trap is surrounded by two nested temperature shields that are kept at around 8 K (inner shield) and 42 K (outer shield). Like the trap electrodes, the shields are made of copper and coated with a gold layer of 0.5 μm thickness on top of a 10 μm silver layer as diffusion barrier to minimize the absorption of thermal radiation. To reach these low temperatures, the shields are connected to the respective temperature stages of a closed-cycle pulse tube cooling system consisting of a cooling head (*RP-082B2,* Sumitomo Heavy Industries Ltd., Tokyo, Japan) and a compressor unit (*F-70H,* Sumitomo Heavy Industries Ltd., Tokyo, Japan) connected via flexible stainless steel gas lines. The cooling power at the respective temperature stages is 40 W at 45 K and 1 W at 4.2 K.

In general, pulse tube coolers are considered as more reliable and as less vibrating in comparison to other systems, like Giffon-McMahon coolers, because of their lack of any moving parts in the cold head [228, 234]. Still, they introduce mechanical vibrations with displacement amplitudes of the order of several microns with a frequency around 1 Hz [240, 241]. In order to compensate for these vibrations as good as possible, the cooling head is equipped with an ultra-low vibration unit (*PT082 ULV,* ColdEdge Technologies Inc, Allentown, PA, USA) mechanically decoupling it from the Paul trap and the surrounding temperature shields. According to the manufacturer, the vibration iso-

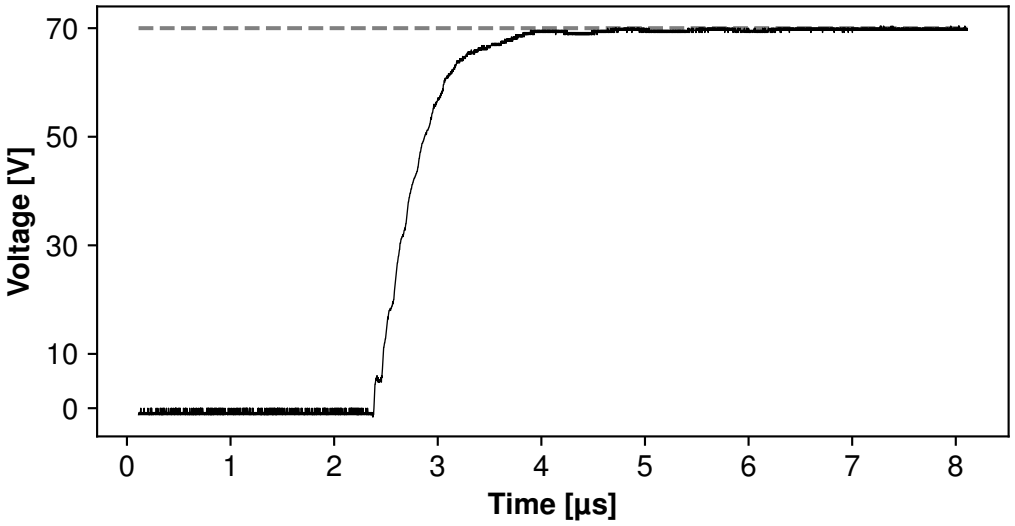

(a)

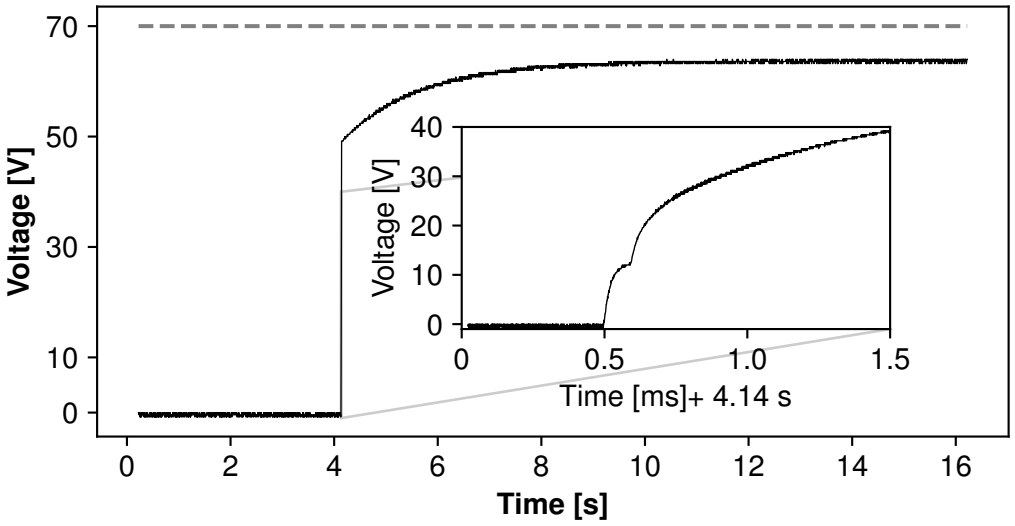

(b)

Figure 3.6 *Rising of the voltage at trap segment 3 switched with the fast HV switch provided by the University of Gießen (T. Dickel et al.). (**a**) shows the switching behavior without additional electronics and no connection to the trap electrodes. (**b**) shows the voltage rising with a connection to the trap electrodes and the RF-DC-mixer in between. In both cases, the zero time position is arbitrarily chosen and has no relation to any trigger signal.*

lation should lower the displacement amplitudes by one order of magnitude, which has already been shown in several experiments [228, 234]. Since the manufacturer could not provide any drawings of the low-vibration unit for a better description of the working principle in Fig. 3.5, see in [226, 234] for more information. To reach the full capacity of the vibration decoupling unit, the cold head has to be suspended from a dedicated mount and is then mechanically connected to the vacuum chamber via a rubber bellow. The latter seals the interface volume between the cold head and the temperature shields and is filled with He gas of $\geq 99.999\,\%$ purity for the temperature exchange. For the LMU setup, the cold head can be mounted to the ceiling, but so far, no influences of the compressor vibrations on the trapping behavior have been observed. Therefore, it is still screwed to the vacuum chamber without taking advantage of the load separation via the ceiling support.

To monitor the temperature during the operation of the cold-head, two silicon diode temperature sensors (*DT-670B-CU,* Lake Shore Cryotronics Inc., Westerville, OH, USA) are placed in vacuum at the different temperature shields.

For the transport of charged particles into the trap volume, the temperature shields have dedicated feedthroughs that are also equipped with electrodes. The apertures at the entrance and exit of the 40 K shield have a thickness of 2 mm and clearance holes of 5 mm in diameter. At a distance of 2 mm in the direction of the trap center, the entrance and exit apertures of the 4 K shield are placed. They are of 1 mm thickness and also have an aperture diameter of 5 mm. At another distance of 2 mm in the direction of the trap center, the linear Paul trap begins.

During the usual operation of the trap setup, the apertures of the 40 K temperature shield are grounded. The entrance and exit apertures of the 4 K shield, however, are used as endcap electrodes of the trap and play a special role in the loading of thorium ions. Similar to the trap segments, they are provided with DC voltages by a precision power supply (*HV400*, Stahl-Electronics, Mettenheim, Germany) and are equipped with fast voltage switches. As these apertures are not part of the RF circuit and therefore not connected to a high-capacity element, they can also be switched within a microsecond.

Apart from the openings along the ion axis, the shields provide four additional lines of sight through the trap center at 30°, 50°, 130°, and 150° relative to the ion axis. In combination with the eight viewports in the CF350 chamber, these 5 mm openings in the shields give access for the Doppler cooling and spectroscopy lasers. The eight viewports are AR coated at the wavelengths of the four diode lasers (*Fused Silica Viewport, AR coated on both sides at* 420 nm*,* 690 nm*,* 980 a*nd* 1092 nm*, mounted on a F40 Flange,* MPF Products Inc., Gray Court, SC, USA). In addition, each temperature shield features another pair of openings perpendicular to the ion axis with diameters of 53 mm (4 K) and 70 mm (40 K). As shown in Fig. 3.5, one of the openings is used to position an in-vacuum imaging system for fluorescence light collection of the trapped ions as close as possible to the trap center. To simultaneously limit the influences of thermal radiation, the imaging system is surrounded with pocket-shaped apertures that form a nested recess into the trap volume and maintain the function of the temperature shields (see also [226]). The collected fluorescence light can leave the trap through another AR-coated viewport and

is then guided to the detector. Further information on the imaging system is given in Sec. 3.11.

The other openings facing the imaging system are reserved for future use and can be covered with gold-coated copper plates. In view of a merge of the cryogenic Paul trap setup with a VUV laser source for the direct excitation of the isomeric state of $^{229}Th^{3+}$, they can be used for the VUV incoupling.

To provide excellent vacuum conditions in the trap chamber, it is pumped from below with a pumping speed of 600 l/s for He (*STP-603*, Edwards GmbH, Feldkirchen, Germany) and an additional backing pump running with a pumping speed of 38 l/s (*TwisTorr 84 FS*, Agilent Technologies Inc., Santa Clara, CA, USA) for He. Without the He buffer-gas applied, the pressure in the chamber is below the measurable range of the vacuum gauge ($< 5 \times 10^{-10}$ mbar) and rises to 2×10^{-9} mbar during the extraction of thorium ions.

3.7 Ion Detection

To detect the ions extracted from the *Buffer-Gas Stopping Cell*, generated in the laser ablation process or ejected from the Paul trap, they must be transported through the Paul trap and the subsequent *QMS 1*. After leaving the *QMS 1* through another aperture of 3 mm diameter and 1 mm thickness, the ions need to overcome an unguided distance of around 10 mm before they reach the detector surface. This free path was chosen to prevent any sparking effects between the detector surfaces at voltages below −1 kV and the QMS exit aperture.

In an earlier development stage of the setup, a microchannel plate detector (MCP) was used for ion detection. It consisted of two detector plates in chevron configuration (GIDS GmbH, Mannhein, Germany) mounted in a commercial assembly (*F9890-13*, Hamamatsu Photonics K. K., Hamamatsu, Japan) with −1.8 kV applied to the front plate. Small electronic signals from ionic impacts were amplified in multiple microchannels and read out via a copper anode behind the back plate. Afterwards, the signal was further amplified in a modified fast-timing preamplifier (*VT 120*, Ortec/Ametek, Oak Ridge, Tn, USA).

Currently, a channel electron multiplier (CEM) (*KBL15RS*, Dr. Sjuts Optomechanik, Göttingen, Germany) is used to detect the transmitted ions. It is usually operated with a bias voltage of −2.4 kV and the amplified ionic signal is read out either with the same Ortec preamplifier or with a low-noise amplifier (*ZFL-1000LN+*, MiniCircuits, Brooklyn, NY, USA). A major advantage of the CEM over the MCP is its compact size. Therefore, it can also be mounted on a linear mechanical feedthrough to be lifted by several millimeters up and down to unblock the ion axis for laser access.

For both detector types, the amplified signals are converted in TTL pulses with a constant fraction discriminator and can be digitized afterwards with a digital-to-analog converter card (*NI-9401*, National Instruments Corp., Austin, TX, USA) of a FPGA module (*cRIO-9064*, National Instruments Corp., Austin, TX, USA) for further signal processing on the laboratory PC (see also Sec. 3.14).

To provide sufficiently low pressures for the operation of the ion detector, a turbopump (*HiPace 80 Neo*, Pfeiffer Vacuum GmbH, Aßlar, Germany) is attached from below.

3.8 Laser Setup for Doppler Cooling of $^{88}Sr^{+}$

As already introduced in Sec. 2.4, the cooling cycle of $^{88}Sr^{+}$ involves laser radiation at 422 nm, driving the main cooling transition from 5s $^2S_{1/2}$ to 5p $^2P_{1/2}$, and at 1092 nm to deplete the dark state 4d $^2D_{3/2}$. For the main cooling transition, a commercial external cavity diode laser (ECDL) is used (*DL pro HP 420_029338*, TOPTICA Photonics SE, Gräfelfing, Germany) with an output power of 41 mW.

Coming with an active temperature stabilization as well as a laser diode current and piezo actuator voltage stabilization, the laser exhibits a very narrow linewidth on short time scales down to 150 kHz at 5 µs integration time according to the manufacturer. Still, it undergoes wavelength drifts over time in free-running mode. To match the linewidth of the main cooling transition of around 20 MHz, the 422 nm laser requires an additional wavelength stabilization to ensure resonant laser cooling for several hours of experimental work.

Following the approach of previous experimental works with Doppler cooled $^{88}Sr^{+}$ ions [242–248], the 422 nm laser is stabilized on the 5s $^2S_{1/2}$ (F=2) $\rightarrow$ 6p $^2P_{1/2}$ (F'=3) atomic transition in ^{85}Rb at $\nu = 710\,962\,401\,328(40)$ kHz [249]. This choice of reference is mainly motivated by the fact that the Rb transition lies only 440 MHz to the red side of the main cooling transition in $^{88}Sr^{+}$ [243, 245]. So, the laser can be directly locked to the absolute external reference and is then frequency shifted to the actual strontium cooling transition.

Fig. 3.7 shows the arrangement of the 422 nm laser head in its steel drawer together with the setup for saturated absorption spectroscopy similar to the one by Shiner et al. [249] to detect the Doppler-free absorption line in the hyperfine structure of ^{85}Rb. Coming from the laser head, the light passes a polarizing beamsplitter and enters, now with linear horizontal polarization, a borosilicate vapor cell (*GC25075-RB*, Thorlabs GmbH, Bergkirchen, Germany) containing a natural isotope ratio of 72.17 % ^{85}Rb and 27.83 % ^{87}Rb [250]. Using a suitable heater and a controller (*GCH25R, TC200*, Thorlabs GmbH, Bergkirchen, Germany), the cell temperature is usually stabilized to 90 °C. After the transmission through the cell, the 422 nm light passes a quarter-wave plate and a neutral density filter (ND 0.5) before it is retro-reflected to the polarizing beamsplitter. Like this, the probe beam for saturated absorption spectroscopy is generated, which has a rotated polarization axis and a lower intensity compared to the initial pump beam. By reaching the polarizing beamsplitter, the probe beam is reflected to a fixed-gain silicon photodetector (*PDA8A2*, Thorlabs GmbH, Bergkirchen, Germany) that feeds the detected signal directly to the digital laser controller (*DLC pro*, TOPTICA Photonics SE, Gräfelfing, Germany) for instant readout of the rubidium absorption signal. By scanning the piezo actuator of the laser grating with a triangular voltage signal, the laser

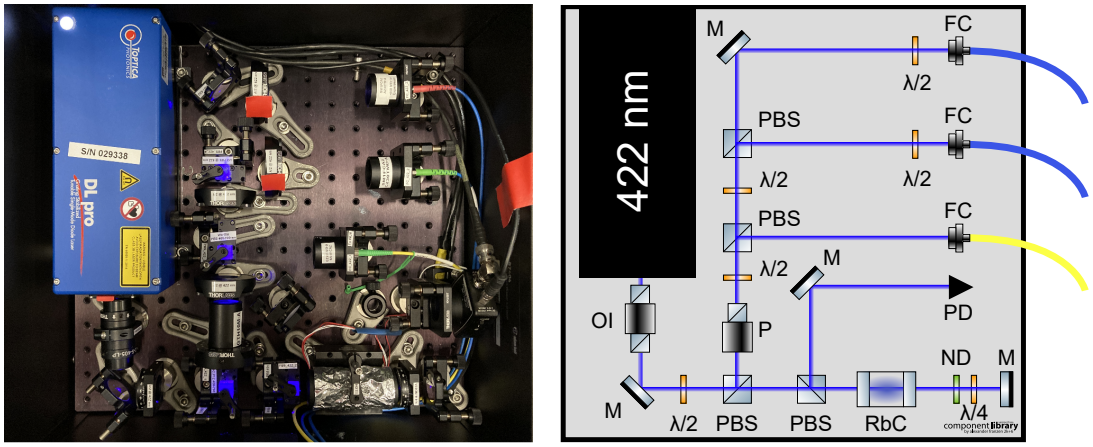

(a) (b)

Figure 3.7 *The 422 nm laser setup assembled in a rack drawer is depicted in a photograph (**a**) and, for better visualization, also as a schematic (**b**). The following abbreviations are used: M = mirror; OI = optical isolator; P = polarizer; λ/2 = half-wave plate; λ/4 = quarter-wave plate, ND = neutral density filter; PBS = polarizing beamsplitter; RbC = rubidium gas cell; FC = fiber coupler; PD = photodiode. Own image, also shown in [225].*

frequency is scanned as well, and the Doppler-free absorption spectrum of ^{85}Rb/^{87}Rb can be revealed.

Fig. 3.8 illustrates which atomic transition peak is chosen for the stabilization of the 422 nm. By directly sending the spectroscopy signal to the DLC pro, the device's internal locking electronics can be used in a so-called top-of-fringe locking scheme. For the generation of an error signal that can be used in a PID (proportional–integral–derivative) control loop, the laser frequency is additionally frequency-modulated. In parallel to the piezo-scan, the laser diode current is modulated with a frequency of 20.4 kHz and an amplitude of ±0.07 mA. Consequently, the amplitude of the spectroscopy signal is manipulated in a fixed phase relation to the modulated diode current and is also proportional to the slope of the atomic transition peak. After a demodulation step following the lock-in technique, the derivative of the spectral shape can be retrieved and used to regulate the diode current and the piezo voltage to the zero-crossing of the spectroscopy signal.

Apart from the Rb-gas cell, the rack drawer contains three fiber coupling stations to transport the 422 nm light to other sections of the setup. One single-mode fiber (*P5-S405-FC-2*, Thorlabs GmbH, Bergkirchen) is connected to a wavelength meter (*WS7-60*, High Finesse GmbH, Tübingen, Germany) for frequency readout. One polarization-maintaining fiber (*P3-405BPM-FC-X*, Thorlabs GmbH, Bergkirchen, Germany) is sending the light to the incoupling setup (see Sec. 3.10) and a second one guides the biggest portion of the power to the frequency shifting setup in the rack drawer below. Polariz-

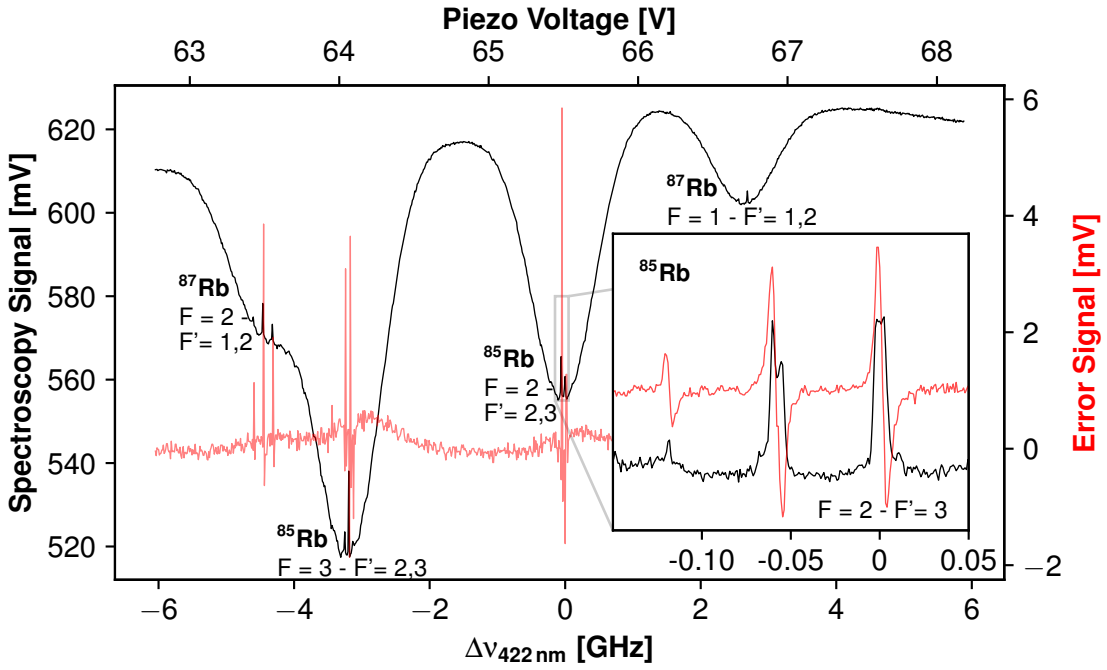

Figure 3.8 *Piezo scan of the* 422 nm *laser frequency over the hyperfine structure resonances in* ^{85} + ^{87}*Rb with a zoom-in on the chosen reference transition in* ^{85}*Rb* ($F = 2 \rightarrow F' = 3$) *(black). The generated error signal for the top-of-fringe locking technique is visible in red. Note that different data were taken for the different views of the spectrum. To generate the frequency axis, a linear fit was applied to the piezo voltage in combination with the results from [249].*

ing beamsplitters are used to regulate the power distribution to the three different fiber couplings.

The frequency up-conversion by 440 MHz required for efficient Doppler cooling of $^{88}Sr^{+}$ ions is achieved with a double-pass through an acousto-optic modulator (AOM), which can be seen in Figure 3.9.

After the outcoupling from the fiber in the AOM drawer, the light passes a zero-order half-wave plate. This is necessary to adjust the polarization axis of the laser light in an orientation perpendicular to the AOM base plate for optimum efficiency in the $+1^{st}$ diffracted order after the first pass through the AOM crystal. In the case of the SiO_2 crystal material of the AOM (*MQ240-A0; 2-UV*, AA Opto-Electronic, Orsay, France), any deviation of the light polarization from the optimum direction instantly result in lower diffraction efficiencies. TeO_2 , another crystal material found in AOM devices, is not that sensitive to the light polarization. Consequently, the incident beam and the back-reflected beam passing the AOM for a second time have to be separated in space and not with the use of different light polarizations for the incident and outgoing beams.

As shown in Figure 3.9, this spatial separation can be realized by aligning the incoming beam vertically off-center through a plano-convex lens (f = 150 mm) to focus on

the active area (1.0 mm × 0.2 mm) of the crystal. To eliminate the disturbing residual 0^{th} and 2^{nd} orders after the first pass through the AOM, they are blocked from two sides with razor blades.

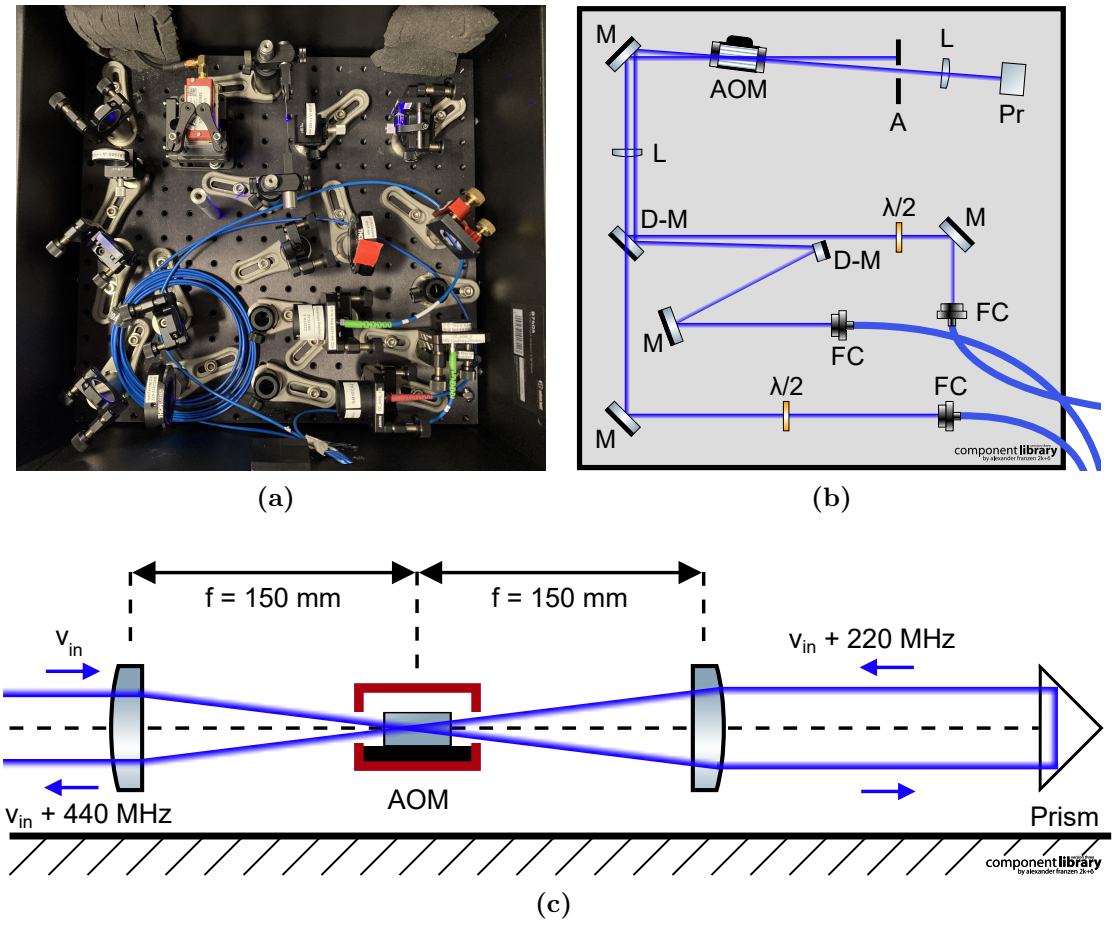

Figure 3.9 *A detailed visualization of the AOM setup with a photograph of the respective rack drawer (**a**), a schematic top view (back-reflected second pass through the AOM partially not visible below the incident beam) (**b**), and a lateral view for a better understanding of the spatial separation of first and second passes (**c**). In the lateral schematic, the 0^{th} and the $+1^{st}$ diffraction orders cannot be resolved.*
The following abbreviations were used: M = mirror; D-M = D-shaped mirror; L = lens; A = adjustable iris; FC = fiber coupler; Pr = prism; λ/2 = half-wave plate. Updated version of own image that is also shown in [225].

The isolated laser beam of the $+1^{st}$ diffracted order can then be sent vertically off-center through another plano-convex lens (f = 150 mm) before it hits a cat's eye reflector (180° prism reflector). At the exit of the prism reflector, the beam is vertically shifted and sent back through the whole lens system and the AOM until it reaches a D-shaped mirror that finally separates it from the beam path of the incoming light. Afterwards,

the 0^{th} and the 1^{st} diffraction orders of the second pass through the AOM are once again separated by another D-shaped mirror and coupled into polarization maintaining fibers. So, 422 nm laser light frequency-shifted by 220 MHz and 440 MHz can be sent to the four-wave laser incoupling section of the setup (see Sec. 3.10).

By using such a configuration, it is also possible to scan the laser frequency around the resonance in ^{88}Sr without changing the frequency of the stabilized laser system itself. The applied modulation frequencies between 190 MHz and 255 MHz at RF signal powers of 2.1 W (or 33.2 dBm) resulted in diffraction efficiencies over the whole modulation frequency range from 32 % to 65 % (see Fig. 3.10).

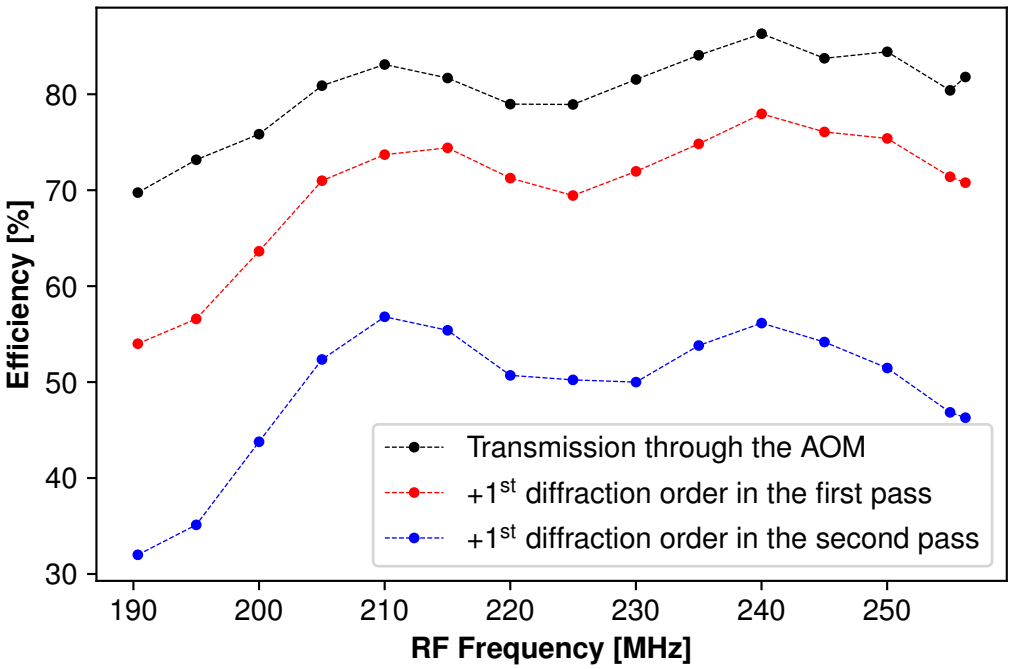

Figure 3.10 *The light transmission efficiency of the first pass through the AOM relative to the incident light power is plotted as a function of the RF modulation frequency applied to the AOM (black). The diffraction efficiencies relative to the initial light power for the $+1^{st}$ order after the first (red) and second (blue) pass are also shown as an evolution of the applied RF frequency.*

The second required laser for the Doppler cooling of $^{88}Sr^{+}$ ions is another ECDL at 1092 nm (*DL pro_021546*, TOPTICA Photonics AG, Gräfelfing, Germany) with an output power of 72 mW. Since the beam profile is rather elliptic, it is corrected using a Galilean telescope of cylindrical lenses (*LJ1629RM-B* and *LK1431RM-B*, Thorlabs GmbH, Bergkirchen, Germany) for higher fiber coupling efficiencies (see also [225]).

Similar to the main cooling laser, the repumper at 1092 nm also requires additional wavelength stabilization to stay on its resonance with a linewidth of around 1.5 MHz. In contrast to the blue cooling laser, no atomic reference is in close vicinity for stabilization. Therefore, it is locked with the wavelength meter to the resonance frequency at

274 589 150(60) MHz, which is known from a previous experiment [248]. To be more specific, the wavelength meter only performs the readout of the laser wavelength that is coupled to the device via a single-mode fiber (*P5-1064y-FC-2*, Thorlabs GmbH, Bergkirchen, Germany) and a multimode fiber switch (*MC8 Multimode Switch, eight inputs, FC/PC,* 12 ms *switching time*, High Finesse GmbH, Tübingen, Germany). The retrieved laser frequency data are then further processed on the laboratory PC by a LabVIEW-based PID controller. Via an FPGA-system (*NI myRIO-1950*, National Instruments Corp., Austin, TX, USA), the digital PID output values are converted into control voltages in the range 0–5 V and can be directly fed to the laser controller. The DLC pro uses the external control signal multiplied by a factor of 1.0 V/V to directly adjust the piezo actuator of the laser grating.

As described in [225], the initial strategy to reduce the wavelength meter's high inaccuracy of 60 MHz consisted in the calibration to the 422 nm laser locked to an absolute frequency reference. Due to the unsolved issue of high instabilities in the wavelength readout of the blue laser introduced by the multimode fiber switch, this approach was discarded. Up to now, the wavelength meter is only calibrated to its internal reference and the 422 nm laser is the only light source in the whole setup stabilized to an atomic reference.

So the stability of the 1092 nm laser is limited by the wavelength meter's specified precision limit of 2 MHz and the maximum accuracy of the frequency lock is 60 MHz.

Considering the optomechanical details, the arrangement inside the rack drawer of the repumping laser is very similar to the one depicted in Fig. 3.7. Neglecting the Rb-gas cell, it also has three fiber coupling stations for light transfer. One single-mode fiber is connected to the wavelength meter, one polarization-maintaining fiber (*P3-1064PM-FC-X*, Thorlabs GmbH, Bergkirchen, Germany) is guiding the light to the incoupling setup before the Paul-trap chamber, and a second polarization-maintaining fiber is freely available. The distribution of the laser power to the three fiber coupling stations is regulated via polarizing beamsplitters.

3.9 Setup for HFS Spectroscopy of $^{229(m)}Th^{3+}$

For the hyperfine structure spectroscopy of $^{229(m)}Th^{3+}$ ions at the $5F_{5/2} \rightarrow 6D_{5/2}$ and the $5F_{7/2} \rightarrow 6D_{5/2}$ transitions, two additional diode lasers at 690 nm and 984 nm are used. The home-built devices described in [225] did not exhibit the required stability for spectroscopy and were replaced by another pair of commercial laser heads (*DL pro_23446* and *DL pro_23450*, TOPTICA Photonics SE, Gräfelfing, Germany).

Similar to the 1092 nm laser head, each of the two spectroscopy lasers is placed in a 19″ rack drawer and has three fiber coupling stations to distribute the laser power to other sections of the apparatus. Using also an analogous stabilization approach, single-mode fibers (*Nufern, SM,*630 nm and *Nufern, SM,*780 nm, SQS Vlaknova optika a.s., Nová Paka, Czech Republic) send power fractions below 1 mW to the wavelength meter via the multimode fiber switch.

To prevent the generation of dark states during the spectroscopy of $^{229(m)}Th^{3+}$, all low-lying hyperfine sublevels of the finestructure levels $^5F_{5/2}$ and $^5F_{7/2}$ have to be simultaneously addressed and emptied, as already shown by Campbell et al. [171, 199, 214]. Since the setup described in this work does not comprise a 1088 nm laser, two schemes to drive the fluorescence in either $^{229}Th^{3+}$ or $^{229m}Th^{3+}$ were elaborated and are presented in Fig. 3.11.

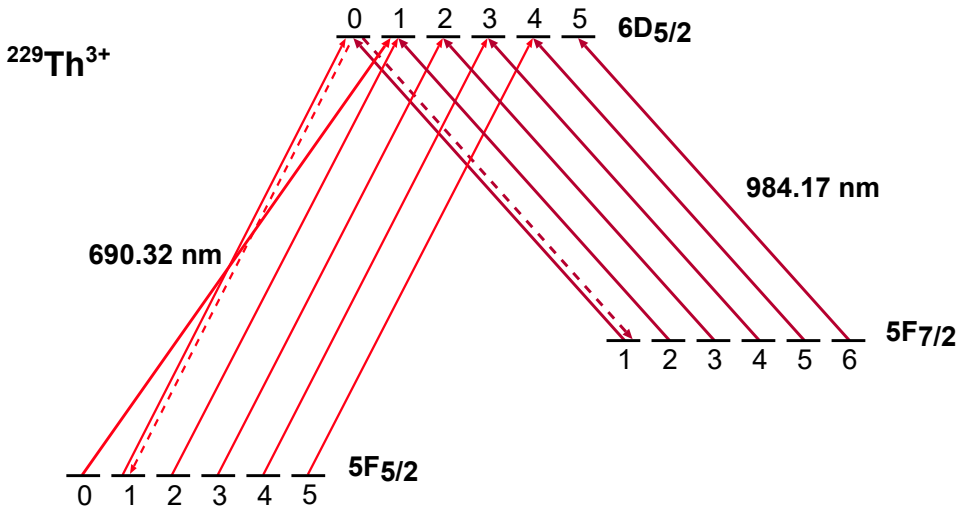

(a)

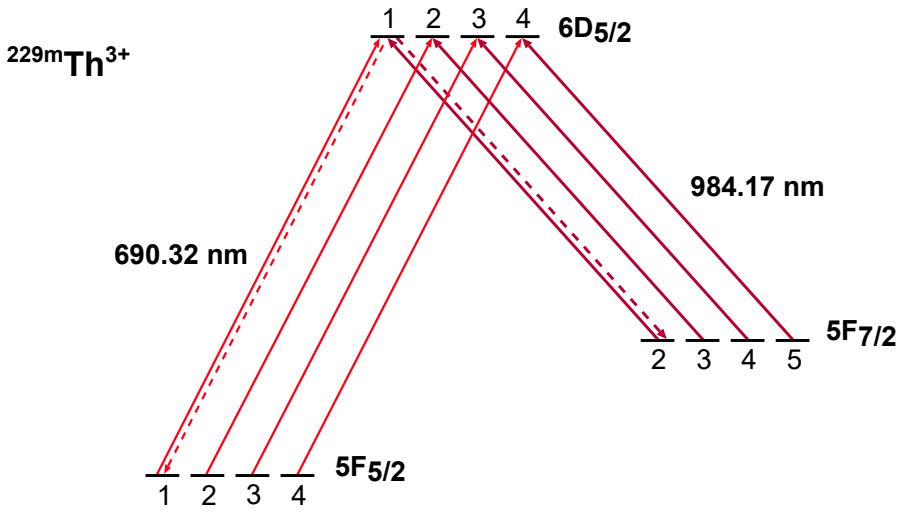

(b)

Figure 3.11 *Two possible schemes to address the hyperfine sublevels in $^{229}Th^{3+}$ (**a**) and in $^{229m}Th^{3+}$ (**b**) for efficient fluorescence detection.*

To generate the multiple frequency components in the spectroscopy lasers (see also Sec. 2.6), they are both coupled into fiber-based EOMs (*M705* and *PM980*, JENOPTIK Optical Systems GmbH, Jena, Germany) that are mounted in the respective rack drawer. For the actual sideband generation during the passage of the $LiNbO_3$ crystal, an RF modulation frequency of a certain power has to be applied. The modulation frequencies listed in Tab. 3.1 and Tab. 3.2 for the realization of the schemes presented in Fig. 3.11 are based on the hyperfine structure calculations described in Sec. 2.5. To facilitate the switching between the nuclear ground state and the isomeric state configuration, the RF modulation frequencies are referenced to the same laser frequency ν_0.

Table 3.1 *List of possible EOM modulation frequencies ν_{EOM} to drive the* 690 nm *hyperfine transitions in $^{229(m)}Th^{3+}$. For the frequency calculation, the isomeric shift for the* 1088 nm *transition published in [13] was used in combination with the most recent results for the hyperfine splitting from [213]. F is the quantum number of the lower state, F' the quantum number of the upper state, ν is the transition frequency with respect to the central resonance ν_0 and ν_{EOM} is the chosen EOM driving frequency. V_{pp} symbolizes the approximate RF signal amplitude for an optimum generation of the first EOM sideband (values with a star (*) are estimated based on previous measurements). In the rightmost column, the devices to generate the modulation frequencies are listed, which are produced by Crystek Corp., Fort Myers, FL, USA and Analog Devices Inc., Wilmington, MA, USA.*

	F	F'	ν [MHz]	ν_{EOM} [MHz]	V_{pp} [Vpp]	Frequency Generation
$5F_{5/2} \rightarrow 6D_{5/2}$; $F = 1 \rightarrow F' = 0$; $\nu_0 = 434\,280\,888(31)$ MHz + 1589.7(95) MHZ						
$^{229}Th^{3+}$	0	1	$\nu_0 - 1121.5(92)$	1121.5	5.9	CVCO55CL5-1100-1200
	2	1	$\nu_0 + 61.3(72)$	61.3	1.2	AD9959
	3	2	$\nu_0 - 444.3(48)$	444.3	1.1	CVCO55CC-0430-0480
	4	3	$\nu_0 - 1644.7(52)$	1644.7	2.8	CVCO55BE-1550-1650
	5	4	$\nu_0 - 3629.4(48)$	3629.4	2.9	CVCO55CC-3500-3700
$^{229m}Th^{3+}$	1	1	$\nu_0 - 1957(25)$	1957	2.8*	CRBV55BE-1820-2100
	2	2	$\nu_0 - 1824(21)$	1824	2.8*	CRBV55BE-1820-2100
	3	3	$\nu_0 - 1443(22)$	1443	2.8*	CV55BE1400-1624
	4	4	$\nu_0 - 589(21)$	589	1.1*	CV55BE0510-0770

The generation of the individual RF signals follows the approach of Uchiyama et al. [251] using several voltage-controlled oscillators (VCOs) that can be additionally attenuated with frequency mixers (*ZX05-30W-S+*, Mini-Circuits, Brooklyn, NY, USA) and a suitable DC voltage. Especially the lower modulation frequencies up to 250 MHz can be generated with a direct digital synthesis (DDS) board (*AD9959*, Analog Devices

Inc., Wilmington, MA, USA). To also apply a frequency sweep of 0 GHz to 1.5 GHz with a variable step size and repetition rate in a similar way as Zitzer et al. [213, 252], two additional DDS boards (*AD9914*, Analog Devices Inc., Wilmington, MA, USA) can be used as generators. An outline of the RF electronics used for individual EOM sideband generation is shown in Fig. 3.12 together with a part list of the hardware in Tab. 3.3.

To adjust the RF signal height of the individual modulation frequency for the generation of the first sideband order in the laser spectrum, a scanning transfer cavity is used that is also described in [225].

So far, no additional bandpass-filters after the frequency generators are applied to filter out the higher-order harmonics usually lying around 15 dB below the signal height of the set frequency.

Table 3.2 *List of possible EOM modulation frequencies ν_{EOM} to drive the* 984 nm *hyperfine transitions in $^{229(m)}Th^{3+}$. For the frequency calculation, the isomeric shift for the* 1088 nm *transition published in [13] was used in combination with the results for the hyperfine splitting from [171, 199]. F is the quantum number of the lower state, F' the quantum number of the upper state, ν is the transition frequency with respect to the central resonance ν_0, and ν_{EOM} is the chosen EOM driving frequency. V_{pp} symbolizes the approximate RF signal amplitude for an optimum generation of the first EOM sideband (values with a star (*) are estimated based on previous measurements). In the rightmost column, the devices to generate the modulation frequencies are listed, which are produced by Crystek Corp., Fort Myers, FL, USA and Analog Devices Inc., Wilmington, MA, USA.*

	F	F'	ν [MHz]	ν_{EOM} [MHz]	V_{pp} [Vpp]	Frequency Generation
$5F_{7/2} \rightarrow 6D_{5/2}$; $F = 1 \rightarrow F' = 0$; $\nu_0 = 304\,609\,454(31)$ MHz + 983.8(128) MHz						
$^{229}Th^{3+}$	2	1	$\nu_0 + 6.5(95)$	6.5	1.1*	*AD9959*
	3	2	$\nu_0 - 343.9(61)$	343.9	2.4	CVCO55CL-0225-0425
	4	3	$\nu_0 - 894.5(48)$	894.5	2.7	CVCO55CC-0860-0960
	5	4	$\nu_0 - 1354.9(45)$	1354.9	3.3	CVCO55CC-1260-1400
	6	5	$\nu_0 - 1301.9(83)$	1301.9	3.3*	CVCO55CC-1260-1400
$^{229m}Th^{3+}$	2	1	$\nu_0 - 846(26)$	846	2.7*	CVCO55CC-0777-0880
	3	2	$-831(21)$	831	2.7*	CVCO55CC-0777-0880
	4	3	$\nu_0 - 825(22)$	825	2.7*	CVCO55CC-0777-0880
	5	4	$\nu_0 - 279(22)$	279	2.4*	CVCO55CL-0225-0425

After passing the respective EOM, the respective laser light is coupled into another polarization-maintaining fiber (*P3-630PM-FC-X* and *P3-980-FC-X*, Thorlabs GmbH, Bergkirchen, Germany) with a fiber connector (*ADAFCPMB1*, Thorlabs GmbH, Bergkirchen,

Germany) and sent to the incoupling setup preceding the Paul-trap chamber. Analogous to the laser setups for strontium Doppler cooling, the power distribution to the fiber coupling stations is done with polarizing beamsplitters.

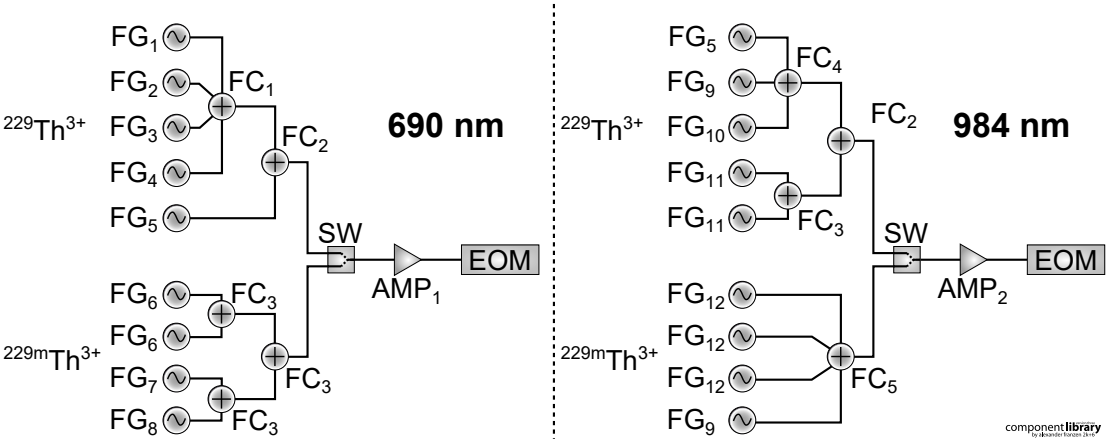

Figure 3.12 *Schematic of the RF electronics used for the modulation of the EOM at the respective wavelength* 690 nm *or* 984 nm *for the hyperfine spectroscopy of* $^{229(m)}Th^{3+}$.

Table 3.3 *Part number designation for the schematic of the used RF electronics in Fig. 3.12. Following abbreviations for the respective manufacturer are used: (Cr) Crystek Corp., Fort Myers, FL, USA; (AD) Analog Devices Inc., Wilmington, MA, USA; (MC) Mini-Circuits, Brooklyn, NY, USA.*

Abbrev.	Part Number	Abbrev.	Part Number
FG_1	*CVCO55CL5-1100-1200*, Cr	FG_{11}	*CVCO55CC-1260-1400*, Cr
FG_2	*CVCO55CC-3500-3700*, Cr	FG_{12}	*CVCO55CC-0777-0880*, Cr
FG_3	*CVCO55CC-0430-0480*, Cr	FC_1	*ZN4PD1-63HP-S+*, MC
FG_4	*CVCO55BE-1550-1650*, Cr	FC_2	*ZFRSC-42-S+*, MC
FG_5	*AD9959*, AD	FC_3	*ZFSC-2-2500-S+*, MC
FG_6	*CRBV55BE-1820-2100*, Cr	FC_4	*ZFSC-3-4-S+*, MC
FG_7	*CV55BE1400-1624*, Cr	FC_5	*ZFSC-4-1-BNC+*, MC
FG_8	*CV55BE0510-0770*, Cr	SW	*ZASWA-2-50DRA+*, MC
FG_9	*CVCO55CL-0225-0425*, Cr	AMP_1	*ZHL-10M4G21W1+*, MC
FG_{10}	*CVCO55CC-0860-0960*, Cr	AMP_2	*ZHL-10W-202-S+*, MC

3.10 Four-Wave Laser Incoupling into the Paul Trap

As described in [225], all four laser wavelengths are aligned into polarization maintaining photonic crystal fibers (PCFs) (*PCF-P-5-3-18E-500*, Schäfter & Kirchhoff GmbH, Hamburg, Germany and *aeroGUIDE-5-PM*, NKT Photonics, A/S, Birkerød, Denmark) to achieve a collinear laser incoupling into the trap via the desired view axis. Fig. 3.13 shows an outline of the opto-mechanical components to achieve the four-wave laser incoupling into these PCFs.

Coming from the different rack drawers via polarization maintaining fibers, the four laser beams are brought to the optical table of the cryogenic Paul-trap chamber. Each of the initially four laser beams can be separately adjusted in power and is then split up to the two PCF fiber couplers (*60FC-LSA-4-M4-24* and *60FC-LSA-4-M4-13*, Schäfter & Kirchhoff GmbH, Hamburg, Germany). Before the fiber coupler, all four colors are overlapped with dichroic mirrors. To block individual laser beams, there are also eight zero-aperture irises mounted in each beam path.

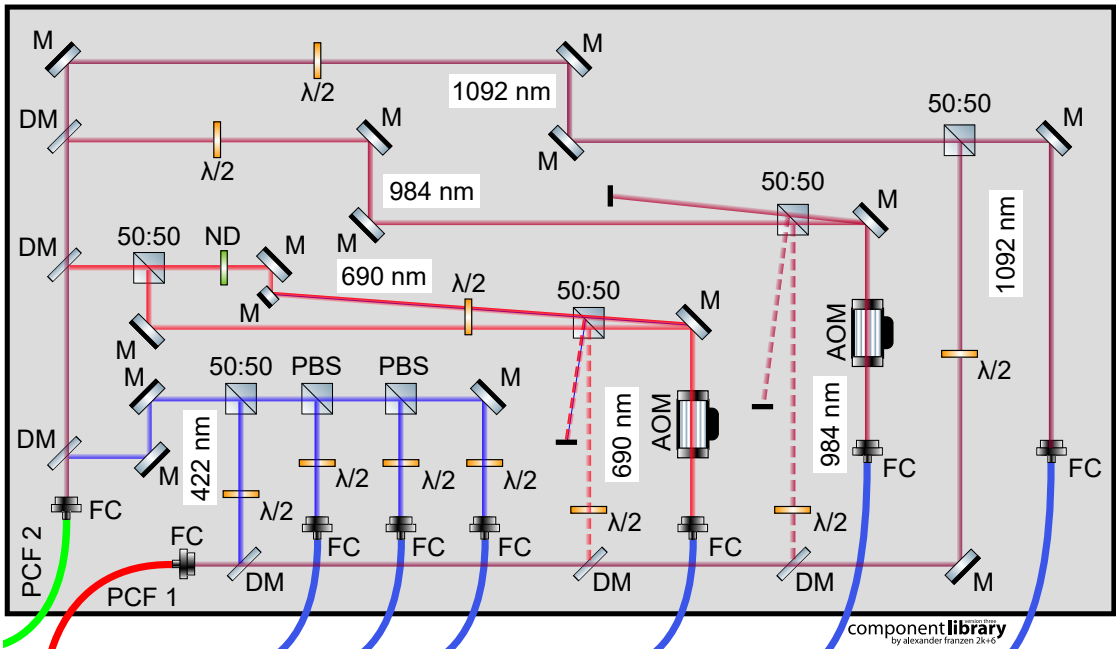

Figure 3.13 *Schematic of the four-wave incoupling setup for the two PCF fibers of Beam 1 (red fiber) and Beam 2 (green fiber). The following abbreviations are used: M = mirror; DM = dicroic mirror; PBS = polarizing beamsplitter; 50:50 = 50:50 beamsplitter; FC = fiber coupler; PCF = photonic crystal fiber; λ/2 = half-wave plate; ND = variable neutral density filter; AOM = acousto-optic modulator. Dashed laser beams represent design options that are prepared in the setup, but were not used in the experiments carried out in this work.*

Depending on the chosen view axis, the PCF fiber out-coupler is positioned in front of the respective viewport, and the collinear beams can be guided through the cryogenic Paul trap with additional broadband steering mirrors.

As an update regarding the details given in [225], the light from both PCFs is coupled out with an achromatic doublet (*AC050-008-A-ML*, Thorlabs GmbH, Bergkirchen, Germany) that can be adjusted depending on the chosen view-axis. As the lens is designed for achromatic corrections in the visible wavelength range, only the 422 nm and 690 nm have a similar beam spot below 1 mm at the trap center whereas the two wavelengths in the IR range reveal spot sizes around 1.5 mm. Currently, the incoupling port at 30° with respect to the ion axis (laser incoupling 1 or *Beam 1*) and the incoupling along the ion axis itself (laser incoupling 2 or *Beam 2*) are default settings for Doppler cooling and laser spectroscopy experiments (see also Fig. 3.1).

For additional control of the spectroscopy lasers, two AOMs (*M1080-T80L-1.5(M)*, ISOMET Corp., Manassas, VA, USA) are inserted in the respective beam paths as optical switches to time and automate the illumination of trapped $^{229}Th^{3+}$ ions. They are both operated with an RF signal at a frequency of 80 MHz provided by a frequency generator (*DG5102*, RIGOL TECHNOLOGIES Co., LTD, Suzhou New District, China), which is further amplified (*ZHL-1-2W+*, Mini-Circuits, Brooklyn, NY, USA) to a signal height of 0.89 Vpp for 690 nm and 1.41 Vpp for 984 nm. With the AOM in the 690 nm beam path, it is also possible to create two laser beams for *Beam 2* at almost the same wavelength that are geometrically separated from each other and can be individually manipulated in their power and frequency modulation. By controlling the AOM modulation frequency, the switching between the different laser configurations can be automated.

3.11 Fluorescence Imaging

The lens system presented in [225] for the collection of the ion fluorescence and the imaging of the trapped ions on the sensor of an EM-CCD camera (*C9100-23B*, Hamamatsu K. K., Hamamatsu, Japan) has been updated. At the beginning of the Doppler cooling experiments, the combination of four lenses with the spatial-filtering system was deemed to be too complicated for the initial search of fluorescence. In addition, the initial target magnification of $M \approx 3$ was considered too small. Therefore, the in-air part of the system was reduced to a single plano-convex lens (*LA1484*, Thorlabs GmbH, Bergkirchen, Germany) with an effective focal length of 300 mm. Together with the in-vacuum aspheric lens (*33-958*, Edmund Optics, Barrington, NJ, USA) with an effective focal length of 50 mm, this update resulted in a magnification of $M \approx 6$. During the experiments, this version of the imaging system (*Version 1*) proved successful, and the spatial filtering has not been applied so far. As the development of the apparatus proceeded and the detection of thorium fluorescence at 690 nm was envisaged, the focal shift of the *Version 1* setup had to be determined. Test measurements in air with a USAF resolution target (*R1DS1N*, Thorlabs GmbH, Bergkirchen, Germany) imitating the ions revealed a focal shift of over 50 mm between the focal planes at 422 nm and 690 nm wavelength, respectively.

For the spectroscopy measurements of $^{229}Th^{3+}$, it is necessary to switch back and forth between the different readout configurations for $^{88}Sr^{+}$ and thorium fluorescence imaging. Consequently, the focal planes for the different readout wavelengths should lie reasonably close to each other to facilitate the operation during the experiment. Therefore, the imaging system was updated again (*Version 2*) with a different pair of lenses (*49-792* and *49-368*, Edmund Optics, Barrington, NJ, USA) that resulted in a focal shift of around 1.2 mm, which is acceptable for a convenient operation.

Both versions of the imaging system have a resolution of better than 7 μm and have a field of view of roughly 1.4 mm that can be imaged on the camera sensor.

As described in [225], the in-vacuum as well as the in-air lens are mounted in lens tubes. Outside the vacuum chamber, a mount for spectral filters is also inserted (*CFS1/M*, Thorlabs GmbH, Bergkirchen, Germany), where different bandwidth filters (*FBH420-10*, *FBH690-10*, and *FBH980-10*, Thorlabs GmbH, Bergkirchen, Germany) can be slid in depending on the desired fluorescence readout mode. For space-saving reasons, the collected fluorescence light is deflected by 90° before it reaches the EM-CCD camera. The EM-CCD camera itself is then mounted in parallel to the ion axis on a three-dimensional stage for optimum positioning and connected to the lens tube system with a flexible rubber bellow (*SM1B3*, Thorlabs GmbH, Bergkirchen, Germany).

To estimate the overall fluorescence photon collection and detection efficiency, the transmission or reflectance of the optics as well as the EM-CCD's quantum efficiency have been taken into account and are listed in Tab. 3.4.

From the estimates presented in the table, the detectable fluorescence signal stemming from $^{229}Th^{3+}$ ions (at 690 nm, 984 nm) is expected to be by three orders of magnitude smaller than the fluorescence signal originating from $^{88}Sr^{+}$ ions (at 422 nm). The choice of 984 nm as readout wavelength for the thorium detection looks a little more favorable than 690 nm, but the shift of the focal planes by over 10 mm in comparison to the 422 nm readout position is prohibitive.

To get a better estimate for the image magnification M induced by the used lens systems, they can be theoretically reduced to a simple thin lens for which the lens-maker's formula applies:

$$\frac{1}{f_{tot}} = \frac{1}{d_o} + \frac{1}{d_i} \tag{3.1}$$

Here, f_{tot} denotes the total focal length of the lens system reduced to a thin lens, d_o the object width, and d_i the image width. The total focal length f_{tot} can be calculated with the focal lengths of the used lenses and the distance between them. d_i is the distance between the focal plane and the image-side principal plane P_2. For the calculation of the principal plane positions P_1 and P_2 of the imaging system, see standard optics textbooks like [165] or use ray-optics simulation programs (e. g. Zemax). After the calculation of d_o with d_i, f_{tot}, and the lens-maker's formula, the magnification can be deduced with $M = d_i/d_o$. Fig. 3.14 illustrates the relation of the different distances and Tab. 3.5 lists the parameters for the two versions of the imaging system.

Only the distances d_2 and d_3 can be measured with high precision. The object widths d_o of the imaging systems, as well as the first distance d_1 between the ion position and the

lens surface, have to be calculated with the lens-maker's formula. In-air measurements or drawings do not account for possible deviations of the actual trapped ion position from the geometrical center of the Paul trap assembly in the design files due to imperfections in the manufacturing process of the vacuum chambers or additional distances introduced by not perfectly tightened copper seals.

Table 3.4 *Fluorescence photon collection and detection efficiencies for the used imaging system. L_1 denotes the in-vacuum photon collection lens and L_2 the in-air focusing lens. The transmission or reflection values for the optical components are taken from the respective data sheets or calculated with the respective data for the AR coatings.*

Lens System	*Version 1* L_1*: 33-958* L_2*: LA1484*		*Version 2* L_1*: 49-792* L_2*: 49-368*	
Wavelength [nm]	422		690	984
Photon Scattering Rate [MHz]	127(5) [201]		≈ 0.16 [214]	≈ 1.31 [214]
Photon Collection [%]	1.5 (maximum solid angle)			
L_1 Transmission [%]	99.65	98.86	97.14	98.24
Viewport Transmission [%]	99.94			
Filter Transmission [%]	97.84		97.39	77.00
L_2 Transmission [%]	91.61	98.86	97.14	98.24
Mirror Reflectivity [%]	95.59		98.38	96.90
EM-CCD QE [%]	65.12		90.90	15.16
Overall Efficiency [%]	0.80	0.90	1.24	0.16
Detectable Photon Rate [kHz]	1015(40)	1139	2.0	2.2

For a rough alignment of the imaging system in place and connected to the trap chamber, a laser beam of a few hundred nW in power is sent through the apertures of the viewport facing the imaging system perpendicular to the ion axis. The lens system makes the beam divergent, but it is sufficient to align the camera and to center the roundish spot on the detector. Later, with ions loaded into the trap, the exact camera position in the focal plane can be found.

In a future iteration of the imaging setup, it is foreseen to install a photomultiplier tube either for the 422 nm or the 690 nm fluorescence readout. Like this, the signals of both ion species could be detected simultaneously, without changing the detector arrangement.

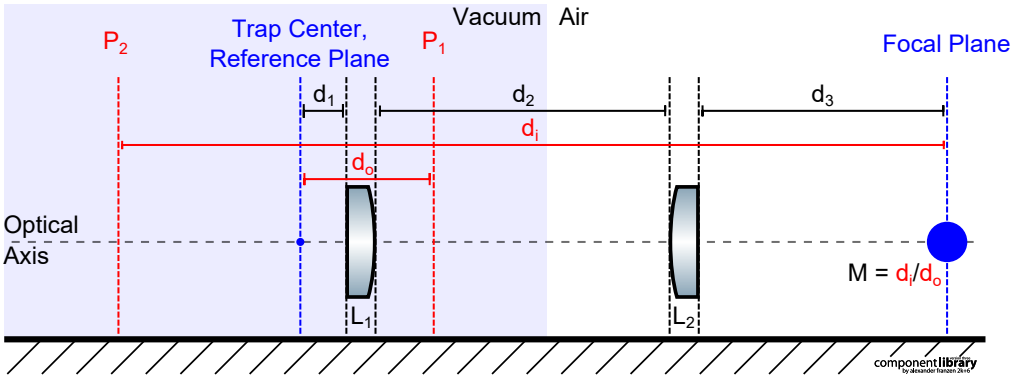

Figure 3.14 *A schematic outline of the lens system used for ion imaging. The indicated distances are necessary parameters to calculate the theoretical magnification of the system. L_1 denotes the in-vacuum photon collection lens, L_2 the in-air focusing lens, P_1 the principal plane position of the object side, P_2 the principal plane position of the image side, d_o the object width and d_i the image width.*

Table 3.5 *Different versions of the ion imaging system and the used distances and positions: (d_1) from the trap center to the surface of the first lens, (d_2) distance between the two lenses, (d_3) from the surface of the second lens to the camera sensor, (P_1) principal plane position on object side, (P_2) principal plane position on image side, (f_{tot}) the focal length of the total lens system, (d_o) the object distance, (d_i) the image distance and (M) the calculated magnification of the imaging system (see also Fig. 3.14). Values marked with a star (*) are calculated with the lens-maker's formula.*

	Version 1 L_1*: 33-958* L_2*: LA1484* 422 nm	*Version 2* L_1*: 49-792* L_2*: 49-368* 422 nm	*Version 2* L_1*: 49-792* L_2*: 49-368* 690 nm
d_1 [mm]	47.0(37)*	46.4(31)*	46.5(32)*
d_2 [mm]	228.5(5)	223.0(5)	
d_3 [mm]	242.0(5)	247.7(5)	
P_1 [mm]	147.5(28)	141.6(26)	142.3(26)
P_2 [mm]	−311.2(121)	−253.0(102)	−255.3(103)
f_{tot}[mm]	126.8(22)	120.8(19)	121.4(19)
d_o [mm]	149.5(31)*	142.7(26)*	143.5(27)*
d_i [mm]	834.3(120)	786.0(100)	789.3(100)
$M = d_i/d_o$	5.7(1)	5.6(1)	5.5(1)

3.12 Setup for Sr^+ Laser Ablation Characterization Measurements

During the first characterization measurements of the strontium ion generation by laser ablation, the experimental apparatus was not yet as developed as presented in Fig. 3.1. Instead of the thorium extraction apparatus and the *Ion Guide* (see also Fig. 3.15), an additional segmented RFQ (*Strontium Extraction RFQ*) was mounted to the entrance of *QMS 2* . It had a rod diameter of 11 mm, an ion axis to rod distance of $r_0 = 5.1$ mm, and consisted of two outer segments of 40 mm and one central segment of 20 mm length. Two circular electrodes with 3 mm apertures on the ion axis acted as endcaps, ablation target mount, and protection of *QMS 2* from ablation residuals. The $SrTiO_3$ target for the laser ablation of strontium ions was directly fixed with Kapton tape on the outer endcap aperture of the RFQ at a distance of 676 mm from the Paul trap center.

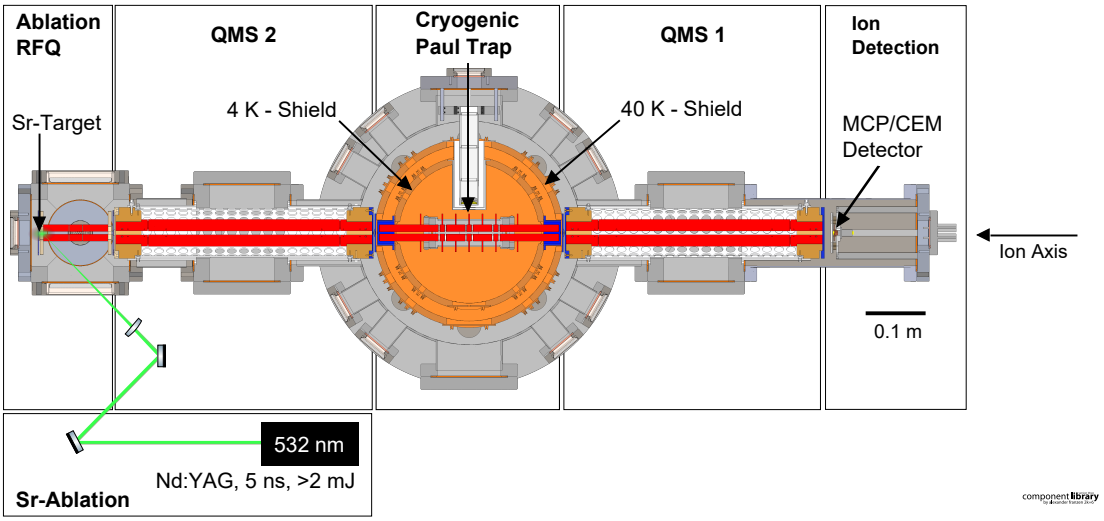

Figure 3.15 *Schematic overview of the cryogenic Paul-trap setup with an MCP detector on the ion axis for first characterization measurements (without the Buffer-Gas Stopping Cell comprising the ^{233}U source, the subsequent Extraction RFQ and Ion Guide). Visible is a horizontal cross-sectional cut of the trap vacuum chamber along the ion axis, with a not-to-scale but logical arrangement of the ablation laser and its optical beam transport components.*

To aim for the target with the ablation laser, it was shot in at an angle of roughly 45° through the 4 mm free spacing between the electrode rods. During these first characterization measurements, the ablation pulse energies deposited on the target with a focused spot diameter of around 300 μm had a varying pulse energy between 1 mJ and 3.5 mJ with a repetition rate of up to 10 Hz to reduce the measurement time and to increase the sample size. To do time-resolved measurements of the ionic counts measured with the MCP, the signals stemming from single ablation pulses were recorded with a multichannel scaler (*SR430*, Stanford Research Systems Inc., California, USA).

Most probably due to a malfunction of the RF electronics, the *Strontium Extraction RFQ* appeared to have a negative influence on the transport of the ablated ions when it was operated. Consequently, the electrodes were mostly grounded for the characterization measurements. As the merge of the main part of the apparatus with the *Buffer-Gas Stopping Cell* and the *Ion Guide* was projected shortly after the conclusion of the ablation characterization measurements, the repair of the RF electronics was not further pursued.

3.13 Setup for the $^{229}Th^{3+}$ Spectroscopy in the Extraction RFQ

Similar to the experiments performed by Thielking et al. [111] and Yamaguchi et al. [13], laser spectroscopy of buffer-gas cooled $^{229}Th^{3+}$ ions was carried out as a proof-of-principle experiment to see thorium fluorescence at 690 nm. Fig. 3.16 shows the modifications outside the vacuum chamber of the *Buffer-Gas Stopping Cell* to conduct the measurements.

To load and confine the ions in a buffer-gas environment, the *Extraction RFQ* can be used as a half-closed trap with the electrode segment 4 as the region of lowest potential. For the incoupling of the spectroscopy lasers at 690 nm and 984 nm wavelength along the ion axis for optimum overlap, a small breadboard with a fiber out-coupler and a steering mirror is mounted on the on-axis viewport facing the ^{233}U source with a flange clamping ring (*VFA275A/M*, Thorlabs GmbH, Bergkirchen, Germany). For the collimation or focusing of the two collinear laser beams transferred via a photonic crystal fiber from the four-wave incoupling setup, a single aspheric lens (*C230TMD-A*, Thorlabs GmbH, Bergkirchen) in the fiber coupler is used. As visible in Fig. 3.16, a dedicated lens system for fluorescence imaging is mounted on the CF100 viewport in the *Extraction RFQ* vacuum chamber section. It consists of two plano-convex 2″ lenses (*LA1050-A* and *LA1979-A*, Thorlabs GmbH, Bergkirchen, Germany) clamped in a lens tube system. From the ion axis to the plane surface of the first lens with a focal length of 99.7 mm, 93.2 mm can be measured (corresponds to the back focal length) and the distance to the second lens with a focal length of 199.3 mm is 98 mm. Theoretically, the focal point of the lens system should lie 208.5 mm behind the second lens and result in a magnification of $M \approx 2$, but due to the system being far from diffraction-limited, the precise focus position is difficult to be experimentally determined. The previously mentioned EM-CCD camera can be mounted with its three-dimensional stage on an optical rail behind the lens tube system, and the gap between the camera and the imaging system can be closed with a rubber bellow for stray-light suppression. Like in the imaging system for the cryogenic Paul trap (see Sec. 3.11), the fluorescence light guided on the camera sensor can be filtered with selected bandpass filters.

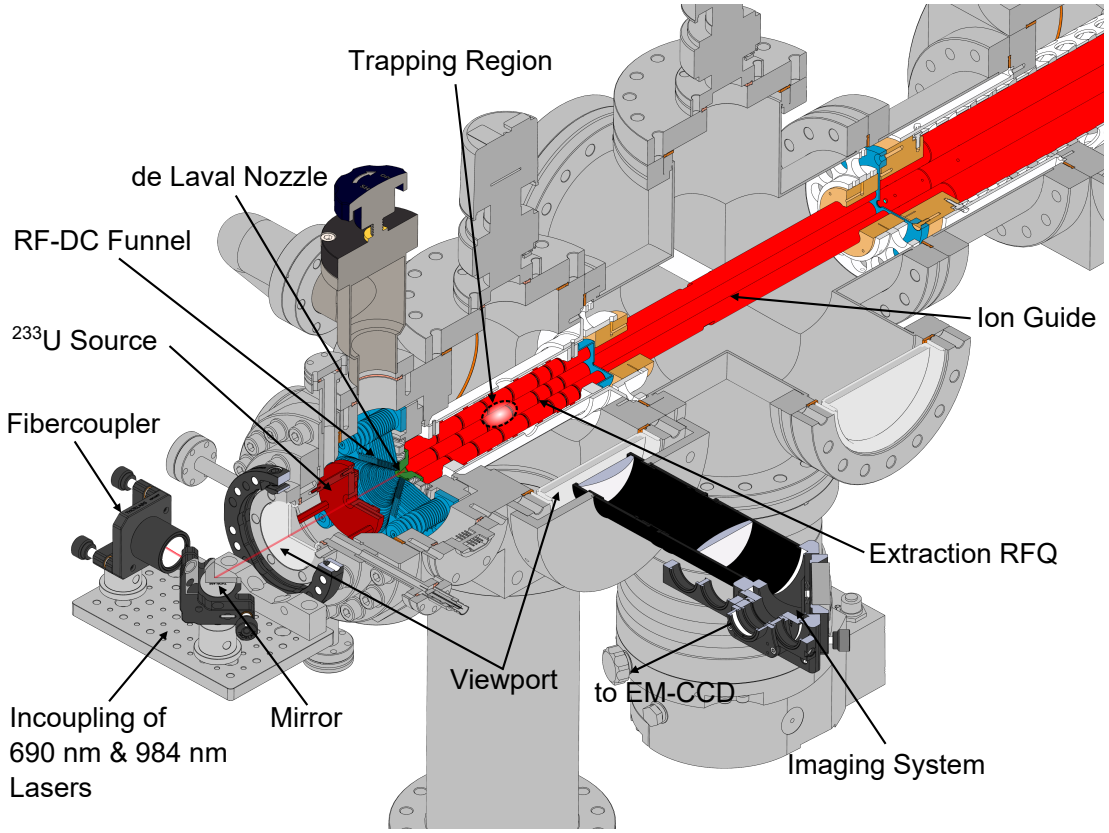

Figure 3.16 *Cutaway drawing of the Buffer-Gas Stopping cell, the Extracion RFQ, the adjoining Ion Guide, and the QMS 2 (from left to right). For the spectroscopy of $^{229}Th^{3+}$ ions confined in the 4^{th} segment of the Extraction RFQ, the* 690 nm *and* 984 nm *are aligned along the ion axis through the de Laval nozzle. The drawing of the lens system for fluorescence imaging is a courtesy of Dr. Markus Wiesinger.*

3.14 Setup Control System

The outlines to control the RF-electronics and the application of DC voltages for the funnel, the *Extraction RFQ*, the *Ion Guide*, the QMSs, and the Paul trap are described in detail in [223, 226]. The schematic shown in Fig. 3.17 depicts the interplay of the laboratory PCs, the FPGA systems, and the other hardware in the setup to achieve the creation and manipulation of Coulomb crystals in the cryogenic Paul trap.

The first laboratory PC (gar-ex-med28, *PC 1*) is mainly responsible for the communication with an FPGA (*NI cRIO-9064*, National Instruments Corp., Austin, TX, USA) comprising four analog-to-digital or digital-to-analog modules (2 x *NI-9239*, *NI-9264* and *NI-9401*) for hardware control. LabVIEW 2018 (National Instruments Corp., Austin, TX, USA) is the software platform for the FPGA programming, FPGA communication, and the readout of the FPGA data. Apart from the stabilization of the RF amplitudes V_{RF} of the two RF phases for the *Extraction RFQ*, the *Ion Guide*, the two

QMSs, and the Paul trap (if operated in a balanced mode), the FPGA is also connected to the Q-switch trigger of the ablation laser. This TTL pulse triggers the trapping routine of strontium ions and initiates the fast voltage switching (switches provided by JLU Gießen) of the central trap segments 3, 4, and 5. Furthermore, the FPGA also receives the ionic signals from the MCP or CEM detector.

The second laboratory PC (gar-ex-med32, *PC 2*) communicates with a second FPGA (*NI myRIO-1950*, National Instruments Corp., Austin, TX, USA) and with four key devices of the experimental setup: the wavelength meter for laser frequency stabilization (*WS7-60*, High Finesse GmbH, Tübingen, Germany), the ablation laser for strontium ion generation (*Q-switched Nd:YAG laser, SN: #03022502,* Quantel USA Inc., Bozeman, MT, USA), the precision power supply for the manipulation of Coulomb Crystal (*HV400*, Stahl-Electronics, Mettenheim, Germany) and the EM-CCD camera for the fluorescence readout (*C9100-23B*, Hamamatsu K. K., Hamamatsu, Japan). LabVIEW 2021 (National Instruments Corp., Austin, TX, USA) is the common software basis for the control of all four devices and the FPGA.

Thorium ion bunching and trapping is dictated by a script controlling the fast voltage switches for the 4 K *Entrance Aperture* and the endcap of the *Extraction RFQ* with TTL signals from the FPGA digital outputs.

For the $^{229}Th^{3+}$ spectroscopy experiments, the routine for the AOM switching and switching between EOM modulation schemes is also running on *PC 2* in combination with the digital outputs of the FPGA.

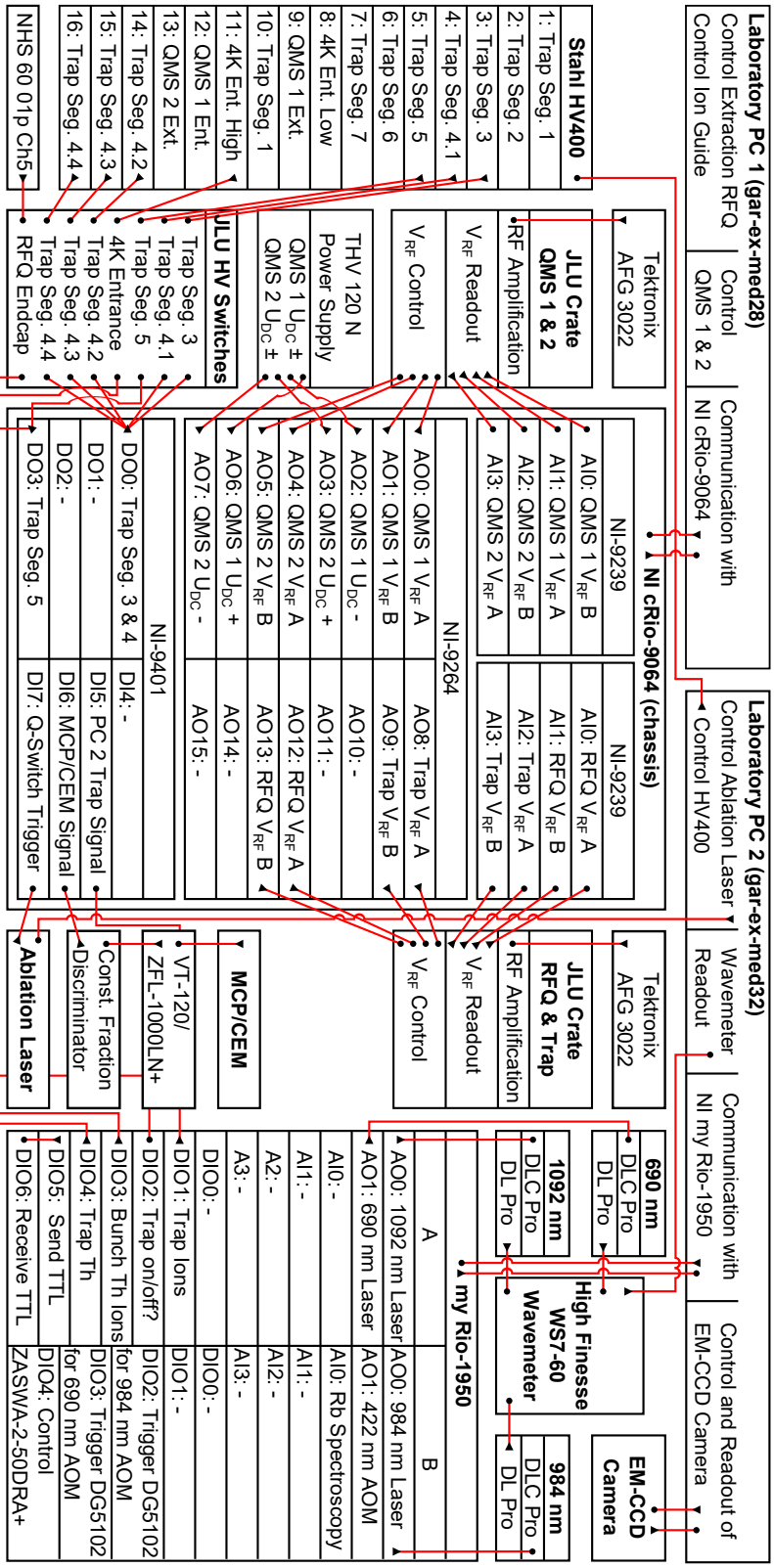

Figure 3.17 *Schematic of the different hardware and software components in the cryogenic Paul-trap setup and how they interplay to trap and laser cool Sr and Th ions. Voltage signal inputs are shown as black circles and signal outputs as black triangles.*

4 Preparatory Measurements

In order to get a deeper insight into the performance of the strontium ablation and trapping process, as well as the Doppler cooling of confined $^{88}Sr^+$ ions, some preparatory measurements have been carried out.

4.1 Characterization of the Sr^+ Laser Ablation Source

Directly after the installation of the laser ablation source of Sr^+ ions, a mass spectroscopy of the ablated ions was performed with a QMS to learn more about the output of the solid-state $SrTiO_3$ ablation target. The scan shown in Fig. 4.1 was carried out during a later experimental campaign with the setup shown in Fig. 3.1 and almost ran over the complete range of mass-to-charge values that can be resolved with the QMS modules. To ablate the ions in a more or less continuous manner with count rates above 1000 cts/s, the laser repetition rate was set to 5 Hz and the pulse energy to around 1.2 mJ. Scanning parameters for *QMS 2* running at an RF frequency of 937 KHz were a resolution of $\Delta m/Q = 2$ u/e and an integration time of 1 s per 0.1 u/e scan step.

The mass scan revealed the three expected mass peaks for a $SrTiO_3$ target at $^{48}Ti^+$, TiO^+, and Sr^+. By zooming closer to the mass peak around 88 u/e, the natural abundance of strontium can be resolved, although the actual isotope distribution is not reflected by the detected peak heights. In comparison to the peaks for $^{86}Sr^+$ and $^{87}Sr^+$ the main peak originating from $^{88}Sr^+$ should be higher by a factor of around 4. This discrepancy could be explained by a saturation of the ion detector for a high number of transmitted ions that results in a disrupted ion count rate. Regarding the usability of the $SrTiO_3$ as a strontium ion source, the mass scan already emphasizes its main advantage: Due to the large difference in the mass-to-charge ratios, the titanium contaminants can be easily discarded by the QMSs. However, for later trapping experiments, special care has to be taken to also exclude the undesired strontium isotopes.

Apart from the mass spectrum of the ablated ions, a deeper understanding of the ablation process had to be gained through a row of characterization measurements in combination with the search for optimum parameters for a reliable operation.

In a first experiment, the influence of the ablation laser-pulse energy on the number of ablated ions and their time-of-flight through the apparatus had to be investigated. At the moment of the experimental campaign, the setup was not as advanced as presented in Fig. 3.1. Instead, an assembly as described in Sec. 3.12 was used. In order to keep

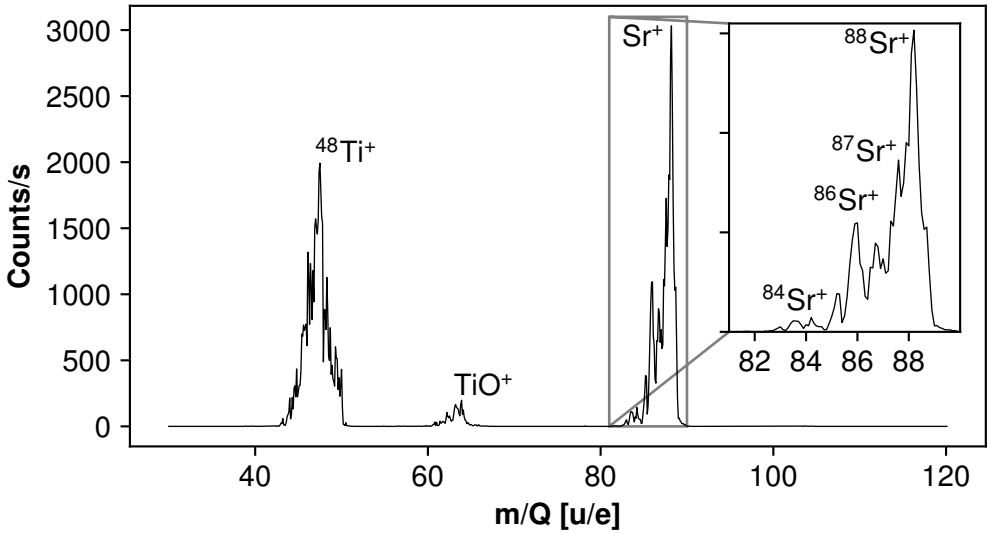

Figure 4.1 *Mass scan of the ablated ions from the $SrTiO_3$ solid-state target performed with QMS 2 with an applied resolution of $\Delta m/Q = 2\,\mathrm{u/e}$ and integration time of 1 s per 0.1 u/e scan step. The ablation laser was operated with a repetition rate of 5 Hz and a pulse energy of around 1.2 mJ. Own representation, also shown in [226].*

the ion count rates higher than 1000 cts/s, *QMS 2*, close to the target, was only used for coarse mass filtering with no DC voltages applied and an RF amplitude of 710.6 Vpp resulting in Mathieu parameters of $a_{Sr} = 0$ and $q_{Sr} = 0.269$ optimized for particles with $m/Q \gtrsim 88\,\mathrm{u/e}$. *QMS 1*, situated in front of the MCP, was operated in a purely transmissive mode with no DC voltages and an RF amplitude of 274.5 Vpp resulting in $a_{Sr} = 0$ and $q_{Sr} = 0.106$ optimized for particles with $m/Q \gtrsim 30\,\mathrm{u/e}$. For every pulse energy setting, MCP signals from 100 shots were accumulated by the multichannel scaler. As the number of ablated ions varies from shot to shot, this is the only way to get meaningful statistics. It is noteworthy that the target also undergoes a conditioning process during the first couple of ablation shots until an approximately stable count rate of at least 1000 cts/s is achieved. Each record was triggered by the Q-switch of the ablation laser and spans 1.28 ms with a bin width of 640 ns.

In addition, a single background measurement with a blocked ablation laser and calibration measurements for every increment of the pulse energy at a standard energy of 2.1 mJ (2.9 J/cm^2) were taken. Like this, a decrease in the count rate due to conditioning effects or a target wear-out (see also in [253]) can be accounted for, and the different measurements stay comparable. Fig. 4.2(a) presents the MCP signals for increasing laser energies from 1 mJ to 3.4 mJ normalized to the maximum of their respective calibration measurement.

To visualize the trend of the ion yield and the arrival time of the first ions at the MCP detector, these two observables are plotted versus the ablation pulse energy in Fig. 4.2(b). The values for the Sr ion yield represent an integral over the total MCP signal (i.e., the count rate) of the measurement step, normalized with respect to the

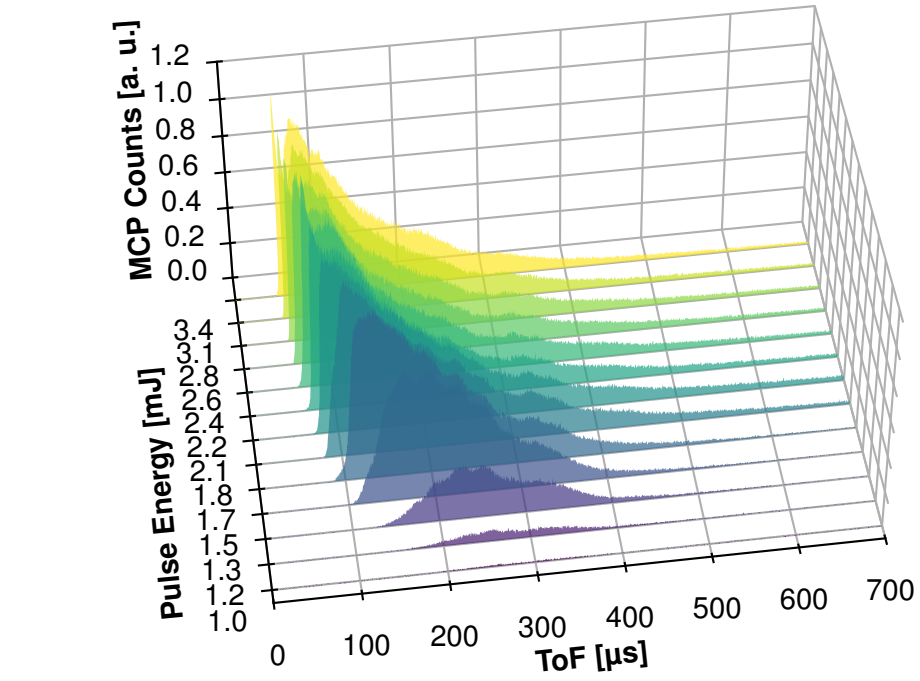

(a)

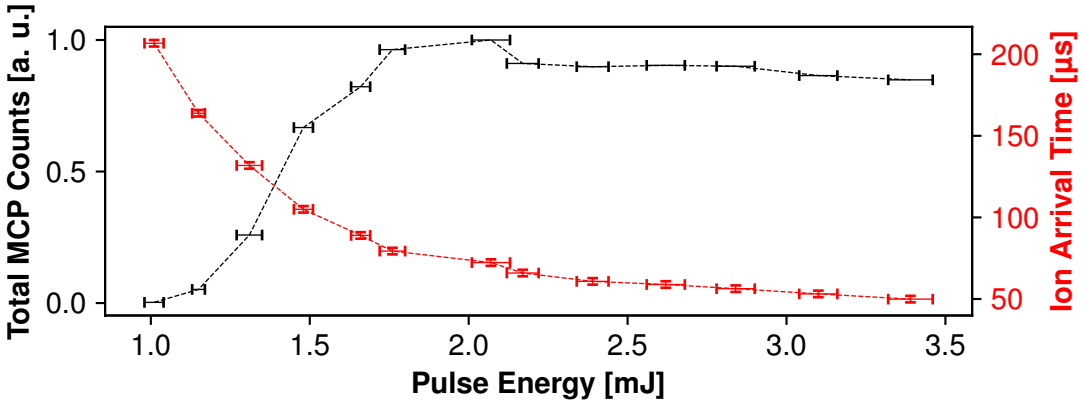

(b)

Figure 4.2 *(a) Evolution of the ionic signal on the downstream MCP (see Fig. 3.15) from ablated Sr ions with the time-of-flight as a function of the ablation laser pulse energy. Each measurement is an average over 100 ablation pulses and is normalized to the maximum value of a calibration measurement at* 2.1 mJ *taken for every setting of the pulse energy. (b) Evolution of the total number of counts per measurement iteration (black) and the arrival time of the ions at the detector (red) as a function of the ablation pulse energy. Also here, the MCP counts are calibrated to a reference measurement done at* 2.1 mJ *pulse energy.*

accompanying calibration measurement. Error bars in the horizontal direction stem from pulse energy measurements averaged over 1000 shots of the ablation laser. Uncertainties for the vertical (time) axis for the determination of the ion arrival time at the detector were estimated to be 2 μs and include the 640 ns from the binning in the multichannel scaler.

From the results plotted in both of the sub-figures of Fig. 4.2, it becomes obvious that the direct generation of ions after ablation requires a certain threshold energy. In the case of the setup presented here, this threshold lies close to 1.1 mJ (1.6 J/cm^2). As soon as the laser energy is sufficient to ablate and ionize the particles in a plasma close to the target surface, the residual pulse energy is transformed into the kinetic energy of the ions.

In Fig. 4.2(b), the black curve describing the total ion number as a function of the ablation pulse energy reveals two different signal evolutions with a turning point around 2.1 mJ. For pulse energies below the turning point, the MCP count rate increases with increasing pulse energy and decreases for pulse energies exceeding 2.1 mJ. In contrast to that, the red curve illustrating the ionic time-of-flight as a function of the ablation pulse energy shows a continuous decrease of the ion arrival time at the detector with increasing pulse energy. One physical explanation for these observations could be the absorption of the pulse energy above a certain threshold energy in the plasma close to the target surface, which was generated by the laser pulse itself. Shielded by the plasma, the crystal surface can no longer provide more free particles, and the laser energy is mainly transformed into kinetic energy of the already generated ions.

According to theory, the ablation plume and its temperature can be further characterized by transforming the time-of-flight distribution into a velocity distribution with the distance between the ablation target and the MCP surface of 1245 mm. Following th approach of [253, 254] and fitting a one-dimensional Maxwell-Boltzmann velocity distribution in the form of

$$f(v) = A \exp\left(-\frac{m_{Sr}(v - v_c)^2}{2k_B T}\right) \tag{4.1}$$

to the data provides an approximation for the temperature T and the center of mass velocity v_c in the plasma close to the surface of the target. The plasma temperature derived from the fits as a function of the laser-pulse energy is depicted in Fig. 4.3 and reaches values up to $303(3) \times 10^3$ K. This corresponds to a center-of-mass velocity of the ablation plume of 15.20(4) km/s. It has to be mentioned that the measured velocity distributions, especially for pulse energies higher than 2 mJ, significantly deviate from the Maxwell-Boltzmann distribution. So, the temperatures presented in Fig. 4.3 can only be considered as rough estimates. A possible reason for the deviations from the expected shape could be the saturation of the MCP detector due to an excessive ion flux at higher ablation pulse energies.

In a second experiment, it was studied how a DC blocking voltage along the ion axis acts on the time-of-flight or velocity distribution of the ablated ions. Similar to the previous experiment, the MCP signal of ablated ions transmitted through the setup was

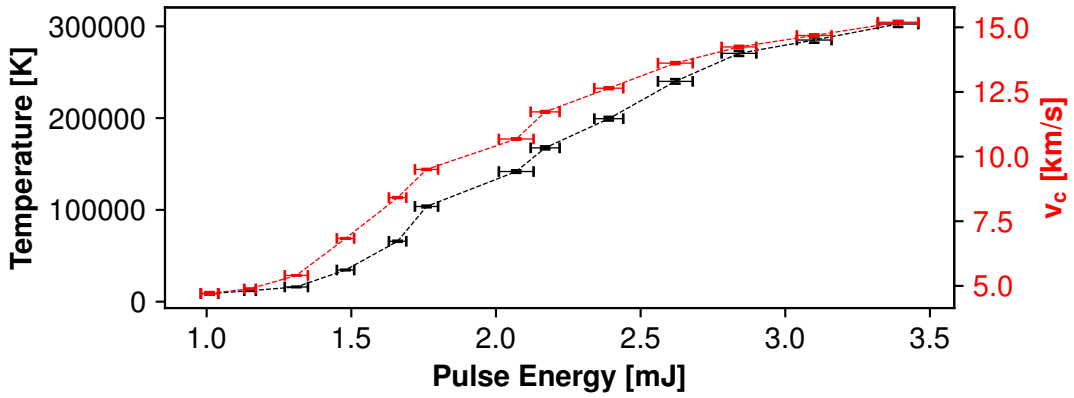

Figure 4.3 *Evolution of the plasma temperature and the center-of-mass velocity in the ablation plume close to the $SrTiO_3$ target deduced from Maxwell-Boltzmann fits to the measured velocity distribution as a function of the ablation laser-pulse energy.*

recorded with the multichannel scaler and accumulated for 1000 shots of the ablation laser set to a pulse energy of 2.1 mJ. The DC blocking voltage was applied in increments of 5 V to the aperture of 3 mm diameter between the *Strontium Extraction RFQ* and the *QMS 2* . As in the previous case, a background measurement without any ablated ions was taken to account for the dark count rate of the detector. For calibration purposes and the monitoring of the ablation stability, one signal accumulation without any blocking voltages was recorded for each voltage increment. Two rounds of measurements were done with the *QMS 2* again set to a coarse transmissive mode with $a_{Sr} = 0$ and $q_{Sr} = 0.269$, and *QMS 1* set to $a_{Sr} = 0$ and $q_{Sr} = 0.106$. In between the two measurements, the ablation spot on the target was changed by slightly moving the last mirror before the focusing lens in the ablation laser setup. The results of a measurement series performed on the same day are presented in Fig. 4.4 and also demonstrate the dependence of the energy distribution of ablated ions on the spot position on the target. This indicates that the choice of the target spot can influence the ion trapping conditions and parameters in a later stage of the experiment.

Apart from that, the plots make clear how the energy distribution of the transmitted ions is influenced by a DC blocking voltage, such as a trap endcap electrode. The higher the counter-acting voltage, the more the low-energy parts of the distribution are removed due to reflections of ions with kinetic energies below the DC potential. Nevertheless, the blocking voltages appear to influence the whole energy spectrum of the transmitted ions as the number of higher-energy particles does not vanish, but decreases with increasing voltage. So, particles may have enough energy to overcome the potential barrier, but are still deflected from the radially confining zone of the ion axis and can no longer be transported to the MCP.

In a second round of measurements carried out consecutively at two different ablation spots, the *QMS 2* was operated in a mass filtering mode (see Fig. 4.5). The additionally applied DC voltage of $U_{DC} \pm 58.4$ V resulted in Mathieu parameters of $a_{Sr} = 0.044$

and $q_{Sr} = 0.269$ to transmit only the particles of $m/Q = 88\,\mathrm{u/e}$ (corresponding to $^{88}Sr^{+}$) with a resolution of $\Delta m/Q = 2.5\,\mathrm{u/e}$. *QMS 1* was operated like in the previous measurements.

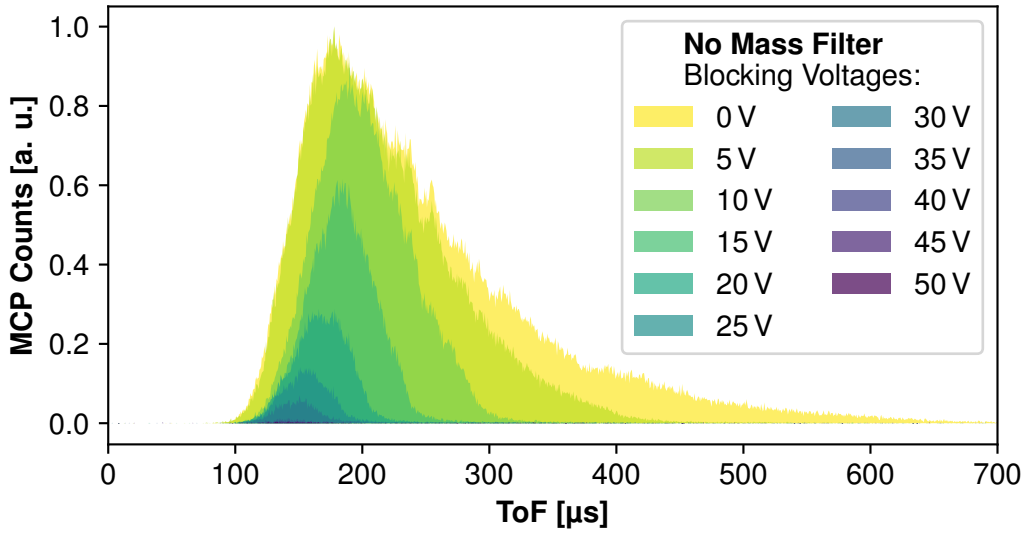

(a) *Measurement series* ***before*** *a change of the spot position on the ablation target.*

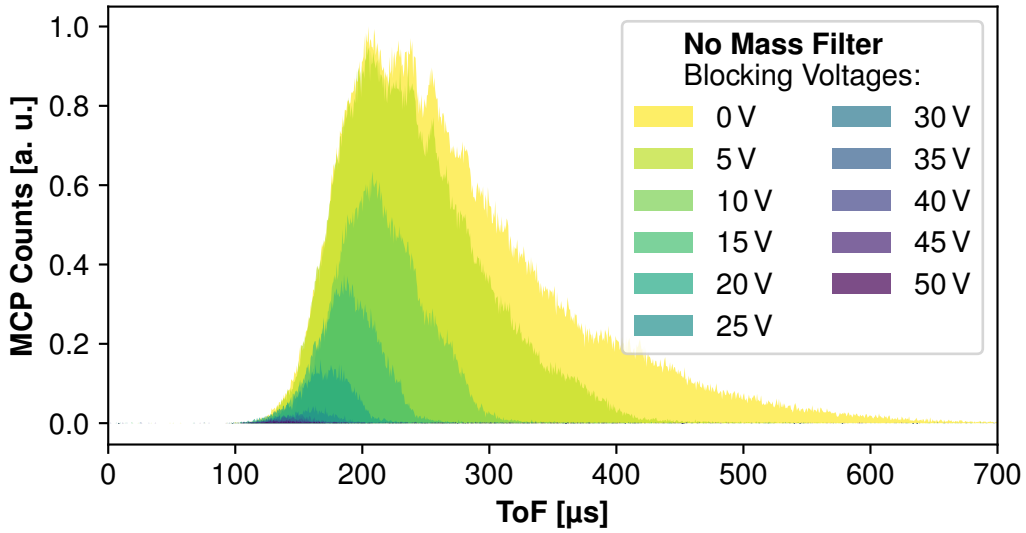

(b) *Measurement series* ***after*** *a change of the spot position on the ablation target.*

Figure 4.4 *MCP signals for different time-of-flight values averaged over 1000 shots with the ablation laser. The temporal distribution of the MCP signal is also shown as a function of a blocking voltage applied to the aperture after the Strontium Extraction RFQ. Both measurement series were carried out consecutively with a turned-off mass filter functionality in QMS 2, but with a change of the spot position on the ablation target between the first (**a**) and the second round of measurements (**b**).*

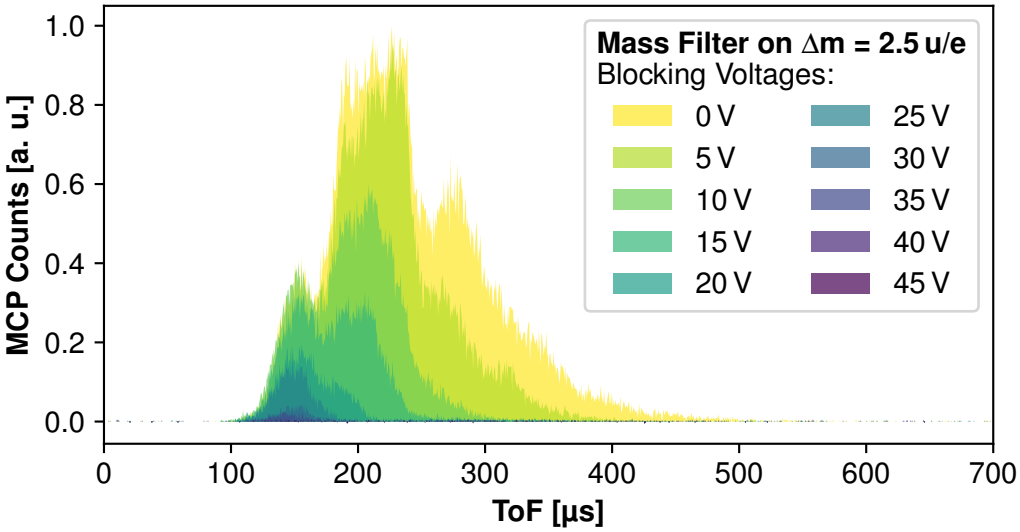

(a) *Measurement series **before** a change of the spot position on the ablation target.*

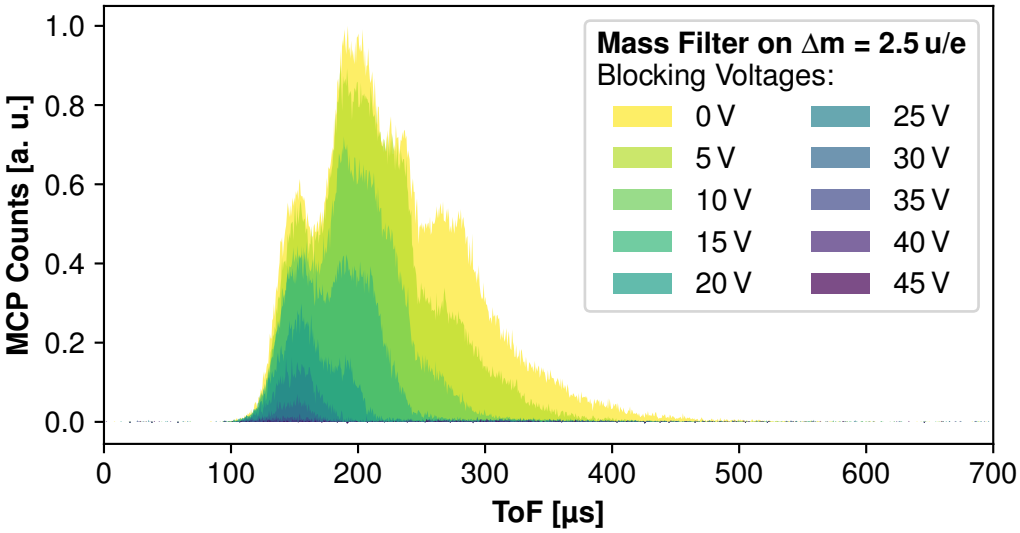

(b) *Measurement series **after** a change of the spot position on the ablation target.*

Figure 4.5 *MCP signals for different time-of-flight values averaged over 1000 shots with the ablation laser. The temporal distribution of the MCP signal is also shown as a function of a blocking voltage applied to the aperture after the Strontium Extraction RFQ. Both measurement series were carried out consecutively with the mass filter functionality in QMS 2 set to $\Delta m/Q = 2.5\,\mathrm{u/e}$, but with a change of the spot position on the ablation target between the first (**a**) and the second round of measurements (**b**).*

By looking at the results depicted in Fig. 4.5, the influence of a spot position change on the ablation target is again visible in the different signal heights and energy distributions. Also, in view of the increasing blocking voltage, the transmitted ions show the

same behavior as in the previous experiment. A major difference compared to the unfiltered particles is the overall shape of the energy distribution, which is less uniform due to the missing strontium isotopes and is less extended to lower energies. Still, a broad range of ion velocities is represented also for the single strontium isotope of interest, which offers sufficient possibilities to use a specific velocity group for ion confinement.

All in all, the used pulse energies for efficient laser ablation in the range between 2 mJ to 3 mJ with fluences between 2.5 J/cm^2 and 4.5 J/cm^2 are similar to the parameters used in other experiments implementing a solid-state $SrTiO_3$ target [231, 233]. An ablation spot on the target may degrade over time depending on the laser power and the repetition rate, but with a surface area of 1 cm^2, a single ablation target can be used for several years to generate Sr^+ ions.

4.2 Trapping and Laser Cooling of Sr^+ Ions

4.2.1 Sr^+ Ion Trapping

After having obtained a good insight into the behavior and output of the laser ablation source of Sr^+ ions, first trapping attempts have been taken. A summarizing visualization of the trap potentials during the ion loading, trapping, and release process is shown in Fig. 4.6.

To create an ion trap, the three central segments 3, 4 & 5 according to the numbering scheme indicated in Fig. 4.6 of the linear Paul trap are used. Starting with the laser pulse as a trigger, the central segment and the rear endcap (segments 3 & 4) are switched on. The temporal difference between the laser trigger and the complete closure of the trap with the front endcap (segment 5) is defined as the loading time t_{load} and is a measure to control the trapping efficiency. Typical loading times lie in the range of $t_{load} = 100\,\mu s$, which corresponds roughly to half of the time-of-flight for a majority of the Sr^+ ions from the ablation target to the MCP detector.

In order to empty the trap, segments 3 & 4 are switched to 0 V again, and released ions reach the detector after 2 ms to 4 ms. After a waiting time of 200 ms after the opening of the trap, also the front endcap is switched off and the trapping cycle can start over with a new laser trigger.

As discussed in the previous chapter, ion creation by laser ablation is only controllable to a certain extent. The ion number and their energy distribution fluctuate from shot to shot, which makes it impossible to trap the same number of ions in consecutive loading cycles. Consequently, the chosen trapping parameters, in particular the DC voltages and the loading time, are optimized only for a certain section of the ablated ion energy distribution. When a combination of DC voltages is set, the optimum loading time can be found by undertaking a scan of the loading time. For this automated routine, the ablation laser is operated with a low repetition rate of 0.2 Hz to cover the trapping time of $t_{trap} = 4\,s$. One measurement cycle for a loading time value comprises two periods of the pulsed ablation laser operation (see also Fig. 4.7) whereby a first amount of ablated ions is transmitted through the trap to the ion detector.

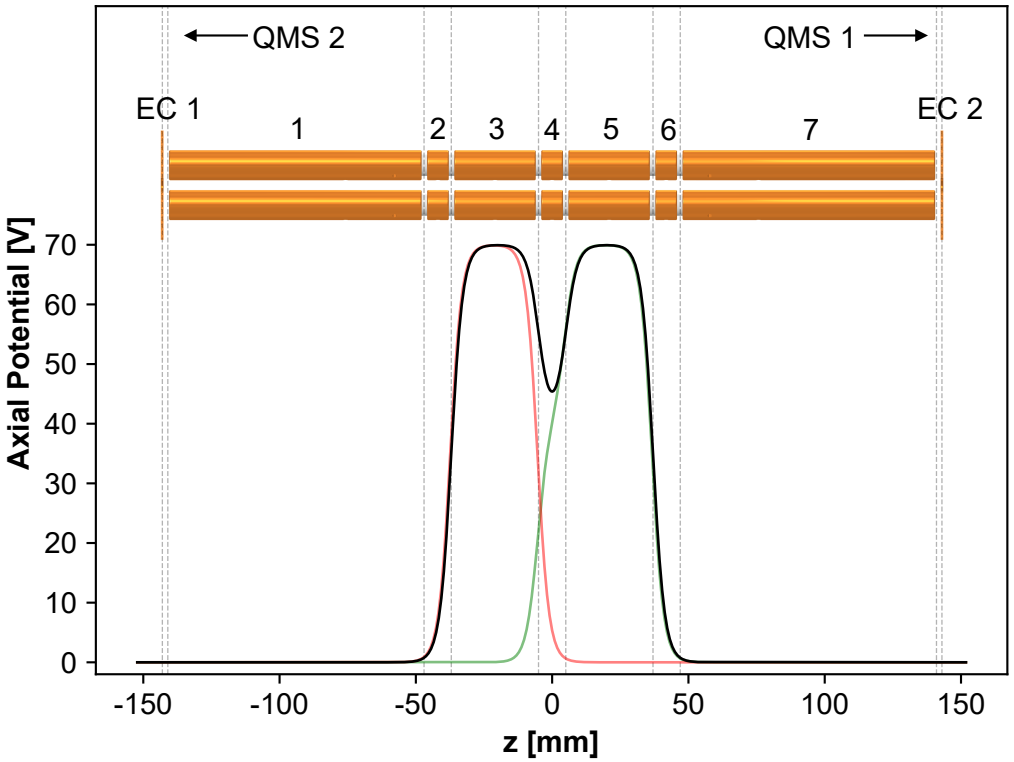

Figure 4.6 *Typical strontium trapping potential (black) calculated with the SIMION simulation software (Version 8.1.1.32) [136] with DC voltages applied to the three central trap segments labeled with 3, 4 & 5:* 70 V, 40 V, 70 V. *Also shown are the potentials for Sr^+ ion loading and release with the respective DC voltages applied:* 70 V, 40 V, 0 V *(green); and* 0 V, 0 V, 70 V *(red).*

After the second ablation pulse and the respective loading time, the trap voltages are applied, turned off, and the released ions are counted by the MCP or CEM. Then, the comparison of the number of transmitted ions with the number of released ions from the trap delivers a rough estimate of the trapping efficiency for the current loading time setting.

During the whole measurement cycle, there are three different time spans for ion count integration: A first one of 1 ms duration starting with the first ablation laser trigger to count the transmitted ions, a second 1 ms span beginning with the second laser pulse trigger to count the ions transmitted in spite of the turned on trap voltages, and a third period of 10 ms beginning with the opening of the trap to count the ions released from the trap. The latter period is longer than the first ones because of the quite long ion release time of up to 4 ms.

For the loading time scans and efficiency measurement presented in Fig. 4.8, the setup was already in a stage of development as presented in Fig. 3.1. In order to prevent the saturation of the ion detector and to get meaningful count rates, the ablation laser-pulse energy was kept around 2.5 mJ. In addition, the mass filter of *QMS 2* was only

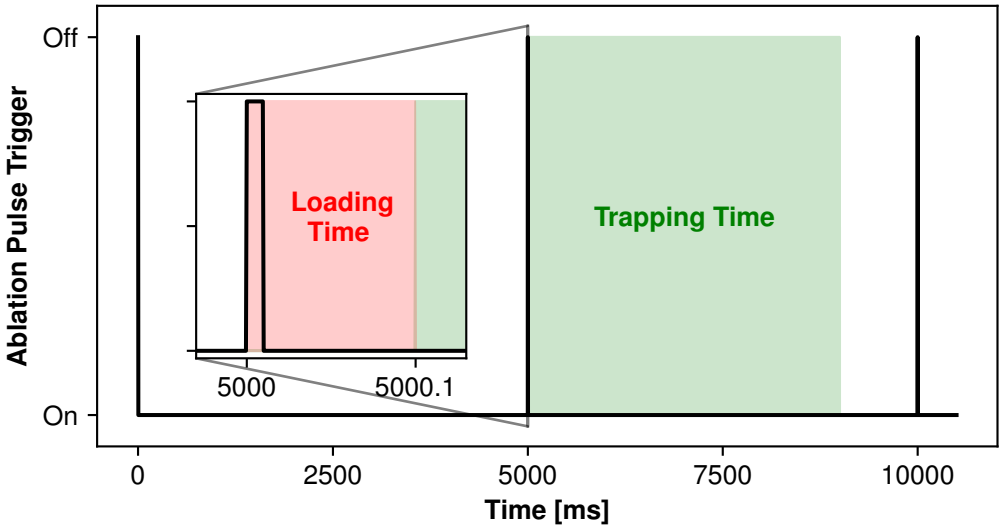

Figure 4.7 *Shown is the timing of a single measurement cycle for a loading time scan. In the present case, the ablation laser repetition rate is* 0.2 Hz *and the loading time* $t_{load} = 100\,\mu$s.

set to a coarse filtering mode with Mathieu parameters $a_{Sr} = 0$ and $q_{Sr} = 0.269$ such that all strontium isotopes contributed to the scan. With the mass filtering function in use to reach a higher isotopic purity, the ion signals from the CEM or MCP detector are too low to perform a meaningful scan of the loading time. *QMS 1* was set to full transmission with $a_{Sr} = 0$ and $q_{Sr} = 0.106$. For the actual trapping experiments for laser spectroscopy, the ablation laser-pulse energy is usually set to 3 mJ or more, to compensate the high ion losses during the mass filtering in *QMS 2* with a typical filter width of $\Delta m/Q = 3$ u/e. The combination of trapping voltages used for the measurement presented in Fig. 4.8 was 90 V, 60 V, 90 V.

The measurement revealed an optimum loading time of $t_{load} = 80\,\mu$s with a trapping efficiency of 9.2(8) %. The efficiency value, however, only represents an upper limit because the ion count number for the transmitted strontium particles cannot fully be trusted. The ion detectors are easily saturated by high amounts of transmitted ions and may deliver misleading results. For a loading time scan, the choice of the laser-pulse energy is therefore always a trade-off between vanishingly low count rates for the ions released from the trap and a possible saturation of the detector with too many ions.

During the scan, the pulse energies of the ablation laser were monitored by sending the laser through a 50:50 beamsplitter and positioning of a pyroelectric sensor in the path of the reflected pulse portion. The results in Fig. 4.8 show some fluctuations in the pulse energy around the mean value at 2.51 mJ with a standard deviation of 0.13 mJ (relative uncertainty 5.1 %). The evolution of the transmitted ion count number with a total mean value of 2919(230) (relative uncertainty 8 %) also indicates an approximately direct dependence of the pulse energy fluctuations on the number of ablated ions. With the laser-pulse energy above the specific ablation threshold energy of the strontium

target, this dependence has been also observed in the first ablation test experiments (see Sec. 4.1) for lower pulse energies. Apparently, for the laser spot position in use for this loading time scan, the plasma absorption of higher pulse energies had not yet occurred.

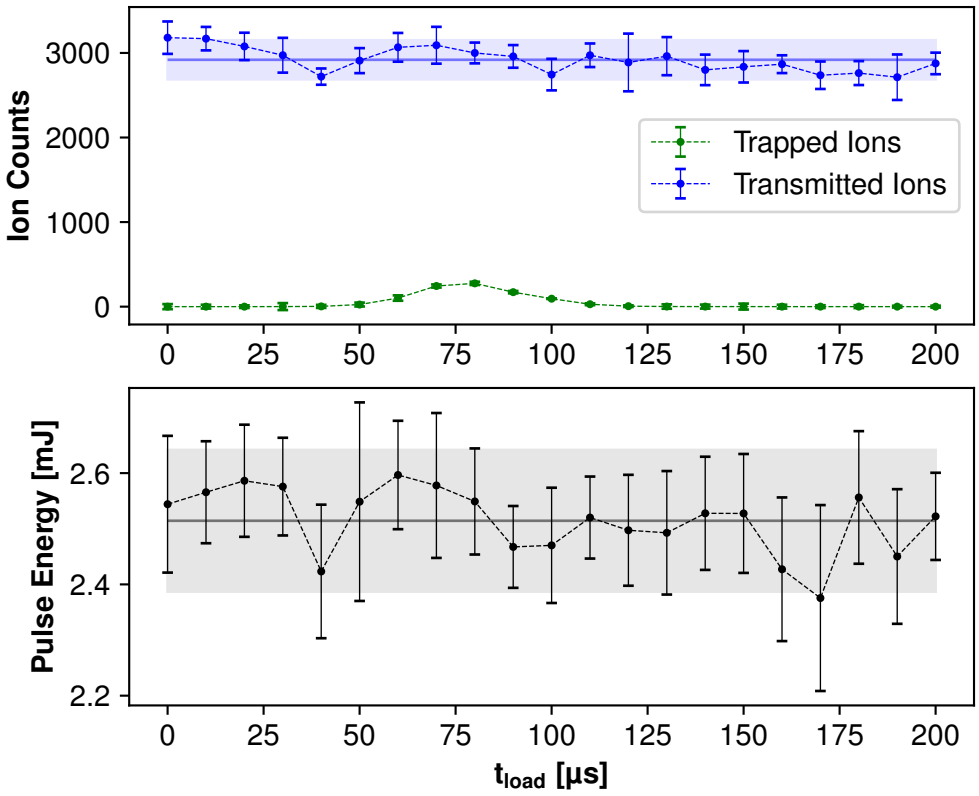

Figure 4.8 *Loading time scan for the trapping of Sr^+, where each data point represents an average of 5 measurements. The mean ion counts value (measured with the CEM) and the standard deviation of transmitted ions over the whole scan are depicted as a horizontal blue line and a transmissive blue rectangle. The monitoring of the ablation laser-pulse energy set to a nominal value of* 2.5 mJ *is shown below in black with an average of 10 values per data point. Again, the total mean value and its standard deviation are shown as a horizontal line and a transmissive rectangle (black).*

In an earlier stage of the strontium trapping experiments, the optimum trapping parameters were a combination of 70 V, 40 V, 70 V applied to the three central trap segments and $t_{load} = 110\,\mu$s. By design, the trap assembly is mounted on a CF350 flange that has to be positioned correctly on the CF350 vacuum chamber to align the trap axis with the ion axes of *QMS 1* and *QMS 2* . After a slight change of the trap axis orientation with respect to the other components, the optimum parameter combination was altered to 90 V, 60 V, 90 V, and $t_{load} = 80\,\mu$s. Apparently, the modification of the setup enhanced the transmission of fast Sr^+ ions.

With regard to the RF voltage application to the electrodes, the balanced scheme with both RF phases applied was initially used for ion confinement. Later, the unbalanced scheme with one rod pair grounded and the higher resonance frequency around 2 MHz turned out to be favorable for the ion storage and is the standard configuration until now.

As previously mentioned, the lifetime of a spot on the ablation target is limited, and the yield of ablated ions decreases after a certain number of penetrations by the laser pulse. In case of longer loading time scans or a higher number of measurements per scan step, such wear-out processes could be observed. Apart from characterization measurements, however, the number of shots on a day of usual operation is limited to around 100, such that the wear-out of a spot is rather reduced. So, the same ablation spot can be used for months.

In the case of a lower ion yield, it also helps to increase the laser power and to ablate ions from deeper-seated crystal layers in the target. At some point, though, it is recommended to change the laser spot, as an increasing laser power also results in higher ion velocities, which requires a modification of the trapping parameters.

There has to be a special remark on the ion trapping behavior with regard to the rather slow ramp-up times of several ms for the trap potential already presented in Sec. 3.6. At the optimum loading time of $t_{load} \approx 100\,\mu$s found via a loading time scan, the trapping potential reached only a depth of around 12 V. So, the trapped ions originate from the lower part of the energy distribution of ablated ions (see Sec. 4.1) with a maximum of around 12 eV and maximum time-of-flights from the ablation target to the trap center of around 136 μs. This means that the quite high voltages for the initial trapping result only from the slow voltage ramp up. In order to reduce the rise time of the switched voltages as well as the applied trapping voltages, the resistors and capacitors in the RF-DC-mixer could be modified, i.e., to half of their current dimensions. With trap voltages switched faster in a future version of the setup, the trapping efficiency might also be increased.

4.2.2 Doppler Cooling of $^{88}Sr^{+}$

After ensuring and optimizing the trapping of ions by monitoring the number of transmitted and trapped strontium ions with either the MCP or CEM ion detector, the first Doppler cooling experiments were performed. Initially, only one laser cooling axis at 30° with respect to the ion axis (also referred to as *Beam 1*) was used with the 422 nm and 1092 nm laser beams collinearly focused on the trap center. For an initial search for the overlap of the ions and the lasers, it is necessary to align the laser beams through the trap chamber and the four 5 mm apertures in the 40 K and 4 K shields lying opposite of each other. Then, several thousand strontium ions can be loaded into the trap, and the two cooling lasers are stabilized on the nominal resonance values. By steering the beams with the mirror in front of the viewport, the fluorescence intensity at 422 nm can be maximized and thus the overlap position can be optimized. For this alignment stage of the system, it is also recommended to scan the 422 nm laser frequency starting

a few hundred MHz to the red of the resonance by applying a sawtooth voltage signal at 20 kHz to the piezo DC offset.

To position the sensor of the EM-CCD camera in the focal plane of the imaging system, it is necessary to load only a few $^{88}Sr^+$ ions and to adjust the cooling lasers slightly below the resonance frequencies for the formation of Coulomb crystals. After lowering the axial trap potential U_z to around 1 V by adjusting the endcap voltages applied to the segments 3 &5, a linear chain of ions is formed. The camera is then moved along the optical axis of the imaging system until single ions are resolved and the optimum resolution is found.

With the imaging system, the laser-ion overlap and the laser frequencies being correctly adjusted, the Doppler cooling behavior can be studied and the trap be further characterized.

During a normal operation, the cooling laser frequencies are fixed. As for the 422 nm laser, the AOM modulation frequency is usually set to 196.7 MHz to efficiently Doppler cool the ions. The frequency of the 1090 nm repumping laser has to be adjusted on a daily basis due to the drifts of the wavelength meter, but is usually stabilized to 274 589 150(60) MHz, which has already been used in a previous experiment [248]. Apart from the daily re-adjustments, the stability of the wavelength meter is sufficient for the Doppler cooling of the strontium ions during a usual operation time in the laboratory.

Doppler cooling of $^{88}Sr^+$ in the cryogenic Paul trap at LMU has been achieved in various configurations and positions of the cooling lasers. After the very first successful experiments were performed at 30° with respect to the ion axis, also the other axes at 50° were used. Since the beams can be aligned through the trap chamber and also sent back onto the confined ions, configurations with retro-reflection were tried out. For a fast and efficient ion cool down, the use of two cooling axes eventually turned out to be a favorable setting and is also the current default, with one beam cooling directly along the ion axis and the other one at an angle of 30°.

In contrast to the setups described in [243, 244, 255], no special measures like additional magnetic fields or the polarization variation of the repumping laser are taken to prevent the population of dark states in the $4d^2D_{3/2}$ state. As pointed out in [246], the Earth's magnetic field prevailing at the location of the ion trap is sufficient to destabilize any occurring dark-states as long as the field vector is tilted with respect to the polarization axis of the laser. This is also the case for the setup at LMU.

A series of EM-CCD images in Fig. 4.9 shows a Coulomb crystal containing 18 $^{88}Sr^+$ ions at different axial trap potential depths. The crystal was laser cooled with laser beams incident at a 50° angle with respect to the ion axis, and each image was taken with an integration time of 1 s.

Additionally, the observed crystal shapes are compared with theoretical Coulomb crystals simulated with SIMION (Version 8.1.1.32 [136]) and the model attached in App. B. Since the camera shows only a projection on a plane at 45° to the z-y-plane, the simulated ion positions also have to be projected, respectively. They are indicated as cyan markers in Fig. 4.9.

The comparison with simulations is useful for scaling the crystal sizes and validating the SIMION model for the trap. By overlapping the simulated and the measured Coulomb crystal images, different values for the image magnification are found. In the one-dimensional case of the linear chain of ions at $U_z = 0.1\,\mathrm{V}$, the magnification is $M = 5.20(2)$ (uncertainty is estimated). As the crystal starts to extend in two dimensions at $U_z = 0.5\,\mathrm{V}$, the magnification value is $M = 5.60(2)$. All three-dimensional crystal shapes formed at potential depths starting at 1 V reveal magnification values of $M = 5.70(2)$.

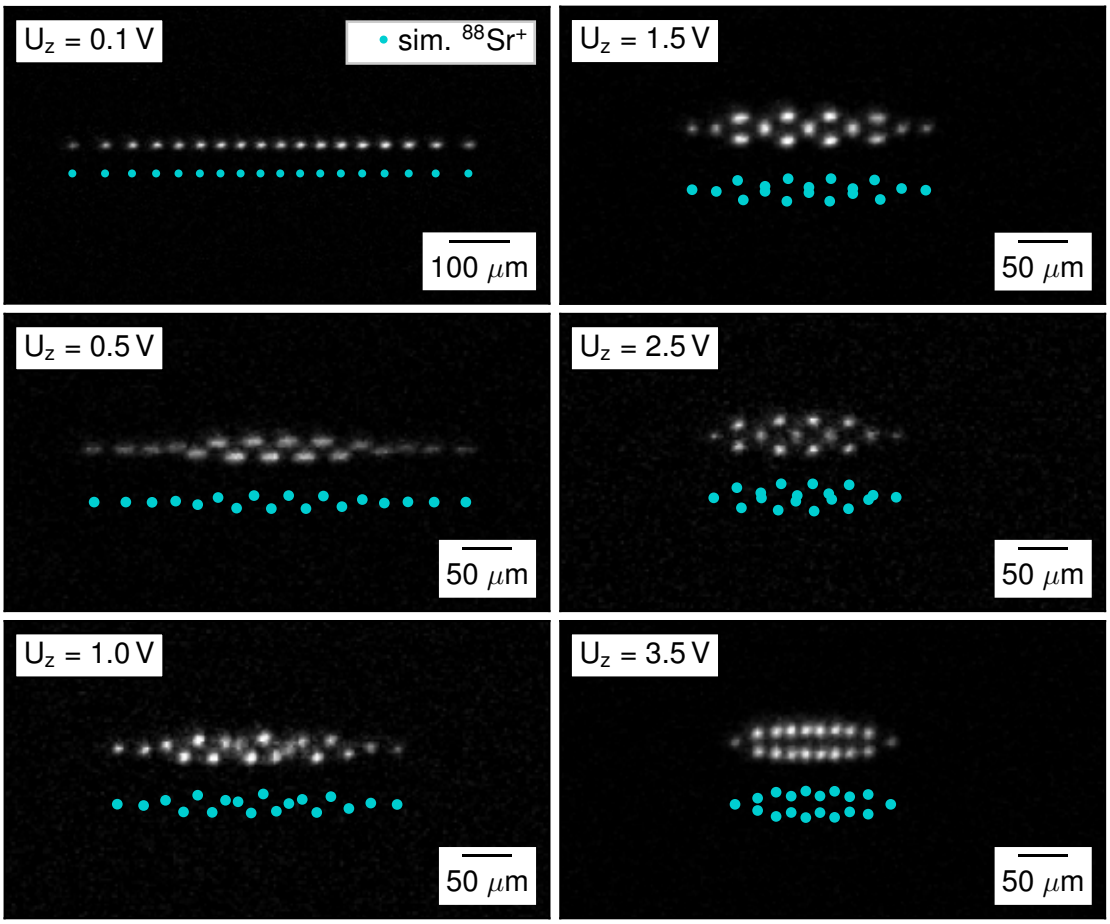

Figure 4.9 *Grayscale EM-CCD camera images of a Coulomb crystal containing 18 $^{88}Sr^+$ ions at different axial potential depths U_z in the cryogenic Paul trap. The integration time for each image is* 1 s. *Crystal images simulated with SIMION (Version 8.1 [136]) are shown in cyan for comparison and are also the basis for the respective image scale.*

Compared with the theoretical magnification value of $M = 5.7(1)$ (see also Sec. 3.11), the scaling of the linear chain deviates by around 9 %. As for the two- and three-dimensional scale, which fits with the simulated crystals, the found magnifications match

the theoretical value or are within its uncertainty. If the linear chain is simulated for axial potential depths of $U_z \approx 0.125\,\mathrm{V}$, the ion positions can be fitted to images with a magnification of $M = 5.6$. Indeed, the power supply for the application of the trap's DC voltages (*HV400*, Stahl-Electronics, Mettenheim, Germany) can induce offset errors of up to $\Delta U_z = \pm 0.1\,\mathrm{V}$. Especially for low axial potential depths, this device-induced offset error can lead to large uncertainties in the set potential depth that most probably are also the reason for the deviation in the magnification value for the linear ion chain.

In general, the simulated Coulomb crystal shapes at the different trap potentials reproduce the measurements to a high degree of agreement. Apart from the contradicting magnification value for the one-dimensional case, the simulations also deliver good approximations for the image scale. Thus, the SIMION model used can be considered a valid tool for theoretically examining the Paul-trap setup and supporting the evaluation of experimental data.

4.2.3 Linewidth of Laser Cooled Sr^+

After ensuring Doppler cooling and the crystallization of the trapped $^{88}Sr^+$ ions, it was necessary to quantify the reached cooling temperatures and to check for other processes like power broadening. For this purpose, the fluorescence intensity at 422 nm was measured while scanning the frequency of one of the cooling lasers over its respective resonance by altering the DC voltage for the piezo actuator of the laser grating. A typical scan speed for the piezo crystal is 1 mV/s over a range of around 0.4 V, which corresponds to a scan speed in frequency space of around 2 MHz/s over a range of around 800 MHz. During a scan, the camera integration time for the fluorescence readout is usually set to 0.1 s and special care has to be taken of the region of interest of the imaging. For an optimum signal-to-noise ratio, the image field of view (FOV) for the data collection has to be limited to the size of the Coulomb crystal and needs to be set before the scan with the crystal to be examined. Especially in the case of few-ion crystals, it is necessary to neglect most of the 512 x 512 pixel camera image and to restrict the FOV to roughly 100 x 10 pixels.

Fig. 4.10 shows the evolution of the fluorescence intensity of different Coulomb crystals as a function of the detuning $\Delta\nu_{422\,\mathrm{nm}}$ of the 422 nm laser with respect to the resonance frequency ν_0. For the presented measurements, a single cooling beam coupled in at the 30° viewport (*Beam 1*) was used with laser powers of 300 μW at 422 nm and 600 μW at 1090 nm. To estimate the laser intensity at the position of the ions, the beam widths were also measured with the beam profiler and gave a width of 0.58(1) mm for 422 nm and 2.14(37) mm for 1090 nm. Based on the beam width measurement, the laser powers to saturate the cooling transitions are 93(10) μW and 5(4) μW, respectively. This means that the applied laser powers were far beyond the saturation threshold and should result in a power broadened linewidth of at least 40 MHz for the 422 nm transition. The application of lower laser powers, intended to decrease the power broadening, resulted in a worse Doppler cooling for the strontium ions and less stable Coulomb crystals. Therefore, it was not further pursued.

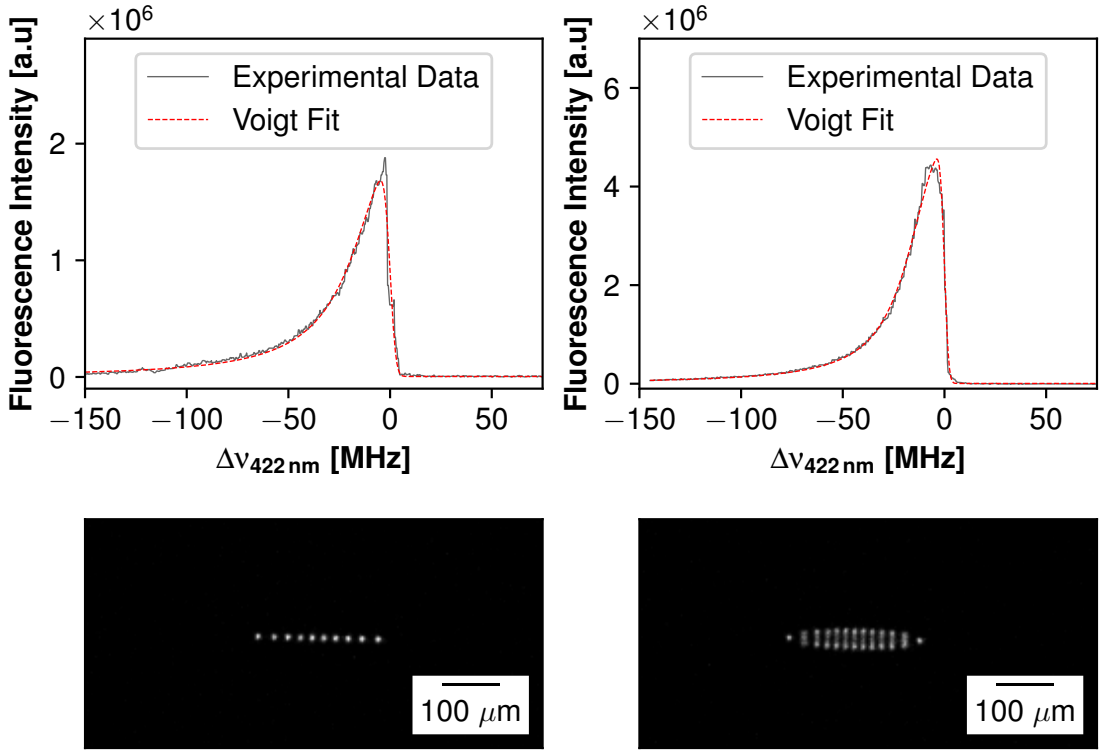

Figure 4.10 *Fluorescence intensity scans at* 422 nm *of trapped* $^{88}Sr^{+}$ *ions. In both cases, the* 422 nm *laser frequency was scanned over the resonance. (**a**) shows the case for 10 ions in the trap at a potential depth of* 1 V *and (**b**) displays a bigger Coulomb crystal of more than 30 ions at a potential depth of* 2 V*. The magnification for both images is* $M = 5.6$*. The laser powers used during the scans were* 300 μW *at* 422 nm *and* 600 μW *at* 1090 nm*.*

For an optimized signal-to-noise ratio, the resonance scan depicted in Fig. 4.10(a) was recorded with a FOV of 100 x 10 pixels and the scan shown in Fig. 4.10(b) with a FOV of 90 x 16 pixels.

As already mentioned in Sec. 3.8, the frequency readout in the blue spectral range with the wavelength meter in combination with the multimode fiber switch delivers no reliable data. Therefore, the ^{85}Rb spectroscopy data, also used for the stabilization of the 422 nm laser, in combination with the absolute frequency values given in [249] can provide a suitable fit for the laser detuning in MHz.

In both cases, the scan shape is asymmetric due to the Doppler heating effect for laser frequencies $\nu_{422\,\mathrm{nm}} > \nu_0$, which instantly reduces the absorption of the cooling light (see also [246, 248]).

The fit function used for the resonance scans is a Voigt profile $V(\nu, \sigma, \gamma/2)$, which is cut-off at the resonance frequency ν_0 [167]. A Voigt profile is defined as the convolution of a normal distribution with standard deviation σ and a Cauchy or Lorentzian distribution with the half-width at half-maximum $\gamma/2$ (γ corresponds to the FWHM), which is why both parameters can be extracted from the fit to obtain information on the ion temperature and the power broadening of the linewidth [164, pp. 42 –49]. To account for the sharp cut-off at the resonance frequency, the Voigt profile is additionally multiplied by an error function of width c :

$$I_{fit}\left(\nu, \sigma, \gamma/2\right) = I_{offset} + I_0 \left[\int G\left(\nu, \sigma\right) L\left(\nu, \gamma/2\right) \mathrm{d}\tau\right] \frac{1}{2}\left[1 + \mathrm{erf}\left(\frac{-(\nu - \nu_0)}{2c\sqrt{2}}\right)\right] \quad (4.2)$$

The normalized Gaussian distribution $G(\nu, \sigma)$ is centered around the resonance frequency ν_0, contains information on the Doppler broadening (see Sec. 2.2.2 and Eq. (2.41) of the linewidth, and is denoted as:

$$G(\nu, \sigma) = \frac{e^{-(\nu-\nu_0)^2/2\sigma^2}}{\sigma\sqrt{2\pi}} \qquad FWHM_G = 2\sigma\sqrt{2\ln(2)} \quad (4.3)$$

The normalized Cauchy or Lorentzian distribution $L\left(\nu, \gamma/2\right)$, also centered around ν_0, accounts for the broadening of the natural linewidth $\delta\nu_0$ due to the laser cooling power exceeding the saturation intensity (see Sec. 2.2.1 and Eq. (2.40)):

$$L\left(\nu, \gamma/2\right) = \frac{\gamma/2}{\pi\left[(\nu - \nu_0)^2 + (\gamma/2)^2\right]} \qquad FWHM_L = \gamma \quad (4.4)$$

In order to find an expression for the full width at half maximum of the Voigt profile, the following numerical expression is used [256]:

$$FWHM_V \approx 0.5343 \times FWHM_L + \sqrt{0.2169 \times FWHM_L^2 + FWHM_G^2} \quad (4.5)$$

Applying the Voigt fit function to the experimental data shown above delivered the results listed in Tab. 4.1. It presents the different contributions to the linewidth, the calculated ion temperatures, and the calculated laser powers applied to the ions.

Independent of the crystal size, both resonance scans have a total Voigt-shaped linewidth $FWHM_V$ exceeding the natural linewidth of $^{88}Sr^+$ of 20 MHz, but are close to the expected power broadened linewidth regarding the applied laser power. For the first scan, the estimate for the ion temperatures is significantly below the Doppler cooling limit of around 0.5 mK, but the large uncertainty of 3.7 mK (stemming from the large uncertainty in the Gaussian-type contribution) underlines the low reliability of this value. However, the laser power of 347(80) μW deduced from the Lorentz contribution to the total line shape coincides quite well with the actually applied power of 300 μW.

For the second scan, on the contrary, the ion temperature value of 102(9) mK and the laser power estimate at 123(37) μW are most probably misleading. Since an ion crystal could be formed, the temperature should be around 10 mK or lower, and the actually applied laser power was higher (300 μW).

Table 4.1 *Results of the two resonance scans shown in Fig. 4.10 based on the Voigt fit function. T denotes the ion temperature calculated from $FWHM_G$, and P_L stands for the laser power calculated from $FWHM_L$.*

	Scan 1 see Fig. 4.10(a)	Scan 2 see Fig. 4.10(b)
$FWHM_V$ [MHz]	43.9(3)	38.9(9)
$FWHM_G$ [MHz]	0(1133)	17.4(8)
$FWHM_L$ [MHz]	43.8(3)	30.7(5)
T [mK]	0.0(37)	102(9)
P_L [µW]	347(80)	123(37)

In summary, the chosen fit model for the measured resonance scans could only give a limited insight into the ion temperature or the amount of laser power applied to the ions. A broadening of the linewidth due to the comparably high laser powers for Doppler cooling or insufficient measures to compensate for the micromotion was expected. So far, the broadened lineshape is also the only reliable information to be extracted from the fit model and agrees with the results of other Sr^+ experiments [243, 246].

It remains questionable, if a better signal-to-noise ratio can improve the data for a more distinct curve fitting. This would require another fluorescence detector with a higher quantum efficiency than the current EM-CCD camera or, in general, an alternative fluorescence readout scheme for a higher photon yield. With regard to the limited solid angle of the imaging system due to the trap geometry, an optimization of the design without changing the total trap assembly is virtually impossible.

It is also possible to monitor the 422 nm fluorescence intensity with a fixed frequency of the main cooling laser while scanning the frequency of the repumping laser at 1090 nm in a similar way as the main cooling laser was scanned in the previous experiment. In contrast to the 422 nm laser, the frequency readout of the infrared repumper could be realized directly with the wavelength meter. The scan shapes are not suitable, though, to learn more about the broadening of the lineshape and the ion temperature. Several resonance scans for different settings of the constant frequency shift of the main cooling laser introduced by the AOM doublepass setup are shown in Fig. 4.11. The plots visualize qualitatively how the shape of the resonance scan changes with the detuning of the AOM frequency shift. The dips in the resonances can be explained by the generation of so-called dark states, which occur when superpositions of Zeeman sub-levels of the $^2S_{1/2}$ and $^2D_{3/2}$ state are coherently driven by the two cooling lasers [246, 257]. The number of dark states, their shape, and their relative strength depend on the magnetic field and the laser polarizations in relation to this field, as well as on the laser detunings and their intensities. For the settings applied in this experiment, only up to two out of eight

dark states were observed (see in [257]). Similar to the experimental findings described in [246], a linear change of the dip position(s) with the detuning of the 422 nm laser in terms of the AOM shift frequency could be observed and is depicted in Fig. 4.12. The red data points with their linear fit revealing a gradient of 1.01(8) MHz/MHz belong to the first dip, which is visible in all six plots. The blue points with a linear fit of gradient 1.18(1) MHz/MHz show the behavior of the second dip visible in the three plots in the right column of Fig. 4.11. In principle, the shift of the dip position should follow the AOM shift with a gradient of 1 MHz/MHz, which is well reflected by the experimental data in red. The slight deviations from the predicted linear correlation of the second dip's position can be explained by the low statistics based on only three data points.

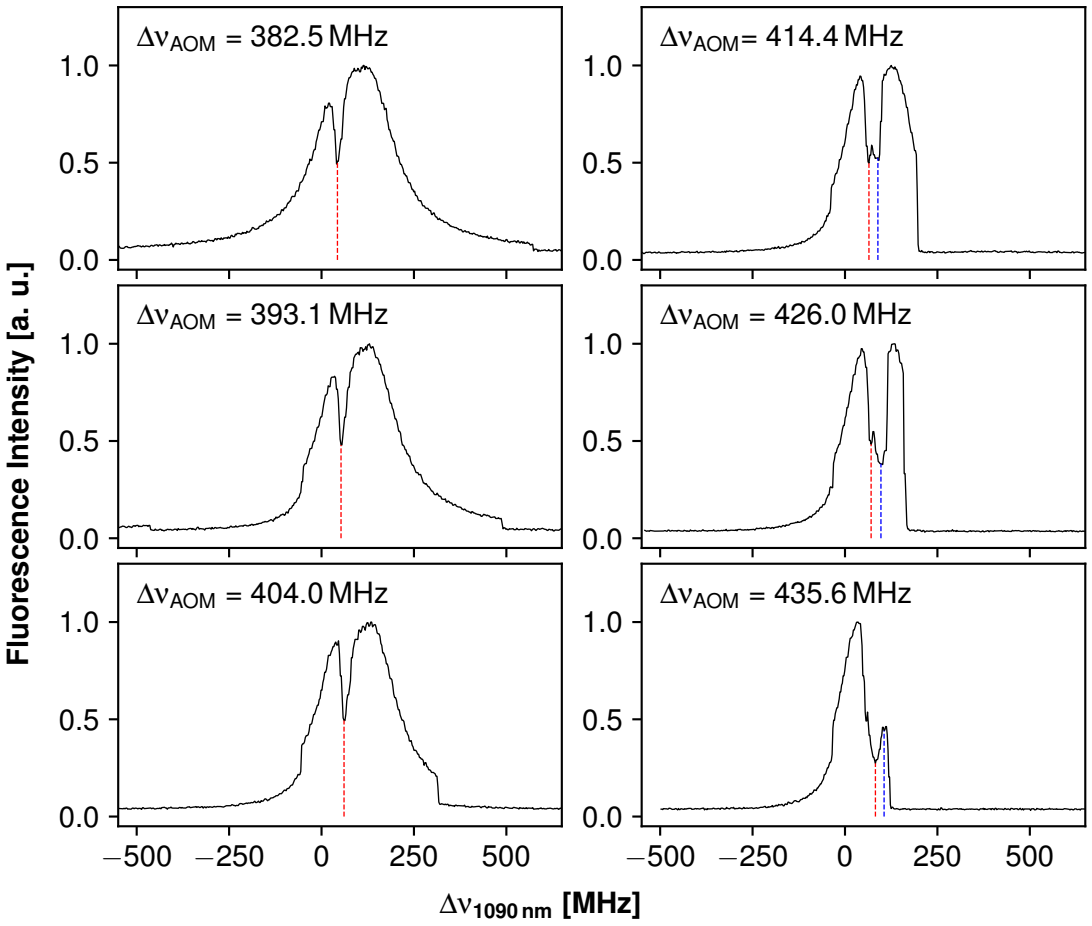

Figure 4.11 *Evolution of the* 422 nm *fluorescence intensity with the detuning* $\Delta\nu_{1090\,\mathrm{nm}}$ *of the* 1090 nm *laser at different settings of the AOM detuning* $\Delta\nu_{AOM}$. *The dips in the scans indicate the position of dark states and are highlighted with red and blue vertical lines. The blue lines belong to the second dark-state dip visible in the three plots of the right column.*

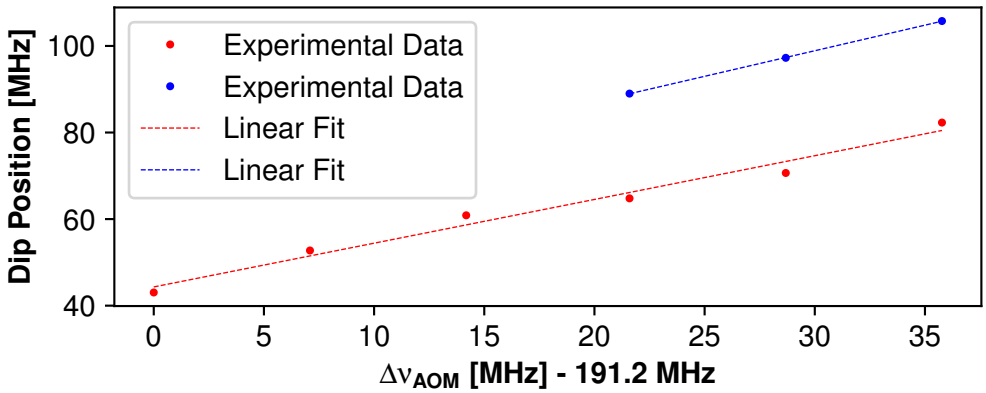

Figure 4.12 *The positions of the first (red) and second (blue) dark-state dips visible in the six plots of Fig. 4.11 are shown as a function of the AOM detuning* $\Delta\nu_{AOM}$ *and fitted with straight lines.*

4.2.4 $^{88}Sr^{+}$Fluorescence Lifetime and Estimate of Vacuum Pressure

As already mentioned before, ion storage times and fluorescence lifetimes at least as long as the isomeric lifetime were one of the main motivations to build the cryogenic Paul trap at LMU. Therefore, this property was further characterized via fluorescence lifetime measurements of trapped $^{88}Sr^{+}$ ions in a room-temperature and a cryogenic environment.

To provide a room-temperature environment for the trap volume, the He cryocooler is simply turned off. The measurements described in the following were performed with the setup already being under vacuum for several months and with a pressure of around 2×10^{-9} mbar in the Paul-trap chamber. In the current setup configuration, it is not possible to directly measure the pressure within the 4 K-shield, and the gauge is therefore mounted outside the trap region, close to the *STP 603* 650 l/s vacuum pump below the optical table. As a result, the measured pressure in the trap chamber at room temperature can only be assumed to be similar to the pressure in the trap volume after several weeks of vacuum pumping.

For the fluorescence lifetime measurements at room temperature, strontium ions were loaded following the same routine as previously described and the fluorescence signal at 422 nm was monitored with the EM-CCD camera at a 200 ms exposure time. To keep the signal-to-noise ratio as high as possible, the region of interest was chosen such that mainly the pixel counts of the monitored ion crystal are taken into account. Results for the decay constant and decay rate in the case of a medium-size Coulomb crystal with several tens of ions are shown in Fig. 4.13.

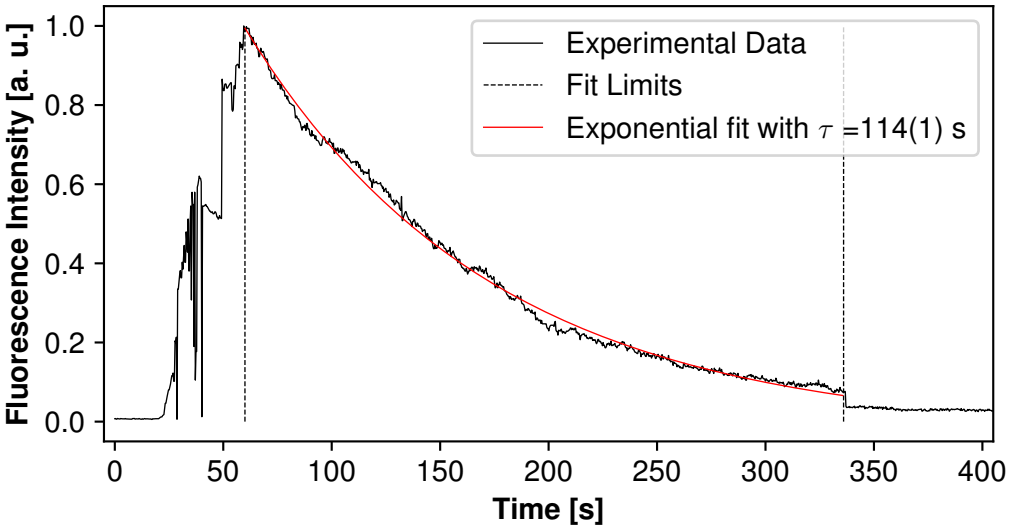

Figure 4.13 422 nm *fluorescence intensity normalized to the maximum intensity of a* $^{88}Sr^+$ *Coulomb crystal containing several tens of ions, recorded with the EM-CCD camera set to* 0.2 s *exposure time. The vertical dashed lines define the region of the exponential fit curve applied to the fluorescence decay with the decay time constant* τ.

In the case of large ion numbers, the evaluation of the data was performed with exponential fit curves using a non-linear least squares algorithm. As visible in Fig. 4.13, the fit curve was applied in a predefined time range with the starting point set to 60 s after the start of the measurement. At this point in time, the ion crystal was fully visible and stable in the trap center with a potential depth of 1 V and $q \approx 0.4$. The measured decay constant of $\tau = 141(1)$ s indicates a fluorescence half-life of $t_{1/2} = 97.7(7)$ s for the strontium ions in the Paul trap at room temperature.

Two possible reasons for a decay behavior of the fluorescence intensity are ion losses due to unstable trapping conditions or chemical reactions with residual gas atoms like hydrocarbons in the trap region. The latter is the more probable reason for the observed decays: after a chemical reaction of the Sr^+ ions with residuals, they are transparent to the cooling lasers and appear as dark ions. With a sufficient amount of unperturbed $^{88}Sr^+$ ions contained in the Coulomb crystal, the dark ions can still be sympathetically cooled. However, as the number of reacting ions increases, the crystal becomes more and more unstable until it falls apart. Exactly this moment is visible as a sudden drop to zero after 336 s in the fluorescence intensity plot of Fig. 4.13 and was also chosen as the end point for the fitting region.

In the case of fluorescence decays recorded with only a few ions in the trap, the decay signal behaves more like a step function and cannot be approximated with an exponential fit to good agreement. Therefore, the evaluation is constrained on the signals of larger Coulomb crystals that provide decay constants comparable to the one shown in Fig. 4.13.

To measure the fluorescence lifetime in a cryogenic environment, the two temperature shields and the trap were cooled down to 40 K and 8 K, respectively, with the He

cryocooler. In the next step, a few-ion crystal was loaded and stored at a potential depth of 1 V in the central trap segment. The starting point of the measurement is defined as the first occurrence of fluorescence. The fluorescence intensity was then monitored and recorded with the EM-CCD camera over a period of approximately eight days and is plotted in Fig. 4.14

In contrast to the stepped or exponential decay curves, the long-term measurement can be described by slow oscillations. They can be mainly attributed to power fluctuations or frequency drifts of the cooling lasers. With the 422 nm laser directly frequency locked to the ^{85}Rb hyperfine transition and the repumping laser at 1092 nm stabilized with the wavelength meter only, contributions to frequency fluctuations might be introduced by the latter. The wavelength meter usually drifts over time and was not calibrated during the measurement. Another possible reason for the observed intensity oscillations could be small polarization changes of the laser light transported through the fibers in the setup. Although they are mainly polarization maintaining, only small changes in the polarization in combination with a polarizing beamsplitter after the respective fiber result in power variations and thus alterations of the fluorescence intensity. In case these power or frequency drifts are too intense, the ion crystal can also vanish, which can be seen, for example, in the low intensity evolution for over an hour after roughly 19 hours of measurement.

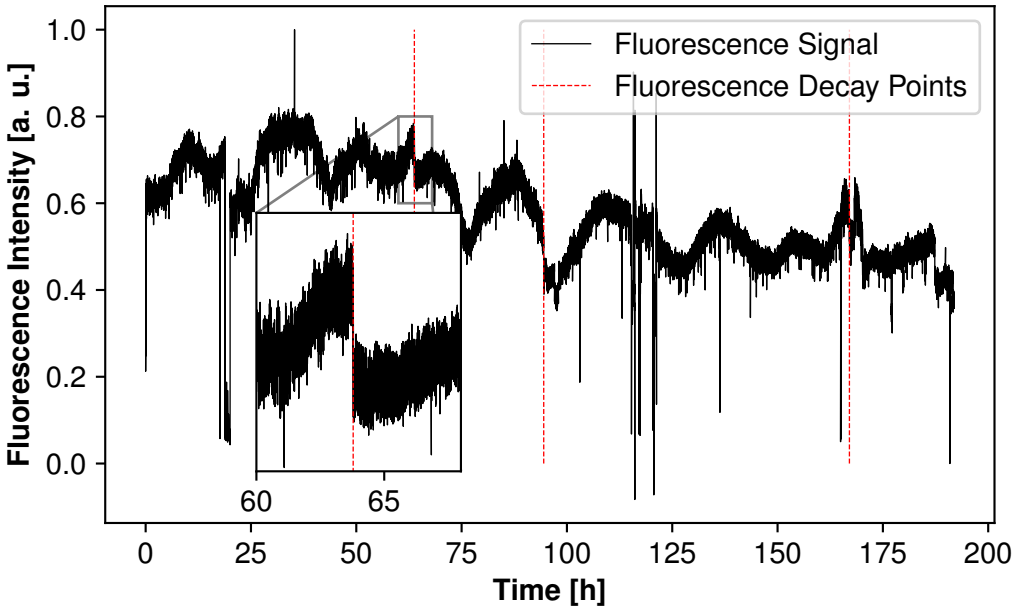

Figure 4.14 422 nm *fluorescence intensity of initially 9* $^{88}Sr^{+}$ *ions, recorded over approximately 8 days and normalized to the maximum intensity peak is shown in black. The three moments of fluorescence decay observed during the visual monitoring of the measurement are indicated with vertical red, dashed lines, and the inset shows a zoomed-in view of the first decay after* 63.8 h.

Fast and intense changes of the intensity to the background level and below usually result from camera readout errors and can be neglected.

During the eight-day measurement, three decays were observed in the fluorescence intensity (see vertical red dashed lines in Fig. 4.14). Due to the strong fluctuations in the fluorescence intensity it was important to also visually monitor the camera images such that the decay times could be well determined to: τ_1 =229 626(2) s ≈ 63.8 h, τ_2 =340 173(2) s ≈ 94.5 h, τ_3 = 601 400(2) s ≈ 167.1 h. The uncertainties in the decay points are made up by the readout time of 1 s, the exposure time of the camera of 0.2 s, and the definition of the zero point as the beginning of the measurement.

The fluctuations of the intensity made it impossible to apply a step-function or an exponential fit curve to the data. Also, the intensity values at the decay times cannot be evaluated for an exponential fit curve with three base points only. Therefore, it remains to give a lower limit for the fluorescence lifetime in the cryogenic Paul trap at $\tau \approx \tau_1 \approx 63.8\,\text{h}$ and with that an upper limit for the decay constant $\Gamma = 1/\tau \approx 4.4 \times 10^{-6}\,1/\text{s}$.

At the end of the long-term measurement, an image of the six remaining fluorescing ions was taken and is shown in Fig. 4.15. With the dark interstitials after the first, the fourth, and the fifth bright Sr ion in the linear chain, it can be clearly seen that the initial nine ions are still in the trap. Decays in the fluorescence intensity and the appearance of dark ions can then only be attributed to chemical, molecule-forming reactions of the strontium ions with residuals in the trap volume. According to [131, p. 179], the only remaining particles or molecules contributing to the residual pressure at temperatures below 20 K are Ne, He, and in particular H_2. All other particles should be frozen out on the temperature shield surrounding the trap. Since the ion position in a linear Coulomb crystal is defined to a higher extent by the charge and not by the ion mass, it is not possible to further confirm this assumption with SIMION simulations of trapped ions.

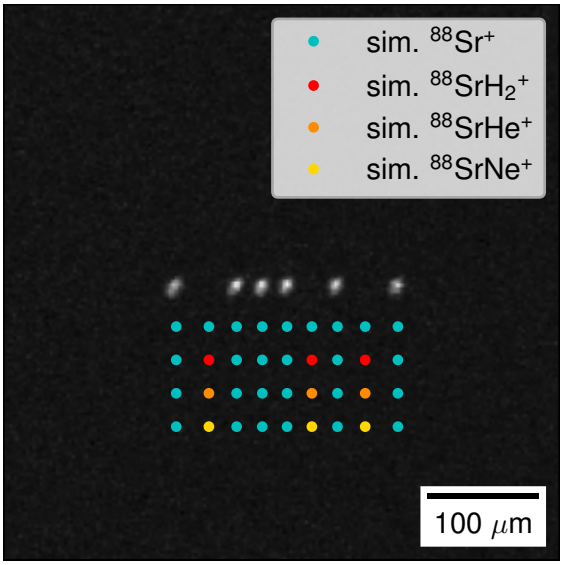

Figure 4.15 *EM-CCD image of the 6 remaining ions fluorescing after the* 8 d *measurement of the fluorescence decay of initially nine ions. Linear chains of ions are simulated with the SIMION software (Version 8.1.1.32) [136] for a pure $^{88}Sr^+$ crystal and crystals with different molecules at the dark ion positions.*

In Fig. 4.15, simulated ion positions of different strontium molecules are compared with a pure $^{88}Sr^+$ ion chain and the real image. For a good fit of the image to the simulations, the image magnification had to be set to $M = 5.45 \approx 5.5$, which lies within the uncertainty range of the calculated magnification $M = 5.6(1)$ for the used imaging

system of *Version 2* (see Sec. 3.11). Although the molecules reveal huge differences in their mass, the position in the crystal is not significantly affected by that.

It remains to further assume H_2 as the main reaction partner for confined ions in the trap. This can then be used to give an estimate for the vacuum pressure in the trap volume at the cryogenic temperature.

One first approach is based on the classical Langevin model [258] and a comparison of the fluorescence lifetimes or in other words the ion collision rates, $\Gamma_{300K} = 1/\tau_{300K}$ at room temperature T_{300K}, and $\Gamma_{8K} = 1/\tau_{8K}$ at cryogenic temperature T_{8K} [157]. With the knowledge of the room-temperature pressure in the trap, the pressure in the cryogenic trap volume can then be given by:

$$P_{8K} = P_{300K} \frac{\Gamma_{8K}}{\Gamma_{300K}} \frac{k_B T_{8K}}{k_b T_{300K}} \tag{4.6}$$

Inserting the previously presented results, P_{8K} can be estimated as 3.1×10^{-14} mbar, which also corresponds to an upper limit due to the underestimation of the cryogenic decay constant.

Another approach directly calculates the partial density of H_2 molecules n_{H_2} in the trap following the Langevin collision model with the Langevin rate coefficient k_L [131, p.168 –180]:

$$n_{H_2} = \frac{1}{\tau k_L} \tag{4.7}$$

The latter can be expressed in a form independent of the collision energy and the particle temperature distribution and solely dependent on the charge state of the ion, the polarizability of hydrogen molecules α, and the reduced mass of the two collision partners μ:

$$k_L = \frac{Qe}{2\epsilon_0} \sqrt{\frac{\alpha}{\mu}} \tag{4.8}$$

The polarizability of hydrogen is given by $\alpha = 4\pi\epsilon_0 a = 4\pi\epsilon_0 \times 0.787 \times 10^{-30}\,\mathrm{m}^3$ with a being the dynamic dipole polarizability [259, 260], and the reduced mass of a hydrogen molecule and a strontium ion is

$$\mu = m_{H_2} m_{Sr} / \left(m_{H_2} + m_{Sr}\right) \tag{4.9}$$

So, the rate coefficient can be evaluated as $k_L \approx 1.49 \times 10^{-15}\,\mathrm{m}^3/\mathrm{s}$ and the upper limit for the partial pressure of the hydrogen molecules p_{H_2} in the trap volume can finally be calculated as

$$p_{H_2}(8\,\mathrm{K}) = n_{H_2} k_B T \approx 3.2 \times 10^{-13}\,\mathrm{Pa} = 3.2 \times 10^{-15}\,\mathrm{mbar} \tag{4.10}$$

Depending on the used model, the estimates of the pressure in the cryogenic trap differ by more than an order of magnitude. Still, both results can be considered as valid approximations and are comparable to the pressure values measured for other cryogenic ion traps [131, 154, 155, 157, 228, 234, 261, 262].

4.3 Extraction of $^{229}Th^{3+}$ Ions

After the successful trapping and laser cooling of strontium ions as well as the characterization of the trap, the extraction of Th^{3+} ions was prepared, and the setup reached the state of development as depicted in Fig. 3.1. To put the *Buffer-Gas Stopping Cell* into operation and to create a continuous beam of thorium ions out of the *Extraction RFQ* , a typical helium gas pressure of 32 mbar was applied together with the voltage settings listed in Tab. 4.2.

For continuous ion extraction, the endcap of the *Extraction RFQ* is set to 0 V and for ion accumulation in segment 8, it is ramped up to 100 V, as can also be seen in Fig. 4.16. In order to generate ion bunches, these two configurations are alternated with a defined time lag as accumulation time via PC control.

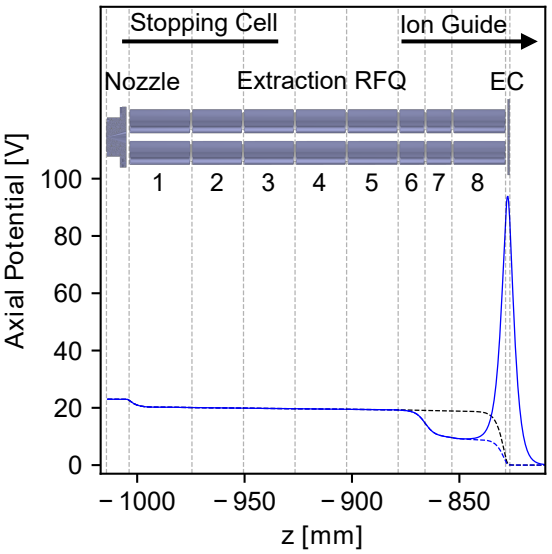

Figure 4.16 *Axial potential from the nozzle to the endcap of the Extraction RFQ for the continuous extraction (dashed black line) of $^{229}Th^{3+}$ ions and the accumulation of ions in segment 8 (solid blue line) with closed endcap. Ion bunching with open endcap is shown with the dashed blue line. All potentials were calculated with the SIMION simulation software (Version 8.1.1.32) [136]. For visualization, a CAD image of all the electrodes generating the axial potential is added as well. Own image, also shown in [226].*

In order to characterize the output of the *Buffer-Gas Stopping Cell*, a mass spectrum of the continuously extracted ions was performed with *QMS 1* running at an RF frequency of 947.09 kHz over the almost complete scanning range and is shown in Fig. 4.17. A CEM was used to detect the ions at the other end of the setup. The scan settings included a mass-to-charge resolution of $\Delta m/Q = 2$ u/e and an integration time of 5 s per 0.1 u/e scan step. For this scan, all previous guiding RFQs were set to transmit ions with mass-to-charge ratios $m/Q \geq 30$ u/e.

Compared to the mass spectra recorded with the first LMU buffer-gas stopping cell (see [8, 19],[14, p.103]), the count rates are smaller by a factor of 20 to 200. This can be mainly accounted for by the lower activity of the ^{233}U source of only 10 kBq compared to the 270 kBq in the old setup, combined with a similar detector dark count rate. Consequently, the signal-to-noise ratio is significantly worse and the clear separation of neighboring peaks in the case of $^{229}Th^{3+}$ and $^{233}U^{3+}$ with mass-to-charge ratios of 76.3 u/e and 77.7 u/e is not as unambiguously possible as in [8].

Table 4.2 *A list of the DC voltages applied to the different electrodes and components in the Buffer-Gas Stopping Cell as well as in the Extraction RFQ for the extraction of $^{229}Th^{3+}$ ions. The values in brackets for the segments 7 and 8 correspond to voltage settings for bunched thorium extraction.*

Electrode/ Component	Voltage [V]	Electrode/ Component	Voltage [V]
^{233}U Source	42.0	*Extraction RFQ 4*	19.6
Funnel 1	37.5	*Extraction RFQ 5*	19.4
Funnel 2	22.5	*Extraction RFQ 6*	19.2
Nozzle	23.2	*Extraction RFQ 7*	19.0 (10.0)
Extraction RFQ 1	20.2	*Extraction RFQ 8*	18.8 (9.0)
Extraction RFQ 2	20.0	*Extraction RFQ Endcap*	100 (closed) 0 (open)
Extraction RFQ 3	19.8		

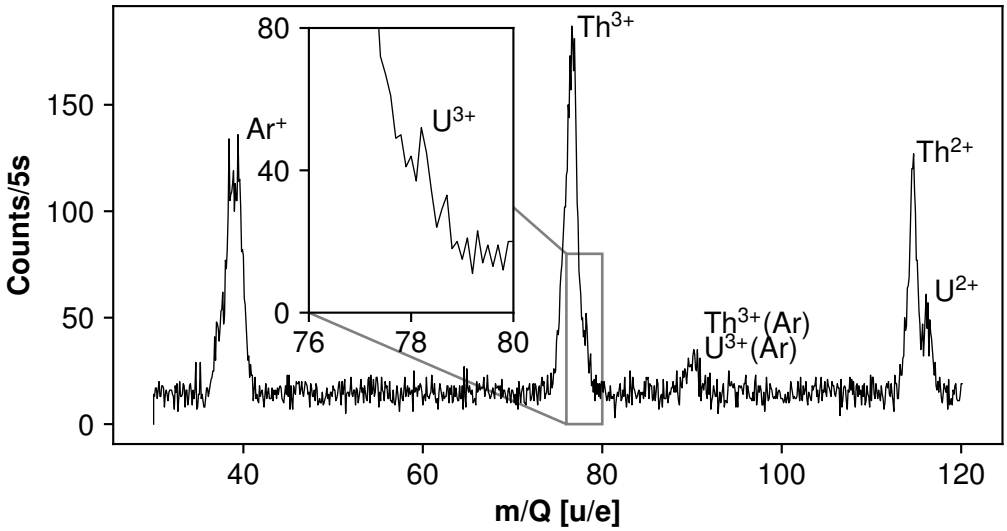

Figure 4.17 *Mass scan of the extracted ions from the buffer gas stopping cell performed with QMS 1 with an applied mass filter of $\Delta m/Q = 2$ u/e and an integration time of* 5 s *per* 0.1 u/e *scan step. Own representation also shown in [226].*

Still, from the amplitude ratio of the peaks originating from $^{229(m)}Th^{2+}$ and $^{233}U^{2+}$ with their respective mass-to-charge ratios 114.5 u/e and 116.5 u/e, an excellent He purity as well as a suitable He pressure can be deduced [14, p. 103].

Apart from the main peaks, also contributions from compounds with argon can be observed, which were also seen in previous measurements [14, p. 100]. The very

prominent peak at mass-to-charge ratio 39 u/e has not been reported so far, but probably stems from a potassium contamination of the funnel electrodes that occurred during the calibration of the QMS modules with a heated ion source (see [223]). Most recent mass spectra of the extracted ions from the stopping cell provided strong evidence to interpret the mass peak as an argon impurity at mass-to-charge ratio 40 u/e. As a noble gas, argon is not easily pumped and is also resistant to a bake-out of the chamber. Therefore, it is a highly likely residual gas candidate.

In principle, both QMS modules can be used to carry out such a mass scan. However, after several comparative measurements, *QMS 1* turned out to be the device with superior mass resolution. Since the two mass separators have the same design, the difference in the resolution can be either explained by inconsistencies in the manufacturing process or the relative position of the two devices with respect to the ion source of the detector.

5 Trapping and Sympathetic Cooling of $^{88}Sr^{+}$ and $^{229}Th^{3+}$ Ions

One of the most crucial goals for this work was the creation of $^{88}Sr^{+}$-$^{229}Th^{3+}$ Coulomb crystal as the starting point for thorium spectroscopy measurements. In the setup depicted in Fig. 3.1, the loading process of such a two-species Coulomb crystal can be described as follows. As a prerequisite for the trapping of thorium ions, a $^{88}Sr^{+}$ Coulomb crystal has to be formed in the center of the cryogenic Paul trap and continuously laser cooled close to the respective resonances of 422 nm and 1092 nm. For the visualization of the applied voltages in the setup during the loading and trapping process of strontium ions, the axial potential from the de Laval nozzle until the rear endcap of the Paul trap is shown in Fig. 5.1. Since the ablation of $^{88}Sr^{+}$ ions takes place in the *Ion Guide*, the *Extraction RFQ* is not affected by the strontium crystal preparation and can be kept closed for the continuous accumulation of thorium ions. As the extraction of thorium only works with a He buffer-gas pressure of at least 25 mbar in the *Buffer-Gas Stopping Cell*, the pressures in the other chambers of the setup, as well as in the trap chamber, are also elevated. To provide the best trapping conditions and to minimize the influence of any residual gas particles in the trap volume, the gas flow is turned off as soon as the $^{229}Th^{3+}$ ions are loaded. As already mentioned in the previous chapter, the ablated ions need to be mass filtered during the transport in *QMS 2*. At an RF frequency of 937 kHz, the usual Mathieu parameters of $a_{Sr} = 0.044$ and $q_{Sr} = 0.269$ can be used to transmit only the particles of $m/Q = 88$ u/e with a resolution of $\Delta m/Q = 2.5$ u/e. Only like this, fast Doppler cooling of a sample of trapped $^{88}Sr^{+}$ with isotopic purity can be ensured. Depending on the desired amount of ions in the trap, the filter resolution of *QMS 2* can be adjusted or the *Ion Guide* can be used as a coarse pre-filter.

Once the trapping and cool down of strontium ions is achieved, the initial trapping potential created by the three central trap electrodes 3, 4 & 5 has to be altered from a configuration of 70 V, 40 V, 70 V or 90 V, 60 V, 90 V to 9 V, 8 V, 9 V. Since the extracted ions from the*Buffer-Gas Stopping Cell* are already pre-cooled and lose even more energy during the accumulation process in the *Extraction RFQ*, their kinetic energy through the setup is mainly dictated by the voltage applied to segment 8 of the *Extraction RFQ* at 9 V. So, the central trap endcaps formed by the trap segments 3 and 5 are adjusted, such that the thorium ions can still be transmitted through the setup. To actually trap them, a second, bathtub-shaped trap potential is formed by using also the trap segments

1, 2, 6 and 7 with an applied voltage of 10 V and the two apertures at the 4 K-shields (EC 1 and EC 2) with 20 V applied (seen Fig. 5.2).

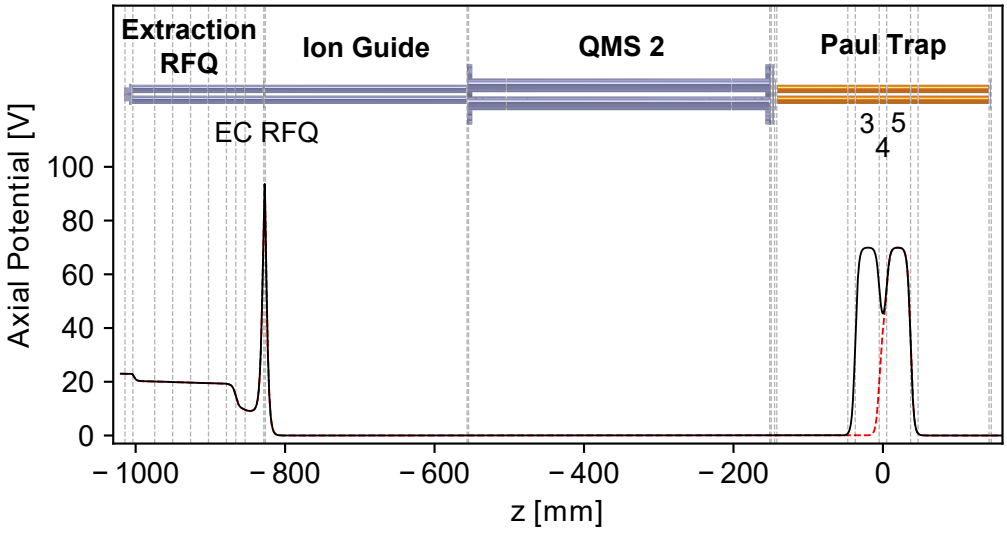

Figure 5.1 *Axial potential along the ion axis from the de Laval nozzle until the second endcap or 4 K-shield aperture of the cryogenic Paul trap. Shown are the instants of $^{88}Sr^{+}$ loading (dashed red line) and strontium confinement (solid black line) with a voltage configuration of 70 V, 40 V, and 70 V applied to the three central trap segments. Both potentials were calculated with the SIMION simulation software (Version 8.1.1.32) [136]. For better visualization, a CAD image of all electrodes generating the axial potential is added.*

With all voltages prepared for the loading of thorium ions, it is necessary to change the settings of *QMS 2* to a DC voltage of $U_{DC} = \pm 49.3$ and an RF amplitude of 605 Vpp. This results in Mathieu parameters of $a_{Th} = 0.112$ and $q_{Th} = 0.688$ to transmit only particles of $m/Q = 75$ u/e with a resolution of $\Delta m/Q = 3$ u/e. The actual mass peak of $^{229}Th^{3+}$ lies at $m/Q = 76.3$ u/e, but to avoid any uranium impurities in the Coulomb crystal, the mass filter is tuned to the rising edge of the mass peak.

The thorium loading process is then started via a PC command, which lowers the voltage of the outer trap's front endcap EC 1 to zero. Afterwards, the endcap voltage of the *Extraction RFQ* is turned off and releases the bunch of accumulated ions from the ^{233}U source. They are mass filtered and transported to the Paul-trap volume, where they are reflected at the rear endcap EC 2. For ion confinement, the endcap voltage at EC 1 has to be ramped up in time before the back-reflected ion bunch can again leave the trap volume. Initially, EC 1 was turned on again 270 μs after the release of the ion bunch from the *Extraction RFQ*. In a later development stage of the setup, this thorium loading time value changed to 185 μs, after an adjustment of the trap's ion axis with respect to the adjoining RFQ sections. As for the already mentioned change in the strontium trapping parameters, this change in the setup resulted in a faster transport of particles or favored the transmission of fast ions.

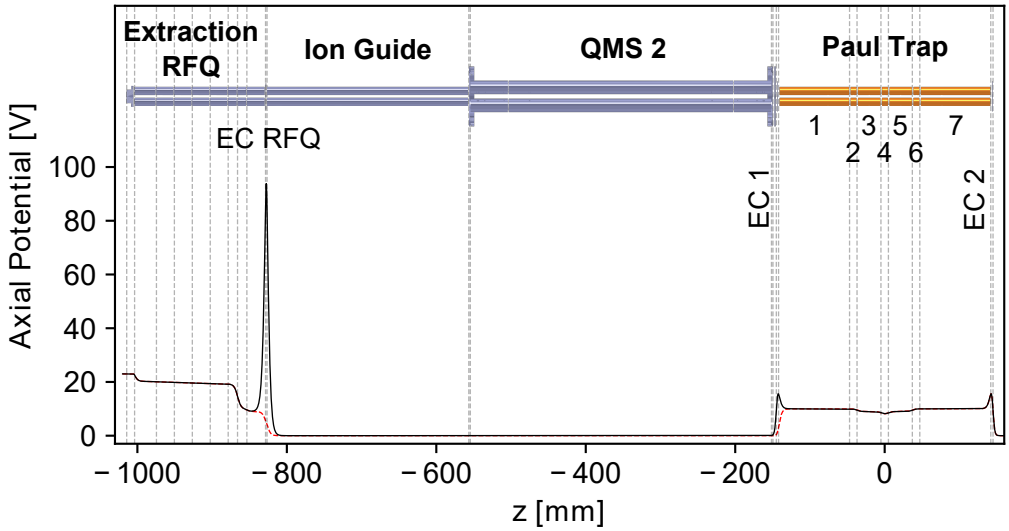

Figure 5.2 *Axial potential along the ion axis from the de Laval nozzle until the second endcap (EC 2) of the cryogenic Paul trap. Shown are the instants of* $^{229}Th^{3+}$ *accumulation in the RFQ with closed endcap (EC RFQ) and a different trap configuration with* 10 V, 10 V, 9 V, 8 V, 9 V, 10 V, 10 V *applied to the seven trap segments (solid black line). The voltage setting of bunched ion release and opening of the front endcap (EC 1) of the trap is shown with a dashed red line. Ion confinement and cooling also occurs in the initial potential configuration. Both potentials were calculated with the SIMION simulation software (Version 8.1.1.32) [136]. For better visualization, a CAD image of all electrodes generating the axial potential is added.*

As the trapped ions are reflected back and forth between the two endcaps EC 1 and EC 2 of the outer bathtub-shaped potential well (EC 1 & 2, segments 1 - 7), they interact with the laser-cooled $^{88}Sr^{+}$ Coulomb crystal in the central trap well (segments 3 - 5) and continuously lose energy at each reflection. This process goes on until their kinetic energy is low enough to be confined by the $U_z = 1$ V axial potential in the central trap well and they are embedded in the strontium crystal.

Fig. 5.3 illustrates the loading process of $^{229}Th^{3+}$ into the cryogenic Paul trap with three EM-CCD images of the 422 nm fluorescence signal stemming from 14 $^{88}Sr^{+}$ ions Doppler cooled with a single laser beam of 422 nm and 1090 nm at an angle of 50° with respect to the ion axis. All images were taken with an integration time of 1.0 s and show the shape of the two-species ion crystal at two different axial potentials. The upper image shows the one-dimensional arrangement of $^{88}Sr^{+}$ ions in a linear chain together with ion positions of a simulated ion crystal calculated with the SIMION software (Version 8.1.1.32 [136]). A fit of the simulation to the camera images with an estimated uncertainty results in a magnification of $M = 5.32(2)$, which does not agree with the theoretical magnification value of $M = 5.7(1)$ for the used imaging system of *Version 1* (see Sec. 3.11).

In the central image, the same 14 strontium ions are shown after the loading of three $^{229}Th^{3+}$ ions. Since they do not fluoresce at 422 nm, they are only indirectly visible

as dark spots between the bright strontium ions. However, their positions are again visualized via a simulation that also resulted in a magnification of $M = 5.32(2)$ and as such also deviating from the theoretical magnification of $M = 5.7(1)$.

As already discussed in Sec. 4.2, these deviations for the magnification values in the case of the linear ion chains at low axial potential depths most probably stem from voltage offset errors of the power supply providing the voltages for the trap segments (*HV400*, Stahl-Electronic, Mettenheim, Germany).

In the lower image, the two-species ion crystal is depicted at an axial potential depth of $U_z = 3.0\,\mathrm{V}$ that results in a 3D crystal shape. The positions of the dark thorium ions are indicated once again with the simulated ion positions that gave a magnification value of $M = 5.60(2)$ within the error bars of the theoretical value of $M = 5.7(1)$. This configuration also shows how the thorium ions are arranged along the ion axis due to their lower mass-to-charge ratio in comparison to $^{88}Sr^{3+}$. This behavior has also been simulated and experimentally demonstrated by Zitzer et al. [252].

In this stage of the experiment, the trapping of $^{229}Th^{3+}$ ions could not be confirmed with absolute certainty, because the thorium fluorescence at 690 nm could not yet be detected. Also, the performed simulations cannot fully confirm the trapping of thorium ions, as the shape of the ion crystal with two species is more dependent on the charge state than on the ion mass. So, simulations with $^{233}U^{3+}$ could also be fitted to the recorded images. As the mass scans of the thorium source (see Fig. 4.17) always revealed a vanishing amount of uranium, the scenario of $^{88}Sr^{+}$-$^{233}U^{3+}$ Coulomb crystals was considered as unlikely, though.

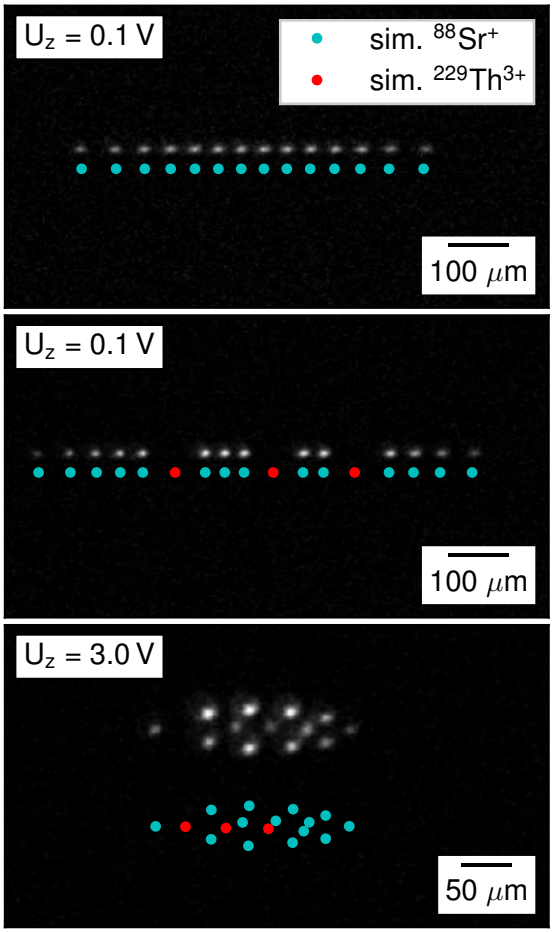

Figure 5.3 *The same Coulomb crystal consisting of 14 $^{88}Sr^{+}$ ions before (upper image) and after (central and lower image) loading of $^{229}Th^{3+}$. The two-species crystal is also shown at different axial potential depths U_z. For the scaling and the visualization of the dark thorium ions, SIMION crystal simulations are added (Version 8.1.1.32 for the linear chains and Version 8.0.4 for the 3D crystal) [136]. Own image, also shown in [226].*

For the search for thorium fluorescence, it was necessary to increase the signal intensity by all means. The main motivations to push the fluorescence signal were the lower photon yield in comparison to $^{88}Sr^{+}$, the uncertainty in the focus position of the imaging system at 690 nm, uncertainties in the correct laser frequencies and EOM settings to address the hyperfine lines, and the readout error of the wavelength meter. Therefore, not linear chains of ions, but larger crystal sizes were envisaged. One example of a large $^{88}Sr^{+}$ crystal before and after the embedding of several hundred $^{229}Th^{3+}$ ions is presented in Fig. 5.4.

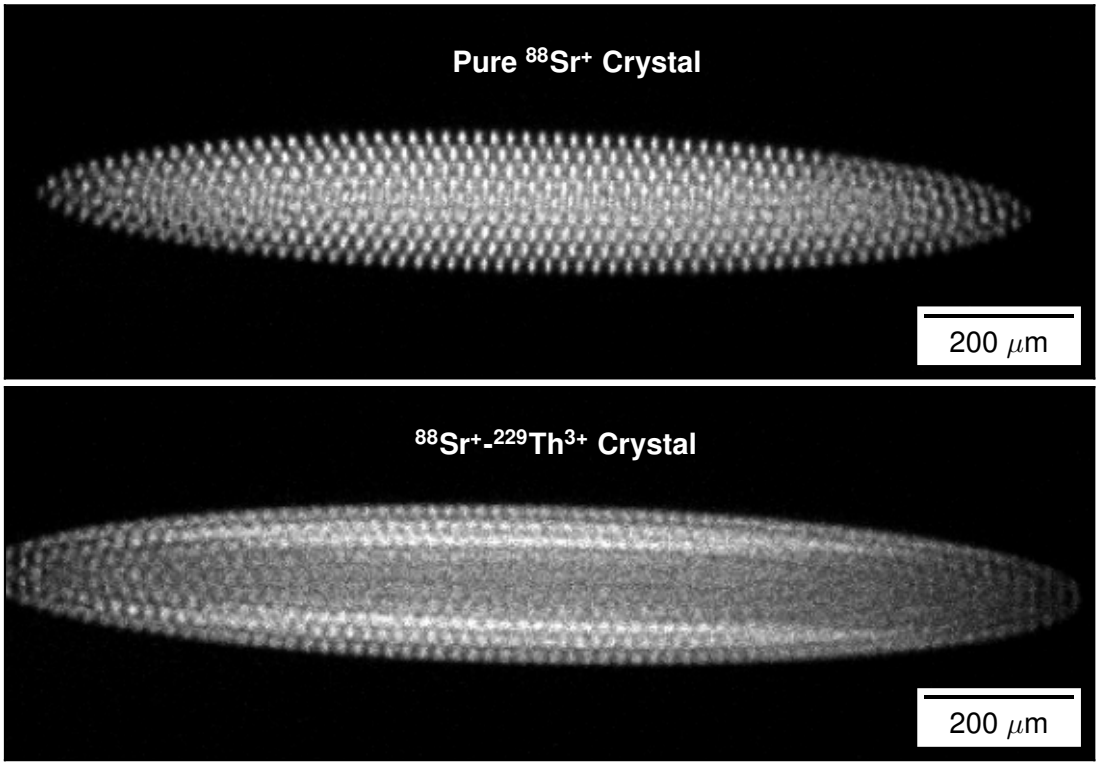

Figure 5.4 *Shown is the* 422 nm *fluorescence of the same* $^{88}Sr^{+}$ *Coulomb crystal before the loading of* $^{229}Th^{3+}$ *in the upper image and after loading in the lower image. For both images, the axial potential was* $U_z = 2\,\mathrm{V}$*, the camera integration time* 0.1 s *and the magnification* $M = 5.6$*.*

As in Fig. 5.3, the thorium ions embedded in the $^{88}Sr^{+}$ Coulomb crystal are only visible as dark ions close to the ion axis. Most probably, the image shows a single shell (around a linear chain) of thorium ions wrapped up by three shells of strontium ions.

For the realization of an ion crystal of this size, two laser beams along the ion axis and at an angle of 30° (as depicted in Fig. 3.1) were necessary to ensure efficient Doppler cooling. Especially during the cool-down process of the thorium ions, two beams were essential. Still, the ion temperature in the Coulomb crystal after the loading of thorium

ions is elevated compared to the pure $^{88}Sr^{+}$ crystal, which is visible in the reduced ion resolution of the lower image in Fig. 5.4.

To trap such a large number of thorium ions, three or more ion bunches from the *Extraction RFQ* are necessary that are successively sent into the trap, whenever the crystal stabilizes again after the cool down. To limit the number of thorium ions per bunch and to enhance the crystal stability, the mass filter of *QMS 2* was usually set to $\Delta m/Q = 0.5\,\mathrm{u/e}$.

6 $^{229}Th^{3+}$ Spectroscopy Experiments

The successful preparation of sympathetically cooled $^{229}Th^{3+}$ Coulomb crystals confined in the cryogenic Paul trap was a major milestone for this work and also represented the starting point for thorium spectroscopy measurements.

6.1 $^{229(m)}Th^{3+}$ Spectroscopy in the Extraction RFQ

After several unsuccessful attempts to detect the $^{229}Th^{3+}$ fluorescence at a wavelength of 690 nm from ions confined in the cryogenic Paul trap, a change of strategy appeared to be the next logical step. As already demonstrated in the experiments of Thielking et al. [111] and Yamaguchi et al. [13], thorium ions can also be stored in a room-temperature He buffer-gas environment inside the *Extraction RFQ* shortly after the *Buffer-Gas Stopping Cell*. The individual hyperfine lines are broadened to a FWHM of about 400 MHz by Doppler broadening, and the requirements for the frequency broadening of the lasers are less demanding than in the experiment of Campbell et al. [171, 199]. Another crucial advantage of the ion storage in a buffer-gas environment is the collisional mixing of the hyperfine states. Due to this hyperfine mixing, there is no need for individual addressing of all hyperfine levels.

So, the setup was prepared for fluorescence readout with the EM-CCD camera attached to the viewport of the *Extraction RFQ* as depicted also in Fig. 3.16. To continuously accumulate the extracted ions in the field of view of the dedicated imaging system, the eight DC voltages of the *Extraction RFQ* were set to form a potential well at segment 4 with the following voltages: 20.2 V, 20.0 V, 19.8 V, 15.0 V, 20.0 V, 20.2 V, 20.4 V, 20.6 V. The endcap of the RFQ was kept at the usual blocking voltage of 100 V. To ensure an ideal overlap of the lasers with the trapped ions, the 690 nm and 984 nm lasers were collinearly focused through the on-axis hole of the ^{233}U source and the de Laval nozzle with laser powers of 70 μW and 100 μW, respectively. Checking the power of the transmitted laser light after the viewport on the detector side of the beamline gave efficiency values of around 70 % for the 690 nm laser and around 20 % for the 984 nm laser. The strong deviations in the transmission efficiency for the different lasers

can be explained by the non-achromatic aspheric lens (*C230TMD-A,* Thorlabs GmbH, Bergkirchen, Germany) in the fiber coupler used for the focusing.

Initially, the 690 nm and the 984 nm laser beams were not frequency broadened and only stabilized with the wavelength meter to frequencies of 434 280 700 MHz and 304 609 250 MHz, which both lie roughly in the center of the respective hyperfine spectrum. Due to the high kinetic energies at room temperature, the particle collisions are sufficient to ensure a homogeneous population of the hyperfine states in $^2F_{5/2}$ and $^2F_{7/2}$.

Although both lasers are focused for the alignment through the nozzle, they generate a lot of stray light, which is further reflected on the metal surfaces in the *Extraction RFQ*. Due to the bandpass filter around 690 nm (*FBH690-10*, Thorlabs GmbH, Bergkirchen, Germany) before the EM-CCD camera, the 984 nm stray light plays a minor role. However, with the high quantum efficiency of the camera for the red frequency spectrum, slight changes in the 690 laser power, even below 1 %, result in pronounced camera signal changes. Therefore, the proven strategy for the $^{88}Sr^+$ fluorescence readout to take a single background image for a whole sequence of camera images in combination with a scanned laser frequency had to be discarded. In addition, the photon yield for the thorium fluorescence was expected to be a factor of 1000 lower than that of strontium. For this reason, the decision was made to perform a differential measurement by subtracting a background image from a signal image. So, a camera snap of 0.5 s integration time with the 984 nm laser blocked was taken as the background image, followed by a camera snapshot with the same exposure time and the repumping laser transmitted as the signal image.

Controlling the irradiation with the 984 nm laser was done with an AOM that could deflect the beam to a fiber coupler or not (see Sec. 3.10). By stacking several of the differential images, it was finally achieved to retrieve the thorium fluorescence signal at 690 nm.

As illustrated in Fig. 6.1, additional background monitoring was done using different regions of interest (ROIs) of the same size for the evolution of the signal and the background. The image also demonstrates that it was not possible to find a distinct focus position but only a domain of higher image resolution ranging over ~ 5 mm. As characterized in test measurements, it was not possible to image a point-like light source correctly due to the use of spherical lenses, which are not diffraction-limited. The use of a diffraction-limited lens system was not necessary, because the ion cloud was only buffer-gas cooled and not as well localized in the trap center as, e.g., the Coulomb crystals in the cryogenic Paul trap. A radial extension of the ion cloud in the *Extraction RFQ* of about 1 mm was expected. Furthermore, segment 4 only allows a bathtub-like potential to be applied. Therefore, an extension in the axial direction of several mm was anticipated.

Since the lens system for the thorium spectroscopy in the *Extraction RFQ* features a solid angle and a detection efficiency similar to the imaging system used in the cryogenic Paul trap, the low signal-to-noise ratio of the thorium fluorescence could also be assumed for the thorium spectroscopy in the trap.

With the described measurement routine and the first signal traces, further optimizations could be made. So, it turned out to be advantageous to frequency broaden the 984 nm repumping laser in a similar way as already shown by Zitzer et al. [213, 263]. By continuously sweeping the EOM modulation frequency with a sawtooth function from 0 MHz to 1.5 GHz in steps of 300 kHz every 9.6 ns, the repumper was broadened to around 3 GHz and could cover the whole hyperfine spectrum of the $5F_{7/2} \rightarrow 6D_{5/2}$ transition. Changing the scan step size up to 1 MHz did not significantly improve the signal. Simultaneously with the frequency broadening, the laser power had to be increased to 1200 μW to have, on average, enough power in each frequency component.

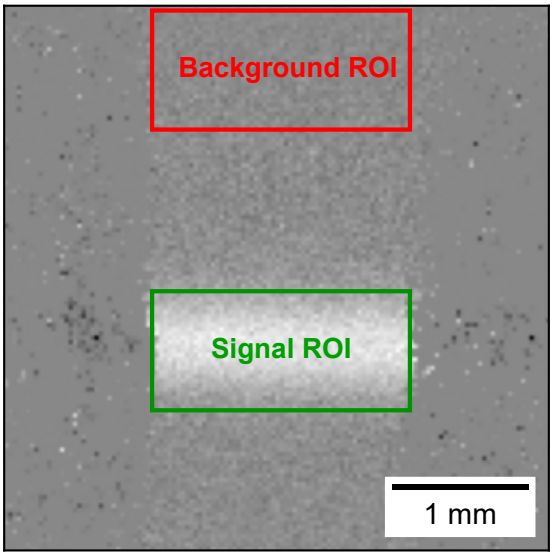

Figure 6.1 *Exemplary image stack of 50 differential camera snaps, each with an integration time of* 0.5 s. *The green and the red rectangles indicate the regions of interest for the thorium fluorescence and the background signal, respectively. The used magnification of* $M = 2$ *corresponds to an approximation for the used lens system.*

Another measure to increase the signal-to-noise ratio and the reproducibility of consecutive measurements was the reloading of the ions in the *Extraction RFQ* by turning on and off the RF voltage after each image stack. Like this, every image stack also had the same starting conditions. Such a behavior could be explained by some sort of dark-state generation in spite of the collisional hyperfine-mixing in the buffer-gas environment. Losses of $^{229}Th^{3+}$ over time regarding the continuous loading of the trap seem to be unlikely.

In this configuration, with the broadened repumper, freshly loaded ions for each image stack and additional background monitoring, the 690 nm laser could be scanned over a frequency range of 6 GHz to record the total Doppler broadened spectrum of the transition. The laser frequency stabilized with the readout of the wavelength meter was constant for the aggregation of 20 differential images and then decreased by 10 MHz for the next image stack. Fig. 6.2 shows the result of the Doppler broadened $^{229}Th^{3+}$ hyperfine-structure spectroscopy scan. In the case of the hyperfine splitting at 690 nm, the isolated $F = 5 \rightarrow F' = 4$ transition peak could be used for a Gaussian fit to retrieve the broadening of the linewidth and a temperature estimate for the confined ions. Since the broadening of the lines is mainly due to the ion temperatures, the approach of using a Voigt profile for fitting was discarded. The Gaussian fit gave a FWHM linewidth of 331(11) MHz corresponding to a temperature of 261(9) K, which is slightly below the expected room temperature of the ion cloud. Yamaguchi et al. obtained a temperature estimate of 400 K for their ion cloud in a He buffer-gas environment of

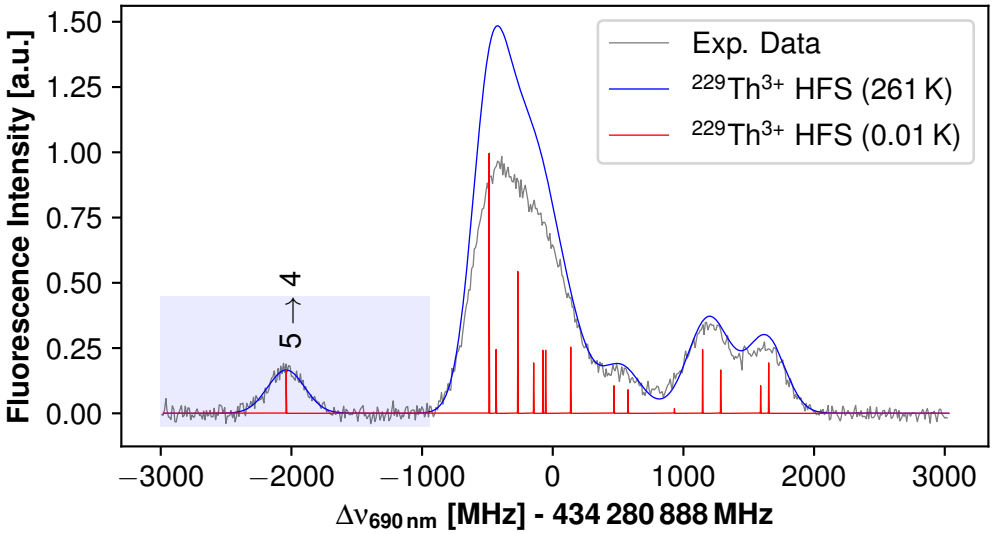

Figure 6.2 *Hyperfine structure spectroscopy of the* 690 nm *transition in* $^{229}Th^{3+}$ *recorded via fluorescence detection at* 690 nm *from ions confined in the Extraction RFQ. The experimental data are normalized to the maximum (black) and overlaid with calculated data for the hyperfine splitting at* 0.01 K *(red) and at* 261 K *(blue) based on the experimental results from [213]. The latter temperature estimate is based on a Gaussian fit to the isolated peak of the* $F = 5 \rightarrow F' = 4$ *transition in a dedicated fit window (shaded blue).*

around 5×10^{-6} mbar [13]. During the thorium spectroscopy in the *Extraction RFQ* of the LMU setup, the residual He pressure in the confinement region was in the low 10^{-3} mbar region, which most probably caused the reduced ion temperatures compared to the experiments of Yamaguchi et al.

In addition to the estimate of the ion temperature, the fit function was used to calculate a scaling factor for the signal height of the theoretical intensity distribution (see also Yamaguchi et al. [13]). The calculated hyperfine splittings based on the results of Zitzer et al. [213] with a Doppler broadened Gaussian linewidth at 0.01 K (shown in red) and the estimated 261(9) K (shown in blue) could be multiplied by the retrieved scaling factor. As visible in Fig. 6.2, the blue curve based on the calculations for the hyperfine splitting, represents well the locations of the individual hyperfine lines, but deviates in the signal height for the transitions between −1000 MHz and 0 MHz frequency detuning. For Yamaguchi et al. [13], the same evaluation method delivered results in good agreement with the experimental findings.

Fluctuations in the amount of ions confined in the RFQ during the measurement due to fluctuations in the He buffer-gas pressure of a few percent cannot explain the specific deviation in the high-intensity signal range. Therefore, the deviations in the results of this work are primarily attributed to saturation effects. A saturation of the hyperfine transitions between −1000 MHz and 0 MHz frequency detuning can be excluded, because of their higher saturation intensities in comparison, e.g., to the $F = 5 \rightarrow F' = 4$

transition. Furthermore, the amplitude ratio of the latter signal peak and the maximum would be higher than 1:10 (predicted by calculations) and not lower as observed in the measurement. Consequently, a saturation of the camera from a certain signal intensity on seems to be the most plausible explanation for the discrepancy between the measured fluorescence signal and the calculated spectrum.

In order to get an idea of the saturation effect for each individual hyperfine transition, a fit model based on the known positions of the hyperfine lines was used. In contrast to the model used for the blue plot in Fig. 6.2, the scaling factor for the amplitude of each transition was switched to a free parameter and afterwards put in relation to the previously determined scaling factor. The width of the transitions of Gaussian shape was kept at the previously found 331(11) MHz. As visible in the upper plot of Fig. 6.3, the experimental results could be well modeled by the adapted fit curve. The lower plot in Fig. 6.3 shows the evolution of the scaling factor for the individual hyperfine lines and reveals the deviations from 1, especially for the lines in the frequency detuning range between −1000 MHz and 0 MHz. The large uncertainties for the hyperfine transitions between −250 MHz and 0 MHz detuning express that in this spectral region, multiple linear combinations of Gaussian peaks can deliver a suitable fit curve.

Another significant deviation from 1 was found for the $F = 1 \rightarrow F' = 1$ transition at 931 MHz frequency detuning, which actually has the lowest transition probability of the hyperfine spectrum at 690 nm (see Sec. 2.5.3). Therefore, a saturation of this transition seems rather unlikely, and the large discrepancy of the scaling factor can also be interpreted as an artifact in the fitting process.

Similar to the scan over the hyperfine splitting of the 690 nm transition, another spectroscopy of the hyperfine spectrum at 984 nm was performed. Fig. 6.4 shows the signal of the 690 nm fluorescence as a function of the frequency detuning of the 984 nm laser.

In contrast to the previous scan of the 690 nm laser, none of the lasers was frequency broadened, and the narrowband 690 nm laser was simply stabilized to a frequency of 434 280 700 MHz. For the EOM broadening of the 690 nm laser line up to 3 GHz for highly efficient repumping, also the 690 nm laser power should have been increased. Since the negative influences of the laser stray light were already severe in the previous setting, an increase in the laser power at the fluorescence readout wavelength would not have been beneficial. The alternative, to record the 984 nm fluorescence signal, could only be done at the expense of the signal-to-noise ratio. Although the low quantum efficiency of the EM-CCD camera at around 15 % in theory should have been balanced by the higher photon scattering rate at this transition, the detection at 690 nm turned out to be the preferable configuration. Without the broadened repumper, the fluorescence signal was slightly reduced, which is why for the scan of the 984 nm each data point corresponds to a stack of 30 differential images. Although it was not frequency broadened, the power of the 984 nm laser was not changed and kept at 1200 μW.

The $^{229}Th^{3+}$ hyperfine splitting of the 984 nm transition lacks a completely isolated transition peak and only offers the semi-isolated $F = 2 \rightarrow F' = 3$ transition to obtain an estimate of the ion temperature from a Gaussian fit curve. The measured Doppler

broadened linewidth of 294(12) MHz corresponds to an ion temperature of 419(17) K. This is a significantly higher temperature in comparison to the previous measurement for the spectroscopy of the hyperfine structure of 690 nm, but lies closer to the temperature value retrieved by Yamaguchi et al. [13].

Possible reasons for the deviating temperature values of the confined ion cloud extracted from the two scans could be the different measurement techniques.

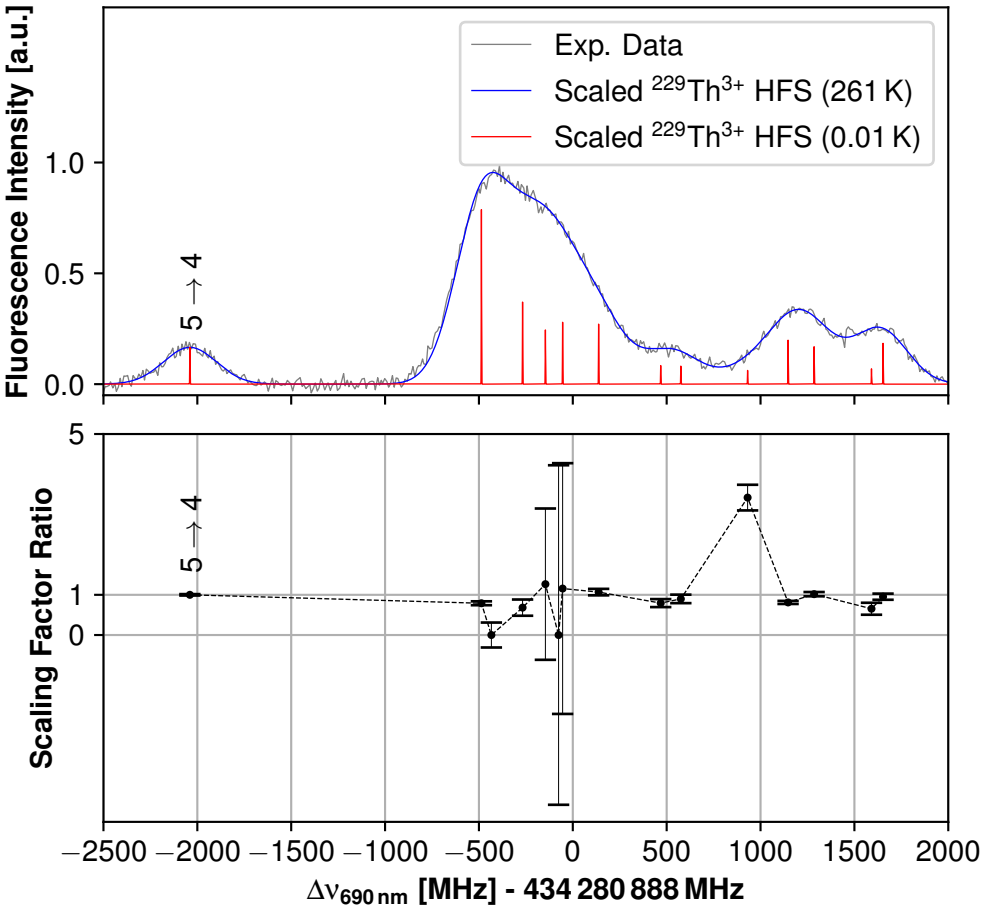

Figure 6.3 *The upper plot shows the hyperfine structure spectroscopy of the* 690 nm *transition in* $^{229}Th^{3+}$ *recorded via fluorescence detection at* 690 nm *from ions confined in the Extraction RFQ. The experimental data are normalized to the maximum (black) and overlaid with fit curves for the hyperfine splitting at* 0.01 K *(red) and at* 261 K *(blue) based on the experimental results from [213]. The latter temperature estimate is based on the previous Gaussian fit to the isolated peak of the* $F = 5 \rightarrow F' = 4$ *transition (see Fig. 6.2). For the curve fitting, the peak-height scaling of each hyperfine transition was a free parameter and was put in relation to the previously found scaling factor for the fit in Fig. 6.2. The evolution of the scaling factor ratio for the individual hyperfine lines is shown in the lower plot as a function of the frequency detuning of the* 690 nm *laser.*

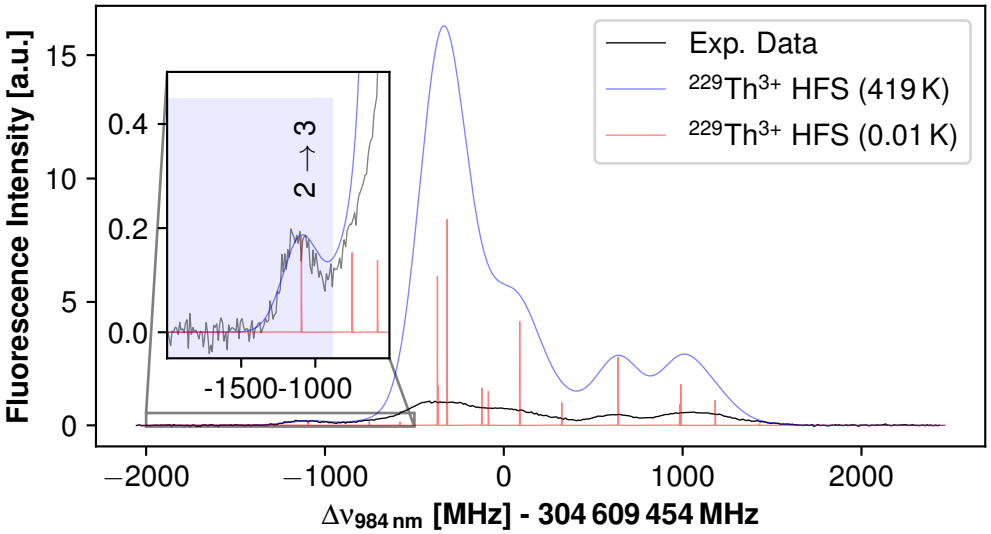

Figure 6.4 *Hyperfine structure spectroscopy of the* 984 nm *transition in* $^{229}Th^{3+}$ *recorded via fluorescence detection at* 690 nm *from ions confined in the Extraction RFQ. The experimental data are normalized to the maximum (black) and overlaid with calculated data for the hyperfine splitting at* 0.01 K *(red) and at* 419 K *(blue) based on the experimental results from [213] and also normalized to their respective maxima. The latter temperature estimate is based on a Gaussian fit to the semi-isolated peak of the* $F = 2 \rightarrow F' = 3$ *transition in the measured hyperfine spectrum.*

In the case of the scan of the 690 nm laser, the frequency broadened 984 nm repumper may have induced a Doppler cooling cycle resulting in lower ion temperatures. On the other hand, the single-mode 984 nm laser with the high power of 1200 μW may have caused a broadened linewidth during the scan over the $5F_{7/2} \rightarrow 6D_{5/2}$ hyperfine structure. However, since the hyperfine spectrum at 984 nm offers not the ideal options for applying a single Gaussian fit curve, the ion temperature value at 261(9) K is considered more reliable.

Nevertheless, the Gaussian fit to the semi-isolated $F = 2 \rightarrow F' = 3$ transition in the 984 nm hyperfine splitting is used to extract a scaling factor. With this scaling factor, calculated hyperfine spectra based on the results of Campbell et al. [171, 199] can be plotted together with the experimental data to compare them with the theoretically expected intensity distribution. As visible in Fig. 6.4, the large deviations of the calculated spectra from the measured data are visible for all transitions with higher probability than the $F = 2 \rightarrow F' = 3$ hyperfine line and also indicate a saturation effect during the measurement.

Analogous to the previous spectroscopy scan of the 690 nm, a fit curve with free parameters for the scaling factors of the individual hyperfine transitions was applied to the data. The results of the comparison with the previously determined scaling factor determined in the Gaussian fit to the $F = 2 \rightarrow F' = 3$ transition are shown in the lower plot of Fig. 6.5. In the frequency detuning range of the 984 nm laser between −500 MHz

and 1300 MHz, the adapted scaling factors are significantly below 1 and clearly show a saturation process. Similar to the previous spectroscopy measurement, the saturation of the EM-CCD during the scan is assumed to be the origin of the large deviations.

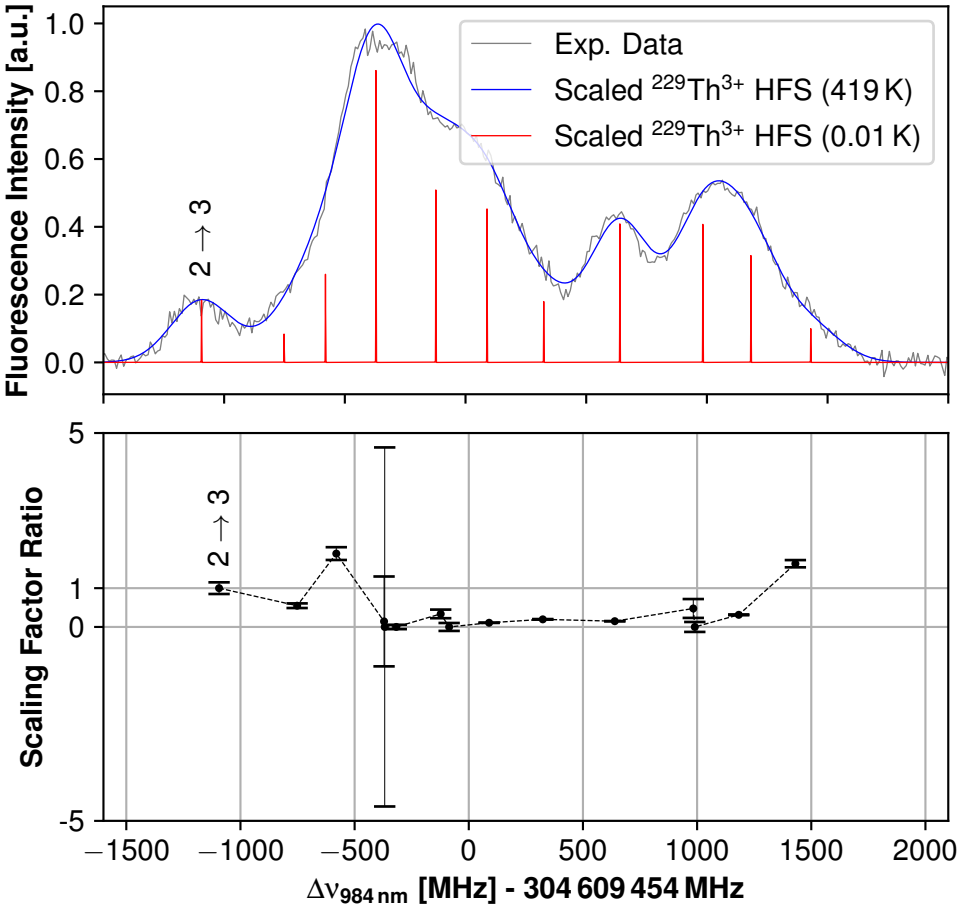

Figure 6.5 *The upper plot shows the hyperfine structure spectroscopy of the* 984 nm *transition in* $^{229}Th^{3+}$ *recorded via fluorescence detection at* 690 nm *from ions confined in the Extraction RFQ. The experimental data are normalized to the maximum (black) and overlaid with fit curves for the hyperfine splitting at* 0.01 K *(red) and at* 419 K *(blue) based on the experimental results from [213]. The latter temperature estimate is based on the previous Gaussian fit to the isolated peak of the* $F = 2 \rightarrow F' = 3$ *transition (see Fig. 6.4). For the curve fitting, the peak-height scaling of each hyperfine transition was a free parameter and was put in relation to the previously found scaling factor for the fit in Fig. 6.4. The evolution of the scaling factor ratio for the individual hyperfine lines is shown in the lower plot as a function of the frequency detuning of the* 984 nm *laser.*

The pronounced uncertainties for the $F = 5 \rightarrow F' = 4$ transition at −371.1 MHz frequency detuning and the $F = 3 \rightarrow F' = 3$ transition at −367.8 MHz frequency

detuning express that there are multiple possible linear combinations of these closely lying Gaussian peaks to deliver a suitable fit curve for the experimental data. The two scaling factors above 1 were found for the two hypferfine transitions $F = 3 \rightarrow F' = 4$ at -580.0 MHz frequency detuning and $F = 4 \rightarrow F' = 5$ at 1430.1 MHz frequency detuning. According to the theory, these hyperfine lines reveal the lowest transition probabilities in the hyperfine spectrum of 984 nm and should therefore not be affected by saturation effects. Consequently, the large scaling factors can also be explained as artifacts in the fitting process.

As the hyperfine structure scan in a buffer-gas environment was only considered as a proof-of-principle measurement for the LMU setup and for time reasons, the records were not repeated for further investigations. Still, the experiments performed with buffer-gas cooled $^{229}Th^{3+}$ ions confined in the *Extraction RFQ* delivered the blueprint for the fluorescence readout strategy applied later for the sympathetically cooled thorium ions in the cryogenic Paul trap.

6.2 $^{229(m)}Th^{3+}$ Spectroscopy in the Cryogenic Paul Trap

Shortly after the hyperfine spectroscopy measurements of $^{229}Th^{3+}$ ions confined in a buffer-gas environment, the EM-CCD camera moved back to its dedicated position attached to the imaging system of the cryogenic Paul trap. With the experiences made during the readout of the faint 690 nm fluorescence signal in the *Extraction RFQ*, absolute care was taken to avoid every unnecessary source of stray light. First of all, the inner surfaces of the 4 K shield close to the trap volume were covered with anodized, black aluminum foil to prevent the reflection of red light from the gold-coated copper surfaces (see also [226]). Then, the initial plan to send the hyperfine spectroscopy lasers on the trapped ions, also under an angle, was discarded because of the laser passage through the 3.57 mm gap between the gold-coated trap electrodes. Although the 690 nm laser beam has a sub-millimeter width, the gap was still narrow enough to send plenty of stray light into the imaging system and the camera. Consequently, the spectroscopy lasers were sent in on axis from the ion detector side with *Beam 2*, as also indicated in Fig. 3.1. The free pathway between the trap electrodes in this direction exhibits a diameter of almost 1 cm and reduces the stray light by more than an order of magnitude.

The fluorescence readout software was further developed and improved for the spectroscopy in the Paul trap, but the basic principle did not change. In a first step, a background image is recorded with the 984 nm repumper light blocked. Then, the AOM deflects the repumping laser light back to the fiber coupling and the trapped ions, and the camera image is recorded at a wavelength of 690 nm. A stack of the images then delivers the thorium fluorescence signal.

For the first fluorescence signals, both lasers were frequency broadened with their respective EOM to 3 GHz with a repeatedly swept modulation frequency running between 0 MHz and 1500 MHz in 300 kHz steps per 9.6 ns. In order to have enough average power in every frequency component, the laser powers were set to 600 μW for the 690 nm laser and 1200 μW for the 984 nm laser. Like in the previous experiment performed in the

Extraction RFQ, the frequency of the 690 nm laser was stabilized to 434 280 700 MHz roughly corresponding to the center of the hyperfine spectrum. The 984 nm repumper was not stabilized to the center of the splitting but to the $F = 1 \rightarrow F' = 0$ transitions at 304 610 517 MHz − 80 MHz (AOM shift), which turned out to be a favorable frequency position in the preceding measurements with buffer-gas cooled thorium ions.

Given the first signals, the optimization process could be started with the positioning of the camera along the imaging axis. According to simulations and test measurements of *Version 2* of the imaging system, the focal plane for 690 nm is 1 mm behind the focal plane for 422 nm light. Since neither the signal height nor the image resolution could be significantly improved by moving the camera, the same position was kept during the experiment while switching between the detection of strontium or thorium fluorescence.

The initial power settings for the two spectroscopy lasers stayed more or less the same throughout all experiments with EOM frequency broadened light, and only the repumping laser power was reduced to 1000 μW.

In the case of the frequency broadened repumper with a swept EOM modulation frequency, the central frequency was eventually optimized by stabilizing it close to the central resonance frequency at 304 609 450 MHz − 80 MHz (AOM shift).

Depending on the requirements for the respective measurement, the choice of EM-CCD readout settings turned out to be crucial. For a maximum signal formed by the summation of pixel counts per image stack, a pixel-binning of 4×4 ($64\,\mu m \times 64\,\mu m$) turned out to be very effective in increasing the signal-to-noise ratio. Furthermore, the Hamamatsu EM-CCD camera can be operated in the so-called "Photon Imaging Mode" especially developed for low signal levels in the single photon range. By applying this setting, the signal intensity can be increased in three levels. However, for the best image quality and the best spatial resolution of single ions, the standard settings with 1×1 binning and the "Photon Imaging Mode" either switched off or adjusted to 1 delivered the best results.

Fig. 6.6 depicts two different $^{88}Sr^{+}$-$^{229}Th^{3+}$ Coulomb crystals in a two-color representation. They were created with an EM-CCD image of the 422 nm strontium fluorescence signal overlaid with a stack of images of the 690 nm thorium fluorescence.

The image resolution in Fig. 6.6(a) is sufficient to distinguish between individual strontium and thorium ions. The ability to resolve and to monitor single thorium ions is of high importance for prospective experiments with the cryogenic Paul-trap setup at LMU, as for example the direct laser excitation of the isomeric state in $^{229}Th^{3+}$ with a VUV laser source. It has to be mentioned, though, that with the current low signal-to-noise ratio of the thorium fluorescence and the associated time-consuming detection process, resolution of single ions is only possible in stable crystal configurations. Such stable crystal configurations are three-dimensional $^{88}Sr^{+}$ crystals enclosing the thorium ions from all sides. A linear chain of $^{88}Sr^{+}$ ions containing several $^{229}Th^{3+}$ ions (see also Fig. 5.3) is more unstable, and the thorium ions start hopping between different crystal positions on a time scale of a few seconds. For such crystal configurations, the current readout scheme delivers a thorium fluorescence signal, but provides only blurred images.

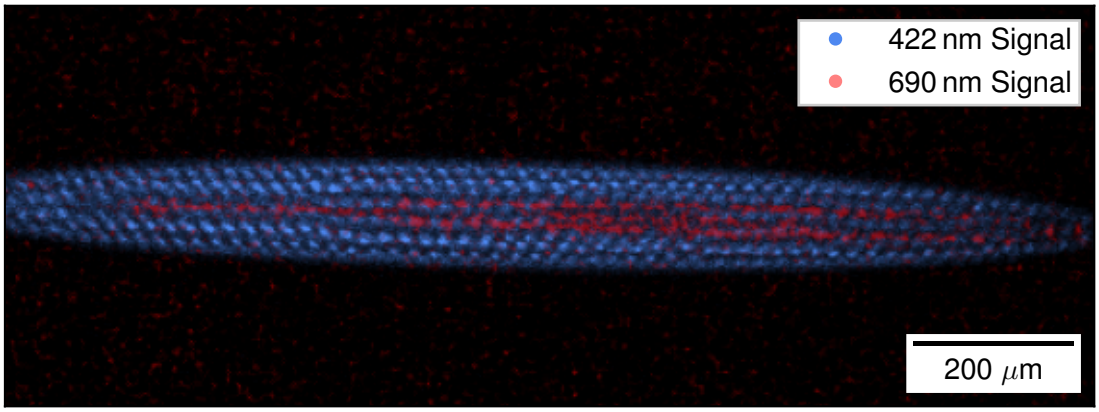

(a)

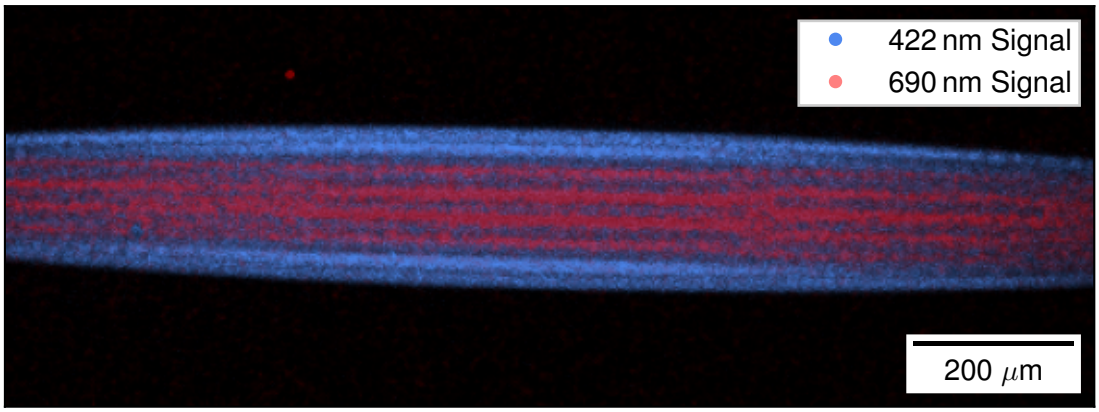

(b)

Figure 6.6 *Two-color images of different $^{88}Sr^{+}$-$^{229}Th^{3+}$ Coulomb crystals. The* 422 nm *fluorescence signal from the strontium ions is depicted in blue with a magnification of* $M = 5.6$ *and the overlaid* 690 nm *fluorescence signal from the thorium ions in red with a magnification of* $M = 5.5$*. The integration time for the blue signals was* 0.1 s *and the red signals are stacks of single measurements with* 1.0 s *exposure time. (**a**) represents a stack of 120 single measurements and (**b**) a stack of 156 measurements.*

The reordering or hopping of trapped ions in a crystal configuration has been previously observed and studied by several research groups in few-ion crystals. Some of them explain the effect mainly by collisions of the trapped ions with background particles in the confinement volume and even use the hopping rates to determine the vacuum quality of their trap setups [55, 264–266]. Abich et al. [267] and Liang et al. [268], on the other hand, consider the ion hopping as a thermally induced effect due to inefficient laser cooling. Rüffert et al. [269] study collision events and the ion temperature as competing sources of crystal reordering events. From own observations, it can be deduced that the

hopping of the ions mainly depends on the degree of confinement and cooling. Regarding the cryogenic environment in the trap volume, collisions of residual gas particles with the confined Coulomb crystal are assumed to be negligible.

So, three-dimensional $^{88}Sr^{+}$ Coulomb crystals with axial potential depths of 3 V to 4 V are the environment to be preferred for the embedding of $^{229}Th^{3+}$ with confining and cooling Coulomb forces in all degrees of freedom. Furthermore, it should be noted that the number of strontium ions should exceed the number of thorium ions by around one order of magnitude for optimum sympathetic cooling. In view of future experiments with a linear chain of $^{88}Sr^{+}$ and $^{229}Th^{3+}$ ions or a single mixed ion pair, an increase of the radial confinement by the use of higher RF frequencies and peak-to-peak amplitudes for the voltages applied to the trap electrodes may help to suppress the reordering of the ion crystals. Also, the laser cooling to the motional ground state of the ions should be considered.

For Fig. 6.6(b), single ions can no longer be resolved, most probably due to a slight defocusing of the camera. Still, the huge amount of $^{229}Th^{3+}$ ions forming a 3D-crystal, which is again wrapped by a strontium crystal, is visible. Such crystal shapes indicate several hundred thorium ions and thus also a non-negligible number of nuclear isomers. Although the single ions cannot be resolved, ion crystals of this type can be useful for the measurement of the isomeric hyperfine structure of $^{229}Th^{3+}$.

A future experimental campaign to measure the isomeric ionic lifetime of $^{229}Th^{3+}$ will most probably have to use two-species crystals similar in size and thorium ion number to the crystal shown in Fig. 6.6(a). In order to monitor the decay of thorium isomers to the nuclear ground state, the ion position has to be resolved. Like this, isomeric decays due to ion loss or chemical reaction with residual gas particles can be detected and excluded from the measurement.

The EOM modulation scheme for the nuclear ground state of $^{229}Th^{3+}$ at 690 nm wavelength (see Tab. 3.1) in combination with a swept broadening to 3 GHz of the 984 nm repumping laser was applied as well. The measured fluorescence signals were of similar quality as the records done with both lasers continuously broadened to 3 GHz. A quantified scan of the individual EOM sidebands over the hyperfine resonances is still pending due to ongoing work towards a suitable hardware and software to control the frequency of the VCOs. This task remains for the near-future developments of the setup.

As also shown by Campbell et al. [171, 199] and Zitzer et al. [213], it was also tried to measure the complete hyperfine structure spectrum of $^{229}Th^{3+}$ at 690 nm. Since the LMU setup does not comprise a 1088 nm laser, the hyperfine mixing of the ground state levels has to be achieved by the 690 nm laser as well. So the fluorescence readout routine was modified as follows: In a first step, a 60 μW, low intensity 690 nm laser beam of narrow linewidth at a defined scan frequency is sent to the ions, whereas the repumping laser is blocked. Like this, a background image can be recorded. Then, both lasers are irradiating the ions frequency broadened to 3 GHz and at powers of 600 μW (690 nm) and 1000 μW (984 nm) to provide a uniform population of the hyperfine states. For this hyperfine-mixing step, the repumper's central frequency is stabilized to 304 610 500 MHz and the red spectroscopy laser's central line is kept at the current scan frequency. In

the third and final step of the routine, the red laser is again switched to the low power setting with a narrow linewidth, the repumper is still frequency broadened, and another image is recorded with the EM-CCD camera. After subtracting the background, the differential image should contain the fluorescence signal at the defined scan frequency. Per scan step, the number of stacked differential images can be set.

Within the framework of this thesis, no meaningful hyperfine structure spectroscopy scan of $^{229}Th^{3+}$ could be measured so far. Probably, the chosen scheme was not suitable for efficient hyperfine mixing, and a 1088 nm laser could provide better results. Another possible reason for the absence of the resolved hyperfine spectrum could be the low number of samples per frequency scan step of only 100. For comparison, Zitzer et al. [213] had a sampling rate of 10 kHz for their fluorescence readout and averaged over 16 s for a single data point. Regarding the duration of at least 300 ms for a single iteration of the previously described readout routine, comparable sample numbers are unreachable for the current configuration of the LMU setup. If the signal-to-noise ratio of the thorium fluorescence cannot be significantly improved, the use of similar readout schemes, comprising a 1088 nm laser in combination with a fast fluorescence readout by a PMT, needs to be considered.

6.3 Fluorescence Lifetime of Trapped $^{229(m)}Th^{3+}$ Ions

Similar to the storage time measurements carried out with Doppler cooled $^{88}Sr^{+}$ ions in the cryogenic Paul trap, also the fluorescence lifetime of sympathetically cooled $^{229}Th^{3+}$ was examined.

The starting point of such a measurement was a two-species $^{88}Sr^{+}$-$^{229}Th^{3+}$ ion crystal comparable in size and thorium ion number to the crystals depicted in Fig. 6.6. For the monitoring of the fluorescence signal over several hours, the readout routine, also used for the generation of the two-color images, was applied. A fluorescence lifetime measurement corresponds then to an image stack of over 15000 differential images. The thorium spectroscopy lasers were operated with powers of 600 μW (690 nm) and 1000 μW (984 nm) and were both frequency broadened. For the red laser, the EOM modulation scheme presented in Tab. 3.1 was applied, and the repumper was operated again with a swept EOM modulation frequency as already described above.

To extract the signal height of a single differential measurement, the differences of consecutive measurements were calculated and put in relation to the timing of the measurement. The low fluorescence signal height is once more reflected by the rather noisy raw data distribution in Fig. 6.7. For a better visualization of the general trend, the experimental data were also filtered with a moving average and approximated with an exponential fit function. The time constant of the fit is $\tau = 8422(1590)$ s, which corresponds to a fluorescence half-life of the trapped $^{229}Th^{3+}$ ions of $t_{1/2} = 5838(1102)$ s. Noteworthy to remind: the vast majority of the trapped Th ions will be in the ground state, therefore, this decay constant is not reflecting in whatever way the isomeric lifetime but rather gives an indication of the achievable storage time of $^{229}Th^{3+}$ in a Coulomb crystal configuration realized in the cryogenic Paul trap at LMU.

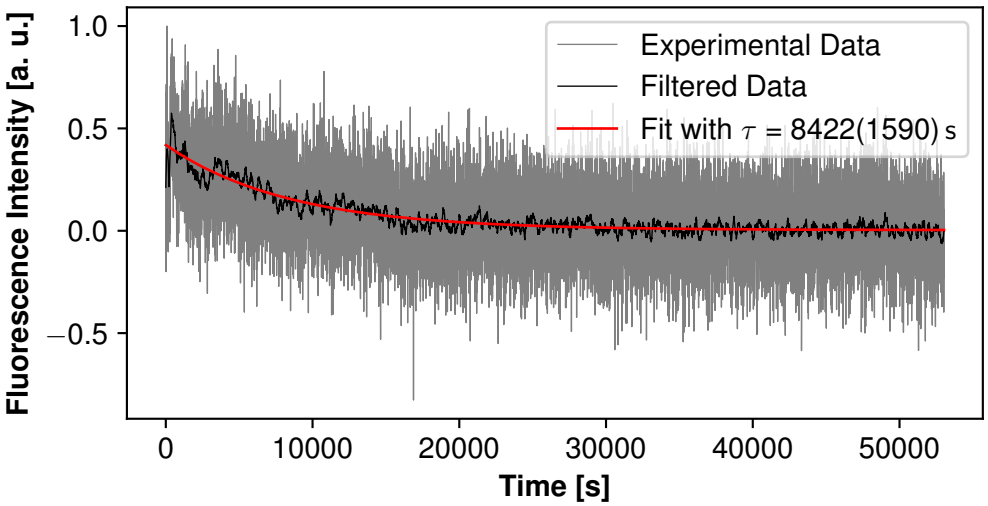

Figure 6.7 690 nm *fluorescence intensity of a* $^{229}Th^{3+}$ *Coulomb crystal containing around 100 ions, normalized to the maximum. Each data point is the integral over a differential image with* 1.0 s *integration time for the background and the signal image. For better visualization, the experimental data were filtered with a moving average (black). The exponential fit curve applied to the experimental data is shown in red.*

This very preliminary result also implies that any experiment with the trapped thorium ions has to be performed within a time of 1.5 h to 2 h before the majority of the $^{229}Th^{3+}$ ions is no longer available. The limitation of the fluorescence lifetime can be explained by the high reactivity of Th^{3+} ions that are more sensitive to residual gas particles in the trap volume than Sr^{+}. This behavior has also been observed in another Paul-trap setup with sympathetically cooled $^{229}Th^{3+}$ [270]. In view of the current (only published) value of 1400^{+600}_{-300} s for the ionic isomeric half-life (determined in a trap environment, however, in the presence of a buffer-gas residual gas component), the achieved fluorescence lifetimes in the LMU setup should be more than sufficient to perform experiments involving the isomeric state.

It was also tried to extract the isomeric half-life of $^{229}Th^{3+}$ from similar measurements by using the dedicated isomeric EOM modulation scheme (see also Tab. 3.1). Although a fluorescence signal was visible, the long fluorescence lifetimes excluded an isomeric decay and only indicated an off-resonant excitation of the nuclear ground state hyperfine sublevels.

7 Conclusion and Outlook

The main goal of this work was the preparation of the cryogenic Paul-trap setup at LMU Munich for the confinement and sympathetic cooling of $^{229}Th^{3+}$ ions with co-trapped $^{88}Sr^{+}$ ions to create thorium Coulomb crystals. Furthermore, the developments of the setup had to be tested and characterized to acquire a profound knowledge of the thorium trapping behavior and the measurement performance.

Starting in 2020, the vacuum and ion-optical setup was already assembled and to a large extent operational. The quadrupole-mass-separators of the setup were already characterized, and the control software for the ion optics was in operation [223]. However, the complete laser setup for $^{88}Sr^{+}$ Doppler cooling and the spectroscopy of $^{229}Th^{3+}$ was designed and built from scratch as a main part of this thesis. Especially, the search for a suitable strontium ion source turned out to be not as straightforward as initially expected, but was sorted out with the setup of the laser ablation from a solid-state target.

In order to achieve sufficient radial confinement and actual trapping of the ablated $^{88}Sr^{+}$ ions as well as of the extracted $^{229}Th^{3+}$ ions in the cryogenic environment, the RF electronics of the trap electrodes had to be modified. Like this, the RF resonance frequency was increased from around 400 kHz to around 2 MHz and higher amplitudes of up to 800 Vpp were reached.

The experiments performed within the framework of this thesis could give a detailed insight into the capabilities of the strontium ablation source and also provide a range of optimum working parameters for strontium trapping. After now more than three years of continuous operation with the same ablation target, this part of the setup can indeed be considered as a workhorse and reliable basis for $^{229}Th^{3+}$ spectroscopy experiments.

Also, the well-established method of strontium Doppler cooling could be implemented for the LMU cryogenic linear Paul trap. The confinement and Doppler cooling to mK temperatures of a single ion or up to several thousand $^{88}Sr^{+}$ ions was demonstrated together with the control of the created Coulomb crystal shapes.

As a next crucial step, the *Buffer-Gas Stopping Cell* based on a LMU design [229] was put into operation and used to demonstrate the extraction of $^{229(m)}Th^{3+}$ and the implantation into a $^{88}Sr^{+}$ Coulomb crystal. Also here, the size and shape of the crystals can be controlled and tuned according to the requirements of the experiment. For the excitation of the hyperfine levels in $^{229}Th^{3+}$, frequency broadened laser light at

690 nm and 984 nm was used in a similar manner as applied in other experiments with trapped thorium ions [213, 252]. In addition, a scheme for the modulation of EOMs was developed, dedicated to separately address the hyperfine sublevels of $^{229}Th^{3+}$ either in the nuclear ground state or in the excited isomeric state.

Regarding the detection of the thorium ion fluorescence, the readout at the 690 nm wavelength turned out to be superior to the readout at 984 nm, in contrast to earlier experiments [171, 199]. Fluorescence lifetime measurements of $^{229}Th^{3+}$ proved the capability of the setup to store the ions for a longer period than the expected isomeric lifetime of around 2000 s [13].

In a wider objective, this work also comprises first exploratory investigations towards a precision measurement of the ionic isomeric half-life of $^{229}Th^{3+}$ in competition with the measurement performed with buffer-gas cooled thorium ions in 2024 by Yamaguchi et al. [13]. It has to be mentioned, though, that the signal-to-noise ratio of the measured thorium fluorescence is very low, and the used detection scheme could not overcome this limit. These restrictions in the fluorescence readout efficiency were mainly the reason for the so far unsuccessful attempts to retrieve the resolved hyperfine spectrum of Doppler cooled $^{229}Th^{3+}$. Up to now, the approach to address the isomeric state with a dedicated EOM modulation scheme could not deliver any conclusive results. Considering the large uncertainties in the calculated isomeric hyperfine transitions, a manual scan of the multiple VCO frequency generators for EOM modulation apparently was not effective enough for the search of the actual isomeric spectrum. Therefore, a PC-controlled, multi-dimensional frequency scan is already being prepared and might help to find an improved EOM modulation scheme tailored for the isomeric state.

So, the task remains for future experiments undertaken with the cryogenic Paul trap at LMU to detect the isomeric state in $^{229}Th^{3+}$ and to determine its full resolved hyperfine spectrum. The latter would provide the foundation for a precise measurement of the ionic isomeric lifetime.

A possible way to improve the signal-to-noise ratio of the thorium fluorescence and also the sampling rate of the fluorescence readout is given in [171, 199, 213, 252] and comprises the implementation of an additional 1088 nm laser for an improved hyperfine mixing of the ground state sublevels. Also, using a PMT, optimized for the 690 nm wavelength, could accelerate the fluorescence readout process and enhance the signal.

A significant improvement of the signal-to-noise ratio of either the strontium or the thorium fluorescence signal, could be achieved by modifying the Paul trap design. Replacing the cylindrical trap electrodes with more compact blade-type electrodes would increase the solid angle for photon collection. In addition, such a design would allow higher RF resonance frequencies together with an enhanced ion confinement.

In the long run, it has to be also considered to update the stabilization scheme of the lasers, which is limited in accuracy and stability, especially for the 1090 nm, 690 nm, and 984 nm wavelengths due to the wavelength meter in use. These limits could be overcome either by a hardware update or the use of a more stable calibration source for the wavelength meter. Schemes for ultimate improvement involving the $^{88}Sr^{+}$ clock

transition at 674 nm [271, 272] in combination with an ultra-broadband frequency comb are also under discussion.

Another hardware-related topic to be mentioned for possible improvement is the RF drive circuit of the trap electrodes, which still requires some minor revisions to decrease the switching times of the trap's DC voltages and to exploit the full potential of the switching modules. So, it might be helpful to change the capacitor and resistor dimensions on the RF-DC mixer board to half of the current values.

On the software side, the whole process from the strontium ablation via the loading of the trap until the implantation of the thorium ions requires additional automation, especially for the envisaged isomeric lifetime measurements.

Apart from the measurement of the isomeric hyperfine structure or the isomeric lifetime, further experiments using the cryogenic Paul-trap setup at LMU are planned: In combination with a VUV laser source, the trap with the confined and Doppler cooled $^{229}Th^{3+}$ ions will be the platform for the direct laser excitation of the isomeric state in $^{229}Th^{3+}$ ions. Like that, the aim for the trap-based approach of the nuclear clock with unperturbed, ionic $^{229m}Th^{3+}$ could be further pursued.

In conclusion, this work made the cryogenic Paul-trap setup at LMU operational, demonstrated the trapping and sympathetic cooling of $^{229}Th^{3+}$ ions with laser-cooled $^{88}Sr^{+}$ ions, showed the fluorescence readout at 690 nm of trapped $^{229}Th^{3+}$ ions, and paved the way for upcoming high-precision laser spectroscopy measurements of unperturbed $^{229(m)}Th^{3+}$ ions at mK temperatures.

Appendices

A HFS Calculations

Table A.1 *Results by Campbell et al. [171, 199] and Zitzer et al. [213] for the hyperfine splitting of the three energy levels in $^{229}Th^{3+}$. The results in the left column taken from [171] represent the basis for the fitting to extract the hyperfine constants. Values listed in the central and right column are calculated with the experimentally determined hyperfine constants given by [171, 199] and [213] and Eq. (2.47).*

F	[171]	[171, 199]	[213]
	ν[MHz]	ν[MHz]	ν[MHz]
Hyperfine Splitting of $6D_{5/2}$			
0	1996.3(78)	1996.1(78)	1999.4(29)
1	1337.1(63)	1336.9(63)	1339.7(25)
2	261.3(41)	261.0(41)	262.8(17)
3	−746.4(28)	−746.6(28)	−746.1(14)
4	−958.6(26)	−958.7(26)	−959.4(08)
5	594.4(47)	594.8(47)	593.1(19)
Hyperfine Splitting of $5F_{5/2}$			
0	868.9(67)	869.1(67)	871.7(22)
1	406.6(54)	406.7(54)	408.8(18)
2	−313.9(35)	−313.8(35)	−312.6(12)
3	−884.1(24)	−884.1(24)	−883.9(08)
4	−691.4(22)	−691.4(22)	−692.1(07)
5	1081.1(40)	1081.0(40)	1080.1(13)
Hyperfine Splitting of $5F_{7/2}$			
1	1012.5(102)	1012.8(102)	
2	346.8(71)	347.1(71)	
3	−378.6(45)	−378.4(45)	
4	−835.7(39)	−835.7(39)	
5	−587.5(37)	−587.6(37)	
6	912.5(68)	912.3(68)	

Table A.2 *Results by Campbell et al. [171, 199] for the HFS transitions in $^{229}Th^{3+}$ at 690 nm in comparison with experimental results found in [213]. The values listed in the left column are directly based on the measured transition frequencies published in [171]. The values in the central and right column, on the other hand, are based on hyperfine splitting calculations with the hyperfine constants published in [171, 199] and [213], respectively. F is the quantum number of the lower state, F' the quantum number of the upper state, ν is the transition frequency with respect to the central resonance ν_0. The frequency uncertainty is given as Gaussian error, $\Delta_2\nu$ is the minimum and maximum frequency uncertainty, and S_{rel} is the relative transition intensity.*

F	F'	[171]		[171, 199]		[213]		S_{rel} [%]
		ν [MHz]	$\Delta_2\nu$	ν [MHz]	$\Delta_2\nu$	ν [MHz]	$\Delta_2\nu$	
$5F_{5/2} \rightarrow 6D_{5/2}$; $\nu_0 = 434\,280\,888(31)$ MHz								
0	0	1127.4(103)	$^{14.5}_{1.1}$	1127.0(103)	$^{20.5}_{0.2}$	1127.7(36)	$^{7.0}_{0.8}$	0.0
0	1	468.2(92)	$^{13.0}_{0.4}$	467.8(92)	$^{18.1}_{1.2}$	468.0(33)	$^{6.2}_{1.0}$	2.8
1	0	1589.7(95)	$^{13.2}_{2.4}$	1589.4(95)	$^{18.4}_{0.7}$	1590.5(34)	$^{6.3}_{0.6}$	2.8
1	1	930.5(83)	$^{11.7}_{0.9}$	930.2(83)	$^{16.1}_{0.3}$	930.8(30)	$^{5.6}_{0.7}$	0.5
1	2	−145.3(68)	$^{9.5}_{1.3}$	−145.7(68)	$^{11.9}_{1.7}$	−146.0(25)	$^{4.2}_{0.9}$	5.1
2	1	1651.0(72)	$^{9.8}_{2.8}$	1650.7(72)	$^{12.5}_{0.8}$	1652.3(27)	$^{4.5}_{0.4}$	5.1
2	2	575.2(54)	$^{7.6}_{0.6}$	574.9(53)	$^{8.4}_{0.5}$	575.4(21)	$^{3.1}_{0.6}$	2.4
2	3	−432.5(45)	$^{6.3}_{0.7}$	−432.8(45)	$^{7.8}_{2.9}$	−433.5(15)	$^{2.7}_{0.8}$	6.4
3	2	1145.4(48)	$^{6.5}_{1.7}$	1145.1(47)	$^{7.9}_{3.4}$	1146.7(19)	$^{2.9}_{1.6}$	6.4
3	3	137.7(37)	$^{5.2}_{0.4}$	137.4(37)	$^{7.3}_{0.0}$	137.8(12)	$^{2.4}_{0.2}$	6.7
3	4	−74.5(35)	$^{5.0}_{0.2}$	−74.6(35)	$^{6.7}_{1.5}$	−75.5(11)	$^{2.1}_{0.3}$	6.3
4	3	−55.0(36)	$^{5.0}_{0.6}$	−55.2(36)	$^{6.8}_{1.2}$	−54.0(12)	$^{2.3}_{0.1}$	6.3
4	4	−267.2(34)	$^{4.8}_{0.4}$	−267.3(34)	$^{6.2}_{0.2}$	−267.3(10)	$^{1.9}_{0.1}$	14.3
4	5	1285.8(52)	$^{6.9}_{2.5}$	1286.2(52)	$^{9.0}_{1.3}$	1285.2(20)	$^{3.2}_{1.0}$	4.4
5	4	−2039.7(48)	$^{6.6}_{1.4}$	−2039.7(48)	$^{8.6}_{0.7}$	−2039.4(15)	$^{2.7}_{0.5}$	4.4
5	5	−486.7(62)	$^{8.7}_{0.7}$	−486.3(62)	$^{11.4}_{0.4}$	−487.0(23)	$^{4.1}_{0.6}$	26.2

Table A.3 *Results by Campbell et al. [171, 199] for the HFS transitions in $^{229}Th^{3+}$ at* 984 nm. *The values listed in the left column are directly based on the measured transition frequencies published in [171]. The values in the right column are based on hyperfine splitting calculations with the hyperfine constants published in [171, 199]. F is the quantum number of the lower state, F' the quantum number of the upper state, ν is the transition frequency with respect to the central resonance ν_0. The frequency uncertainty is given as Gaussian error, $\Delta_2\nu$ is the minimum and maximum frequency uncertainty, and S_{rel} is the relative transition intensity.*

F	F'	[171]		[171, 199]		S_{rel} [%]
		ν [MHz]	$\Delta_2\nu$	ν [MHz]	$\Delta_2\nu$	
$5F_{7/2} \rightarrow 6D_{5/2}$; $\nu_0 = 304\,609\,454(31)$ MHz						
1	0	983.8(128)	$^{18.0}_{2.4}$	983.2(128)	$^{25.3}_{0.2}$	2.8
1	1	324.6(120)	$^{16.5}_{3.9}$	324.1(120)	$^{22.9}_{0.8}$	3.0
1	2	−751.2(110)	$^{14.3}_{6.1}$	−751.8(109)	$^{18.8}_{2.1}$	0.5
2	1	990.3(95)	$^{13.4}_{0.8}$	989.8(95)	$^{18.1}_{1.3}$	5.4
2	2	−85.5(82)	$^{11.2}_{3.0}$	−86.0(82)	$^{14.0}_{0.1}$	4.5
2	3	−1093.2(76)	$^{9.9}_{4.3}$	−1093.7(77)	$^{13.4}_{3.4}$	0.6
3	2	639.9(61)	$^{8.6}_{0.4}$	639.4(60)	$^{9.7}_{0.0}$	8.9
3	3	−367.8(53)	$^{7.3}_{1.7}$	−368.2(53)	$^{9.2}_{3.4}$	5.2
3	4	−580.0(52)	$^{7.1}_{1.9}$	−580.3(52)	$^{8.6}_{1.9}$	0.4
4	3	89.3(48)	$^{6.7}_{1.1}$	89.0(48)	$^{9.1}_{1.9}$	13.6
4	4	−122.9(47)	$^{6.5}_{1.3}$	−123.0(47)	$^{8.5}_{0.4}$	4.9
4	5	1430.1(61)	$^{8.6}_{0.8}$	1430.4(61)	$^{11.3}_{0.6}$	0.2
5	4	−371.1(45)	$^{6.3}_{1.1}$	−371.1(45)	$^{8.4}_{0.3}$	19.6
5	5	1181.9(60)	$^{8.4}_{1.0}$	1182.3(60)	$^{11.2}_{1.4}$	3.3
6	5	−318.1(82)	$^{11.5}_{2.1}$	−317.5(83)	$^{15.3}_{0.5}$	27.1

B SIMION Simulation Model

B.1 Model Geometry

Geometry file (.gem) to generate the model of the ion guiding components from the de Laval nozzle to the ion detection plane after *QMS 1* in SIMION.

```
; Ions fly in z-direction

;define box for SIMION 8.1
pa_define(85,85,8000,planar,xy,E,0.2, 0.2, 0.2)
;define box for SIMION 8.0
;pa_define(17,17,1600,planar,xy,E,1, 1, 1)


# local ref = 1
;for a finer grid size in x and y direction define a higher ref
; all data are given in mm/ref
# local MCP_r_outer = 31.5
; outer radius of the -2000V electrode clamping the MCP plates on the lower grounded electrode
# local MCP_r_inner = 15
; inner radius of the -2000V electrode clamping the MCP plates on the lower grounded electrode
#local MCP_t = 3
; thickness of the MCP electrode
#local QMS1_entrance_t = 2
; thickness of the MQS1 entrance aperture
#local QMS1_entrance_r = 1.5
; radius of the QMS1 entrance aperture
# local QMS_rod_r = 9*ref
;rod radius of the QMS rods
# local QMS_ion_rod_d = (24.013/sqrt(2))*ref
; distance from ion axis to center of QMS rod
# local Brubaker_l = 50*ref
;length of the Bruaker lenses
; distances between the Brubaker lenses and the QMS rods are 1 mm
# local QMS_l = 300*ref
;length of the QMS
; distance between the Brubaker lens and the QMS1 exit aperture is 1 mm
# local QMS1_exit_r = 2.5*ref
;radius of the QMS1 exit aperture. The size of the electrode can than be chosen arbitrarily.
# local QMS1_exit_t = 1*ref
;thickness of the QMS1 exit aperture
; distance between the QMS1 exit aperture and the 40 K aperture is 2 mm
# local FortyK_r = 2.5*ref
# local FortyK_t = 2*ref
;radius of the 40 K apertures to the trap region
# local FortyK_s = 30*ref
;radius of the whole electrode plate
; distance between the 40K and the 4 K electrode is 2 mm
# local FourK_r = 2.5*ref
;radius of the 4K apertures to the trap region
# local FourK_s = 20*ref
;radius of the whole electrode
# local FourK_t = 1*ref
; thickness of the 4 K electrode
; distance between the 4K electrode and the trap rods is 2 mm
# local Trap_rod_r = 5.5*ref
;radius of the Paul trap rods.
# local Trap_ion_rod_d= (14.566/sqrt(2))*ref
;distance from ion axis to center of Trap rod
; define the different rod lengths. The order of the different segments is rodl3, rodl1,
; rodl2, rodl1, rodl2, rodl1, rodl3. The segments have a 2 mm distance between each other.
# local Trap_rod_l1 = 8*ref
```

```
# local Trap_rod_l2 = 30*ref
# local Trap_rod_l3 = 93*ref


;distance between QMS2 and the exit aperture of the QMS 2 is 1 mm
#local QMS2_Entrance_r = 2.5*ref
;radius of the QMS2 entrance aperture
#local QMS2_Entrance_t = 1*ref
; thickness of the QMS2 entrance aperture
#local QMS2_Entrance_s =30*ref
; radius of the whole QMS2 Entrance aperture (actually 40 mm)
; distance between the QMS2 entrance aperture and the Ion Guide is 1 mm
# local IonGuide_r = 5.5*ref
; radious of the Ion Guide electrodes
# local IonGuide_l = 269*ref
; length of the Ion Guide electrodes
; distance between the Ion Guide and the RFQ endcap is 1 mm
# local RFQ_Endcap_r = 1*ref
; radius of the extraction RFQ endcap aperture
# local RFQ_Endcap_t = 1*ref
; thickness of the extraction RFQ endcap aperture
# local RFQ_Endcap_s = 30*ref
; radius of the whole electrode (actually 35)
; distance between the extraction RFQ endcap and the last RFQ segment is 1 mm
# local RFQ_rod_r = 5.5*ref
; radius of the extraction RFQ rods
# local RFQ_ion_rod_d= (15/sqrt(2))*ref
; distance from ion axis to center of Extraction RFQ rod
# local RFQ_rod_l1 = 28*ref
# local RFQ_rod_l2 = 23*ref
#local RFQ_rod_l3 = 11.5*ref
#local RFQ_rod_l4 = 24*ref
; distance between the Extraction RFQ segments is 1 mm. There are in total 8 segments:
; 5 x l1 , 2 x l2 , 1 x l1
; distance between the first Extraction RFQ segment and the nozzle is 1.5 mm
# local Nozzle_l1 = 8.2 *ref
;Nozzle consists of three parts. Two tapered cylinders and a normal one in between
# local Nozzle_r1 = 3 * ref
; radius of opening to RFQ
# local Nozzle_r2 = 0.2*ref
; radius of the inner cylinder
# local Nozzle_l2 = 0.3 * ref
; length of the inner straight cylinder
# local Nozzle_r3 = 1*ref
;radius of the opening to the buffer gas cell
# local Nozzle_l3 = 0.8*ref
;length of the second tapered cylinder

# local d1 = 1*ref
;corresponds to a distance of 1 mm
# local d2 = 2*ref
; corresponds to a distance of 2mm
# local d3 = 10.2
; distance between the MCP and the QMS1 entrance

; Starting Point is the MCP at the exit of the QMS1 exit

; position the first Brubaker lens of QMS 1


locate (0,0,$(5),1,0,0,0)
{

        electrode(1){

                fill{
                        within{cylinder($(0), $(0), $(MCP_t), $(MCP_r_outer), $(MCP_r_outer), $(MCP_t))}
                        notin{cylinder($(0), $(0), $(MCP_t), $(MCP_r_inner), $(MCP_r_inner), $(2))}
                }
        }
}

locate (0,0,$(5 + MCP_t + d3),1,0,0,0)
{

        electrode(2){

                fill{
                        within{cylinder($(0), $(0), $(QMS1_entrance_t), $(90), $(90), $(QMS1_entrance_t))}
                        notin{cylinder($(0), $(0), $(QMS1_entrance_t), $(QMS1_entrance_r), $(QMS1_entrance_r),
                                $(QMS1_entrance_t))}
                }
        }
```

```
}

locate(0,0,$(5 + MCP_t + d3 + QMS1_entrance_t + d1),1,0,0,0)
{



        electrode(3){

                fill{
                        within{cylinder($(QMS_ion_rod_d), 0, $(Brubaker_l), $(QMS_rod_r), $(QMS_rod_r),
                                $(Brubaker_l))}
                }

        }
        electrode(4){

                fill{
                        within{cylinder(0, $(QMS_ion_rod_d), $(Brubaker_l), $(QMS_rod_r), $(QMS_rod_r),
                                $(Brubaker_l))}
                }

        }

}

; position the QMS of QMS1

locate(0,0,$(5 + MCP_t + d3 + QMS1_entrance_t + d1 + Brubaker_l + d1),1,0,0,0)
{



        electrode(5){

                fill{
                        within{cylinder($(QMS_ion_rod_d), 0, $(QMS_l), $(QMS_rod_r), $(QMS_rod_r), $(QMS_l))}
                }

        }
        electrode(6){

                fill{
                        within{cylinder(0, $(QMS_ion_rod_d), $(QMS_l), $(QMS_rod_r), $(QMS_rod_r), $(QMS_l))}
                }

        }


}

; position the second Brubaker lens of QMS 1

locate(0,0,$(5 + MCP_t + d3 + QMS1_entrance_t + d1 + Brubaker_l + QMS_l + 2*d1),1,0,0,0)
{



        electrode(7){

                fill{
                        within{cylinder($(QMS_ion_rod_d), 0, $(Brubaker_l), $(QMS_rod_r), $(QMS_rod_r),
                                $(Brubaker_l))}
                }

        }

        electrode(8){

                fill{
                        within{cylinder(0, $(QMS_ion_rod_d), $(Brubaker_l), $(QMS_rod_r), $(QMS_rod_r),
                                $(Brubaker_l))}
                }

        }


}

; position the QMS 1 exit aperture

locate(0,0,$(5 + MCP_t + d3 + QMS1_entrance_t + d1 + Brubaker_l + QMS_l + Brubaker_l +
3*d1),1,0,0,0)
```

```
{



        electrode(9){

                fill{
                        within{cylinder($(0), $(0), $(QMS1_exit_t), $(90), $(90), $(QMS1_exit_t))}
                        notin{cylinder($(0), $(0), $(QMS1_exit_t), $(QMS1_exit_r), $(QMS1_exit_r),
                                $(QMS1_exit_t))}
                }
        }

}

; position the 40 K shield aperture

locate(0,0,$(5 + MCP_t + d3 + QMS1_entrance_t + d1 + Brubaker_l + QMS_l + Brubaker_l +
QMS1_exit_t + 3*d1 + d2), 1,0,0,0)
{



        electrode(10){

                fill{
                        within{cylinder($(0), $(0), $(FortyK_t), $(90), $(90), $(FortyK_t))}
                        notin{cylinder($(0), $(0), $(FortyK_t), $(FortyK_r), $(FortyK_r), $(FortyK_t))}
                }
        }

}

; position the 4 K shield aperture

locate(0,0,$(5 + MCP_t + d3 + QMS1_entrance_t + d1 + Brubaker_l + QMS_l + Brubaker_l +
QMS1_exit_t  + FortyK_t + 3*d1 + 2*d2),1,0,0,0)
{



        electrode(11){

                fill{
                        within{cylinder($(0), $(0), $(FourK_t), $(90), $(90), $(FourK_t))}
                        notin{cylinder($(0), $(0), $(FourK_t), $(FourK_r), $(FourK_r), $(FourK_t))}
                }
        }

}

; position the Trap segment 1

locate(0,0,$(5 + MCP_t + d3 + QMS1_entrance_t + d1 + Brubaker_l + QMS_l + Brubaker_l +
QMS1_exit_t + FortyK_t + FourK_t + 3*d1 + 3*d2),1,0,0,0)
{



        electrode(12){

                fill{
                        within{cylinder($(Trap_ion_rod_d), 0, $(Trap_rod_l3), $(Trap_rod_r), $(Trap_rod_r),
                                $(Trap_rod_l3))}
                }

        }
        electrode(13){

                fill{
                        within{cylinder(0, $(Trap_ion_rod_d), $(Trap_rod_l3), $(Trap_rod_r), $(Trap_rod_r),
                                $(Trap_rod_l3))}
                }

        }

}

; position the Trap segment 2

locate(0,0,$(5 + MCP_t + d3 + QMS1_entrance_t + d1 + Brubaker_l + QMS_l + Brubaker_l +
QMS1_exit_t + FortyK_t + FourK_t + Trap_rod_l3 + 3*d1 + 4*d2),1,0,0,0)
{
```

```
        electrode(14){

                fill{
                        within{cylinder($(Trap_ion_rod_d), 0, $(Trap_rod_l1), $(Trap_rod_r), $(Trap_rod_r),
                                $(Trap_rod_l1))}
                }

        }
        electrode(15){

                fill{
                        within{cylinder(0, $(Trap_ion_rod_d), $(Trap_rod_l1), $(Trap_rod_r), $(Trap_rod_r),
                                $(Trap_rod_l1))}
                }

        }

}

; position the Trap segment 3

locate(0,0,$(5 + MCP_t + d3 + QMS1_entrance_t + d1 + Brubaker_l + QMS_l + Brubaker_l +
QMS1_exit_t + FortyK_t + FourK_t + Trap_rod_l3 + Trap_rod_l1 + 3*d1 + 5*d2),1,0,0,0)
{



        electrode(16){

                fill{
                        within{cylinder($(Trap_ion_rod_d), 0, $(Trap_rod_l2), $(Trap_rod_r), $(Trap_rod_r),
                                $(Trap_rod_l2))}
                }

        }
        electrode(17){

                fill{
                        within{cylinder(0, $(Trap_ion_rod_d), $(Trap_rod_l2), $(Trap_rod_r), $(Trap_rod_r),
                                $(Trap_rod_l2))}
                }

        }

}

; position the Trap segment 4

locate(0,0,$(5 + MCP_t + d3 + QMS1_entrance_t + d1 + Brubaker_l + QMS_l + Brubaker_l +
QMS1_exit_t + FortyK_t + FourK_t + Trap_rod_l3 + Trap_rod_l1 + Trap_rod_l2 + 3*d1 +6*d2),1,0,0,0)
{



        electrode(18){

                fill{
                        within{cylinder($(Trap_ion_rod_d), 0, $(Trap_rod_l1), $(Trap_rod_r), $(Trap_rod_r),
                                $(Trap_rod_l1))}
                }

        }
        electrode(19){

                fill{
                        within{cylinder(0, $(Trap_ion_rod_d), $(Trap_rod_l1), $(Trap_rod_r), $(Trap_rod_r),
                                $(Trap_rod_l1))}
                }

        }

}

; position the Trap segment 5

locate(0,0,$(5 + MCP_t + d3 + QMS1_entrance_t + d1 + Brubaker_l + QMS_l + Brubaker_l +
QMS1_exit_t + FortyK_t + FourK_t + Trap_rod_l3 + Trap_rod_l1 + Trap_rod_l2 + Trap_rod_l1 +
3*d1 + 7*d2),1,0,0,0)
{
```

```
        electrode(20){

                fill{
                        within{cylinder($(Trap_ion_rod_d), 0, $(Trap_rod_l2), $(Trap_rod_r), $(Trap_rod_r),
                                $(Trap_rod_l2))}
                }

        }
        electrode(21){

                fill{
                        within{cylinder(0, $(Trap_ion_rod_d), $(Trap_rod_l2), $(Trap_rod_r), $(Trap_rod_r),
                                $(Trap_rod_l2))}
                }

        }

}

; position the Trap segment 6

locate(0,0,$(5 + MCP_t + d3 + QMS1_entrance_t + d1+ Brubaker_l + QMS_l + Brubaker_l +
QMS1_exit_t + FortyK_t + FourK_t+ Trap_rod_l3 + Trap_rod_l1 + Trap_rod_l2 + Trap_rod_l1 +
Trap_rod_l2 + 3*d1 + 8*d2),1,0,0,0)
{



        electrode(22){

                fill{
                        within{cylinder($(Trap_ion_rod_d), 0, $(Trap_rod_l1), $(Trap_rod_r), $(Trap_rod_r),
                                $(Trap_rod_l1))}
                }

        }
        electrode(23){

                fill{
                        within{cylinder(0, $(Trap_ion_rod_d), $(Trap_rod_l1), $(Trap_rod_r), $(Trap_rod_r),
                                $(Trap_rod_l1))}
                }

        }

}

; position the Trap segment 7

locate(0,0,$(5 + MCP_t + d3 + QMS1_entrance_t + d1+ Brubaker_l + QMS_l + Brubaker_l +
QMS1_exit_t + FortyK_t + FourK_t + Trap_rod_l3 + Trap_rod_l1 + Trap_rod_l2 + Trap_rod_l1 +
Trap_rod_l2 + Trap_rod_l1 +3*d1 + 9*d2),1,0,0,0)
{



        electrode(24){

                fill{
                        within{cylinder($(Trap_ion_rod_d), 0, $(Trap_rod_l3), $(Trap_rod_r), $(Trap_rod_r),
                                $(Trap_rod_l3))}
                }

        }
        electrode(25){

                fill{
                        within{cylinder(0, $(Trap_ion_rod_d), $(Trap_rod_l3), $(Trap_rod_r), $(Trap_rod_r),
                                $(Trap_rod_l3))}
                }

        }

}

; position the second 4 K shield aperture

locate(0,0,$(5 + MCP_t + d3 + QMS1_entrance_t + d1+ Brubaker_l + QMS_l + Brubaker_l +
QMS1_exit_t + FortyK_t + FourK_t + Trap_rod_l3 + Trap_rod_l1 + Trap_rod_l2 + Trap_rod_l1 +
Trap_rod_l2 + Trap_rod_l1 + Trap_rod_l3 + 3*d1 + 10*d2),1,0,0,0)
{
```

```
        electrode(26){

                fill{
                        within{cylinder($(0), $(0), $(FourK_t), $(90), $(90), $(FourK_t))}
                        notin{cylinder($(0), $(0), $(FourK_t), $(FourK_r), $(FourK_r), $(FourK_t))}
                }
        }

}

; position the second 40 K shield aperture

locate(0,0,$(5 + MCP_t + d3 + QMS1_entrance_t + d1 + Brubaker_l + QMS_l + Brubaker_l +
QMS1_exit_t + FortyK_t + FourK_t + Trap_rod_l3 + Trap_rod_l1 + Trap_rod_l2 + Trap_rod_l1 +
Trap_rod_l2 + Trap_rod_l1 + Trap_rod_l3 + FourK_t + 3*d1 + 11*d2),1,0,0,0)
{



        electrode(27){

                fill{
                        within{cylinder($(0), $(0), $(FortyK_t), $(90), $(90), $(FortyK_t))}
                        notin{cylinder($(0), $(0), $(FortyK_t), $(FortyK_r), $(FortyK_r), $(FortyK_t))}
                }
        }

}

;position the QMS2 exit aperture
locate(0,0,$(5 + MCP_t + d3 + QMS1_entrance_t + d1 + Brubaker_l + QMS_l + Brubaker_l +
QMS1_exit_t + FortyK_t + FourK_t + Trap_rod_l3 + Trap_rod_l1 + Trap_rod_l2 + Trap_rod_l1 +
Trap_rod_l2 + Trap_rod_l1 + Trap_rod_l3 + FourK_t + FortyK_t + 3*d1+ 12 *d2), 1,0,0,0)
{



        electrode(28){

                fill{
                        within{cylinder($(0), $(0), $(QMS1_exit_t), $(90), $(90), $(QMS1_exit_t))}
                        notin{cylinder($(0), $(0), $(QMS1_exit_t), $(QMS1_exit_r), $(QMS1_exit_r),
                                $(QMS1_exit_t))}
                }
        }

}

; position the second Brubaker lens of QMS 2
locate(0,0,$(5 + MCP_t + d3 + QMS1_entrance_t + d1+ Brubaker_l + QMS_l + Brubaker_l +
QMS1_exit_t + FortyK_t + FourK_t + Trap_rod_l3 + Trap_rod_l1 + Trap_rod_l2 + Trap_rod_l1 +
Trap_rod_l2 + Trap_rod_l1 + Trap_rod_l3 + FourK_t + FortyK_t + QMS1_exit_t + 4*d1+12*d2),
1,0,0,0)
{



        electrode(29){

                fill{
                        within{cylinder($(QMS_ion_rod_d), 0, $(Brubaker_l), $(QMS_rod_r), $(QMS_rod_r),
                                $(Brubaker_l))}
                }

        }
        electrode(30){

                fill{
                        within{cylinder(0, $(QMS_ion_rod_d), $(Brubaker_l), $(QMS_rod_r), $(QMS_rod_r),
                                $(Brubaker_l))}
                }

        }

}

; position the QMS of QMS2

locate(0,0,$(5 + MCP_t + d3 + QMS1_entrance_t + d1 + Brubaker_l + QMS_l + Brubaker_l +
QMS1_exit_t + FortyK_t + FourK_t + Trap_rod_l3 + Trap_rod_l1 + Trap_rod_l2 + Trap_rod_l1 +
```

```
Trap_rod_l2 + Trap_rod_l1 + Trap_rod_l3 + FourK_t + FortyK_t + QMS1_exit_t + Brubaker_l +
5*d1 + 12*d2),1,0,0,0)
{



        electrode(31){

                fill{
                        within{cylinder($(QMS_ion_rod_d), 0, $(QMS_l), $(QMS_rod_r), $(QMS_rod_r), $(QMS_l))}
                }

        }
        electrode(32){

                fill{
                        within{cylinder(0, $(QMS_ion_rod_d), $(QMS_l), $(QMS_rod_r), $(QMS_rod_r), $(QMS_l))}
                }

        }


}

; position the first Brubaker lens of QMS 2

locate(0,0,$(5 + MCP_t + d3 + QMS1_entrance_t + d1+ Brubaker_l + QMS_l + Brubaker_l +
QMS1_exit_t + FortyK_t + FourK_t + Trap_rod_l3 + Trap_rod_l1 + Trap_rod_l2 + Trap_rod_l1 +
Trap_rod_l2 + Trap_rod_l1 + Trap_rod_l3 + FourK_t + FortyK_t + QMS1_exit_t + Brubaker_l +
QMS_l + 6*d1 + 12*d2),1,0,0,0)
{



        electrode(33){

                fill{
                        within{cylinder($(QMS_ion_rod_d), 0, $(Brubaker_l), $(QMS_rod_r), $(QMS_rod_r),
                                $(Brubaker_l))}
                }

        }
        electrode(34){

                fill{
                        within{cylinder(0, $(QMS_ion_rod_d), $(Brubaker_l), $(QMS_rod_r), $(QMS_rod_r),
                                $(Brubaker_l))}
                }

        }

}

; position of the QMS 2 Entrance aperture
locate(0,0,$(5 + MCP_t + d3 + QMS1_entrance_t + d1 + Brubaker_l + QMS_l + Brubaker_l +
QMS1_exit_t + FortyK_t + FourK_t + Trap_rod_l3 + Trap_rod_l1 + Trap_rod_l2 + Trap_rod_l1 +
Trap_rod_l2 + Trap_rod_l1 + Trap_rod_l3 + FourK_t + FortyK_t + QMS1_exit_t + Brubaker_l +
QMS_l + Brubaker_l + 7*d1 + 12*d2),1,0,0,0)
{



        electrode(35){

                fill{
                        within{cylinder($(0), $(0), $(QMS2_Entrance_t), $(90), $(90), $(QMS2_Entrance_t))}
                        notin{cylinder($(0), $(0), $(QMS2_Entrance_t), $(QMS2_Entrance_r), $(QMS2_Entrance_r),
                                $(QMS2_Entrance_t))}
                }
        }

}

; position the Ion Guide
locate(0,0,$(5 + MCP_t + d3 + QMS1_entrance_t + d1 + Brubaker_l + QMS_l + Brubaker_l +
QMS1_exit_t + FortyK_t + FourK_t + Trap_rod_l3 + Trap_rod_l1 + Trap_rod_l2 + Trap_rod_l1 +
Trap_rod_l2 + Trap_rod_l1 + Trap_rod_l3 + FourK_t + FortyK_t + QMS1_exit_t + Brubaker_l +
QMS_l + Brubaker_l + 7*d1 + 12*d2 + QMS2_Entrance_t + d1),1,0,0,0)
{

        electrode(36){
                fill{
                        within{cylinder($(RFQ_ion_rod_d), 0, $(IonGuide_l), $(IonGuide_r), $(IonGuide_r),
```

```
                                $(IonGuide_l))}
                }

        }
        electrode(37){

                fill{
                        within{cylinder(0, $(RFQ_ion_rod_d), $(IonGuide_l), $(IonGuide_r), $(IonGuide_r),
                                $(IonGuide_l))}
                }

        }

}

; position of the Extraction RFQ exit aperture
locate(0,0,$(5 + MCP_t + d3 + QMS1_entrance_t + d1 + Brubaker_l + QMS_l + Brubaker_l +
QMS1_exit_t + FortyK_t + FourK_t + Trap_rod_l3 + Trap_rod_l1 + Trap_rod_l2 + Trap_rod_l1 +
Trap_rod_l2 + Trap_rod_l1 + Trap_rod_l3 + FourK_t + FortyK_t + QMS1_exit_t + Brubaker_l +
QMS_l + Brubaker_l + 7*d1 + 12*d2 + QMS2_Entrance_t + d1 + IonGuide_l + d1),1,0,0,0)
{

        electrode(38){

                fill{
                        within{cylinder($(0), $(0), $(RFQ_Endcap_t), $(90), $(90), $(RFQ_Endcap_t))}
                        notin{cylinder($(0), $(0), $(RFQ_Endcap_t), $(RFQ_Endcap_r), $(RFQ_Endcap_r),
                                $(RFQ_Endcap_t))}
                }
        }

}

; position Extraction RFQ Segment 8
locate(0,0,$(5 + MCP_t + d3 + QMS1_entrance_t + d1 + Brubaker_l + QMS_l + Brubaker_l +
QMS1_exit_t + FortyK_t + FourK_t + Trap_rod_l3 + Trap_rod_l1 + Trap_rod_l2 + Trap_rod_l1 +
Trap_rod_l2 + Trap_rod_l1 + Trap_rod_l3 + FourK_t + FortyK_t + QMS1_exit_t + Brubaker_l +
QMS_l + Brubaker_l + 7*d1 + 12*d2 + QMS2_Entrance_t + d1 + IonGuide_l + d1 + RFQ_Endcap_t
+ d1),1,0,0,0)
{

        electrode(39){
                fill{
                        within{cylinder($(RFQ_ion_rod_d), 0, $(RFQ_rod_l4), $(IonGuide_r), $(IonGuide_r),
                                $(RFQ_rod_l4))}
                }

        }
        electrode(40){

                fill{
                        within{cylinder(0, $(RFQ_ion_rod_d), $(RFQ_rod_l4), $(IonGuide_r), $(IonGuide_r),
                                $(RFQ_rod_l4))}
                }

        }

}

; position the Extraction RFQ Segment 7
locate(0,0,$(5 + MCP_t + d3 + QMS1_entrance_t + d1 + Brubaker_l + QMS_l + Brubaker_l +
QMS1_exit_t + FortyK_t + FourK_t + Trap_rod_l3 + Trap_rod_l1 + Trap_rod_l2 + Trap_rod_l1 +
Trap_rod_l2 + Trap_rod_l1 + Trap_rod_l3 + FourK_t + FortyK_t + QMS1_exit_t + Brubaker_l +
QMS_l + Brubaker_l + 7*d1 + 12*d2 + QMS2_Entrance_t + d1 + IonGuide_l + d1 + RFQ_Endcap_t
+ d1 + RFQ_rod_l4 + d1),1,0,0,0)
{

        electrode(41){

                fill{
                        within{cylinder($(RFQ_ion_rod_d), 0, $(RFQ_rod_l3), $(RFQ_rod_r), $(RFQ_rod_r),
                                $(RFQ_rod_l3))}
                }

        }
        electrode(42){

                fill{
                        within{cylinder(0, $(RFQ_ion_rod_d), $(RFQ_rod_l3), $(RFQ_rod_r), $(RFQ_rod_r),
                                $(RFQ_rod_l3))}
                }

        }
```

```
}

; position the Extraction RFQ Segment 6
locate(0,0,$(5 + MCP_t + d3 + QMS1_entrance_t + d1 + Brubaker_l + QMS_l + Brubaker_l +
QMS1_exit_t + FortyK_t + FourK_t + Trap_rod_l3 + Trap_rod_l1 + Trap_rod_l2 + Trap_rod_l1 +
Trap_rod_l2 + Trap_rod_l1 + Trap_rod_l3 + FourK_t + FortyK_t + QMS1_exit_t + Brubaker_l +
QMS_l + Brubaker_l + 7*d1 + 12*d2 + QMS2_Entrance_t + d1 + IonGuide_l + d1 + RFQ_Endcap_t
+ d1+RFQ_rod_l4 + d1 + RFQ_rod_l3 + d1),1,0,0,0)
{

        electrode(43){

                fill{
                        within{cylinder($(RFQ_ion_rod_d), 0, $(RFQ_rod_l3), $(RFQ_rod_r), $(RFQ_rod_r),
                                $(RFQ_rod_l3))}
                }

        }
        electrode(44){

                fill{
                        within{cylinder(0, $(RFQ_ion_rod_d), $(RFQ_rod_l3), $(RFQ_rod_r), $(RFQ_rod_r),
                                $(RFQ_rod_l3))}
                }

        }

}

; position the Extraction RFQ Segment 5
locate(0,0,$(5 + MCP_t + d3 + QMS1_entrance_t + d1 + Brubaker_l + QMS_l + Brubaker_l +
QMS1_exit_t + FortyK_t + FourK_t + Trap_rod_l3 + Trap_rod_l1 + Trap_rod_l2 + Trap_rod_l1 +
Trap_rod_l2 + Trap_rod_l1 + Trap_rod_l3 + FourK_t + FortyK_t + QMS1_exit_t + Brubaker_l +
QMS_l + Brubaker_l + 7*d1 + 12*d2 + QMS2_Entrance_t + d1 + IonGuide_l + d1 + RFQ_Endcap_t
+ d1 + RFQ_rod_l4 + d1 + RFQ_rod_l3 + d1 + RFQ_rod_l3 + d1),1,0,0,0)
{

        electrode(45){

                fill{
                        within{cylinder($(RFQ_ion_rod_d), 0, $(RFQ_rod_l2), $(RFQ_rod_r), $(RFQ_rod_r),
                                $(RFQ_rod_l2))}
                }

        }
        electrode(46){

                fill{
                        within{cylinder(0, $(RFQ_ion_rod_d), $(RFQ_rod_l2), $(RFQ_rod_r), $(RFQ_rod_r),
                                $(RFQ_rod_l2))}
                }

        }

}

; position the Extraction RFQ Segment 4
locate(0,0,$(5 + MCP_t + d3 + QMS1_entrance_t + d1 + Brubaker_l + QMS_l + Brubaker_l +
QMS1_exit_t + FortyK_t + FourK_t + Trap_rod_l3 + Trap_rod_l1 + Trap_rod_l2 + Trap_rod_l1 +
Trap_rod_l2 + Trap_rod_l1 + Trap_rod_l3 + FourK_t + FortyK_t + QMS1_exit_t + Brubaker_l +
QMS_l + Brubaker_l + 7*d1 + 12*d2 + QMS2_Entrance_t + d1 + IonGuide_l + d1 + RFQ_Endcap_t
+ d1+RFQ_rod_l4 + d1 + RFQ_rod_l3 + d1 + RFQ_rod_l3 + d1 + RFQ_rod_l2 + d1),1,0,0,0)
{

        electrode(47){

                fill{
                        within{cylinder($(RFQ_ion_rod_d), 0, $(RFQ_rod_l2), $(RFQ_rod_r), $(RFQ_rod_r),
                                $(RFQ_rod_l2))}
                }

        }
        electrode(48){

                fill{
                        within{cylinder(0, $(RFQ_ion_rod_d), $(RFQ_rod_l2), $(RFQ_rod_r), $(RFQ_rod_r),
                                $(RFQ_rod_l2))}
                }

        }

}
```

```
; position the Extraction RFQ Segment 3
locate(0,0,$(5 + MCP_t + d3 + QMS1_entrance_t + d1 + Brubaker_l + QMS_l + Brubaker_l +
QMS1_exit_t + FortyK_t + FourK_t + Trap_rod_l3 + Trap_rod_l1 + Trap_rod_l2 + Trap_rod_l1 +
Trap_rod_l2 + Trap_rod_l1 + Trap_rod_l3 + FourK_t + FortyK_t + QMS1_exit_t + Brubaker_l +
QMS_l + Brubaker_l + 7*d1 + 12*d2 + QMS2_Entrance_t + d1 + IonGuide_l + d1 + RFQ_Endcap_t
+ d1+RFQ_rod_l4 + d1 + RFQ_rod_l3 + d1 + RFQ_rod_l3 + d1 + RFQ_rod_l2 + d1 + RFQ_rod_l2 +
d1),1,0,0,0)
{

        electrode(49){

                fill{
                        within{cylinder($(RFQ_ion_rod_d), 0, $(RFQ_rod_l2), $(RFQ_rod_r), $(RFQ_rod_r),
                                $(RFQ_rod_l2))}
                }

        }
        electrode(50){

                fill{
                        within{cylinder(0, $(RFQ_ion_rod_d), $(RFQ_rod_l2), $(RFQ_rod_r), $(RFQ_rod_r),
                                $(RFQ_rod_l2))}
                }

        }

}

; position the Extraction RFQ Segment 2
locate(0,0,$(5 + MCP_t + d3 + QMS1_entrance_t + d1 + Brubaker_l + QMS_l + Brubaker_l +
QMS1_exit_t + FortyK_t + FourK_t + Trap_rod_l3 + Trap_rod_l1 + Trap_rod_l2 + Trap_rod_l1 +
Trap_rod_l2 + Trap_rod_l1 + Trap_rod_l3 + FourK_t + FortyK_t + QMS1_exit_t + Brubaker_l +
QMS_l + Brubaker_l + 7*d1 + 12*d2 + QMS2_Entrance_t + d1 + IonGuide_l + d1 + RFQ_Endcap_t
+ d1 + RFQ_rod_l4 + d1+ RFQ_rod_l3 + d1+ RFQ_rod_l3 + d1 + RFQ_rod_l2 + d1+ RFQ_rod_l2 +
d1 + RFQ_rod_l2 + d1),1,0,0,0)
{

        electrode(51){

                fill{
                        within{cylinder($(RFQ_ion_rod_d), 0, $(RFQ_rod_l2), $(RFQ_rod_r),
                                $(RFQ_rod_r), $(RFQ_rod_l2))}
                }

        }
        electrode(52){

                fill{
                        within{cylinder(0, $(RFQ_ion_rod_d), $(RFQ_rod_l2), $(RFQ_rod_r), $(RFQ_rod_r),
                                $(RFQ_rod_l2))}
                }

        }

}

; position the Extraction RFQ Segment 1
locate(0,0,$(5 + MCP_t + d3 + QMS1_entrance_t + d1 + Brubaker_l + QMS_l + Brubaker_l +
QMS1_exit_t + FortyK_t + FourK_t + Trap_rod_l3 + Trap_rod_l1 + Trap_rod_l2 + Trap_rod_l1 +
Trap_rod_l2 + Trap_rod_l1 + Trap_rod_l3 + FourK_t + FortyK_t + QMS1_exit_t + Brubaker_l +
QMS_l + Brubaker_l + 7*d1 + 12*d2 + QMS2_Entrance_t + d1 + IonGuide_l + d1 + RFQ_Endcap_t
+ d1+RFQ_rod_l4 + d1 + RFQ_rod_l3 + d1 + RFQ_rod_l3 + d1 + RFQ_rod_l2 + d1 + RFQ_rod_l2 +
d1 + RFQ_rod_l2 + d1 + RFQ_rod_l2 + d1 ),1,0,0,0)
{

        electrode(53){

                fill{
                        within{cylinder($(RFQ_ion_rod_d), 0, $(RFQ_rod_l1), $(RFQ_rod_r), $(RFQ_rod_r),
                                $(RFQ_rod_l1))}
                }

        }
        electrode(54){

                fill{
                        within{cylinder(0, $(RFQ_ion_rod_d), $(RFQ_rod_l1), $(RFQ_rod_r), $(RFQ_rod_r),
                                $(RFQ_rod_l1))}
                }

        }
```

```
}

; position of the Nozzle
locate(0,0,$(5 + MCP_t + d3 + QMS1_entrance_t + d1 + Brubaker_l + QMS_l + Brubaker_l +
QMS1_exit_t + FortyK_t + FourK_t + Trap_rod_l3 + Trap_rod_l1 + Trap_rod_l2 + Trap_rod_l1 +
Trap_rod_l2 + Trap_rod_l1 + Trap_rod_l3 + FourK_t + FortyK_t + QMS1_exit_t + Brubaker_l +
QMS_l + Brubaker_l + 7*d1 + 12*d2 + QMS2_Entrance_t + d1 + IonGuide_l + d1 + RFQ_Endcap_t
+ d1+RFQ_rod_l4 + d1 + RFQ_rod_l3 + d1 + RFQ_rod_l3 + d1 + RFQ_rod_l2 + d1 + RFQ_rod_l2 +
d1 + RFQ_rod_l2 + d1 + RFQ_rod_l2 + d1 + RFQ_rod_l1 + 1.5*ref),1,0,0,0)
{

        electrode(55){
                fill{
                        within{cylinder($(0), $(0), $(9.3*ref), $(90), $(90), $(9.3*ref))}
                        notin{cylinder($(0), $(0), $(9.3*ref), $(0.2*ref), $(0.2*ref), $(9.3*ref))
                        }
                }
        }
}
```

B.2 SIMION Workbench Script

Workbench script (.lua) to simulate the Coulomb crystals in the Paul trap. To reduce the simulation time, it helps to reduce the SIMION model to the trap segments of interest. For a usual crystal simulation, the particles are created in the central trap segment with a velocity of 0.001 eV and a linear damping parameter of 1.

```
        simion.workbench_program()

        print "NOTE: Before use, set TQual = 0 or -1, enable "
        print "Grouped flying, set Repulsion to Factor = 1, and"
        print "enable Dots flying at maximum speed (use slider)."

        -- DC voltages adjustable during flight:

        adjustable _40K_1 = 0.0     -- 40 K shield on Th side
        adjustable _4K_1 = 0.0      -- 4 K shield on Th side
        adjustable _Trap1_axis_DC = 0.0  -- Trap segment 1 DC offset.
        adjustable _Trap2_axis_DC = 0.0  -- Trap segment 2 DC offset.
        adjustable _Trap3_axis_DC = 0.0  -- Trap segment 3 DC offset.
        adjustable _Trap4_axis_DC = 0.0  -- Trap segment 4 DC offset.
        adjustable _Trap5_axis_DC = 0.0  -- Trap segment 5 DC offset.
        adjustable _Trap6_axis_DC = 0.0  -- Trap segment 6 DC offset.
        adjustable _Trap7_axis_DC = 0.0  -- Trap segment 7 DC offset.
        adjustable _4K_2 = 0.0     -- 40 K shield on Th side
        adjustable _40K_2 = 0.0      -- 4 K shield on Th side

        -- Stokes' law damping factor (if enabled)
        adjustable _linear_damping      = 1.0    -- linear damping factor


        -- Variables adjustable only at beginning of flight:


        adjustable phase_angle_deg = 0.0    -- quad entry phase angle of ion (deg)
        local phaseshift = 0.0
        adjustable Trap_RF_freq = 1940E3  -- RF frequency of Trap (Hz)
        adjustable Trap_RF_A = 300          -- RF Amplitude (V)
        adjustable pe_update_each_usec    = 0.05

        local TOF_ion


        -- Note: Using circular rods, the radius of the rods themselves
        -- should optimally be approximately 1.1487 * r_0.

        -- Temporary variables used internally.
        local scaled_rf  -- a factor used in the RF component
        local Trap_omega -- RF frequency in Hz expressed in radians/$\mu$s
        local ARFQ_omega
        local Trap_tempvolts
        local theta      -- phase_angle_deg (expressed in units of radians)
        local last_pe_update = 0.0 -- last potential energy surface update time ($\mu$sec)
```

```
-- SIMION segment called by SIMION at the start of ion flight for each potential
-- array instance to initialize adjustable electrode voltages in that instance.
-- NOTE: Code here can always more generally be placed instead in the
--   fast_adjust segment.  Typically, the only reason for an
--   init_p_values segment is to initialize static (not time-dependent)
--   voltages all at once, avoiding executing code on every time-step as done
--   in a fast_adjust segment.  This is intended to improve performance
--   (though in some cases could reduce it).

-- set all the DC voltages of the apertures
function segment.init_p_values()
adj_elect10 = _40K_1
adj_elect11 = _4K_1
adj_elect26 = _4K_2
adj_elect27 = _40K_2

end

-- SIMION segment called by SIMION to set adjustable electrode voltages
-- in the current potential array instance.
-- NOTE: this is called frequently, multiple times per time-step (by
-- Runge-Kutta), so performance concerns here can be important.
--------------



function segment.fast_adjust()
-- === Overview of the equations ===
--
-- The quadrupole mass filter has four rods with sinusoidal (RF)
-- waveforms applied to them.  Opposing rods have the same voltage,
-- so there are only two voltages, V1 and V2, to define:
--
--   V1 =  (U - V sin(omega*t + theta))
--   V2 = -(U - V sin(omega*t + theta))
--
-- where t is time (microseconds), omega is the angular frequency
-- (radians/microsecond), theta is a phase offset, and U and V
-- are respectively the magnitudes of the DC and RF voltage components.
--
-- U and V are proportional, respectively, to the more system independent
-- Mathieu constants a and q, and the stability of the system is
-- determined by the values of these constants.
--
--   V = (1/4) * r_0^2 * omega^2 * (m/e) * q
--   U = (1/8) * r_0^2 * omega^2 * (m/e) * a = (1/2) * V * (a/q)
--
-- where r_0 is half the minimum distance between opposite rods,
-- and (m/e) is the mass-to-charge ratio of the particle.
--
-- The stable region has a local maximum of a at
--
--   q_max ~ 0.70600, a_max ~ 0.23699
--
-- (This is the intersection of the Mathieu curves -a_0(q) and b_1(q)
--  on the q-a plane.)
--
-- Note the DC/RF ratio: U/V = (1/2)*(a/q) ~ 0.167839(9).
--
-- a_max is the limit of stability.  Typically we operate the system
-- at some fraction (_percent_tune/100), just under one, of a_max.
--
-- Note below the use of a unit conversion_factor ~
--   (1.66053886*10^-27 kg/u) * (1.602176462*10^-19 C/e)^-1 *
--   (2*PI rad/cycle)^2 * (0.01 m/cm)^2
-- which is used for (1/4) * (unit conversion factor) * q ~ 7.22(2)e-12.
-- (The actual constant chosen by Dahl differs slightly--this is non-ideal
-- system using round rods and fringe fields, so it could be tuned
-- differently from the ideal, hyperbolic electrode case.)


-- Initialize constants if not already initialized.
-- These constants don't change during particle flight,
-- so we can calculate them once and reuse them.
-- Reusing them is a bit more efficient (~25% by one estimate)
-- than recalculating them on every fast_adjust call.
--scaled_rf = effective_radius_in_cm^2 * freqency_hz^2 * 7.11016e-12
theta = phase_angle_deg * (math.pi / 180)
Trap_omega = Trap_RF_freq * (1E-6 * 2 * math.pi)

--local rfvolts = scaled_rf * _amu_mass_per_charge
```

```
--local dcvolts = rfvolts * _percent_tune * ((1/100) * 0.1678399)
Trap_tempvolts = sin(ion_time_of_flight * Trap_omega + theta) * Trap_RF_A


-- Finally, apply adjustable voltages to rod electrodes.
-- Apply the RF Voltage only to one electrode pair
adj_elect12 = _Trap1_axis_DC + Trap_tempvolts
adj_elect13 = _Trap1_axis_DC
adj_elect14 = _Trap2_axis_DC + Trap_tempvolts
adj_elect15 = _Trap2_axis_DC
adj_elect16 = _Trap3_axis_DC + Trap_tempvolts
adj_elect17 = _Trap3_axis_DC
adj_elect18 = _Trap4_axis_DC + Trap_tempvolts
adj_elect19 = _Trap4_axis_DC
adj_elect20 = _Trap5_axis_DC + Trap_tempvolts
adj_elect21 = _Trap5_axis_DC
adj_elect22 = _Trap6_axis_DC + Trap_tempvolts
adj_elect23 = _Trap6_axis_DC
adj_elect24 = _Trap7_axis_DC + Trap_tempvolts
adj_elect25 = _Trap7_axis_DC


end
-- Stokes' law collision model
--
-- See the SIMION "drag" example for more detail discussion on
-- the following code.
--
-- D.Manura-2006-08 - based drag\drag.lua example.
-- (c) 2006 Scientific Instrument Services, Inc. (Licensed under SIMION 8.0)


-- Apply Stokes' law viscous effects to ion motion.
-- This is designed to be called inside a SIMION accel_adjust segment.
function segment.accel_adjust()
if ion_time_step == 0   then return end -- skip if zero time step
if _linear_damping == 0 then return end -- skip if damping set to zero

-- Compute correction factor.
_linear_damping = abs(_linear_damping)         -- force damping factor positive
local tterm = ion_time_step * _linear_damping  -- time constant
local factor = (1 - exp(-tterm)) / tterm       -- correction factor

-- Compute new x, y, and z accelerations.
-- This following the differential equation
--   da/dt = -v*linear_damping
-- with the correction factor for dt being finite.
-- Note: ion_v[xyz]_mm is particle velocity in mm/usec.
--       ion_a[xyz]_mm is particle acceleration in mm/usec^2.
ion_ax_mm = factor * (ion_ax_mm - ion_vx_mm * _linear_damping)
ion_ay_mm = factor * (ion_ay_mm - ion_vy_mm * _linear_damping)
ion_az_mm = factor * (ion_az_mm - ion_vz_mm * _linear_damping)
end

-- SIMION segment called by SIMION after every time-step.
function segment.other_actions()
-- Update potential energy surface display periodically.
-- The performance overhead of this in non-PE views is only a few percent.
-- NOTE: the value inside abs(...) can be negative when a new ion is flown.
if abs(ion_time_of_flight - last_pe_update) >= pe_update_each_usec then
last_pe_update = ion_time_of_flight
sim_update_pe_surface = 1    -- Request a PE surface display update.
end
-- create a file that saves the ion positions to be plotted. Only start after a
-- certain run time to minimize the amount of saved data points
if abs(ion_time_of_flight) >= 100E3 then
file = io.open("x.txt","a")
file:write(tostring(ion_number)..","..tostring(ion_time_of_flight)..","
..tostring(ion_px_mm)..","..tostring(ion_py_mm)..","..tostring(ion_pz_mm).."\n" )
file:close()
end
-- end the ion fly time after 10 additional runs
if abs(ion_time_of_flight) >= 100010 then
ion_splat = 1
end

end

-- SIMION segment called by SIMION to override time-step size on each time-step.
function segment.tstep_adjust()
-- For the trajectory calculation to be reliable, the time step size should
-- be no more than some fraction of the RF period so that the ion sees each
-- RF cycle as it exists.
```

```
-- In the SIMION quadruople example under minimum trajectory quality (0)
-- and default conditions, ion_time_step is already below one-tenth the
-- RF period, so this code isn't really necessary.  However, this code
-- reduces the chance of surprises in case the conditions are changed
-- and trajectory quality factor is set too low.
-- The performance overhead of this is quite low (~1%).

-- Keep time step size <= X usec.
ion_time_step = min(ion_time_step, 0.1)  -- X usec
end
```

References

1. O. Hahn. Über eine neue radioaktive Substanz im Uran. *Berichte der deutschen chemischen Gesellschaft (A and B Series)* **54,** 1131–1142. doi:10.1002/cber.19210540602 (1921) (cit. on p. 1).
2. P. Walker & Z. Podolyák. 100 years of nuclear isomers—then and now. *Physica Scripta* **95,** 044004. doi:10.1088/1402-4896/ab635d (2020) (cit. on p. 1).
3. F. Kondev, M. Wang, W. Huang, *et al.* The NUBASE2020 evaluation of nuclear physics properties. *Chinese Physics C* **45,** 030001. doi:10.1088/1674-1137/abddae (2021) (cit. on pp. 1, 2).
4. G. Sletten, V. Metag & E. Liukkonen. Picosecond fission isomers in even-even Cm isotopes. *Physics Letters B* **60,** 153–156. ISSN: 0370-2693. doi:10.1016/0370-2693(76)90411-1 (1976) (cit. on p. 1).
5. F. Hagemann, L. I. Katzin, M. H. Studier, *et al.* The $(4n + 1)$ Radioactive Series: The Decay Products of U^{233}. *Phys. Rev.* **72,** 252–252. doi:10.1103/PhysRev.72.252 (1947) (cit. on p. 1).
6. A. C. English, T. E. Cranshaw, P. Demers, *et al.* The $(4n + 1)$ Radioactive Series. *Phys. Rev.* **72,** 253–254. doi:10.1103/PhysRev.72.253 (1947) (cit. on p. 1).
7. L. Kroger & C. Reich. Features of the low-energy level scheme of ^{229}Th as observed in the α-decay of ^{233}U. *Nuclear Physics A* **259,** 29–60. ISSN: 0375-9474. doi:10.1016/0375-9474(76)90494-2 (1976) (cit. on pp. 1, 9).
8. L. von der Wense, B. Seiferle, M. Laatiaoui, *et al.* Direct detection of the ^{229}Th nuclear clock transition. *Nature* **533,** 47–51. doi:10.1038/nature17669 (2016) (cit. on pp. 1, 2, 9, 11, 35, 55, 56, 59, 111).
9. E. Peik & C. Tamm. Nuclear laser spectroscopy of the 3.5 eV transition in Th-229. *Europhysics Letters (EPL)* **61,** 181–186. doi:10.1209/epl/i2003-00210-x (2003) (cit. on pp. 1, 7, 8).
10. J. Tiedau, M. V. Okhapkin, K. Zhang, *et al.* Laser Excitation of the Th-229 Nucleus. *Phys. Rev. Lett.* **132,** 182501. doi:10.1103/PhysRevLett.132.182501 (2024) (cit. on pp. 1, 2, 9, 12, 13).
11. R. Elwell, C. Schneider, J. Jeet, *et al.* Laser Excitation of the ^{229}Th Nuclear Isomeric Transition in a Solid-State Host. *Phys. Rev. Lett.* **133,** 013201. doi:10.1103/PhysRevLett.133.013201 (2024) (cit. on pp. 1, 2, 9, 12, 13).

12. C. Zhang, T. Ooi, J. S. Higgins, *et al.* Frequency ratio of the ^{229m}Th nuclear isomeric transition and the ^{87}Sr atomic clock. *Nature* **633,** 63–70. ISSN: 1476-4687. doi:10.1038/s41586-024-07839-6 (2024) (cit. on pp. 1, 2, 3, 7, 8, 9, 10, 11, 12, 13, 16, 47, 48).

13. A. Yamaguchi, Y. Shigekawa, H. Haba, *et al.* Laser spectroscopy of triply charged ^{229}Th isomer for a nuclear clock. *Nature.* ISSN: 1476-4687. doi:10.1038/s41586-024-07296-1 (2024) (cit. on pp. 2, 3, 13, 17, 43, 46, 47, 48, 49, 74, 75, 83, 121, 124, 126, 136).

14. L. von der Wense. *On the direct detection of ^{229m}Th* PhD thesis (München, 2017) (cit. on pp. 2, 3, 9, 56, 111, 112).

15. A. D. Ludlow, M. M. Boyd, J. Ye, *et al.* Optical atomic clocks. *Rev. Mod. Phys.* **87,** 637–701. doi:10.1103/RevModPhys.87.637 (2015) (cit. on pp. 2, 4, 5, 6, 7).

16. V. Barci, G. Ardisson, G. Barci-Funel, *et al.* Nuclear structure of ^{229}Th from γ-ray spectroscopy study of ^{233}U α-particle decay. *Phys. Rev. C* **68,** 034329. doi:10.1103/PhysRevC.68.034329 (2003) (cit. on pp. 2, 53).

17. E. Browne & J. Tuli. Nuclear Data Sheets for A = 229. *Nuclear Data Sheets* **109,** 2657–2724. ISSN: 0090-3752. doi:10.1016/j.nds.2008.10.001 (2008) (cit. on p. 2).

18. M. Verlinde, S. Kraemer, J. Moens, *et al.* Alternative approach to populate and study the ^{229}Th nuclear clock isomer. *Phys. Rev. C* **100,** 024315. doi:10.1103/PhysRevC.100.024315 (2019) (cit. on p. 2).

19. L. v.d. Wense, B. Seiferle, M. Laatiaoui, *et al.* Determination of the extraction efficiency for ^{233}U source α-recoil ions from the MLL buffer-gas stopping cell. *The European Physical Journal A* **51,** 29. ISSN: 1434-601X. doi:10.1140/epja/i2015-15029-8 (2015) (cit. on pp. 3, 111).

20. S. Köhler, R. Deißenberger, K. Eberhardt, *et al.* Determination of the first ionization potential of actinide elements by resonance ionization mass spectroscopy. *Spectrochimica Acta Part B: Atomic Spectroscopy* **52,** 717–726. ISSN: 0584-8547. doi:10.1016/S0584-8547(96)01670-9 (1997) (cit. on pp. 3, 4).

21. B. Seiferle. *Characterization of the Th-229 nuclear clock transition* PhD thesis (Ludwig-Maximilians-Universität München, München, 2019) (cit. on pp. 3, 14, 15).

22. T. Mayer-Kuckuk. *Kernphysik, Eine Einführung* 7th ed. ISBN: 978-3-519-13223-3. doi:10.1007/978-3-322-84876-5 (Vieweg+Teubner Verlag Wiesbaden, 2002) (cit. on pp. 4, 14, 36, 37).

23. B. Seiferle, L. von der Wense & P. G. Thirolf. Lifetime Measurement of the ^{229}Th Nuclear Isomer. *Phys. Rev. Lett.* **118,** 042501. doi:10.1103/PhysRevLett.118.042501 (2017) (cit. on pp. 4, 55).

24. F. F. Karpeshin & M. B. Trzhaskovskaya. Impact of the electron environment on the lifetime of the ^{229}Th^m low-lying isomer. *Phys. Rev. C* **76,** 054313. doi:10.1103/PhysRevC.76.054313 (2007) (cit. on p. 4).

25. L. von der Wense & B. Seiferle. The ^{229}Th isomer: prospects for a nuclear optical clock. *The European Physical Journal A* **56,** 277. ISSN: 1434-601X. doi:10.1140/epja/s10050-020-00263-0 (2020) (cit. on pp. 4, 6, 7, 8, 9, 14).

26. V. F. Strizhov & E. V. Tkalya. Decay channel of low-lying isomer state of the ^{229}Th nucleus Possibilities of experimental investigation. *Soviet Physics - JETP (English Translation)* **72,** 387–390. ISSN: 0038-5646 (1991) (cit. on p. 4).

27. E. V. Tkalya. Excitation of low-lying isomer level of the nucleus ^{299}Th by optical photons. *JETP Lett* **55** (1992) (cit. on p. 4).

28. E. Tkalya. Probability of nonradiative excitation of nuclei in transitions of an electron in an atomic shell. *Journal of Experimental and Theoretical Physics* **75,** 200–209. ISSN: 1063-776 (1992) (cit. on p. 4).

29. F. Karpeshin, I. Band, M. Trzhaskovskaya, *et al.* Optical pumping ^{229m}Th through NEET as a new effective way of producing nuclear isomers. *Physics Letters B* **372,** 1–7. ISSN: 0370-2693. doi:10.1016/0370-2693(96)00036-6 (1996) (cit. on p. 4).

30. F. Karpeshin, I. Band & M. Trzhaskovskaya. 3.5-eV isomer of ^{229m}Th: How it can be produced. *Nuclear Physics A* **654,** 579–596. ISSN: 0375-9474. doi:10.1016/S0375-9474(99)00303-6 (1999) (cit. on p. 4).

31. S. G. Porsev & V. V. Flambaum. Electronic bridge process in ^{229}Th^{+}. *Phys. Rev. A* **81,** 042516. doi:10.1103/PhysRevA.81.042516 (2010) (cit. on p. 4).

32. S. G. Porsev, V. V. Flambaum, E. Peik, *et al.* Excitation of the Isomeric ^{229m}Th Nuclear State via an Electronic Bridge Process in ^{229}Th^{+}. *Phys. Rev. Lett.* **105,** 182501. doi:10.1103/PhysRevLett.105.182501 (2010) (cit. on p. 4).

33. A. G. Radnaev, C. J. Campbell & A. Kuzmich. Observation of the 717-nm electric quadrupole transition in triply charged thorium. *Phys. Rev. A* **86,** 060501. doi:10.1103/PhysRevA.86.060501 (2012) (cit. on p. 4).

34. P. V. Bilous, E. Peik & A. Pálffy. Laser-induced electronic bridge for characterization of the ^{229m}Th $\rightarrow$ ^{229g}Th nuclear transition with a tunable optical laser. *New Journal of Physics* **20,** 013016. doi:10.1088/1367-2630/aa9cd9 (2018) (cit. on p. 4).

35. N.-Q. Cai, G.-Q. Zhang, C.-B. Fu, *et al.* Populating ^{229m}Th via two-photon electronic bridge mechanism. *Nuclear Science and Techniques* **32,** 59. ISSN: 2210-3147. doi:10.1007/s41365-021-00900-3 (2021) (cit. on p. 4).

36. L. Li, Z. Li, C. Wang, *et al.* Scheme for the excitation of thorium-229 nuclei based on electronic bridge excitation. *Nuclear Science and Techniques* **34,** 24. ISSN: 2210-3147. doi:10.1007/s41365-023-01169-4 (2023) (cit. on p. 4).

37. J. Jespersen & J. Fitz-Randolph. *From Sundials to Atomic Clocks - Understanding Time and Frequency* (National Institute of Standards and Technology, Monograph 155, 1999) (cit. on p. 4).

38. W. Thomson & P. G. Tait. *Elements of Natural Philosphy* 2nd ed. ISBN: 9810239807 (Cambridge Universtiy Press, Cambridge, England, 1879) (cit. on p. 4).

39. H. Lyons. The Atomic Clock. *Instruments* **22,** 133–135 (1949) (cit. on p. 4).

40. M. Lombardi. A Historical Review of U.S. Contributions to the Atomic Redefinition of the SI Second in 1967. *Journal of research of the National Institute of Standards and Technology* **122.** doi:10.6028/jres.122.029 (2017) (cit. on pp. 4, 5).

41. L. Essen & J. V. L. Parry. An Atomic Standard of Frequency and Time Interval: A Cæsium Resonator. *Nature* **176,** 280–282. ISSN: 1476-4687. doi:10.1038/176280a0 (1955) (cit. on p. 5).

42. J. Reichert, R. Holzwarth, T. Udem, *et al.* Measuring the frequency of light with mode-locked lasers. *Optics Communications* **172,** 59–68. ISSN: 0030-4018. doi:10.1016/S0030-4018(99)00491-5 (1999) (cit. on p. 5).

43. S. A. Diddams, D. J. Jones, J. Ye, *et al.* Direct Link between Microwave and Optical Frequencies with a 300 THz Femtosecond Laser Comb. *Phys. Rev. Lett.* **84,** 5102–5105. doi:10.1103/PhysRevLett.84.5102 (2000) (cit. on p. 5).

44. T. W. Hänsch. Nobel Lecture: Passion for precision. *Rev. Mod. Phys.* **78,** 1297–1309. doi:10.1103/RevModPhys.78.1297 (2006) (cit. on p. 5).

45. J. L. Hall. Nobel Lecture: Defining and measuring optical frequencies. *Rev. Mod. Phys.* **78,** 1279–1295. doi:10.1103/RevModPhys.78.1279 (2006) (cit. on p. 5).

46. E. Peik, T. Schumm, M. S. Safronova, *et al.* Nuclear clocks for testing fundamental physics. *Quantum Science and Technology* **6,** 034002. doi:10.1088/2058-9565/abe9c2 (2021) (cit. on pp. 6, 9).

47. F. Riehle. Optical clock networks. *Nature Photonics* **11,** 25–31. ISSN: 1749-4893. doi:10.1038/nphoton.2016.235 (2017) (cit. on p. 6).

48. P. Gill. When should we change the definition of the second? *Philosophical Transactions of the Royal Society A: Mathematical, Physical and Engineering Sciences* **369,** 4109–4130. doi:10.1098/rsta.2011.0237 (2011) (cit. on p. 6).

49. N. Poli, C. Oates, P. Gill, *et al.* Optical atomic clocks. *Rivista del Nuovo Cimento* **36.** doi:10.1393/ncr/i2013-10095-x (2014) (cit. on p. 6).

50. J. C. Bergquist, S. R. Jefferts & D. J. Wineland. Time Measurement at the Millennium. *Physics Today* **54,** 37–42. ISSN: 0031-9228. doi:10.1063/1.1366066 (2001) (cit. on pp. 6, 7).

51. D. Allan. Statistics of atomic frequency standards. *Proceedings of the IEEE* **54,** 221–230. doi:10.1109/PROC.1966.4634 (1966) (cit. on p. 7).

52. W. Riley & D. Howe. *Handbook of Frequency Stability Analysis* en. 2008 (cit. on p. 7).

53. in. *Frequency Standards* 47–79 (John Wiley & Sons, Ltd, 2003). ISBN: 9783527605996. doi:10.1002/3527605991.ch3 (cit. on p. 7).

54. W. M. Itano, J. C. Bergquist, J. J. Bollinger, *et al.* Quantum projection noise: Population fluctuations in two-level systems. *Phys. Rev. A* **47,** 3554–3570. doi:10.1103/PhysRevA.47.3554 (1993) (cit. on p. 7).

55. M. C. Marshall, D. A. R. Castillo, W. J. Arthur-Dworschack, *et al.* High-Stability Single-Ion Clock with 5.5×10^{-19} Systematic Uncertainty. *Phys. Rev. Lett.* **135,** 033201. doi:10.1103/hb3c-dk28 (2025) (cit. on pp. 7, 131).

56. A. Aeppli, K. Kim, W. Warfield, *et al.* Clock with 8×10^{-19} Systematic Uncertainty. *Phys. Rev. Lett.* **133,** 023401. doi:10.1103/PhysRevLett.133.023401 (2024) (cit. on p. 7).

57. C. J. Campbell, A. G. Radnaev, A. Kuzmich, *et al.* Single-Ion Nuclear Clock for Metrology at the 19th Decimal Place. *Phys. Rev. Lett.* **108,** 120802. doi:10.1103/PhysRevLett.108.120802 (2012) (cit. on p. 7).

58. *Global Positioning System, Standard Positionong Service, Performance Standard* (Department of Defense, USA, 2020) (cit. on p. 8).

59. P. G. Thirolf, B. Seiferle & L. von der Wense. The 229-thorium isomer: doorway to the road from the atomic clock to the nuclear clock. *Journal of Physics B: Atomic, Molecular and Optical Physics* **52,** 203001. doi:10.1088/1361-6455/ab29b8 (2019) (cit. on pp. 8, 9, 56).

60. P. G. Thirolf, S. Kraemer, D. Moritz, *et al.* The thorium isomer ^{229m}Th: Review of status and perspectives after more than 50 years of research. *The European Physical Journal Special Topics* **233,** 1113–1131. ISSN: 1951-6401. doi:10.1140/epjs/s11734-024-01098-2 (2024) (cit. on pp. 8, 9).

61. T. E. Mehlstäubler, G. Grosche, C. Lisdat, *et al.* Atomic clocks for geodesy. *Reports on Progress in Physics* **81,** 064401. doi:10.1088/1361-6633/aab409 (2018) (cit. on p. 8).

62. M. Bondarescu, R. Bondarescu, P. Jetzer, *et al.* The potential of continuous, local atomic clock measurements for earthquake prediction and volcanology. *EPJ Web of Conferences* **95,** "04009". doi:10.1051/epjconf/20149504009 (2015) (cit. on p. 8).

63. P. G. Thirolf, B. Seiferle & L. von der Wense. Improving Our Knowledge on the ^{229m}Thorium Isomer: Toward a Test Bench for Time Variations of Fundamental Constants. *Annalen der Physik* **531,** 1800381. doi:10.1002/andp.201800381 (2019) (cit. on pp. 8, 9).

64. S. G. Karshenboim. Some possibilities for laboratory searches for variations of fundamental constants. *Canadian Journal of Physics* **78,** 639–678. doi:10.1139/p00-045 (2000) (cit. on p. 8).

65. J.-P. Uzan. The fundamental constants and their variation: observational and theoretical status. *Rev. Mod. Phys.* **75,** 403–455. doi:10.1103/RevModPhys.75.403 (2003) (cit. on p. 8).

66. V. V. Flambaum. Enhanced Effect of Temporal Variation of the Fine Structure Constant and the Strong Interaction in ^{229}Th. *Phys. Rev. Lett.* **97,** 092502. doi:10.1103/PhysRevLett.97.092502 (2006) (cit. on p. 8).

67. M. S. Safronova, U. I. Safronova, A. G. Radnaev, *et al.* Magnetic dipole and electric quadrupole moments of the ^{229}Th nucleus. *Phys. Rev. A* **88,** 060501. doi:10.1103/PhysRevA.88.060501 (2013) (cit. on pp. 8, 37).

68. J. C. Berengut, V. A. Dzuba, V. V. Flambaum, *et al.* Proposed Experimental Method to Determine α Sensitivity of Splitting between Ground and 7.6 eV Isomeric States in ^{229}Th. *Phys. Rev. Lett.* **102,** 210801. doi:10.1103/PhysRevLett.102.210801 (2009) (cit. on pp. 8, 37, 43).

69. K. Beeks, G. A. Kazakov, F. Schaden, *et al.* Fine-structure constant sensitivity of the Th-229 nuclear clock transition. doi:10.48550/arXiv.2407.17300 (cit. on p. 8).

70. A. Hayes & J. Friar. Sensitivity of nuclear transition frequencies to temporal variation of the fine structure constant or the strong interaction. *Physics Letters B* **650,** 229–232. ISSN: 0370-2693. doi:10.1016/j.physletb.2007.05.021 (2007) (cit. on p. 8).

71. A. C. Hayes, J. L. Friar & P. Möller. Splitting sensitivity of the ground and 7.6 eV isomeric states of ^{229}Th. *Phys. Rev. C* **78,** 024311. doi:10.1103/PhysRevC.78.024311 (2008) (cit. on p. 8).

72. V. V. Flambaum, N. Auerbach & V. F. Dmitriev. Coulomb energy contribution to the excitation energy in 229Th and enhanced effect of α variation. *Europhysics Letters* **85,** 50005. doi:10.1209/0295-5075/85/50005 (2009) (cit. on p. 8).

73. J. C. Berengut & V. V. F. and. Testing Time-Variation of Fundamental Constants using a ^{229}Th Nuclear Clock. *Nuclear Physics News* **20,** 19–22. doi:10.1080/10619127.2010.506119 (2010) (cit. on p. 8).

74. P. Fadeev, J. C. Berengut & V. V. Flambaum. Sensitivity of ^{229}Th nuclear clock transition to variation of the fine-structure constant. *Phys. Rev. A* **102,** 052833. doi:10.1103/PhysRevA.102.052833 (2020) (cit. on p. 8).

75. A. Derevianko & M. Pospelov. Hunting for topological dark matter with atomic clocks. *Nature Physics* **10,** 933–936. ISSN: 1745-2481. doi:10.1038/nphys3137 (2014) (cit. on p. 9).

76. A. Arvanitaki, J. Huang & K. Van Tilburg. Searching for dilaton dark matter with atomic clocks. *Phys. Rev. D* **91,** 015015. doi:10.1103/PhysRevD.91.015015 (2015) (cit. on p. 9).

77. K. Van Tilburg, N. Leefer, L. Bougas, *et al.* Search for Ultralight Scalar Dark Matter with Atomic Spectroscopy. *Phys. Rev. Lett.* **115,** 011802. doi:10.1103/PhysRevLett.115.011802 (2015) (cit. on p. 9).

78. A. Hees, J. Guéna, M. Abgrall, *et al.* Searching for an Oscillating Massive Scalar Field as a Dark Matter Candidate Using Atomic Hyperfine Frequency Comparisons. *Phys. Rev. Lett.* **117,** 061301. doi:10.1103/PhysRevLett.117.061301 (2016) (cit. on p. 9).

79. M. S. Safronova, D. Budker, D. DeMille, *et al.* Search for new physics with atoms and molecules. *Rev. Mod. Phys.* **90,** 025008. doi:10.1103/RevModPhys.90.025008 (2018) (cit. on p. 9).

80. Y. V. Stadnik. New bounds on macroscopic scalar-field topological defects from nontransient signatures due to environmental dependence and spatial variations of the fundamental constants. *Phys. Rev. D* **102,** 115016. doi:10.1103/PhysRevD.102.115016 (2020) (cit. on p. 9).

81. K. Beeks, T. Sikorsky, T. Schumm, *et al.* The thorium-229 low-energy isomer and the nuclear clock. *Nature Reviews Physics* **3,** 238–248. doi:10.1038/s42254-021-00286-6 (2021) (cit. on pp. 9, 45).

82. L. von der Wense, B. Seiferle & P. G. Thirolf. Towards a ^{229}Th-Based Nuclear Clock. *Measurement Techniques* **60,** 1178–1192. ISSN: 1573-8906. doi:10.1007/s11018-018-1337-1 (2018) (cit. on p. 9).

83. B. Seiferle, L. von der Wense, P. V. Bilous, *et al.* Energy of the ^{229}Th nuclear clock transition. *Nature* **573,** 243–246. doi:10.1038/s41586-019-1533-4 (2019) (cit. on pp. 9, 12, 55, 59).

84. T. Sikorsky, J. Geist, D. Hengstler, *et al.* Measurement of the ^{229}Th Isomer Energy with a Magnetic Microcalorimeter. *Phys. Rev. Lett.* **125,** 142503. doi:10.1103/PhysRevLett.125.142503 (2020) (cit. on p. 9).

85. S. Kraemer, J. Moens, M. Athanasakis-Kaklamanakis, *et al.* Observation of the radiative decay of the ^{229}Th nuclear clock isomer. *Nature* **617,** 706–710. ISSN: 1476-4687. doi:10.1038/s41586-023-05894-z (2023) (cit. on pp. 9, 12, 13).

86. K. Beeks, T. Sikorsky, V. Rosecker, *et al.* Growth and characterization of thorium-doped calcium fluoride single crystals. *Scientific Reports* **13,** 3897. ISSN: 2045-2322. doi:10.1038/s41598-023-31045-5 (2023) (cit. on p. 9).

87. K. Beeks, T. Sikorsky, F. Schaden, *et al.* Optical transmission enhancement of ionic crystals via superionic fluoride transfer: Growing VUV-transparent radioactive crystals. *Phys. Rev. B* **109,** 094111. doi:10.1103/PhysRevB.109.094111 (2024) (cit. on p. 9).

88. C. Zhang, L. von der Wense, J. F. Doyle, *et al.* $^{229}ThF_4$ thin films for solid-state nuclear clocks. *Nature* **636,** 603–608. ISSN: 1476-4687. doi:10.1038/s41586-024-08256-5 (2024) (cit. on pp. 10, 12).

89. F. Schaden, T. Riebner, I. Morawetz, *et al.* Laser-induced quenching of the Th-229 nuclear clock isomer in calcium fluoride. *Phys. Rev. Res.* **7,** L022036. doi:10.1103/PhysRevResearch.7.L022036 (2025) (cit. on p. 10).

90. J. S. Higgins, T. Ooi, J. F. Doyle, *et al.* Temperature Sensitivity of a Thorium-229 Solid-State Nuclear Clock. *Phys. Rev. Lett.* **134,** 113801. doi:10.1103/PhysRevLett.134.113801 (2025) (cit. on p. 10).

91. Q. Xiao, G. Penyazkov, R. Yu, *et al.* Proposal for the generation of continuous-wave vacuum ultraviolet laser light for Th-229 isomer precision spectroscopy. doi:10.48550/arXiv.2406.16841 (cit. on p. 10).

92. Q. Xiao, G. Penyazkov, X. Li, *et al.* A continuous-wave vacuum ultraviolet laser for the nuclear clock. doi:10.48550/arXiv.2507.19449 (cit. on p. 10).

93. V. Lal, M. V. Okhapkin, J. Tiedau, *et al.* Continuous-wave laser source at the 148 nm nuclear transition of Th-229. doi:10.48550/arXiv.2507.17719 (cit. on p. 10).

94. B. R. Beck, C. Wu, P. Beiersdorfer, *et al.* Improved Value for the Energy Splitting of the Ground-State Doublet in the Nucleus ^{229m}Th (2009) (cit. on p. 10).

95. B. R. Beck, J. A. Becker, P. Beiersdorfer, *et al.* Energy Splitting of the Ground-State Doublet in the Nucleus ^{229}Th. *Phys. Rev. Lett.* **98,** 142501. doi:10.1103/PhysRevLett.98.142501 (2007) (cit. on pp. 10, 11).

96. A. Yamaguchi, H. Muramatsu, T. Hayashi, *et al.* Energy of the ^{229}Th Nuclear Clock Isomer Determined by Absolute γ-ray Energy Difference. *Phys. Rev. Lett.* **123,** 222501. doi:10.1103/PhysRevLett.123.222501 (2019).

97. R. G. Helmer & C. W. Reich. An excited state of ^{229}Th at 3.5 eV. *Phys. Rev. C* **49,** 1845–1858. doi:10.1103/PhysRevC.49.1845 (1994) (cit. on pp. 10, 11, 17).

98. A. M. Dykhne & E. V. Tkalya. Matrix element of the anomalously low-energy (3.5±0.5 eV) transition in ^{229}Th and the isomer lifetime. *Journal of Experimental and Theoretical Physics Letters* **67,** 251–256. doi:10.1134/1.567659 (1998) (cit. on pp. 11, 17).

99. G. M. Irwin & K. H. Kim. Observation of Electromagnetic Radiation from Deexcitation of the ^{229}Th Isomer. *Phys. Rev. Lett.* **79,** 990–993. doi:10.1103/PhysRevLett.79.990 (1997) (cit. on p. 11).

100. E. V. Tkalya, A. N. Zherikhin & V. I. Zhudov. Decay of the low-energy nuclear isomer ^{229}Th$^m(3/2^+, 3.5\pm1.0\text{eV})$ in solids (dielectrics and metals): A new scheme of experimental research. *Phys. Rev. C* **61,** 064308. doi:10.1103/PhysRevC.61.064308 (2000) (cit. on pp. 11, 12).

101. E. V. Tkalya. Spontaneous emission probability for M1 transition in a dielectric medium: ^{229m}Th(3/2+, 3.5±1.0 eV) decay. *Journal of Experimental and Theoretical Physics Letters* **71,** 311–313. ISSN: 1090-6487. doi:10.1134/1.568349 (2000) (cit. on pp. 11, 12).

102. E. Browne, E. B. Norman, R. D. Canaan, *et al.* Search for decay of the 3.5-eV level in ^{229}Th. *Phys. Rev. C* **64,** 014311. doi:10.1103/PhysRevC.64.014311 (2001) (cit. on p. 11).

103. A. Aas, H. Mach, M. Borge, *et al.* Enhanced and quenched B(E1) transition rates between parity doublet bands in ^{227}Ra. *Nuclear Physics A* **611,** 281–314. ISSN: 0375-9474. doi:10.1016/S0375-9474(96)00312-0 (1996) (cit. on p. 11).

104. A. Aas, H. Mach, J. Kvasil, *et al.* Quenched E1 transition rates in ^{231}Th. *Nuclear Physics A* **654,** 499–522. ISSN: 0375-9474. doi:10.1016/S0375-9474(99)00307-3 (1999) (cit. on p. 11).

105. V. G. Soloviev. *Theory of Atomic Nuclei, Quasi-particle and Phonons* 1st ed. (Pergamon Press, Oxford, England, 1976) (cit. on p. 11).

106. E. Ruchowska, W. A. Płóciennik, J. Żylicz, *et al.* Nuclear structure of ^{229}Th. *Phys. Rev. C* **73,** 044326. doi:10.1103/PhysRevC.73.044326 (2006) (cit. on pp. 11, 13, 17).

107. Z. O. Guimarães-Filho & O. Helene. Energy of the $3/2^+$ state of ^{229}Th reexamined. *Phys. Rev. C* **71,** 044303. doi:10.1103/PhysRevC.71.044303 (2005) (cit. on pp. 11, 13).

108. E. V. Tkalya, C. Schneider, J. Jeet, *et al.* Radiative lifetime and energy of the low-energy isomeric level in ^{229}Th. *Phys. Rev. C* **92,** 054324. doi:10.1103/PhysRevC.92.054324 (2015) (cit. on pp. 11, 12, 13).

109. N. Minkov & A. Pálffy. Reduced Transition Probabilities for the Gamma Decay of the 7.8 eV Isomer in ^{229}Th. *Phys. Rev. Lett.* **118,** 212501. doi:10.1103/PhysRevLett.118.212501 (2017) (cit. on pp. 11, 16, 17).

110. N. Minkov & A. Pálffy. Theoretical Predictions for the Magnetic Dipole Moment of ^{229m}Th. *Phys. Rev. Lett.* **122,** 162502. doi:10.1103/PhysRevLett.122.162502 (2019) (cit. on p. 12).

111. J. Thielking, M. V. Okhapkin, P. Głowacki, *et al.* Laser spectroscopic characterization of the nuclear-clock isomer ^{229m}Th. *Nature* **556,** 321–325. doi:10.1038/s41586-018-0011-8 (2018) (cit. on pp. 12, 37, 43, 46, 47, 48, 49, 83, 121).

112. G. Alaga, K. Alder, A. Bohr, *et al.* Intensity rules for beta and gamma transitions to nuclear rotational states. *Dan. Mat. Fys. Medd.* **29** (1955) (cit. on p. 12).

113. G. Alaga. New Type of Selection Rules in β Decay of Strongly Deformed Nuclei. *Phys. Rev.* **100,** 432–433. doi:10.1103/PhysRev.100.432 (1955) (cit. on p. 12).

114. G. Alaga. Selection rules for beta and gamma particle transitions in strongly deformed nuclei. *Nuclear Physics* **4,** 625–631. ISSN: 0029-5582. doi:10.1016/0029-5582(87)90066-6 (1957) (cit. on p. 12).

115. Y. Shigekawa, A. Yamaguchi, K. Suzuki, *et al.* Estimation of radiative half-life of ^{229m}Th by half-life measurement of other nuclear excited states in ^{229}Th. *Phys. Rev. C* **104,** 024306. doi:10.1103/PhysRevC.104.024306 (2021) (cit. on pp. 12, 17).

116. M. Daimon & A. Masumura. High-accuracy measurements of the refractive index and its temperature coefficient of calcium fluoride in a wide wavelength range from 138 to 2326 nm. *Appl. Opt.* **41,** 5275–5281. doi:10.1364/AO.41.005275 (2002) (cit. on p. 12).

117. Q. Zheng, X. Wang & D. Thompson. Temperature-dependent optical properties of monocrystalline CaF_2, BaF_2, and MgF_2. *Opt. Mater. Express* **13,** 2380–2391. doi:10.1364/OME.496246 (2023) (cit. on p. 12).

118. T. Hiraki, K. Okai, M. Bartokos, *et al.* Controlling ^{229}Th isomeric state population in a VUV transparent crystal. *Nature Communications* **15,** 5536. ISSN: 2041-1723. doi:10.1038/s41467-024-49631-0 (2024) (cit. on pp. 12, 13).

119. J. Jeet. *Search for the low lying transition in the ^{229}Th Nucleus* eng. PhD thesis (UCLA, Los Angeles, 2018) (cit. on p. 12).

120. P. V. Bilous, G. A. Kazakov, I. D. Moore, *et al.* Internal conversion from excited electronic states of ^{229}Th ions. *Phys. Rev. A* **95,** 032503. doi:10.1103/PhysRevA.95.032503 (2017) (cit. on p. 14).

121. P. Bilous. *Towards a nuclear clock with the ^{229}Th isomeric transition* PhD thesis (Ruprecht-Karls Universität, Heidelberg, 2018). doi:10.17617/2.3026914 (cit. on p. 14).

122. N. Takigawa & K. Washiyama. *Fundamentals of Nuclear Physics* 1st ed. ISBN: 978-4-431-55377-9. doi:10.1007/978-4-431-55378-6 (Springer Tokyo, 2017) (cit. on pp. 14, 15).

123. A. Bohr & B. R. Mottelson. *Nuclear Structure, Volume 1: Single-Particle Motion* 2nd ed. ISBN: 9810239807 (World Scientific Publishing Co. Pte. Ltd., Singapore, 1998) (cit. on pp. 14, 15, 16).

124. W. Paul & M. Raether. Das elektrische Massenfilter. *Zeitschrift für Physik* **140,** 262–273. ISSN: 0044-3328. doi:10.1007/BF01328923 (1955) (cit. on pp. 19, 20).

125. W. Paul. Electromagnetic Traps for Charged and Neutral Particles (Nobel Lecture). *Angewandte Chemie International Edition in English* **29,** 739–748. doi:10.1002/anie.199007391 (1990) (cit. on pp. 19, 20).

126. S. Earnshaw. On the nature of the molecular forces which regulate the constitution of the luminiferous ether. *Transactions of the Cambridge Philosophical Society* **7,** 97 (1848) (cit. on p. 19).

127. J. Eschner, G. Morigi, F. Schmidt-Kaler, *et al.* Laser cooling of trapped ions. *J. Opt. Soc. Am. B* **20,** 1003–1015. doi:10.1364/JOSAB.20.001003 (2003) (cit. on pp. 19, 31).

128. F. G. Major, V. N. Gheorghe & G. Werth. *Charged particle traps: Physics and techniques of charged particle field confinement* 1st ed. ISBN: 978-3-540-22043-5. doi:10.1007/b137836 (Springer-Verlag Berlin Heidelberg, 2005) (cit. on pp. 19, 21, 22, 25, 27, 30, 31, 32, 33).

129. W. Paul & H. Steinwedel. Notizen: Ein neues Massenspektrometer ohne Magnetfeld. *Zeitschrift für Naturforschung A* **8,** 448–450. doi:doi:10.1515/zna-1953-0710 (1953) (cit. on pp. 19, 20).

130. W. Paul, H. P. Reinhard & U. von Zahn. Das elektrische Massenfilter als Massenspektrometer und Isotopentrenner. *Zeitschrift für Physik* **152,** 143–182. ISSN: 0044-3328. doi:10.1007/BF01327353 (1958) (cit. on pp. 20, 21).

131. L. Schmöger. *Kalte hochgeladene Ionen für Frequenzmetrologie* PhD thesis (Ruprecht-Karls-Universität Heidelberg, Heidelberg, 2017). doi:10.11588/heidok.00023214 (cit. on pp. 21, 23, 24, 25, 26, 31, 63, 109, 110).

132. É. Mathieu. Mémoire sur le mouvement vibratoire d'une membrane de forme elliptique. *Journal de mathématiques pures et appliquées* **13,** 137–203 (1868) (cit. on p. 21).

133. N. McLachlan. *Theory and Application of Mathieu Functions* 1st ed. (Clarendon Press, Oxford, UK, 1947) (cit. on p. 21).

134. M. Drewsen & A. Brøner. Harmonic linear Paul trap: Stability diagram and effective potentials. *Phys. Rev. A* **62,** 045401. doi:10.1103/PhysRevA.62.045401 (2000) (cit. on pp. 23, 25, 26).

135. M. G. Raizen, J. M. Gilligan, J. C. Bergquist, *et al.* Ionic crystals in a linear Paul trap. *Phys. Rev. A* **45,** 6493–6501. doi:10.1103/PhysRevA.45.6493 (1992) (cit. on pp. 23, 25, 26).

136. D. A. Dahl. SIMION for the personal computer in reflection. *International Journal of Mass Spectrometry* **200.** Volume 200: The state of the field as we move into a new millenium, 3–25. ISSN: 1387-3806. doi:10.1016/S1387-3806(00)00305-5 (2000) (cit. on pp. 24, 95, 99, 100, 109, 111, 116, 117, 118).

137. D. J. Wineland, C. Monroe, W. M. Itano, *et al.* Experimental issues in coherent quantum-state manipulation of trapped atomic ions. *Journal of Research of the National Institute of Standards and Technology* **103,** 259–328. doi:10.6028/jres.103.019 (1998) (cit. on pp. 23, 24, 25).

138. H. Dehmelt. in (eds D. Bates & I. Estermann) 53–72 (Academic Press, 1968). doi:10.1016/S0065-2199(08)60170-0 (cit. on p. 25).

139. D. Leibfried, R. Blatt, C. Monroe, *et al.* Quantum dynamics of single trapped ions. *Rev. Mod. Phys.* **75,** 281–324. doi:10.1103/RevModPhys.75.281 (2003) (cit. on pp. 25, 28, 31).

140. M. Knoop, N. Madsen & R. C. Thompson. *Trapped Charged Particles* doi:10.1142/q0004 (WORLD SCIENTIFIC (EUROPE), 2016) (cit. on pp. 25, 27, 31).

141. D. R. Denison. Operating Parameters of a Quadrupole in a Grounded Cylindrical Housing. *Journal of Vacuum Science and Technology* **8,** 266–269. ISSN: 0022-5355. doi:10.1116/1.1316304 (1971) (cit. on p. 27).

142. A. Reuben, G. Smith, P. Moses, *et al.* Ion trajectories in exactly determined quadrupole fields. *International Journal of Mass Spectrometry and Ion Processes* **154,** 43–59. ISSN: 0168-1176. doi:10.1016/0168-1176(96)04374-1 (1996) (cit. on p. 27).

143. D. J. Douglas & N. V. Konenkov. Influence of the 6th and 10th spatial harmonics on the peak shape of a quadrupole mass filter with round rods. *Rapid Communications in Mass Spectrometry* **16,** 1425–1431. doi:10.1002/rcm.735 (2002) (cit. on p. 27).

144. F. Vedel & J. André. Influence of space charge on the computed statistical properties of stored ions cooled by a buffer gas in a quadrupole rf trap. *Phys. Rev. A* **29,** 2098–2101. doi:10.1103/PhysRevA.29.2098 (1984) (cit. on p. 27).

145. Q. A. Turchette, Kielpinski, B. E. King, *et al.* Heating of trapped ions from the quantum ground state. *Phys. Rev. A* **61,** 063418. doi:10.1103/PhysRevA.61.063418 (2000) (cit. on pp. 27, 59).

146. R. G. DeVoe & C. Kurtsiefer. Experimental study of anomalous heating and trap instabilities in a microscopic ^{137}Ba ion trap. *Phys. Rev. A* **65,** 063407. doi:10.1103/PhysRevA.65.063407 (2002) (cit. on pp. 27, 59).

147. S. Narayanan, N. Daniilidis, S. A. Möller, *et al.* Electric field compensation and sensing with a single ion in a planar trap. *Journal of Applied Physics* **110,** 114909. doi:10.1063/1.3665647 (2011) (cit. on p. 27).

148. N. Daniilidis, S. Narayanan, S. A. Möller, *et al.* Fabrication and heating rate study of microscopic surface electrode ion traps. *New Journal of Physics* **13,** 013032. doi:10.1088/1367-2630/13/1/013032 (2011) (cit. on pp. 27, 59).

149. A. Härter, A. Krükow, A. Brunner, *et al.* Long-term drifts of stray electric fields in a Paul trap. *Applied Physics B* **114,** 275–281. ISSN: 1432-0649. doi:10.1007/s00340-013-5688-7 (2014) (cit. on pp. 27, 59).

150. H. Leuthner & G. Werth. Buffer-gas-cooled ion clouds in a classical Paul trap: superimposed stability diagrams and trapping capacity investigations. *Applied Physics B* **114,** 89–98. ISSN: 1432-0649. doi:10.1007/s00340-013-5657-1 (2014) (cit. on p. 27).

151. A. K. Hansen, O. O. Versolato, Ł. Kłosowski, *et al.* Efficient rotational cooling of Coulomb-crystallized molecular ions by a helium buffer gas. *Nature* **508,** 76–79. ISSN: 1476-4687. doi:10.1038/nature12996 (2014) (cit. on p. 27).

152. G. Gabrielse, X. Fei, L. A. Orozco, *et al.* Thousandfold improvement in the measured antiproton mass. *Phys. Rev. Lett.* **65,** 1317–1320. doi:10.1103/PhysRevLett.65.1317 (1990) (cit. on p. 28).

153. G. Gabrielse, A. Khabbaz, D. S. Hall, *et al.* Precision Mass Spectroscopy of the Antiproton and Proton Using Simultaneously Trapped Particles. *Phys. Rev. Lett.* **82,** 3198–3201. doi:10.1103/PhysRevLett.82.3198 (1999) (cit. on p. 28).

154. M. Schwarz, O. O. Versolato, A. Windberger, *et al.* Cryogenic linear Paul trap for cold highly charged ion experiments. *Review of Scientific Instruments* **83,** 083115. doi:10.1063/1.4742770 (2012) (cit. on pp. 28, 54, 63, 110).

155. T. Leopold, S. A. King, P. Micke, *et al.* A cryogenic radio-frequency ion trap for quantum logic spectroscopy of highly charged ions. *Review of Scientific Instruments* **90,** 073201. doi:10.1063/1.5100594 (2019) (cit. on pp. 28, 58, 63, 110).

156. L. Schmöger, O. O. Versolato, M. Schwarz, *et al.* Coulomb crystallization of highly charged ions. *Science* **347,** 1233–1236. doi:10.1126/science.aaa2960 (2015) (cit. on pp. 28, 54).

157. G. Pagano, P. W. Hess, H. B. Kaplan, *et al.* Cryogenic trapped-ion system for large scale quantum simulation. *Quantum Science and Technology* **4,** 014004. doi:10.1088/2058-9565/aae0fe (2018) (cit. on pp. 28, 110).

158. T. W. Hänsch & A. L. Schawlow. Cooling of gases by laser radiation. *Optics Communications* **13,** 68–69. ISSN: 0030-4018. doi:10.1016/0030-4018(75)90159-5 (1975) (cit. on pp. 28, 30).

159. D. J. Wineland & H. Dehmelt. Proposed $10^{14}\Delta\nu < \nu$ Laser Fluorescence Spectroscopy on Ti^+ Mono-Ion Oscillator iii. *Bulletin of the American Physical Society* **20,** 63 (1975) (cit. on p. 28).

160. W. Neuhauser, M. Hohenstatt, P. Toschek, *et al.* Optical-Sideband Cooling of Visible Atom Cloud Confined in Parabolic Well. *Phys. Rev. Lett.* **41,** 233–236. doi:10.1103/PhysRevLett.41.233 (1978) (cit. on p. 28).

161. D. J. Wineland, R. E. Drullinger & F. L. Walls. Radiation-Pressure Cooling of Bound Resonant Absorbers. *Phys. Rev. Lett.* **40,** 1639–1642. doi:10.1103/PhysRevLett.40.1639 (1978) (cit. on pp. 28, 34).

162. W. Heisenberg. Über den anschaulichen Inhalt der quantentheoretischen Kinematik und Mechanik. *Zeitschrift für Physik* **43,** 172–198. doi:10.1007/BF01397280 (1927) (cit. on p. 28).

163. F. Schwabl. *Quantenmechanik (QM I): Eine Einführung* 7th ed. ISBN: 973-3-540-73674-5. doi:10.1007/978-3-540-73675-2 (Springer-Verlag Berlin Heidelberg, 2007) (cit. on p. 28).

164. W. Demtröder. *Laserspektroskopie: Grundlagen und Techniken* 5th ed. ISBN: 978-3-540-33793-5. doi:10.1007/978-3-540-33793-5 (Springer-Verlag Berlin Heidelberg, 2007) (cit. on pp. 28, 30, 103).

165. E. Hecht. *Optik* 7th ed. ISBN: 978-3-11-052664-6. doi:10.1515/9783110526653 (De Gruyter, Berlin, Boston, 2018) (cit. on pp. 28, 30, 79).

166. H. J. Metcalf & P. van der Straten. *Laser Cooling and Trapping* ISBN: 0-387-98728-2. doi:10.1007/978-1-4612-1470-0 (Springer-Verlag New York, 1999) (cit. on pp. 29, 30).

167. M. Wiesinger, F. Stuhlmann, M. Bohman, *et al.* Trap-integrated fluorescence detection with silicon photomultipliers for sympathetic laser cooling in a cryogenic Penning trap. *Review of Scientific Instruments* **94,** 123202. ISSN: 0034-6748. doi:10.1063/5.0170629 (2023) (cit. on pp. 30, 103).

168. D. J. Wineland & W. M. Itano. Laser cooling. *Physics Today* **40,** 34–40. doi:10.1063/1.881076 (1987) (cit. on pp. 30, 31, 32).

169. D. J. Wineland & W. M. Itano. Laser cooling of atoms. *Phys. Rev. A* **20,** 1521–1540. doi:10.1103/PhysRevA.20.1521 (1979) (cit. on pp. 31, 32).

170. H. J. Metcalf & P. van der Straten. Laser cooling and trapping of neutral atoms. *The Optics Encyclopedia: Basic Foundations and Practical Applications* **1,** 975–1014. doi:10.1002/9783527600441.oe005 (2007) (cit. on p. 31).

171. C. J. Campbell. *Trapping, laser cooling, and spectroscopy of Thorium IV* PhD thesis (Georgia Institute of Technology, 2011) (cit. on pp. 32, 35, 37, 39, 40, 43, 46, 47, 48, 49, 73, 75, 121, 127, 132, 136, 142, 143, 144).

172. M. Marciante, C. Champenois, A. Calisti, *et al.* Ion dynamics in a linear radio-frequency trap with a single cooling laser. *Phys. Rev. A* **82,** 033406. doi:10.1103/PhysRevA.82.033406 (2010) (cit. on p. 32).

173. J. J. Bollinger, D. J. Heinzen, F. L. Moore, *et al.* Electrostatic modes of ion-trap plasmas. *Phys. Rev. A* **48,** 525–545. doi:10.1103/PhysRevA.48.525 (1993) (cit. on p. 32).

174. E. L. Pollock & J. P. Hansen. Statistical Mechanics of Dense Ionized Matter. II. Equilibrium Properties and Melting Transition of the Crystallized One-Component Plasma. *Phys. Rev. A* **8,** 3110–3122. doi:10.1103/PhysRevA.8.3110 (1973) (cit. on pp. 32, 33).

175. J. P. Hansen. Statistical Mechanics of Dense Ionized Matter. I. Equilibrium Properties of the Classical One-Component Plasma. *Phys. Rev. A* **8,** 3096–3109. doi:10.1103/PhysRevA.8.3096 (1973) (cit. on p. 32).

176. R. C. T. and. Ion Coulomb crystals. *Contemporary Physics* **56,** 63–79. doi:10.1080/00107514.2014.989715 (2015) (cit. on pp. 32, 33, 35).

177. D. F. V. James. Quantum dynamics of cold trapped ions with application to quantum computation. *Applied Physics B* **66,** 181–190. ISSN: 1432-0649. doi:10.1007/s003400050373 (1998) (cit. on p. 32).

178. V. Blūms, M. Piotrowski, M. I. Hussain, *et al.* A single-atom 3D sub-attonewton force sensor. *Science Advances* **4,** eaao4453. doi:10.1126/sciadv.aao4453 (2018) (cit. on p. 32).

179. *Ion Traps for Tomorrow's Applications* in (eds M. Knoop, I. Marzoli & G. Morigi) **189** (IOS Press, Amsterdam, 2015). ISBN: 978-1-61499-526-5 (cit. on p. 32).

180. F. Diedrich, E. Peik, J. M. Chen, *et al.* Observation of a Phase Transition of Stored Laser-Cooled Ions. *Phys. Rev. Lett.* **59,** 2931–2934. doi:10.1103/PhysRevLett.59.2931 (1987) (cit. on p. 32).

181. D. J. Wineland, J. C. Bergquist, W. M. Itano, *et al.* Atomic-Ion Coulomb Clusters in an Ion Trap. *Phys. Rev. Lett.* **59,** 2935–2938. doi:10.1103/PhysRevLett.59.2935 (1987) (cit. on p. 32).

182. M. Drewsen. Ion Coulomb crystals. *Physica B: Condensed Matter* **460.** Special Issue on Electronic Crystals (ECRYS-2014), 105–113. ISSN: 0921-4526. doi:10.1016/j.physb.2014.11.050 (2015) (cit. on p. 33).

183. S. Ichimaru. Strongly coupled plasmas: high-density classical plasmas and degenerate electron liquids. *Rev. Mod. Phys.* **54,** 1017–1059. doi:10.1103/RevModPhys.54.1017 (1982) (cit. on p. 33).

184. W. L. Slattery, G. D. Doolen & H. E. DeWitt. *N* dependence in the classical one-component plasma Monte Carlo calculations. *Phys. Rev. A* **26,** 2255–2258. doi:10.1103/PhysRevA.26.2255 (1982) (cit. on p. 33).

185. G. S. Stringfellow, H. E. DeWitt & W. L. Slattery. Equation of state of the one-component plasma derived from precision Monte Carlo calculations. *Phys. Rev. A* **41,** 1105–1111. doi:10.1103/PhysRevA.41.1105 (1990) (cit. on p. 33).

186. R. T. Farouki & S. Hamaguchi. Thermal energy of the crystalline one-component plasma from dynamical simulations. *Phys. Rev. E* **47,** 4330–4336. doi:10.1103/PhysRevE.47.4330 (1993) (cit. on p. 33).

187. D. H. E. Dubin & T. M. O'Neil. Trapped nonneutral plasmas, liquids, and crystals (the thermal equilibrium states). *Rev. Mod. Phys.* **71,** 87–172. doi:10.1103/RevModPhys.71.87 (1999) (cit. on p. 33).

188. R. W. Hasse & V. V. Avilov. Structure and Madelung energy of spherical Coulomb crystals. *Phys. Rev. A* **44,** 4506–4515. doi:10.1103/PhysRevA.44.4506 (1991) (cit. on p. 33).

189. J. Allsopp, J. Diprose, B. R. Heazlewood, *et al.* Convolutional neural network approach to ion Coulomb crystal image analysis. *The Journal of Chemical Physics* **163,** 044201. ISSN: 0021-9606. doi:10.1063/5.0272967 (2025) (cit. on p. 33).

190. Y. Yin & S. Willitsch. Ion counting and temperature determination of Coulomb-crystallized laser-cooled ions in traps using convolutional neural networks. *Phys. Rev. Appl.* **24,** 034013. doi:10.1103/zggq-xcbg (2025) (cit. on p. 33).

191. A. Mortensen. *Aspects of Ion Coulomb Crystal based Quantum Memory for Light* PhD thesis (University of Aarhus, 2005) (cit. on p. 34).

192. D. J. Larson, J. C. Bergquist, J. J. Bollinger, *et al.* Sympathetic cooling of trapped ions: A laser-cooled two-species nonneutral ion plasma. *Phys. Rev. Lett.* **57,** 70–73. doi:10.1103/PhysRevLett.57.70 (1986) (cit. on pp. 34, 35).

193. M. Bohman, V. Grunhofer, C. Smorra, *et al.* Sympathetic cooling of a trapped proton mediated by an LC circuit. *Nature* **596,** 514–518. ISSN: 1476-4687. doi:10.1038/s41586-021-03784-w (2021) (cit. on p. 35).

194. P. Bowe, L. Hornekær, C. Brodersen, *et al.* Sympathetic Crystallization of Trapped Ions. *Phys. Rev. Lett.* **82,** 2071–2074. doi:10.1103/PhysRevLett.82.2071 (1999) (cit. on p. 35).

195. K. Mølhave & M. Drewsen. Formation of translationally cold MgH^+ and MgD^+ molecules in an ion trap. *Phys. Rev. A* **62,** 011401. doi:10.1103/PhysRevA.62.011401 (2000) (cit. on p. 35).

196. K. Groot-Berning, F. Stopp, G. Jacob, *et al.* Trapping and sympathetic cooling of single thorium ions for spectroscopy. *Phys. Rev. A* **99,** 023420. doi:10.1103/PhysRevA.99.023420 (2019) (cit. on p. 35).

197. F. Stopp, K. Groot-Berning, G. Jacob, *et al.* Catching, trapping and *in-situ*-identification of thorium ions inside Coulomb crystals of $^{40}Ca^+$ ions. *Hyperfine Interactions* **240,** 073201. doi:10.1007/s10751-019-1579-6 (2019) (cit. on p. 35).

198. B. B. Blinov, L. Deslauriers, P. Lee, *et al.* Sympathetic cooling of trapped Cd^+ isotopes. *Phys. Rev. A* **65,** 040304. doi:10.1103/PhysRevA.65.040304 (2002) (cit. on p. 35).

199. C. J. Campbell, A. G. Radnaev & A. Kuzmich. Wigner Crystals of ^{229}Th for Optical Excitation of the Nuclear Isomer. *Phys. Rev. Lett.* **106,** 223001. doi:10.1103/PhysRevLett.106.223001 (2011) (cit. on pp. 35, 37, 39, 40, 43, 47, 48, 73, 75, 121, 127, 132, 136, 142, 143, 144).

200. U. I. Safronova, W. R. Johnson & M. S. Safronova. Excitation energies, polarizabilities, multipole transition rates, and lifetimes in Th IV. *Phys. Rev. A* **74,** 042511. doi:10.1103/PhysRevA.74.042511 (2006) (cit. on pp. 35, 38).

201. A. Gallagher. Oscillator Strengths of Ca II, Sr II, and Ba II. *Phys. Rev.* **157,** 24–30. doi:10.1103/PhysRev.157.24 (1967) (cit. on pp. 36, 80).

202. F. J. Sullivan. Strontium Lines in Arc and Solar Spectra. *Univ. Pittsburtg Bull.* **35,** 1–8 (1938) (cit. on p. 36).

203. J. E. Sansonetti. Wavelengths, Transition Probabilities, and Energy Levels for the Spectra of Strontium Ions (Sr II through Sr XXXVIII). *Journal of Physical and Chemical Reference Data* **41,** 013102-013102–119. doi:10.1063/1.3659413 (2012) (cit. on p. 36).

204. I. I. Sobelman. *Atomic Spectra and Radiative Transitions* 2nd ed. ISBN: 978-3-540-54518-7. doi:10.1007/978-3-642-76907-8 (Springer Berlin, Heidelberg, 1992) (cit. on pp. 37, 38, 41).

205. C. Schwartz. Theory of Hyperfine Structure. *Phys. Rev.* **97,** 380–395. doi:10.1103/PhysRev.97.380 (1955) (cit. on p. 37).

206. W. Dankwort, J. Ferch & H. Gebauer. Hexadecapole interaction in the atomic ground state of ^{165}Ho. *Zeitschrift für Physik* **267,** 229–237. ISSN: 0044-3328. doi:10.1007/BF01669225 (1974) (cit. on p. 37).

207. K. Beloy, A. Derevianko & W. R. Johnson. Hyperfine structure of the metastable $^3P_2$ state of alkaline-earth-metal atoms as an accurate probe of nuclear magnetic octupole moments. *Phys. Rev. A* **77,** 012512. doi:10.1103/PhysRevA.77.012512 (2008) (cit. on p. 37).

208. K. Beloy. Hyperfine Structure in $^{229g}Th^{3+}$ as a Probe of the $^{229g}Th \rightarrow ^{229m}$ Th Nuclear Excitation Energy. *Phys. Rev. Lett.* **112,** 062503. doi:10.1103/PhysRevLett.112.062503 (2014) (cit. on p. 37).

209. I. V. Hertel & C.-P. Schulz. *Atome, Moleküle und optische Physik 1. Atomphysik und Grundlagen der Spektroskopie* 1st ed. ISBN: 978-3-540-30613-9. doi:10.1007/978-3-540-30617-7 (Springer Berlin, Heidelberg, 2008) (cit. on pp. 37, 41, 42).

210. N. Stone. Table of nuclear magnetic dipole and electric quadrupole moments. *Atomic Data and Nuclear Data Tables* **90,** 75–176. ISSN: 0092-640X. doi:10.1016/j.adt.2005.04.001 (2005) (cit. on p. 37).

211. S. Gerstenkorn, P. Luc, J. Verges, *et al.* Hyperfine structure, magnetic and quadrupole moments of the thorium 229 isotope Structures hyperfines du spectre d'étincelle, moment magnétique et quadrupolaire de l'isotope 229 du thorium. *J.Phys.France* **35,** 483–495. doi:10.1051/jphys:01974003506048300 (1974) (cit. on p. 37).

212. S. G. Porsev, M. S. Safronova & M. G. Kozlov. Precision Calculation of Hyperfine Constants for Extracting Nuclear Moments of ^{229}Th. *Phys. Rev. Lett.* **127,** 253001. doi:10.1103/PhysRevLett.127.253001 (2021) (cit. on p. 37).

213. G. Zitzer, J. Tiedau, C. E. Düllmann, *et al.* Laser spectroscopy on the hyperfine structure and isotope shift of sympathetically cooled $^{229}Th^{3+}$ ions. *Phys. Rev. A* **111,** L050802. doi:10.1103/PhysRevA.111.L050802 (2025) (cit. on pp. 37, 39, 40, 43, 46, 47, 49, 74, 75, 123, 124, 126, 127, 128, 132, 133, 136, 142, 143).

214. C. J. Campbell, A. V. Steele, L. R. Churchill, *et al.* Multiply Charged Thorium Crystals for Nuclear Laser Spectroscopy. *Phys. Rev. Lett.* **102,** 233004. doi:10.1103/PhysRevLett.102.233004 (2009) (cit. on pp. 38, 73, 80).

215. G. Racah. Theory of Complex Spectra. II. *Phys. Rev.* **62,** 438–462. doi:10.1103/PhysRev.62.438 (1942) (cit. on p. 41).

216. A. R. Edmonds. *Angular Momentum in Quantum Mechanics* (Princeton Universtiy Press, Princeton; New Jersey, USA, 1957) (cit. on p. 42).

217. J. Thielking. *Hyperfine studies of Th-229 in its nuclear ground and isomeric state* PhD thesis (Physikalisch-Technische Bundesanstalt (PTB), Braunschweig, 2020). doi:10.7795/110.20200831 (cit. on pp. 42, 43).

218. V. Sonnenschein, I. D. Moore, S. Raeder, *et al.* The search for the existence of ^{229m}Th at IGISOL. *The European Physical Journal A* **48,** 52. ISSN: 1434-601X. doi:10.1140/epja/i2012-12052-3 (2012) (cit. on p. 43).

219. M. S. Safronova, S. G. Porsev, M. G. Kozlov, *et al.* Nuclear Charge Radii of ^{229}Th from Isotope and Isomer Shifts. *Phys. Rev. Lett.* **121,** 213001. doi:10.1103/PhysRevLett.121.213001 (2018) (cit. on p. 43).

220. J. T. Milek & M. Neuberger. in *Linear Electrooptic Modular Materials* 5–14 (Springer US, Boston, MA, 1972). ISBN: 978-1-4684-6168-8. doi:10.1007/978-1-4684-6168-8_2 (cit. on p. 50).

221. B. E. A. Saleh & M. C. Teich. in *Fundamentals of Photonics* 696–736 (John Wiley & Sons, Ltd, 1991). ISBN: 9780471213741. doi:https://doi-org/10.1002/0471213748.ch18 (cit. on p. 50).

222. T. Kawanishi. in *Electro-optic Modulation for Photonic Networks: Precise and high-speed control of lightwaves* 121–167 (Springer International Publishing, Cham, 2022). ISBN: 978-3-030-86720-1. doi:10.1007/978-3-030-86720-1_6 (cit. on p. 51).

223. D. Moritz. *Commissioning and Characterization of the Ion Guide and Mass Selection System for the Nuclear Clock Setup* Master's thesis (LMU München, München, 2020) (cit. on pp. 53, 54, 61, 84, 113, 135).

224. B. Seiferle, D. Moritz, **K. Scharl**, *et al.* Extending Our Knowledge about the ^{229}Th Nuclear Isomer. *Atoms* **10.** ISSN: 2218-2004. doi:10.3390/atoms10010024 (2022) (cit. on pp. 53, 54, 59).

225. **K. Scharl**, S. Ding, G. Holthoff, *et al.* Setup for the Ionic Lifetime Measurement of the ^{229m}Th^{3+} Nuclear Clock Isomer. *Atoms* **11.** ISSN: 2218-2004. doi:10.3390/atoms11070108 (2023) (cit. on pp. 53, 54, 59, 68, 70, 71, 72, 75, 77, 78, 79).

226. D. Moritz, **K. Scharl**, M. Wiesinger, *et al.* A cryogenic Paul trap for probing the nuclear isomeric excited state ^{229m}Th^{3+}. *The European Physical Journal D* **79,** 127. ISSN: 1434-6079. doi:10.1140/epjd/s10053-025-01071-1 (2025) (cit. on pp. 53, 55, 56, 57, 61, 65, 84, 88, 111, 112, 118, 129).

227. M. Drewsen, C. Brodersen, L. Hornekær, *et al.* Large Ion Crystals in a Linear Paul Trap. *Phys. Rev. Lett.* **81,** 2878–2881. doi:10.1103/PhysRevLett.81.2878 (1998) (cit. on p. 53).

228. P. Micke, J. Stark, S. A. King, *et al.* Closed-cycle, low-vibration 4 K cryostat for ion traps and other applications. *Review of Scientific Instruments* **90,** 065104. doi:10.1063/1.5088593 (2019) (cit. on pp. 54, 63, 65, 110).

229. J. B. Neumayr, P. G. Thirolf, D. Habs, *et al.* Performance of the MLL-IonCatcher. *Review of Scientific Instruments* **77,** 065109. ISSN: 0034-6748. doi:10.1063/1.2213154 (2006) (cit. on pp. 55, 135).

230. K. Eberhardt, C. E. Düllmann, R. Haas, *et al.* Actinide targets for fundamental research in nuclear physics. *AIP Conference Proceedings* **1962,** 030009. ISSN: 0094-243X. doi:10.1063/1.5035526 (2018) (cit. on p. 56).

231. D. R. Leibrandt, R. J. Clark, J. Labaziewicz, *et al.* Laser ablation loading of a surface-electrode ion trap. *Phys. Rev. A* **76,** 055403. doi:10.1103/PhysRevA.76.055403 (2007) (cit. on pp. 57, 94).

232. P. B. Antohi, D. Schuster, G. M. Akselrod, *et al.* Cryogenic ion trapping systems with surface-electrode traps. *Review of Scientific Instruments* **80,** 013103. doi:10.1063/1.3058605 (2009) (cit. on pp. 57, 58).

233. A. Osada & A. Noguchi. Deterministic loading of a single strontium ion into a surface electrode trap using pulsed laser ablation. *Journal of Physics Communications* **6,** 015007. doi:10.1088/2399-6528/ac4b4a (2022) (cit. on pp. 57, 94).

234. T. Dubielzig, S. Halama, H. Hahn, *et al.* Ultra-low-vibration closed-cycle cryogenic surface-electrode ion trap apparatus. *Review of Scientific Instruments* **92,** 043201. doi:10.1063/5.0024423 (2021) (cit. on pp. 58, 63, 65, 110).

235. R. Spivey, I. Inlek, Z. Jia, *et al.* High-Stability Cryogenic System for Quantum Computing With Compact Packaged Ion Traps. *IEEE Transactions on Quantum Engineering* **3,** 1–11. ISSN: 2689-1808. doi:10.1109/TQE.2021.3125926 (2022) (cit. on p. 58).

236. E. K. Haettner. *A novel radio frequency quadrupole system for SHIPTRAP & new mass measurements of rp nuclides* Dissertation, Justus-Liebig-Universität Gießen, 2011. PhD thesis (Justus-Liebig-Universität Gießen, Gießen, 2011), 163 (cit. on p. 61).

237. E. Haettner, W. R. Plaß, U. Czok, *et al.* A versatile triple radiofrequency quadrupole system for cooling, mass separation and bunching of exotic nuclei. *Nuclear Instruments and Methods in Physics Research Section A: Accelerators, Spectrometers, Detectors and Associated Equipment* **880,** 138–151. ISSN: 0168-9002. doi:10.1016/j.nima.2017.10.003 (2018) (cit. on p. 61).

238. W. M. Brubaker. An improved quadrupole mass analyzer. *Adv. Mass Spectrom* **4,** 293–299 (1968) (cit. on p. 61).

239. M. Schwarz. *Lasermanipulation von rotationsgekühlten Molekülionen in einer neuen kryogenen Paul-Falle* PhD thesis (Ruprecht-Karls-Universität Heidelberg, Heidelberg, 2012). doi:10.11588/heidok.00013535 (cit. on p. 63).

240. C. Wang & J. G. Hartnett. A vibration free cryostat using pulse tube cryocooler. *Cryogenics* **50,** 336–341. ISSN: 0011-2275. doi:10.1016/j.cryogenics.2010.01.003 (2010) (cit. on p. 63).

241. H. Cao. Vibration control for mechanical cryocoolers. *Cryogenics* **128,** 103595. ISSN: 0011-2275. doi:10.1016/j.cryogenics.2022.103595 (2022) (cit. on p. 63).

242. A. A. Madej, L. Marmet & J. E. Bernard. Rb atomic absorption line reference for single Sr^+ laser cooling systems. *Applied Physics B* **67,** 229–234. doi:10.1007/s003400050498 (1998) (cit. on p. 67).

243. A. G. Sinclair, M. A. Wilson & P. Gill. Improved three-dimensional control of a single strontium ion in an endcap trap. *Optics Communications* **190,** 193–203. ISSN: 0030-4018. doi:10.1016/S0030-4018(01)01057-4 (2001) (cit. on pp. 67, 99, 104).

244. D. J. Berkeland. Linear Paul trap for strontium ions. *Review of Scientific Instruments* **73,** 2856–2860. doi:10.1063/1.1489073 (2002) (cit. on pp. 67, 99).

245. M. Brownnutt. *$^{88}Sr^{+}$ ion trapping techniques and technologies for quantum information processing* PhD thesis (Imperial College London, London, 2007) (cit. on p. 67).

246. S. Removille, R. Dubessy, B. Dubost, *et al.* Trapping and cooling of Sr^{+}ions: strings and large clouds. *Journal of Physics B: Atomic, Molecular and Optical Physics* **42,** 154014. doi:10.1088/0953-4075/42/15/154014 (2009) (cit. on pp. 67, 99, 102, 104, 105).

247. B. Dubost, R. Dubessy, B. Szymanski, *et al.* Isotope shifts of natural Sr^{+} measured by laser fluorescence in a sympathetically cooled Coulomb crystal. *Phys. Rev. A* **89,** 032504. doi:10.1103/PhysRevA.89.032504 (2014) (cit. on p. 67).

248. K. Jung, K. Yamamoto, Y. Yamamoto, *et al.* All-diode-laser cooling of Sr^{+} isotope ions for analytical applications. *Japanese Journal of Applied Physics* **56,** 062401. doi:10.7567/jjap.56.062401 (2017) (cit. on pp. 67, 72, 99, 102).

249. A. D. Shiner, A. A. Madej, P. Dubé, *et al.* Absolute optical frequency measurement of saturated absorption lines in Rb near 422 nm. *Applied Physics B* **89,** 595–601. doi:10.1007/s00340-007-2836-y (2007) (cit. on pp. 67, 69, 102).

250. Z. Zhang, J. Ma, L. Zhang, *et al.* Rubidium Isotope Ratios of International Geological Reference Materials. *Geostandards and Geoanalytical Research* **n/a.** doi:10.1111/ggr.12484 (cit. on p. 67).

251. A. Uchiyama, K. Harada, K. Sakamoto, *et al.* Effective multiple sideband generation using an electro-optic modulator for a multiple isotope magneto-optical trap. *Review of Scientific Instruments* **89.** 123111. ISSN: 0034-6748. doi:10.1063/1.5054748 (2018) (cit. on p. 74).

252. G. Zitzer, J. Tiedau, M. V. Okhapkin, *et al.* Sympathetic cooling of trapped Th^{3+} alpha-recoil ions for laser spectroscopy. *Phys. Rev. A* **109,** 033116. doi:10.1103/PhysRevA.109.033116 (2024) (cit. on pp. 75, 118, 136).

253. B. M. White, P. J. Low, Y. de Sereville, *et al.* Isotope-selective laser ablation ion-trap loading of $^{137}Ba^{+}$ using a $BaCl_2$ target. *Phys. Rev. A* **105,** 033102. doi:10.1103/PhysRevA.105.033102 (2022) (cit. on pp. 88, 90).

254. G. Vrijsen, Y. Aikyo, R. F. Spivey, *et al.* Efficient isotope-selective pulsed laser ablation loading of $^{147}Yb^{+}$ ions in a surface electrode trap. *Opt. Express* **27,** 33907–33914. doi:10.1364/OE.27.033907 (2019) (cit. on p. 90).

255. G. P. Barwood, P. Gill, G. Huang, *et al.* Sub-kHz "clock" transition linewidths in a cold trapped $^{88}Sr^{+}$ in low magnetic fields using 1092-nm polarisation switching. *Optics Communications* **151,** 50–55. ISSN: 0030-4018. doi:10.1016/S0030-4018(97)00743-8 (1998) (cit. on p. 99).

256. J. F. Kielkopf. New approximation to the Voigt function with applications to spectral-line profile analysis. *J. Opt. Soc. Am.* **63,** 987–995. doi:10.1364/JOSA.63.000987 (1973) (cit. on p. 103).

257. I. Siemers, M. Schubert, R. Blatt, *et al.* The "Trapped State" of a Trapped Ion-Line Shifts and Shape. *Europhysics Letters* **18,** 139. doi:10.1209/0295-5075/18/2/009 (1992) (cit. on pp. 104, 105).

258. P. Langevin. Une formule fondamentale de théorie cinétique, 245–88 (1905) (cit. on p. 110).

259. R. D. Johnson III. NIST Standard Reference Database 101. *NIST Computational Chemistry Comparison and Benchmark Database.* doi:DOI:10.18434/T47C7Z (2022) (cit. on p. 110).

260. T. N. Olney, N. Cann, G. Cooper, *et al.* Absolute scale determination for photoabsorption spectra and the calculation of molecular properties using dipole sum-rules. *Chemical Physics* **223,** 59–98. ISSN: 0301-0104. doi:10.1016/S0301-0104(97)00145-6 (1997) (cit. on p. 110).

261. J. Repp, C. Böhm, J. R. Crespo López-Urrutia, *et al.* PENTATRAP: a novel cryogenic multi-Penning-trap experiment for high-precision mass measurements on highly charged ions. *Applied Physics B* **107,** 983–996. ISSN: 1432-0649. doi:10.1007/s00340-011-4823-6 (2012) (cit. on p. 110).

262. S. Sellner, M. Besirli, M. Bohman, *et al.* Improved limit on the directly measured antiproton lifetime. *New Journal of Physics* **19,** 083023. doi:10.1088/1367-2630/aa7e73 (2017) (cit. on p. 110).

263. G. Zitzer, J. Tiedau, M. V. Okhapkin, *et al.* Sympathetic cooling of trapped Th^{3+} alpha-recoil ions for laser spectroscopy. *Phys. Rev. A* **109,** 033116. doi:10.1103/PhysRevA.109.033116 (2024) (cit. on p. 123).

264. K. R. Brown, J. Kim & C. Monroe. Co-designing a scalable quantum computer with trapped atomic ions. *npj Quantum Information* **2,** 16034. ISSN: 2056-6387. doi:10.1038/npjqi.2016.34 (2016) (cit. on p. 131).

265. A. M. Hankin, E. R. Clements, Y. Huang, *et al.* Systematic uncertainty due to background-gas collisions in trapped-ion optical clocks. *Phys. Rev. A* **100,** 033419. doi:10.1103/PhysRevA.100.033419 (2019) (cit. on p. 131).

266. Y. Aikyo, G. Vrijsen, T. W. Noel, *et al.* Vacuum characterization of a compact room-temperature trapped ion system. *Applied Physics Letters* **117,** 234002. ISSN: 0003-6951. doi:10.1063/5.0029236 (2020) (cit. on p. 131).

267. K. Abich, A. Keil, D. Reiss, *et al.* Thermally activated hopping of two ions trapped in a bistable potential well. *Journal of Optics B: Quantum and Semiclassical Optics* **6,** S18. doi:10.1088/1464-4266/6/3/004 (2004) (cit. on p. 131).

268. J. Liang & P. C. Haljan. Hopping of an impurity defect in ion crystals in linear traps. *Phys. Rev. A* **83,** 063401. doi:10.1103/PhysRevA.83.063401 (2011) (cit. on p. 131).

269. L.-A. Rüffert, E. A. Dijck, L. Timm, *et al.* Domain formation and structural stabilities in mixed-species Coulomb crystals induced by sympathetically cooled highly charged ions. *Phys. Rev. A* **110,** 063110. doi:10.1103/PhysRevA.110.063110 (2024) (cit. on p. 131).

270. G. Zitzer. Private Communication. 2025 (cit. on p. 134).

271. P. Dubé, J. E. Bernard & M. Gertsvolf. Absolute frequency measurement of the $^{88}Sr^{+}$ clock transition using a GPS link to the SI second. *Metrologia* **54,** 290. doi:10.1088/1681-7575/aa5e60 (2017) (cit. on p. 137).

272. M. Steinel, H. Shao, M. Filzinger, *et al.* Evaluation of a $^{88}Sr^{+}$ Optical Clock with a Direct Measurement of the Blackbody Radiation Shift and Determination of the Clock Frequency. *Phys. Rev. Lett.* **131,** 083002. doi:10.1103/PhysRevLett.131.083002 (2023) (cit. on p. 137).

Publications and Presentations

List of Publications

1. D. Moritz, **K. Scharl**[1], M. Wiesinger, G. Holthoff, T. Teschler, M. I. Hussain, J. R. Crespo López-Urrutia, T. Dickel, S. Ding, C. E. Düllmann, E. R. Hudson, S. Kraemer, L. Löbell, C. Mokry, J. Runke, B. Seiferle, L. von der Wense, F. Zacherl and P. G. Thirolf. A cryogenic Paul trap for probing the nuclear isomeric excited state $^{229\mathrm{m}}Th^{3+}$. *The European Physical Journal D.* **79**, 127. doi: 10.1140/epjd/s10053-025-01071-1 (2025)

2. R. Elwell, J. E. S. Terhune, C. Schneider, H. W. T. Morgan, H. Bao Tran Tan, U. C. Perera, D. A. Rehn, M. C. Alfonso, L von der Wense, B. Seiferle, **K. Scharl**, P. G. Thirolf, A. Derevianko and E. R. Hudson. ^{229}Th Nuclear Spectroscopy in an Opaque Material: Laser-Based Conversion Electron Mössbauer Spectroscopy of $^{229}ThO_2$. Submitted to *Nature*. Review process ongoing. Preprint: 10.48550/arXiv.2506.03018

3. S. V. Pineda, P. Chhetri, S. Bara, Y. Elskens, S. Casci, A. N. Alexandrova, M. Au, M. Athanasakis-Kaklamanakis, M. Bartokos, K. Beeks, C. Bernerd, A. Claessens, K. Chrysalidis, T. E. Cocolios, J. G. Correia, H. De Witte, R. Elwell, R. Ferrer, R. Heinke, E. R. Hudson, F. Ivandikov, Yu. Kudryavtsev, U. Köster, S. Kraemer, M. Laatiaoui, R. Lica, C. Merckling, I. Morawetz, H. W. T. Morgan, D. Moritz, L. M. C. Pereira, S. Raeder, S. Rothe, F. Schaden, **K. Scharl**, T. Schumm, S. Stegemann, J. Terhune, P. G. Thirolf, S. M. Tunhuma, P. Van Den Bergh, P. Van Duppen, A. Vantomme, U. Wahl and Z. Yue. Radiative decay of the ^{229m}Th nuclear clock isomer in different host materials. *Phys. Rev. Research.* **7**, 013052. doi: 10.1103/PhysRevResearch.7.013052 (2025)

4. P. G. Thirolf, S. Kraemer, D. Moritz and **K. Scharl**. The thorium isomer ^{229m}Th: review of status and perspectives after more than 50 years of research. *Eur. Phys. J. Spec. Top.* **233**(5), 1113-1131. doi: 10.1140/epjs/s11734-024-01098-2 (2024)

[1] Co-first authorship

5. **K. Scharl**[2], S. Ding, G. Holthoff, M. I. Hussain, S. Kraemer, L. Löbell, D. Moritz, T. Rozibakieva, B. Seiferle, F. Zacherl and P. G. Thirolf. Setup for the Ionic Lifetime Measurement of the $^{229m}Th^{3+}$ Nuclear Clock Isomer. *Atoms.* **11**(108). doi: `10.3390/atoms11070108` (2023)

6. B. Seiferle, D. Moritz, **K. Scharl**, S. Ding, F. Zacherl, L. Löbell and P. G. Thirolf. Extending Our Knowledge about the ^{229}Th Nuclear Isomer. *Atoms.* **10**(24). doi: `10.3390/atoms10010024` (2022)

List of Presentations

1. Nuclear Clock ERC Meeting, PTB, Braunschweig, "Status of the $^{229(m)}Th$ Hyperfine Structure Laser Spectroscopy at LMU", May 2025

2. DPG Frühjahrstagung (SAMOP), Bonn, "Towards a Precision Measurement of the ^{229m}Th Isomeric Lifetime via Hyperfine Structure Laser Spectroscopy", March 2025

3. Nuclear Clock ERC Meeting, TU Wien, Vienna, "A Cryogenic Paul Trap Experiment for Laser Spectroscopy of the $^{229m}Th^{3+}$ Nuclear Clock Isomer ", April 2024

4. DPG Frühjahrstagung (SAMOP), Freiburg, "A Cryogenic Paul Trap Experiment for Laser Spectroscopy of the $^{229m}Th^{3+}$ Nuclear Clock Isomer", March 2024

5. Nuclear Clock ERC Meeting, LMU Munich, Munich, "Preparations for sympathetic laser cooling of $^{229m}Th^{3+}$ via $^{88}Sr^{+}$", April 2023

6. DPG Frühjahrstagung (SAMOP), Hannover, "Preparations for sympathetic laser cooling of $^{229m}Th^{3+}$ via $^{88}Sr^{+}$", March 2023

7. Nuclear Clock ERC Meeting, PTB, Berlin, "Towards the Lifetime Measurement of the $^{229m}Th^{3+}$ Nuclear Clock Isomer", May 2022

8. "100 Years of Nuclear Isomers" EMMI Conference, Harnack-Haus, Berlin, "Towards the Lifetime Measurement of the $^{229m}Th^{3+}$ Nuclear Clock Isomer", May 2022 **(poster)**

9. DPG Frühjahrstagung (SAMOP), Erlangen, "Towards the Lifetime Measurement of the $^{229m}Th^{3+}$ Nuclear Clock Isomer", March 2022

10. LS Parodi Chair Seminar, LMU München, Munich "Lifetime Measurement of the Isomeric State in $^{229}Th^{3+}$", June 2021

11. Nuclear Clock ERC Meeting, Online Event, "Lifetime Measurement of the Isomeric State in $^{229}Th^{3+}$", March 2021

[2]First authorship

Acknowledgements

First of all, I want to thank Prof. Dr. Peter G. Thirolf for giving me the opportunity to work in this interesting field, his near-endless trust in me to tackle the technical challenges to perform the experiments of this work, and his encouraging words during hard times in the laboratory.

Next to Peter, I am very grateful for my first postdoctoral supervisor, Dr. Benedict Seiferle, who gave me a great introduction into the research field of ^{229m}Th and made the start in the laboratory during the pandemic in 2020 and 2021 very enjoyable. After Benedict, many thanks also go to Dr. Shiqian Ding, Dr. Sandro Kraemer, Dr. Mahmood I. Hussain, and Dr. Markus Wiesinger for their advice and support to get our wonderful machine up and running.

Many thanks also go to my colleagues in the lab and the office: Daniel Moritz, Georg Holthoff, Tamila Teschler, Sultan Alzahrani, Florian Zacherl, Lilli Löbell, Tim Teuner, Jakob Rebhan, and Erin Grace Fitzpatrick. Thank you all for the good working atmosphere and the versatile support in case I was in need of a special tool, a cell phone charger, or a beer in the evening. A special thanks goes to our two Italian colleagues, Dr. Nazarena Tortorelli and Beatrice Villata, for organizing nice social events with their exquisite home-cooked food. Mille Grazie!

I want to thank Prof. Dr. Katia Parodi as well as Prof. Dr. Jörg Schreiber, Dr. Jona Bortfeld, Prof. Dr. Marco Riboldi, Dr. Chiara Gianoli, Petra Glier, Eileen Helm, and the other members of the chair for the relaxed and productive atmosphere at the chair of medical physics. For good times during the work and also off the Garching-Campus, special thanks go to the Aperitivo-gang Giulio Lovatti, Francesco Evangelista, Caroline Steinbrecht, Beatrice Foglia, Angelica Noto, Ze Huang, Dr. Prasannakumar Palaniappan, and Dr. Munetaka Nitta.

I will always remember with joy the birthday of Dr. Franz Englbrecht as the starting point of a spontaneous clubbing night. Franz, Dr. Sonja Gerlach, Laura Geulig, Leonard Doyle, Michael Bachhammer, Dr. Martin Speicher, many thanks for this fantastic night and for keeping me off from raiding the bar of "089-Bar".

Acknowledgements

Experimental physics is, in many regards, also a question of equipment. I want to thank Julia Liese, Anna-Katharina Schmidt, and Dr. Vitaly Wirthl for helping me with components and devices on short notice more often than I wished.

With Prof. Dr. Jörg Schreiber, Julia and Anna made the annual chair retreat in Wartaweil a musical experience - many thanks for the fun and cheerful evenings.

When it comes to hardware, mechanical components, and other lab supplies, I could also always count on Florian Saran, Dr. Hans-Friedrich Wirth, the LMU mechanical workshop with Rolf Oehm, Thomas Seppeur, and Roland Schmid, as well as on the LMU electronics workshop with Dr. Andre Zibell and Fabian Eschenbrücher.

I enjoyed the work in an international research collaboration with the TU Vienna, PTB Braunschweig, Universität Würzburg, ILT Fraunhofer, and the University of Delaware. I especially want to thank Prof. Dr. Thorsten Schumm, Dr. Kjeld Beeks, Michael Bartokos, Ira Morawetz, Fabian Schaden, Dr. Johannes Tiedau, Dr. Tomas Sikorsky, Tobias Kirschbaum, and Stephan Wissenberg for good times during the annual ERC synergy meetings.

I also want to acknowledge the tremendous support in laser technical details from Dr. Maksim Okhapkin at PTB in the early phase of the PhD and the strategic advice on our setup design given by Dr. Lars von der Wense and Dr. Akira Ozawa.

A big thank you goes to Gregor Zitzer from the PTB team for inspiring discussions, suggestions for experimental procedures, and the fun evening at the DPG conference in Bonn (involving Kölsch).

Either in Los Angeles or at the Oktoberfest in Munich, I enjoyed the time with our thorium colleagues from the USA. Many thanks go to Prof. Dr. Eric Hudson, Dr. Ricky Elwell, and James Terhune also for connecting me with Prof. Dr. Nick Hutzler and Dr. Hao Wu, who gave me valuable information on how to buy and install a good-value second-hand ablation laser.

For the enlightening discussions on atomic spectroscopy and enjoyable moments at DPG conferences, I thank the members of our little journal club from MPQ, Jorge Moreno, Florian Egli, and Muhammad Thariq.

Johannes Flommersfeld and Jana Steuer, you made studying physics fun! Many thanks for the great memories since our first T0 exercise sheet.

During the whole doctorate, the monthly Stammtisch in Munich with my close friends Felizitas Backhaus, Serafín Unglert, Hansjörg Geier, Sebastian Stecher, and Lukas Schilling was the best occasion to cheer me up when things in the lab were not running as smoothly as they should. Thanks, guys!

Michael Schweinberger, Sebastian Stolte, Tobias Würfel, and Tim Fürmann, thank you for your friendship and companionship through sports, school, theater, studies, and above all, life itself.

I am deeply grateful for the wholehearted support of my family through every circumstance and challenge, and for the opportunity to study and pursue a PhD in Munich, which cannot always be taken for granted.

With all my heart, I want to thank my best companion and love of my life, Alessia, for her unlimited support, patience, and encouragement during the last six years.
Thank You!